LANTHANUM STRONTIUM VANADATE IN SOLID OXIDE FUEL CELLS

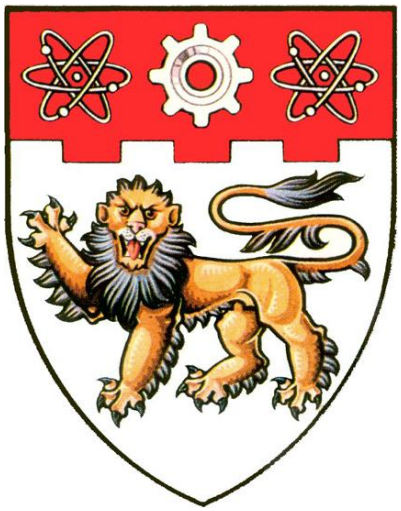

GE XIAOMING

School of Mechanical and Aerospace Engineering

Nanyang Technological University

2012

LANTHANUM STRONTIUM VANADATE IN SOLID OXIDE FUEL CELLS

GE XIAOMING

School of Mechanical & Aerospace Engineering

A thesis submitted to the Nanyang Technological University in fulfilment of the requirements for the Degree of Doctor of Philosophy

2011

ACKNOWLEDGEMENTS

Here I would like to express my most sincere appreciation and gratitude to my supervisor, Professor Chan Siew Hwa, for his considerate guidance and encouragement all throughout this PhD project. I have learnt so much for his expertise in the fields of solid oxide fuel cells and mathematical modelling. More than a supervisor, it is his personality, lifestyle, and working philosophy that inspire me all through this four-year odyssey.

I thank Dr. Liu Qinglin for his initial effort on launching this PhD project. I also thank Mr. Chen Xinbing, Mr. Alireza Babaei, and Dr. Zhang Lan for miscellaneous discussions. Mr. Zhao Cunlu is acknowledged for introducing me the computational tool, Wolfram Mathematica® 7. Ms. Fang Yanan (School of MSE) is acknowledged for her kindly help in X-ray powder diffraction characterization. My warmest acknowledgement goes to Dr. Fu Changjing for insightful discussions over versatile project topics. My thanks also extend to all technicians in Fuel Cell Laboratory (ERI@N), Materials Laboratory A, and Computer Aided Engineering Laboratory for technical guidance and assistance.

ABSTRACT

Solid oxide fuel cells (SOFCs) are high temperature energy conversion devices with the advantages of fuel flexibility and high efficiency. Limitations of SOFC cermet anodes have been stimulating oxide anodes. Lanthanum strontium vanadate, $La_{1-x}Sr_xVO_3$ (LSV, $0 \leq x \leq 1$), have been synthesized and examined as potential SOFC anode materials. LSV appear to be chemically compatible with yttria-stabilized zirconia (YSZ) at least up to 1300 ℃. Electrode performance is evaluated by impedance spectroscopy and dc polarization between 800 to 1000 ℃. Good electrode performance is achieved with LSV(x = 0.2, 0.3, 0.4, 0.5)–YSZ composite anodes, in both pure H_2 and 3% H_2O humidified CH_4. For half-cells with $La_{0.6}Sr_{0.4}VO_3$–YSZ anode, polarization resistance is 0.85 Ω cm^2 and 1.38 Ω cm^2 at 900 ℃ in pure H_2 and wet CH_4, respectively. When drawing a current of 0.2 A/cm^2 at 900 ℃, the overpotential is 0.13 V in pure H_2, and slightly higher in wet CH_4, 0.20 V. Further optimization of electrode microstructures is needed to maximize the performance of LSV for potential SOFC application.

LSV synthesized by soft chemistry methods show higher catalytic activity than those via solid state reactions. To elucidate the interfacial reaction behaviours, impedance responses of LSV8020 (50 wt. %)–YSZ anodes are recorded and interpreted in H_2–H_2O–He atmosphere. The typical impedance pattern corresponds to three types of physical phenomena, viz. reaction impedance, gas concentration impedance, and inductive loops that only emerge at highly biased conditions. The gas concentration impedance is significantly inhibited in wet atmosphere. A detrimental water effect is observed for up to 15 vol. % H_2O.

The double layer structure of solid oxide fuel cell anode/electrolyte interfaces is simulated by Markov Chain Monte Carlo methods. A case study is carried out on lanthanum strontium vanadate (LSV)/yttria-stabilized zirconia (YSZ). The density of oxygen vacancies directly adjacent to the LSV/YSZ interface is one order of magnitude higher than the bulk value of YSZ. The spatial variation of oxygen vacancies in the double layer region exhibits exponential decay behaviour. The double layer undergoes pronounced relaxations when the interfaces are under anodic biases in the range from 0

to 150 mV. The results indicate that 70–80% of the oxygen vacancies are immobilized in the Helmholtz–Perrin layer. The rationale has wide applications on elucidating anodic reaction mechanisms and potential distributions across anode/electrolyte interfaces.

The double layer of electrode/electrolyte interfaces plays a fundamental role in determining the performance of solid state electrochemical cells. The double layer capacitance is one of the most-studied descriptors of the double layer. This project examines a case study on LSV/YSZ interfaces that are exposed in solid oxide fuel cell anode environment. The apparent double layer capacitance is obtained from impedance spectroscopy. The intrinsic double layer capacitance is evaluated based on Stern's method in conjunction with the Volta potential analysis across LSV/YSZ interfaces. Both the apparent and the intrinsic double layer capacitances exhibit right-skewed volcano patterns, when the interfaces are subjected to anodic biases from 0 to 150 mV. The apparent double layer capacitance is about one order of magnitude larger than the intrinsic double layer capacitance. This discrepancy roots in the inconsistent surface areas that are involved. This capacitance analysis would provide a more realistic estimate of the TPBs of on-running solid-state electrochemical devices.

Electrochemical reactions in solid oxide fuel cells take place around three-phase boundaries (TPBs). The electrochemically active zones (EAZs) are generated in three-dimensions around the TPBs of on-running SOFCs. This project investigates the behaviours of TPBs and EAZs via a case study on LSV–YSZ composite anode. A percolating binary particle aggregate, based on geometric random loose packing model and traditional sintering theory, is constructed to represent the LSV–YSZ anode. The TPB lengths of LSV–YSZ anodes are evaluated from the coordination numbers and sintering necks among particles in the particle aggregate. Empirical interrelations among TPBs, EAZs, active electrode thickness, in-depth penetration of electrocatalysts of polarized LSV–YSZ anode are established.

The feasibility of LSV-based SOFCs fed with practical feedstocks, e.g. syngas, town gas, coal gas, and biogas, has been proven in this project. The exchange current densities of LSV anodes in various atmospheres are in the range from 0.05 to 0.2 A/cm^2. The typical overpotential is about 60 mV in H_2 and at 900 ℃. LSV anodes are not coked by

deposited carbon when exposed to carbon-forming gases. More interestingly, LSV undergoes continuous activation, rather than poisoning, when exposed to gases containing 50 ppm H_2S. The beneficial H_2S effect is due to the nanostructured sulphur compounds that are in situ generated by interactions between LSV and H_2S. LSV-based SOFCs have demonstrated with negligible performance degradation in carbon-forming and H_2S-containing gases for more than 500 hours.

LIST OF PUBLICATIONS

Journal Articles

[1] X. M. Ge,* Y. N. Fang, and S. H. Chan, Design and optimization of composite electrodes in solid oxide cells. *Fuel Cells*, 2012, DOI: 10.1002/fuce.201100074.

[2] X. M. Ge, L. Zhang, Y. N. Fang, J. Zeng, and S. H. Chan,* Robust solid oxide cells for alternate power generation and carbon conversion. *RSC Advances*, 2011, **1**, 715–724.

[3] X. M. Ge,* C. J. Fu, and S. H. Chan, Double layer capacitance of anode/solid-electrolyte interfaces. *Physical Chemistry Chemical Physics*, 2011, **13**, 15134–15142.

[4] X. M. Ge,* C. J. Fu, and S. H. Chan, Double layer structure in solid oxide fuel cell anode/electrolyte interfaces: a Monte Carlo study. *Electrochemistry Communications*, 2011. **13**:792–795.

[5] X. M. Ge,* C. J. Fu, and S. H. Chan, Three phase boundaries and electrochemically active zones of lanthanum strontium vanadate–yttria-stabilized zirconia anodes in solid oxide fuel cells. *Electrochimica Acta*, 2011. **56**: 5947–5953.

[6] X. M. Ge and S. H. Chan,* Lanthanum strontium vanadate as potential anodes for solid oxide fuel cells. *Journal of the Electrochemical Society*, 2009. **156**(3): B386–B391.

Conference Proceedings

[7] X. M. Ge and S. H. Chan, Impedance identification of lanthanum strontium vanadate anode in H_2-H_2O-He atmosphere. *ECS Transactions*, 2009. **25**(2) 2249-2258.

Table of Contents

LIST OF TABLES

LIST OF FIGURES

List of Symbols

SUBSCRIPTS

a	activation	m	melting; monosized
dl	double layer	max	maximum
eff	effective	Ox	oxidized
el	electronic	p	polarization
G	Gouy	Re	reduced
geo	geometric	surf	surface
H	Helmholtz	2D	2 dimensional
i	ionic	3D	3 dimensional
latt	lattice		

SUPERSCRIPTS

app	apparent	n	number
A	area	s	surface
int	intrinsic	V	volumetric

ROMAN SYMBOLS

Symbol	Meaning	Usual Units	Section Reference
A	area	cm^2	4.3.5
a	particle radius	μm	4.4.3
C	capacitance	$\mu F/cm^2$	4.1.2
D	diffusion coefficient;	mol/cm^2;	4.1.3;
	dimension	none	4.4.2
d	thickness of the double layer;	Nm;	4.1.2;
	particle size	μm	4.4.2
e	charge	C	4.3
E	energy;	eV;	3.3.2;

	biased potential	V	4.2
f	frequency;	/s;	3.3.2;
	acceptance probability	none	4.2
H	Enthalpy;	kJ/mol;	1.2.2;
	Hamiltonian	eV	4.2
h	anode layer thickness	μm	4.4.2
i	current density	A/cm^2	5.4
K	normalized curvature difference	none	4.4.3
k	area normalizing factor;	none;	4.3.5;
	packing density coefficient	none	4.4.2
L	thickness of the Nernst diffusion layer;	mm;	4.1.3;
	grid size	none	4.2
l	distance	μm	4.4.4
N	number of oxygen vacancies;	none;	4.2;
	coordination number	none	4.4.2
n	exponential factor of constant phase element;	none ;	4.1.2;
	oxygen vacancy density	$/cm^3$	4.3
p	pressure;	bar;	2.4.3;
	transition probability	none	4.2
q	realization probability	none	4.2
P	power density	W/cm^2	2.2
Q	activation energy of sintering	eV	4.4.3
q	charge	C	4.2
r	ionic radius;	nm;	4.3.2;
	relative particle size	none	4.4.2
R	resistance	Ω	2.4.3
s	perimeter of sintering neck	μm	4.4.4
T	temperature	℃	2.3
t	time	s	4.4.3
w	in-depth penetration of electrocatalyst	nm	4.4.4
x	radius of sintering neck	μm	4.4.3
z	normalized distance;	nm/nm;	4.2;

	complex impedance	Ω cm^2	4.3

GREEK SYMBOLS

Symbol	Meaning	Usual Units	Section Reference
α	geometric factor	none	4.4.2
δ	oxygen non-stoichiometry;	none;	3.2;
	surface thickness	μm	4.4.3
ε	void fraction	none	4.4.2
η	packing density;	none;	4.4.2;
	overpotential	mV	5.4
θ	surface coverage;	cm^2/cm^2;	4.2;
	constant phase angle of CPE	^{o}	4.3
κ	proportionality factor;	none;	4.4.4;
	electrode degradation rate	none	5.4
λ	line charge density	C/cm	4.2
μ	chemical potential;	eV;	4.3;
	shear modulus	Pa	4.4.3
ρ	charge density;	C/cm^3;	4.2;
	materials density ;	g/cm^3 ;	4.4.2;
	radius of curvature;	μm;	4.4.3;
	density of TPB	μm/μm^3	4.4.4
σ	conductivity	S/cm	3.2
τ	time constant	S	4.1.2
χ	outer potential	V	4.3
Ψ	Volta potential	V	4.2
Ω	atomic volume	nm^3	4.4.3
ω	angular frequency	/s	4.1.2

ABBREVIATIONS

Abbreviations	Meaning	Section References
AFC	alkaline fuel cell	1.1
APU	auxiliary power unit	1.1

APXPS	ambient pressure XPS	4.3.5
ATR	autothermal reforming	1.2.2
CNLS	complex nonlinear least squares	4.3
CPE	constant phase element	4.1.2
EAZ	electrochemical active zone	4.4
EDX	energy dispersive X-ray spectroscopy	3.4.2
EIS	electrochemical impedance spectroscopy	4.1.2
G–C	Gouy–Chapman	4.2
GFW	generalized Warburg impedance	4.1.3
GIR	gradual internal reforming	1.2
H–P	Helmholtz–Perrin	4.2
HT-	high temperature	1.1
IT-	intermediate temperature	1.1
LEV	Levenburg–Marquardt	5.5
LSV	lanthanum strontium vanadate	1.3
LSM	lanthanum strontium manganite	3.4.1
MC	Monte Carlo	4.2
MCMC	Markov Chain Monte Carlo	4.2
MFC	mass flow controller	5.2
MIEC	mixed ionic and electronic conductor	2.4
NDL	Nernst diffusion layer	4.1.2
OCV	open circuit voltage	2.1
oHp	outer Helmholtz plane	4.1.2
SMR	steam methane reforming	1.2.1
SEM	scanning electron microscopy	3.3.2
SOC	solid oxide cell	5.5
SOFC	solid oxide fuel cell	1.1
TEC	thermal expansion coefficient	2.4.2
TPB	three phase boundary	4.1.2
XPS	X-ray photoelectron spectroscopy	2.3
XRD	X-ray diffraction	3.2
YSZ	yttria-stabilised zirconia	1.3

Chapter 1. Introduction

1.1 Introduction of Fuel Cells

Introducing the fuel cell concept over 160 years ago, Sir William Grove would have been proud of the booming fuel cell research and development all over the world. With technical breakthroughs since the last four decades, fuel cells have been demonstrating their down-to-earth applications by the reduced cost, improved performance, and increased reliability. They are also gaining commercial momentum because of human being's continuous pursuit for sustainable energy and low-carbon economy. Fuel cells own environmental advantages against conventional power generation devices (e.g. gas turbines, internal combustive engines) with the merits of high energy utilization efficiency and reduced pollutant emissions.

Fuel cells are electrochemical energy conversion devices that directly convert chemical energy of a fuel into electrical energy. Based on the electrolyte used, fuel cells can be classified into: (*i*) polymer electrolyte membrane fuel cell (PEMFC), (*ii*) alkaline fuel cell (AFC), (*iii*) phosphoric acid fuel cell (PAFC), (*iv*) molten carbonate fuel cell (MCFC), and (*v*) solid oxide fuel cell (SOFC). A single SOFC consists of two porous electrodes that are separated by a dense yet oxygen ion conducting electrolyte. On the cathode (air electrode) side, oxygen is reduced to oxygen ions which are then pumped through the electrolyte. On the anode (fuel electrode) side, fuels are oxidized by the pumped oxygen ions to liberate the electrons. The Gibbs free energy difference between the two electrodes forces the electrons to flow through the external electrical circuit.

SOFC is not a heat engine and its efficiency is not limited by Carnot principle. It can achieve high efficiencies of 40-60 % (Onda *et al.*, 2003). Over the past decades, R&D activities have focused on cheap materials and low-cost processing methods (Menzler *et al*., 2003; Gaudon *et al*., 2004; Neagu *et al*., 2006; Rossignol *et al*., 2011). Many of them were aimed to lower the operating temperature by using highly conductive oxygen ion conductors (Boulc'h and Djurado, 2002). Advanced SOFC fabrication techniques make cells with small resistance, enabling SOFCs to operate at temperatures down to

500 ℃ (Nesaraj, 2010). The ideal SOFC operating temperature is still controversial. While intermediate temperature SOFC (IT-SOFC, 600 ℃ < T < 800 ℃) can reduce the cost, high temperature SOFC (HT-SOFC, 800 ℃ < T < 1000 ℃) is more efficient. Furthermore, high quality waste heat can be recuperated from HT-SOFC for heating the inlet fuels. HT-SOFC can be coupled to traditional gas turbines to make the energy efficiency even higher. SOFC is closed related to other technologies, such as ceramic ion-conducting membranes, oxygen generator, and ceramic electrochemical reactors. Such a synergy reduces investment risk and encourages entrepreneurial efforts on developing SOFC devices for stationary and distributed power generation, vehicle motive power, and auxiliary power units (APUs).

1.2 Fuel challenges

International Energy Agency (IEA) projected a series of scenarios of energy consumption and structure from now to 2030 if current legislations and policies remain unchanged. It sees global primary energy demand, e.g. on fossil fuel, nuclear fuel, solar energy, and biomass, rising by 1.5%/year on average between 2007 and 2030. World energy demand is projected to grow at an annual rate of 2.5% to 2030, in equivalent to 4,800 GW powder-generation capacity by 2030 (International Energy Agency, 2009). On the other hand, the society pays great concerns on environment issues such as global CO_2 emission and climate change. Note that how the Nobel Peace Prize for 2007 went to the Intergovernmental Panel on Climate Change (IPCC) and the former US Vice President Albert Gore. SOFC seems to be one of the solutions on tackling with these energy and environmental issues. Current status and challenges of two most common SOFC fuels, i.e. hydrogen and reforming gas, are introduced herein.

1.2.1 Hydrogen

Hydrogen is believed to be an important end-use energy carrier, in the fields of transportation, power generation, and portable power systems. Molecular hydrogen is a clean burning fuel. It is the most effective and environment-favourable feedstock to fuel cells. Hydrogen has been extensively used in industry (e.g. chemicals synthesis, refinery, electronics, and metal processing) but not as a fuel. In recent years, world-wide hydrogen demand rockets to meet rigorous government policies and regulations. Among announced projects over the world, the USA is the most ambitious

one in transiting "hydrocarbon economy" to green "hydrogen economy". In 2001, its National Hydrogen Vision Meeting sketched a blueprint for the public confidence in hydrogen as an energy carrier. It launched a 4-year Hydrogen Fuel Initiative with budget of $1.2 billion since 2004, to develop the technology needed for commercially viable hydrogen-powered fuel cells.

The future of hydrogen economy can be exciting, but it is yet to come. Some of the major barriers are cost, technological uncertainty, and infrastructure set-up. Hydrogen is just an energy carrier that must be produced by consuming energy. World-wide hydrogen production has relied on fossil fuels since 1988: 48% from natural gas, 30% from refinery/chemical off-gases, 18% from coal, and the rest from electrolysis (Armor, 1999). Hitherto, 95% of hydrogen in the USA is produced via steam methane reforming (SMR). Green technologies such as photo-electrolysis have long been considered as ultimate solutions. Nevertheless, they would be commercially available only in late 2000s or into the 22^{nd} century (Armor, 1999). The future of hydrogen production cost is still unclear, even for mature technologies such as SMR. It is believed that the cost of hydrogen production must be reduced by a factor of 3 to 10 to make it economically competitive. As shown in Table 1-1, the cost-reduction timelines in the roadmap have always been postponed. In addition, the numbers in Table 1-1 do not include the cost of CO_2 sequestration. The most updated roadmap was given in Figure 6.1 of Ref. (US Department of Energy, 2009). CO_2 sequestration is not yet a proven technology, though demonstration projects for CO_2 storage are on the way. In conclusion, the "green" hydrogen fuel is hitherto not so green as claimed.

Besides the hydrogen production cost, the infrastructure cost is also of great uncertainty. The infrastructure includes gas pipelines, power plants, and electricity transmission and distribution facilities. While some existing infrastructure (e.g. natural gas pipelines and distribution stations) might be utilized, specific upgrades are compulsory particularly in sectors of hydrogen storage and distribution. The technologies that are needed to convert the natural gas infrastructure for hydrogen are available now, but they are not yet cost-effective. The capital investment that was involved in order to maintain and improve the hydrogen infrastructure was estimated to be several hundred billion dollars for the USA (US Department of Energy, 2002). The cost of worldwide pipeline-based distribution systems are in the range of $0.1 to $1.0 trillion with the

assumption of large-scale and centralized hydrogen production. It would cost as high as $20 trillion till 2030 (International Energy Agency, 2007). Private capital investment is essential to build up the hydrogen infrastructure. However, the private involvement may not be forthcoming in the absence of sustained public policy supports (e.g. stringent national or international regulations on CO_2 emission) and technological advances (e.g., significant breakthroughs in hydrogen production, storage, and utilization technologies).

Table 1-1 Targeted cost of hydrogen production

Production methods	Plan at 2003 (MPR Associates, 2005)		Plan at 2006 (US Department of Energy, 2006)	
	Goal	Target Year	Goal	Target Year
Natural gas and fossil fuels reforming	$ 1.50 / Kg* (delivered, without CO_2 sequestration)	2010	$ 2.50 / gge* (delivered)	2010
			$ 2.00 / gge (delivered)	2015
Biomass gasification	$ 1.50 / Kg (at plant gate)	2015	$ 3.80 / gge (delivered)	2012
			$ 3.00/ gge (delivered)	2017
Electrolysis	$2.00-2.50 / Kg (at plant gate)	2010	$ 3.70/ gge (delivered) from distributed electrolysis	2012
			$ 3.00/ gge (at plant gate) from distributed electrolysis	2017
			$ 3.10/ gge at plant gate ($ 4.80/ gge delivered) from central wind electrolysis	2012
			<$2.00/ gge at plant gate (<$ 3.00/ gge delivered) from central wind electrolysis	2017
Photo-electrochemical Water Splitting	$5.00 / Kg (at plant gate)	2015	$ 3.00/ gge at plant gate ($ 4.00/ gge delivered)	2017
Nuclear heat	Demonstration of technical Capability at competitive price	2015	Commercia-scale, economically feasible production	2017

* A kg of hydrogen contains approximately the same amount of energy as one gallon of gasoline, or one gallon of gasoline equivalent (gge).

Ultrahigh-purity hydrogen is necessary for PEMFC, which has been developed for transportation and portable applications. Unlike PEMFC which is highly sensitive to CO poisoning, SOFC readily utilizes CO as fuel. SOFC provides a shortcut to use reforming gas instead of hydrogen, thus providing high efficiency in energy conversion. Hydrogen production via hydrocarbon reforming will be introduced in Chapter 1.2.2. Advantages and disadvantages for SOFC coupling with reforming process are subsequently discussed.

1.2.2 Reforming gas

Reforming gas, or syngas, is a gas mixture that contains varying amount of CO and H_2. Typical production methods include steam reforming of hydrocarbons, coal gasification, biomass cleaning and reforming, etc. In this section only the steam reforming, which is the dominant process in industry, is discussed.

Fuel processing is the process that converts commercially available hydrocarbon fuels to fuel gas reformates (EG&G Services, 2004). It includes fuel cleaning, fuel conversion, reformate gas separation, and fuel purification. The system complexity depends on the targeted fuel cell type and the properties of raw feedstocks and deliverables. For example, in order to avoid CO poisoning ultrafine purification of reforming gases is compulsory for PEMFC. The reforming process can be classified into external reforming and internal reforming, based on whether the fuel processing is incorporated within the SOFC devices.

A typical external reforming system consists of a series of gas purification and catalytic chemical reactors, followed by impurity clean-up systems. The primary fuel reforming may be accomplished with or without a catalyst via one of three major types: (*i*) steam reforming; (*ii*) partial oxidation reforming; (*iii*) autothermal reforming (ATR). As mentioned in Chapter 1.2.1, natural gas is the main feedstock of hydrocarbon reforming via SMR. On an industrial scale, SMR is the cheapest and most effective method for hydrogen production. SMR is a complex process which at least includes:

$$CH_4 + \text{steam} \rightarrow CO + 3H_2 \qquad \text{(Equation 1-1)}$$

$$CO + \text{steam} \rightarrow CO_2 + H_2 \qquad \text{(Equation 1-2)}$$

$$CO_2 + H_2 \rightarrow CO + H_2O \qquad \text{(Equation 1-3)}$$

$$2CO \rightarrow CO_2 + C \qquad \text{(Equation 1-4)}$$

$$CH_4 \rightarrow C + 2H_2 \qquad \text{(Equation 1-5)}$$

Reaction 1-1 is highly endothermic (ΔH = +206.1 kJ/mol) so that the operating

temperature of SMR is often higher than 800°C. According to Reactions 1-1 and 1-2, excess steam is added into the reactor in order to maximize the hydrogen yield and avoid carbon deposition. However, too much steam inevitably leads to low system efficiency. These disadvantages are overweighed by its higher H_2 yield than other reforming methods, such as partial oxidation and ATR. One of the main challenges of SMR is to balance the heat input through the reformer tubes with the reaction heat. The catalysts are in a packed bed, with a series of tubes surrounded by combusting gas that supply heat to the endothermic reactions. Alternatively, reforming catalysts are applied onto the walls of heat exchanger together with a combustion catalyst on the other side to provide the heat. This arrangement requires much more active catalysts than conventional Ni-based materials. Ni-based catalysts are low-cost but are prone to carbon deposition (Reactions 1-4 and 1-5). Carbon deposition not only leads to carbon loss of the fuels, but more importantly also cokes the catalysts. Increasing steam, hydrogen, and CO_2 concentrations alleviates carbon deposition but reduces system efficiency. Furthermore, the system demands upstream sulphur removal processes. Finding cost-effective and high performance catalysts with carbon resistance and sulphur tolerance continues to be a challenge.

One of the distinguished advantages of SOFC is the possibility of utilizing practical hydrocarbon fuels, by virtue of internal reforming of hydrocarbon fuels within its anode chamber. Converting the hydrocarbon fuels directly in the anode chamber simplifies the whole system and offers cost advantages. Under practical conditions, nearly half of the heat produced by the exothermic oxidation reactions could be absorbed by the reforming processes. It lowers the cell cooling requirement and consequently reduces the required amount of air passing to the cathode side. It increases the system efficiency by eliminating the energy penalty associated with transferring the heat for the heat supply in an external reformer. The cooling effect could be harmful if the induced thermal stress leads to mechanical failure of cell components. Alternatively, gradual internal reforming (GIR) mitigates this deleterious effect by applying a slab of dry reforming agent above the anode (Klein *et al.*, 2008a).

Carbon deposition and impurity poisoning (mostly H_2S) remain to be the critical issues for SOFC with Ni-cermet internal reforming catalysts and anodes. Conventional steam

reforming requires large quantities of steam (mostly CH_4:CO_2 < 1:3) are added to the hydrocarbon fuels in order to avoid carbon deposition. Much higher CH_4: CO_2 ratios are tolerable in the circumstance of GIR (Georges *et al.*, 2006). Additionally, the output fuel gas from reforming process should be carefully cleaned to remove H_2S down to several parts per million (ppm) levels. These are undesirable because of the fuel dilution and the added processing cost. Another problem of the internal reforming is the steep temperature gradient along the fuel channels. At the inlet of a cell where the fuel concentration is high, the fuel reforming process dominates so that the inlet region is cooled significantly below the feed temperature. Meanwhile, the temperature increases when the fuel flows downstream to where the exothermic fuel oxidation dominates. Localized heating and cooling lead to significant thermal stress and, potentially, to system failure.

1.3 Project goals

SOFC technology is on the verge of commercialization now. Both research institutions and commercial organizations are launching SOFC projects for down-to-earth applications in niche markets, such as stationary power generations and auxiliary power units (APUs). Hitherto, the major hurdles for SOFC commercialization are the cost and reliability. One of the approaches on cost reduction is to feed SOFC with practical fuels, rather than using the expensive hydrogen that are actually produced from hydrocarbons. Another approach is to improve the impurity (mostly sulphur) tolerance of electrocatalysts. Advanced anode materials that are capable of hydrocarbon utilization and of high sulphur tolerance would be of great interests to SOFC community.

A technological challenge of feeding SOFC with practical hydrocarbon fuels is that conventional anodes, such as Ni–YSZ cermets, are prone to carbon deposition and sulphur poisoning. Several approaches are proposed to solve or mitigate these problems: (*i*) optimizing operating conditions such as temperature and voltage, (*ii*) tailoring the state-of-the-art Ni–cermet anodes by doping and alloying, and (*iii*) seeking alternative anode materials. The third approach is adopted in this project as the first two approaches both lead to system inefficiency and complexity.

This project, therefore, aims to explore a new type of anode materials that are suitable for SOFC fed on practical fuels. A class of perovskite oxides, lanthanum strontium vanadate (LSV), exhibits great potential for this kind of application. It not only suppresses carbon deposition but also withstands sulphur-containing hydrocarbon fuels such as natural gas, coal gas, and biogas. Material synthesis and preliminary electrode performance evaluation represent the Phase 1 of this project. In Phase 2, fundamental works on the reaction mechanism, interfacial structures, and electrode microstructure are investigated thoroughly. Finally in Phase 3, the optimized electrode is subjected to half cell testing and fed by various practical fuels.

1.4 Objectives of research project

- To prove the concept by feeding SOFC with practical fuels
- To synthesis, characterize, and optimize vanadate anode materials
- To establish chemical, electrochemical, and microstructural relationships
- To investigate the interfacial and fuel oxidation mechanisms

1.5 Scope of research project

The scope of the research project is outlined as below:

a. To explore new anode materials in the vanadate category for SOFC fed with practical fuels, in particular
    - Choosing the right materials
    - Powder synthesis
    - Materials characterization of the as-synthesized powders
    - Electrode engineering (e.g. power property, baking history, composition, sintering temperature, microstructure etc.)
    - Thermal, redox, and long-term operating stability

b. To establish the interrelationships between chemical, interfacial, electrochemical, and microstructural properties anode/electrode interfaces, in particular
    - Impedance spectroscopy analysis under various atmosphere
    - Monte Carlo simulation of the anode/electrolyte double layer structure

- Modified Poisson–Boltzmann theory on establishing the potential-dependent Gouy–Chapman capacitance
- The Volta potential analysis in obtaining the double layer capacitance
- Interrelationship between three phase boundaries and electrochemically active zone

c. To fabricate the half cell SOFCs with vanadate anodes
   - Running on practical fuels, e.g. simulated natural gas, syngas, biogas, and coal gas
   - Fuel impurity
   - Carbon deposition
   - Performance degradation analysis

1.6 Thesis layout

Chapter 2 reviews various anodes targeting to hydrocarbon utilizations, viz. Ni-cermet, Cu-cermet, and various oxides (zirconia-based and ceria-based fluorite, tungsten bronze, rutile, pyrochlore, chromite perovskite, titanate perovskite, double perovskite).

Chapter 3 describes the initial exploration and evaluation of lanthanum strontium vanadate (LSV) as potential SOFC anodes, including powder synthesis, materials structure and thermo-stability, half cell and single cell electrode performance.

Chapter 4 represents a comprehensive study on elucidating the interfacial structure of LSV/YSZ interfaces by impedance spectroscopy, Monte Carlo simulation, modified Poisson–Boltzmann theoretical analysis, and analytical modelling on anode microstructure, three phase boundaries, and electrochemically active zones.

Chapter 5 demonstrates the feasibility of LSV anodes for SOFCs fed with practical fuels. LSV anodes exhibit salient catalytic activity in various simulated practical fuels, e.g. syngas, coal gas, biogas, and town gas.

Chapter 6 provides conclusions, main achievements, and recommendations.

Chapter 2. Literature review

Technical challenges of hydrogen and reforming gases had been introduced in Chapter 1. Fundamental principles of SOFC operation will be introduced in Chapter 2.1. The recent research progress on hydrocarbon utilization in SOFCs is then reviewed. For SOFC operating on hydrocarbon fuels, the most critical issue is to develop anodes that do not catalyze carbon formation and have comparable performance with state-of-the-art Ni-cermet anodes.

2.1 SOFC fundamentals

The definition of "direct hydrocarbon utilization" or "direct utilization" has not been clear. The controversy pervades in literature over precisely what should be called as direct oxidation, direct conversion, or direct utilization of hydrocarbons in SOFCs. Mogensen and Kammer defined it as "conversion in the SOFC without pre-mixing the fuel gas with steam or CO_2, and without processing the fuel before it enters the cell stack." (Mogensen and Kammer, 2003). It means that direct utilization is the direct electrochemical oxidation with the open-circuit voltage (OCV) of the fuel cell equal to the Nernst potential. So to speak, any processes that involve hydrocarbon cracking and electrochemical oxidation of the cracking products are beyond the category of "direct oxidation". This appears to be quite a stringent definition and might not be of practical merits. Alternatively, McIntosh and Gorte envisaged that direct utilization should encompass the conventional use of hydrocarbon fuel with small amount of steam (e.g. 3% H_2O) being co-fed with hydrocarbons, regardless of the exact reaction pathways (McIntosh and Gorte, 2004). McIntosh and Gorte's loose definition is adopted all through this study but merely for pragmatic reasons.

Oxygen molecules are reduced to oxygen ions at the cathode. Driven by the electrochemical potential difference between anode and cathode, oxygen ions are pumped through electrolyte. They finally reach the anode and are consumed in terms of electrochemical fuel oxidation,

$$C_nH_{2n+2} + (3n+1)O^{2-} \rightarrow nCO_2 + (n+1)H_2O + (6n+2)e^- \quad . \qquad \text{(Equation 2-1)}$$

Taking CH_4 as an example, Reaction (2-1), i.e., step ③ shown in Fig. 2-1, is unlikely to occur in one step. Thermal cracking of CH_4 is inevitable in typical SOFC operating temperatures. Some of the resulted compounds can be oxidized electrochemically. The cracking products include carbon, hydrogen, and some chain/cyclised hydrocarbons. The cracking process might proceed as: (*i*) oxidation of cracked carbon and hydrogen (Step 1 and Step 4 in Fig. 2-1) or (*ii*) oxidation of intermediate from free radical reactions (Step 5 and Step 7 in Fig. 2-1). Some of the reactions are proposed as below (Mogensen and Kammer, 2003):

$$CH_4 \rightarrow C + H_2 \qquad \text{(Equation 2-2)}$$

$$C + O^{2-} \rightarrow CO, CO_2 \qquad \text{(Equation 2-3)}$$

$$H_2 + O^{2-} \rightarrow H_2O \qquad \text{(Equation 2-4)}$$

$$CH_4 + O^{2-} \rightarrow CH_3OH + 2e^- \qquad \text{(Equation 2-5)}$$

$$CH_3OH + 2O^{2-} \rightarrow HCOOH + H_2O + 4e^- \qquad \text{(Equation 2-6)}$$

$$HCOOH + O^{2-} \rightarrow CO_2 + H_2O + 2e^- \qquad \text{(Equation 2-7)}$$

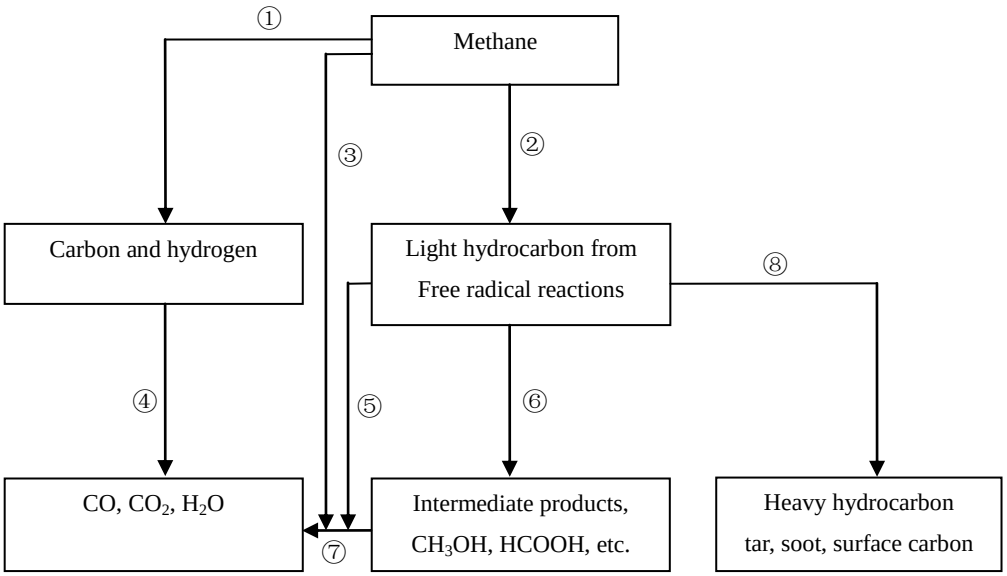

Figure 1-1 Flow chart of hydrocarbon utilization in SOFC (methane as example)

The exact reaction could be a combination of all the reactions mentioned above. Additionally, fuel reactions are related and influenced by other physical and chemical phenomena within the anode chamber, such as gas diffusion, gas conversion, mass transportation, and surface adsorption/desorption. In Chapter 2, literature review focuses on those cermets and conductive oxide anodes attempting for hydrocarbon utilization. Ni-cermets are introduced in Chapter 2.2. Efforts are then paid to Cu-cermets in Chapter 2.3. Conductive oxide anode materials, mainly perovskite and briefly fluorite, rutile, pyrochlore, and tungsten bronze, are finally reviewed in Chapter 2.4. Merits and drawbacks of these materials for hydrocarbon fuel utilization are analysed and commented from case to case.

2.2 Nickel cermets

Large amounts of steam with steam/carbon (S/C) ratio larger than 2 are routinely added into hydrocarbons that are used as fuels for SOFCs with Ni-cermet anodes. In contrast, Murray *et al.* demonstrated that Ni-cermet could be utilized for direct hydrocarbon SOFCs with no or little co-fed H_2O (Murray *et al.*, 1999). Cells with Ni–YSZ anode could yield R_p around 1 Ω cm^2 in 3% H_2O–CH_4 fuel with stable operation up to 100 h at 600 ℃. A temperature window between 550 ℃ to 650 ℃, in which carbon is not stable, was pinpointed. The thermal cracking of methane to carbon and hydrogen was inhibited below 650 ℃. On the other hand, the disproportionation of CO to carbon and CO_2 was shifted to CO above 550 ℃. Another benefit might came from the yttria doped ceria (YDC) interlayer that were sandwiched between the 8 μm-thick YSZ electrolyte and the electrodes, noting that YDC is known to have good dry reforming ability and resistance to carbon formation. The OCV of these cells was significantly lower than the potential predicted from thermodynamics, e.g. 1.2–1.4 V in typical SOFC operating temperatures. It indicated that the dominating reactions were the oxidation of cracked compounds, either carbon and hydrogen, or light hydrocarbons from free radical reactions. That approach had fostered three well-known strategies on utilizing Ni-cermets for direct hydrocarbon utilization. The first strategy, Strategy *a*, is to carefully control the operating temperature and the anodic environment. The second strategy, Strategy *b*, is to mix or dope carbon-resistance species into Ni-cermet. The third strategy, Strategy *c*, is to add a buffer layer or dry reforming layer above the anode layer.

Table 2-1 Single cell SOFC with Ni-cermet anodes fed with hydrocarbon fuels

Anode	Electrolyte	Cathode	Strategies for hydrocarbon utilization	References
Pure methane				
Ni–YSZ	YSZ	LSCF–GDC	*a**	(Lin *et al.*, 2005)
Ni–GDC–Ru (1-10 wt.%)	20 μm GDC	SSC	*b**	(Hibino *et al.*, 2002)
Ni–YSZ (support)	Tubular ~20 μm YSZ	LSCF–SDC	*c**	(Li *et al.*, 2007a)
SDC	LSGM (0.5 mm)	LSCo	*b*	(Nabae *et al.*, 2006)
Ni–SDC	ScSZ (2.5 mm)	Pt	*c*	(Asamoto *et al.*, 2009)
Ni–SDC	SDC	SSCi–SDC	*b*	(Zhu *et al.*, 2006)
Ni–YSZ	YSZ (10 μm)	LSM–YSZ	*c*	(Zhan *et al.*, 2006)
Impregnated Ni in LSC–YSZ	LSGM (0.5 mm)	LSC	*b*	(Nabae and Yamanaka, 2009)
Ni–YSZ– 10% starch	YSZ	LSCF–GDC	*c*	(Lin *et al.*, 2006)
Ni–YSZ	YSZ	LSM	*c*	(Klein *et al.*, 2008b)
Wet methane (3% H_2O)				
Ni–ScSZ	ScSZ	LSM	*a*	(Sumi *et al.*, 2004)
Pd/Ni/ceria impregnated YSZ	YSZ	Pt or LSM	*b*	(Qiao *et al.*, 2009)
Ni–YSZ	YSZ (8 μm)	LSM	*c*	(Murray *et al.*, 1999)
Sn-doped Ni–YSZ	YSZ (20–30 μm)	LSM	*a*	(Kan and Lee, 2010)
Ni–ScSZ	ScSZ	PCM	*b*	(Huang *et al.*, 2006a)
Ni-YSZ and Ni–ScSZ	YSZ and ScSZ	LSM	*a*	(Sumi *et al.*, 2010)
Wet natural gas				
Ni–YSZ	YSZ	LSM–YSZ LSCF–YSZ	*a*	(Liu and Barnett, 2003)
Methanol				
Ni–YSZ	YSZ (10 μm)	LSM–YSZ	*a*	(Jiang and Virkar, 2003)
Butane				
Ni–LSCM–GDC	GDC (0.4–0.6 mm)	LSCF–SDC	*b*	(Liu *et al.*, 2002)
Isooctane				
Ni–YSZ	YSZ	LSCF–GDC	*c*	(Zhan and Barnett, 2005a, Zhan and Barnett, 2005b)
Ni–YSZ	YSZ (10 μm)	LSM–YSZ	*a*	(Murray *et al.*, 2006)

a: operating under current loading; b: mixing or coating with carbon-resistant species; c: adding buffer layer above the anode layer.

Various hydrocarbon fuels, such as methane, natural gas, butane, and isooctane, had been used as fuels fed to SOFCs with Ni-cermet anodes. Alcohols, which carry sufficient oxygen to avoid carbon deposition, can also be utilized as fuels. Some examples are shown in Table 2-1. Thin-electrolyte cells in this category can achieve high maximum power density (P_{max}). P_{max} as high as 2 W/cm^2 at 800 ℃ had been

reported to SOFCs fed with wet methane (Sumi *et al.*, 2004). Stable operation longer than 1000 h was achieved at 600 ℃ with P_{max} at 0.58 W/cm^2 for large cells (Nabae *et al.*, 2006). Table 2-1 also shows the three strategies to mitigate the coking problem of the state-of-the-art Ni-cermet anodes for hydrocarbon fuels. It is interesting to note that ceria was always used in all the three strategies. Ceria-based oxygen ion conductors are effective in carbon removal and hydrocarbon reforming, because of their higher catalytic activity than YSZ (Trovarelli, 1996). For Strategy *a*, the two parameters under manipulation are the operating temperature and the current (or voltage). The operating temperature is usually within the range from 550 to 850 ℃. Otherwise, catastrophic carbon deposition on Ni reaction sites occurs and/or CO disproportionation takes place. Long-term exposure under the OCV condition, where carbon deposition is deemed to be most severe, should be avoided for Ni-cermets fed with hydrocarbon fuels. Carbon deposition could also be somewhat suppressed under current loading, as oxygen ions pumped from the cathode side might remove carbonaceous compounds if deposited. The addition of noble metals was the common practice of Strategy *b*. It utilized the excellent catalytic activity of noble metals for hydrocarbon reforming (Saeki *et al.*, 1994; Babaei *et al.*, 2009; Babaei and Jiang, 2010). Pd and Ru are most commonly used in SOFCs because of relatively low cost than other noble metals. For Strategy *c*, a catalyst layer (or disc) is applied above the anode layer for the purpose of dry reforming of hydrocarbon fuels. Typical catalyst discs are composed of two Ru-ceria layers on both sides of porous support (Zhan and Barnett, 2005a), or Ir-ceria pressed onto Ni–YSZ anodes (Klein *et al.*, 2008b). Carbon deposition is thus avoided because it is hydrogen-rich gases instead of hydrocarbon fuels that reach onto the anode surface.

Though SOFC with Ni–cermet anodes has been successfully run on hydrocarbon fuels in laboratory-scale, the extension to industry-scale application is still uncertain. Carbon deposition on Ni-cermet anodes is irreversible so that any unforeseeable accident will result in catastrophic cell failure. In addition, three phase boundaries (TPBs) usually extend not more than 10 μm from the electrolyte interface to composite anode. Strategies employing high O^{2-} flux through the electrolyte for carbon removal cease to function for the regions outside TPBs. This implies that Strategy *a* cannot benefit the non-reactive areas of the Ni–cermet anodes. The protection of the anode strictly relies on the steam and CO_2 reforming. While it may be possible to maintain

reasonable conversions and high steam concentrations over small-scale, it becomes rather challenging for anode-supported large cells.

2.3 Copper cermets

The effectiveness of carbon suppression in Ni-cermet anodes, as introduced in Chapter 2.2, is still on doubt. For cermet anodes, an alternative way to avoiding carbon deposition is to replace Ni with metals that are poor catalysts for carbon formation. The metal is supposed to be stable at high operating temperatures and oxygen partial pressures (pO_2) of the anode atmosphere. Metals that would be oxidized by steam and metals with low melting temperatures are, therefore, excluded. Precious metals are beyond the consideration because of their high cost. As a compromise of the above two criteria Cu seems to be a good choice. Cu does not catalyze carbon formation and is stable at typical SOFC pO_2 range. One of the disadvantages of Cu (T_m = 1083 ℃) is its low melting temperature as compared with Ni (T_m = 1453 ℃). This implies that Cu may be of poor thermal stability during the SOFC operation. Another issue comes from the anode fabrication procedures. As the melting temperatures of CuO (T_m = 1201 ℃) and Cu_2O (T_m = 1235 ℃) are much lower than NiO (T_m = 1984 ℃), conventional firing processes are not applicable to Cu–cermet. Furthermore, it is necessary to incorporate separated oxidation catalysts in order to achieve satisfactory electrode performance, because Cu is a very poor fuel oxidation catalyst.

Since 2000, Gorte *et al.* at University of Pennsylvania had pioneered Cu-based cermets for direct hydrocarbon utilization (Park *et al.*, 2000). They developed a method for high temperature sintering of electrolyte and low temperature sintering of electrode (Park *et al.*, 2001). The fabrication method they used is called "dual tape-casting". In the tape casting, electrolyte powders (mostly YSZ) are mixed with various organic additives that work as binder, plasticizer, surfactants, etc. The slurry is casted into tapes over the carrier and is then slowly dried. A second layer with pore formers (e.g. graphite, PMMA, starch) is spread onto the first layer. Afterwards, the organic species and pore formers were then burnt out, leaving porous YSZ layer as electrode skeleton and dense YSZ layer as electrolyte. Cu and ceria are impregnated into the porous YSZ layer from relevant metal nitrate solutions. It is fired at right temperatures for decomposition and electrode sintering. Cell performance of Cu–YSZ anodes was poor

Table 2-2 Single cell SOFCs with Cu–cermet anodes fed with hydrocarbon fuels.

Cell configuration	Fuel	P_{max} (W/cm^2)[a]	Reference
Cu-based anodes			
Cu–ceria–YSZ/YSZ(60 μm)/LSM–YSZ	C_4H_{10}	0.13	(McIntosh *et al.*, 2002)
	C_7H_8 (diluted by N_2)	0.1	(Kim *et al.*, 2001)
	Vegetable oil	0.06	(Zhou *et al.*, 2007)
	C_4H_{10} (preoxidized in O_2)	0.12	(Costa-Nunes *et al.*, 2003)
Cu–ceria–YSZ/Ni–ScSZ/ScSZ /PCM	C_2H_5OH	0.41[b]	(Ye *et al.*, 2009)
		0.31[c]	
Cu–ceria–LSGM/LSGM(440 μm)/LSCF–LSGM	H_2	0.22	(An *et al.*, 2004)
	C_4H_{10}	0.11	
Cu–YSZ-ceria/YSZ/LSM–YSZ	C_3H_8	0.05	(Zhan and Lee, 2010)
Cu–ceria–LDC/LSGM/SCF	CH_4	0.1[b]	(Bi and Zhu, 2009)
Cu–ceria–SDC/SDC (340 μm)/LSCF–SDC	C_4H_{10}	0.18	(Lu *et al.*, 2004)
Cu–ceria–LSGM/LSGM (440 μm)/LSCF–LSGM		0.08	
Cu–ceria–ScSZ/ScSZ(60 μm)/LSCF–ScSZ		0.15	
Cu-based anodes decorated with precious metals			
Cu–Pd–ceria–YSZ/YSZ(100 μm)/LSM–YSZ	CH_4	0.28	(McIntosh *et al.*, 2003)
	C_4H_{10}	0.15	
Cu–Co(Ru)–$Zr_{0.35}Ce_{0.65}O_{2-\delta}$ /YSZ (50 μm)/LSM	C_2H_5OH	0.45[b]	(Cimenti and Hill, 2010)
Alloyed Cu-based anodes			
Cu–Ni–ceria–YSZ/YSZ(60 μm)/LSM–YSZ	CH_4	0.3[b]	(Kim *et al.*, 2002)
	C_4H_{10}	0.12	(Lee *et al.*, 2004)
Cu–Co–ceria–YSZ/YSZ(50 μm)/LSM–YSZ	CH_4	0.25[b]	(Lee *et al.*, 2005)
	C_4H_{10}	0.14	(Lee *et al.*, 2004)
Cu–Co–ceria/YSZ/LSM	CH_4(80%)–H_2	0.09[c]	(Fuerte *et al.*, 2011)

[a]: Testing temperature is 700 ℃ without explicit specifications; [b]: 800 ℃; [c]: 750 ℃.

even when Cu was alloyed with Ni (Kim *et al.*, 2002). Ceria, an oxide with fast oxygen exchange kinetics, was incorporated as the fuel oxidation catalyst. Cu-ceria-YSZ anodes had been proven to be well competent for hydrocarbon utilizations (Table 2-2). Anyway, SOFCs with ceria as electrocatalyst alone is not so satisfactory. That is the reason why small amount of precious metals, e.g. Pd, were always incorporated.

Cu–cermet anodes are usually operated at intermediate temperatures. High temperatures above 800 ℃ are strongly prohibited with regard to the low melting temperature of Cu. After initial reduction at 700 ℃ the Cu within the porous YSZ layer forms a electronically percolating network. After annealing at 900 ℃ for 5 h, unfortunately, it had been sintered into unconnected particles. The Cu sintering rendered significant increase of the ohmic resistance during fuel cell operations (Gross *et al.*, 2007b). A common practice to solve this problem is to incorporate more refractory metals into Cu cermets. As shown in Table 2-2, bimetallic electrodes such as Cu–Ni, Cu–Cr, and Cu–Co had been evaluated in terms of their effectiveness on the improvement of thermal stability. Ni was reported to loss catalytic activity after alloying with Cu. Cu–Ni cermet anodes containing more than 20 % Ni was prone to carbon deposition. The carbon cannot be removed during the loading conditions and inevitably led to cell failure (Lee *et al.*, 2004). Cu and Cr (T_m = 1907 ℃) is immiscible and Cr is not expected to catalyze carbon formation. As chromium oxide was unable to be reduced in anodic environment, Cu–Cr based cermets were prepared via Cr electrodeposition onto the anode. Cu–Cr cermet anodes were tested in 80% H_2–20% H_2O to evaluate the redox stability in anodic environment. It was found that the Cr in Cu–Cr cermets was completely oxidized after 20-hour exposure and at 900 ℃ (Gross *et al.*, 2007b).

Cu–Co bimetallic anodes seem to have better performance than that of Cu–Ni and Cu–Cr. Co (T_m = 1907 ℃) remains reduced under similar conditions as that of Ni. Unlike Ni, Co has limited solubility with Cu at SOFC operating temperatures. Free-energy calculations indicated that Cu was segregated on to the surface of Co (Kim *et al.*, 2000). Cu–Co cermet anodes can be prepared by co-impregnation or electrodeposition. X-ray photoelectron spectroscopy (XPS) results showed that Cu is

segregated onto the surface to form a Cu over-layer after the annealing at 600 ℃ (Lee *et al.*, 2005). Carbon deposition is thus suppressed because the inert Cu is segregated onto the surface. Thermal stability was also improved as a result of Co incorporation. Bimetallic anode containing 5 % electrodeposited Co and 13 % Cu did not lose its conductivity after annealing at 900 ℃ for 50 h in wet H_2. Co-cermet anodes formed large amounts of carbon when exposed to dry methane at 800 ℃ for 3 h, the Co-plated Cu electrode showed no observable carbon formation under the same conditions (Gross *et al.*, 2007a).

2.4 Oxides

The limitations of cermet anodes have led to the development of oxide anode materials. Oxide anode materials are desirable to be mixed ionic and electronic conductors (MIECs), which both have high electronic conductivity and ionic conductivity. The electrochemical oxidation is then not confined to TPBs but extends to the whole oxide anode surfaces. To be a practical oxide anode material involves many more considerations besides the catalytic activity. Steele *et al.* proposed several empirical criteria of oxide anodes for complete methane oxidation (Steele *et al.*, 1990). These criteria included:

1) Good electronic conductivity (preferably > 100 S/cm) at anode operating potentials (-0.7 to -0.9V). Probably n-type behaviour preferable.
2) Predominant anion lattice disorder to enhance oxygen diffusion coefficients.
3) High values for oxygen surface exchange kinetics.
4) Fabrication of porous adherent films with minimal processing problems.
5) Compatibility with solid electrolyte.

Until now there is few oxides meet all the above criteria. Ni-, Co- and Fe- based oxides are seldom used as SOFC anodes, as they easily precipitate from the corresponding oxides in reducing conditions. Typical redox couples in SOFC anode materials are $Cr^{3+/4+}$, $Ti^{3+/4+}$, $Mn^{3+/4+}$, $Ce^{3+/4+}$, $Mo^{5+/6+}$, $V^{3+/4+}$, $Nb^{3+/4+}$, etc. The n-type conducting oxides are favourable because the conductivity increases when the pO_2 decreases. Based on the material structure, the explored oxide anodes can be briefly classified in fluorite, rutile, tungsten bronze, pyrochlore, perovskite, and double perovskite (Table 2-3). Oxide materials, with the highlights on perovskite and double perovskite, are

reviewed in this chapter.

2.4.1 Fluorite

2.4.1.1 Zirconia-based

Coordination numbers of cation and anion in fluorite structure are 8 and 4, respectively. Low valence cations (3+ or 2+ cations) are doped into the fluorite lattice to create oxygen vacancies. At elevated temperatures the oxygen vacancies thus created may become mobile and produce ionic conductivity. Further introduction of multivalent elements could lead to mixed electronic and ionic conductor (MIEC) behaviours. Take ceria and zirconia as a comparison. Ce^{4+} could be partially reduced to Ce^{3+}, thus doped or undoped ceria becomes MIEC at low pO_2. While the electronic conduction can be induced into ceria, it is difficult to reduce Zr^{4+} to Zr^{3+} even at low pO_2. The electronic conduction of zirconia has to be introduced by dopants. For this purpose many types of transition metal oxides, such as TiO_2, MnO_x, Tb_4O_7, Nb_2O_5 and WO_3, can be doped into zirconia (Huang and Weppner, 1996). The electronic conductivity of these materials under reducing atmosphere is, however, not high enough for SOFC anode applications.

The first row transition elements exhibit the solubility in zirconia varying from case to case, among which Ti and Nb show highest solubility. Ti, the reduction of which leads to n-type electronic conduction, has high solubility in YSZ. At 1500 ℃, up to 18 at% Ti^{4+} can be dissolved into cubic fluorite ZrO_2– (7–10 at%)Y_2O_3 structure. A large region of TiO_2–Y_2O_3–ZrO_2 system had high vacancy concentrations up to 16%, e.g., $Zr_{0.21}Y_{0.62}Ti_{0.17}O_{1.69}$ (Feighery *et al.*, 1999). Electronic conduction of Ti-doped zirconia was attributed to a Ti^{4+}/Ti^{3+} small polaron hopping mechanism (Swider and Worrell, 1996). Modest electrode performance had been observed for Ti-doped zirconia anodes (Mantzouris *et al.*, 2007). The soluble limit of Nb into zirconia was as high as 25%. The ionic conductivity of Nb-doped zirconia was rather negligible— 10^{-3} to 10^{-5} S/cm at typical SOFC temperatures. The electronic conductivity was low because Nb was difficult to be reduced (Fagg *et al.*, 2003a). In_2O_3 and ZrO_2 may form a complete solid solution at high temperatures. The ionic conductivity of 25 at% In doped ZrO_2 was not low (~10^{-1} S/cm at 1000 ℃), but the material was unstable at low pO_2 and at high temperatures (Sasaki *et al.*, 1994). The solubility of Fe_2O_3 in ZrO_2 was

about 4 at% at high temperatures (Matsui and Takigawa, 1990). 20 mol% Fe_2O_3 could be dissolved into zirconia, but zirconia with such high Fe_2O_3 content was not stable after fired at 800 ℃ (Cao *et al.*, 2000). The solubility of MnO_x in ZrO_2 was around 12 at% at high temperature, though high value up to 30 mol% had been reported (Kim and Choi, 2000). The solubility of NiO in YSZ was only about 2 at% at 1600 ℃ (Park and Choi, 1999).

To summarize, Mn, Fe, and Ni are unsuitable dopants of zirconia. Small solubility of Fe and Ni in zirconia makes them difficult to form an effective percolation path for electron transfer. Mn-doped YSZ is likely to be a mixed p-type conductor with dominant ionic conduction at low pO_2, usually observed in various Mn-containing materials. Ti-doped ZrO_2 is more favourable, but the Ti-content is still not high enough to generate an effective percolation network for electron transfer. Nb and In also have large solubility in ZrO_2, but the solid solutions suffer structural change in typical SOFC anodic environment. Due to the high level of doping, these zirconia-based oxides exhibit fairly low ionic conductivity (<0.01S/cm). Despite of the incorporation of high-level reducible ions into ZrO_2, the electronic conductivity of doped zirconia is still quite low (<0.1 S/cm). Selected conductivity values of doped zirconia are given in Table 2-3 for reference.

2.4.1.2 Ceria-based

Ceria-based cermets, such as Cu-ceria-YSZ as introduced in Chapter 2.3, are good SOFC anodes for direct hydrocarbon utilization. In contrast, what introduced in Chapter 2.4.1.2 are pure ceria-based oxides as SOFC anodes. Doped or undoped ceria themselves could be SOFC anodes if considerable electronic conduction can be introduced into the fluorite lattice. The Ce ion of ceria is reduced from Ce^{4+} to Ce^{3+} in SOFC anode environments, thus resulting in the electronic conduction. Alternatively, the cation doping can also create electronic conduction in ceria. The conductivity of some doped ceria are shown in Table 2-3. High conductivity of gadolinia- and samaria-doped ceria is attributed to the good match of the ionic radii between the dopant ions and Ce ions. La-doped ceria had been synthesised via co-precipitation method, where La^{3+} were thought to be distributed randomly (Suda *et al.*, 2006). Although the conductivity of Tb-doped ceria is lower than those with other dopants, there might be

advantageous effects of the Tb^{4+}/Tb^{3+} redox couple in real anodic conditions (Martinez-Arias *et al.*, 2005). The conductivity of doped ceria is relatively low but surprisingly doped ceria anodes always show modest performance even without the electronic conductor within the anode. Gadolinia doped ceria has shown good catalytic activity for the oxidation of methane with little or no carbon deposition. Modest performance was achieved for $Ce_{0.6}Gd_{0.4}O_{2-\delta}$ exposed to H_2 instead of CH_4 (Marina and Mogensen, 1999; Marina *et al.*, 1999). Anyway ceria-based cermet anodes are preferable over single phase ceria anodes, as long as the electrode conductivity is concerned.

2.4.2 Rutile

Rutile (TiO_2) has a tetragonal structure with a distorted hexagonal close packed anion arraying with the octahedral vacancy sites occupied by cations. Edge-sharing octahedra in rutile can facilitate electron transfer and results in high electronic conductivity (Table 2-3). Oxygen vacancies might also be introduced into the rutile lattice. However, the mobility of oxygen vacancies in rutile, if existed, is relatively low as comparing to many other oxides. The reason is that the oxygen ion octahedra have to be rotated if the oxygen vacancies are to jump from one octahedron to the next. The rotation of edge-sharing octahedra in rutile is much harder than that of corner-sharing octahedra in perovskite. This might be the reason why TiO_2 is a poor ionic conductor. NbO_2, the reduced form of Nb_2O_5, was completely miscible with TiO_2 from 900 to 1300 ℃. The conductivity of TiO_2–Nb_2O_5 solid solution reached ~10^2 S/cm at 1000 ℃, but surprisingly its reaction kinetics was very poor both in H_2 and CH_4 (Table 2-3). The thermal expansion coefficient (TEC) of reduced TiO_2–NbO_2 was 2.3 ×10^{-6} /K– a quarter of that of YSZ (Tao and Irvine, 2004b). The incorporation of Cr_2O_3 into TiO_2–NbO_2 renders it redox stable but compromises the conductivity (Lashtabeg *et al.*, 2009). These drawbacks somewhat inhibit rutile-based oxides as suitable candidates for SOFC anodes.

2.4.3 Tungsten bronze

Oxides with the general formula $A_2BM_5O_{15}$ (with M= Nb, Ta, Mo, W; A and B= Ba, Na, etc.) show the tungsten bronze structure. It can be obtained from the perovskite by rotating some of the MO_6 octahedra. In so doing 40 % of the large cation sites (A2 sites)

are increased in size from tetra-capped square prisms to penta-capped pentagonal prisms, 20% remains essentially unchanged (A1 site), and the remaining 40% of the sites are decreased in size (C site). The formula may be written as $A_{0.6}BO_3$ when the small size A-sites are left empty (Tao and Irvine, 2004b). The distortion of the octahedra means that some B-O bonds is extended and some are short than the average. The connection of the short B-O bond may supply a percolation path for charge transfer, possibly leading to high electronic conductivity.

The conductivity of tungsten bronze in reducing environment is about four orders higher than that in air. Among the various (Ba, Sr, Ca, La)$_{0.6}M_xNb_{1-x}O_3$ (M = Ni, Mg, Mn, Fe, Cr, In, Sn) tungsten bronzes, $Sr_{0.2}Ba_{0.4}Ti_{0.2}Nb_{0.8}O_3$ exhibits the highest conductivity (10 S/cm at $pO_2 = 10^{-20}$ bar and at 930 ℃), as shown in Table 2-3. In contrast, the conductivity in air is only around 10^{-3} S/cm at 930 ℃, as oxygen vacancies are generated only under reducing conditions. The conductivity increases with decreasing pO_2 and reaches 1–10 S/cm at $pO_2 < 10^{-17}$ bar. The electrochemical performance of tungsten bronze anodes is poor. Polarization resistance (R_p) of $(Sr_{1-x}Ba_x)_{0.6}Ti_{0.2}Nb_{0.8}O_{3-\delta}$ is around 28 Ω cm^2 at 930 ℃ (Kaiser *et al.*, 2000). The introduction of Mn into the tungsten bronze structure is supposed to reduce R_p. Even though, the corresponding reaction kinetics is still inferior to fluorite oxides, such as doped zirconia and doped ceria. In addition, the TEC of these compounds (e.g., 6.7×10^{-6} K^{-1} for $Sr_{0.2}Ba_{0.4}Ti_{0.2}Nb_{0.8}O_{3-\delta}$) are significantly lower than that of zirconia (Kaiser *et al.*, 2000). The TEC mismatch of these tungsten bronze oxides with YSZ poses sheer problems.

2.4.4 Pyrochlore

Pyrochlore-type oxides, $A_2B_2O_7$, can be derived from fluorite by removing 1/8 of the oxygen ions, ordering the two cations, and ordering the oxygen vacancies. $A_2B_2O_7$ pyrochlore structure is formed of the cation radius of the two cations falls into a specific range. Readers who are interested in structural studies on pyrochlore are recommended to study Wuensch's exhaustive review on $A_2B_2O_7$ (A= Y, Gd, Sc, Yb, Ca, etc.; B= Sn, Ti, Zr, etc.) structures (Wuensch *et al.*, 2000). Substituting B sites with larger B' ions progressively drive the pyrochlore structure to complete disorder, producing oxygen ion conductivity greater than 10^{-2} S/cm at 1000 ℃. The pyrochlore, $Gd_2Ti_2O_7$ (GT), were considered as potential SOFC anodes. Both the magnitude and the type of conduction

(ionic and/or electronic) was found to be influenced by dopant size, site location (A or B cation sublattice) and net dopant density (Kramer *et al.*, 1994). Ca doping into the A site was found to increase the ionic conductivity up to two orders of magnitude. In contrast, other alkaline earth dopants (Sr and Mg) induced a drop in ionic and an enhancement in electronic conductivity due to the large dopant-host size mismatch.

High ionic conductivity and mixed ionic and electronic conductivity pyrochlore had been reported, such as $(Gd_{0.98}Ca_{0.02})_2Ti_2O_7$. It could be a potential parent phase. R_p as low as 0.2 Ω cm^2 at 950 ℃ had been reported for pyrochlore anodes exposed to H_2S-containing hydrogen atmosphere (Zha *et al.*, 2005a). Table 2-3 lists doped pyrochlore for potential SOFC anode applications, among which Mo doped titanate pyrochlore was especially promising. The $Gd_2Ti_2O_7$–$Gd_2Mo_2O_7$ solid solution, with the advantage of stabilizing $Gd_2Mo_2O_7$ at high pO_2, is the popular parent pyrochlore structure. These solid solutions do exhibit high electrical conductivity, but they are stable only within a certain pO_2 range. The pO_2 boundary largely depends on the temperature. The $Gd_2(Ti_{1-x}Mo_x)_2O_7$ solid solution phase is, therefore, not a redox stable material at high temperatures. A chemical compatibility study between $Gd_2(Ti_{1-x}Mo_x)_2O_7$ and YSZ indicated no significant reactions in the reducing environment at 1000 ℃ (Porat *et al.*, 1997c; Porat *et al.*, 1997b). So far, the studied pyrochlore phases are either redox unstable or poorly conducting. It needs more efforts to find an ideal redox stable mixed conductor in the pyrochlore category.

2.4.5 Perovskite

Perovskite is the name of the mineral $CaTiO_3$. Its structure consists of corner-shared TiO_6 octahedra with the large Ca^{2+} situating at corners of the unit cell. More generally, ABO_3 compounds having structure based on this architecture are also called perovskite. The powerful perovskite structure can adapt considerable lattice mismatch between the (A–X) and (B–X) bond lengths, even in the cases that more than one A-site cation and/or M-site cation species are present. In addition, the large tolerance of atomic vacancies and the formation of intergrowth structures extend this family even further. Some perovskites can accommodate a large content of oxygen vacancies, thus making them as potential oxygen ion conductors. Perovskite always allows first-row transition metal ions to be introduced into the B-site lattices and rare-earth and lanthanoid ions into

A-site lattices. First-row transition metal ions usually exhibit multi-valence under different fuel atmospheres. This might represent the origin of high electronic conductivity if the electrons are well delocalized. Good ionic and mixed conductivity has been found in several perovskite oxides. A systematic review of the transport phenomena in perovskites had been given (Goodenough, 2004).

Perovskite covers the whole spectrum of SOFC components– electrolyte, anode, cathode, and interconnector. Single cells entirely based on perovskites had been demonstrated (Tao *et al.*, 2005). Sr- and Mg- doped $LaGaO_3$ (LSGM) exhibit high oxygen ionic conductivity and are used as electrolyte materials (Haavik *et al*., 2004), though their mechanical strength and chemical stability is inferior to YSZ. Manganite, ferrite, and cobaltite perovskites have modest ionic but high electronic conductivity. They have been proven to be good SOFC cathode materials. Sr-doped $LaMnO_3$ and Sr-doped $LaCo(Fe)O_3$ are used as cathodes for HT-SOFC and IT-SOFC, respectively (Berenov *et al*., 2010; Laguna-Bercero *et al*., 2010). Doped lanthanum chromites, like Sr-doped $LaCrO_3$, are extensively used as interconnect materials. In contrast, not so many perovskites are competent for SOFC anode application, as far as the chemical stability in reducing environment and electrical conductivity are concerned. In Chapter 2.4.5.1 and 2.4.5.2, chromite and titanate single perovskites used as SOFC anodes are reviewed, respectively. Further discussions also cover double perovskites and Ruddlesden–Popper series that belong to an extended definition of perovskite.

2.4.5.1 Chromite

Lanthanum-chromite (LC)-based materials have been used as SOFC interconnect materials, where Sr and Ca are the typical dopants. The electrical conductivity of Sr-doped $LaCO_3$ (LSC) was around 20 S/cm in air but was decreased when exposed to reducing environments (Simner *et al.*, 2000). A good TEC match between the LSC with YSZ is achieved by tailoring the Sr content of LSC. The sinterability of LSC to electrolyte (e.g., YSZ) is very poor so that it is essentially inert to fuel oxidation. Little or no reforming activity or direct oxidation of CH_4 had been observed on lanthanum chromites (Metcalfe and Baker, 1996). Anyway, this group of materials can be used as the parent material for SOFC anode application, as long as the excellent chemical stability of LSC is retained.

R_p of bare Ca-doped $LaCO_3$ (LCC) was around 86 Ω cm^2 at 850 ℃ in H_2. R_p is reduced to 21 Ω cm^2 with 10% Mg doping in M-site, i.e. replacing Cr. R_p can be further reduced to 5 Ω cm^2 in H_2 via 3% V doped into M site, but it was as high as 30 Ω cm^2 in CH_4 (Primdahl *et al.*, 2001). Multivalent first row transition metals, such as Fe, Mn, Co, Ni, Ti, form redox couples that facilitate electron transfer when doped into LSC. Slight doping of Ru into LSC had also been attempted (Combemale *et al.*, 2009). Promising results were reported for Fe, Ni and Co doped LSC. However, all of them cannot withstand the SOFC anodic environment for long time, either second phases form or metal precipitates from the perovskite structure. Ti and Mn are believed to be the more effective dopants than Fe, Co, and Ni in low pO_2 conditions.

The conductivity of Ti-doped LSC (LSCT) was around 10^{-4}–10^{-2} S/cm, much lower than 0.1 S/cm that was required for the SOFC electrode application (Steele *et al.*, 1990). R_p of LSCT, with Ti content in LSCT in the range from 20% to 50%, was higher than 40 Ω cm^2 in H_2 at 857 ℃ (Pudmich *et al.*, 2000). Mn is supposed to be another promising dopant, as $LaMnO_3$–based oxides are good cathode materials for HT-SOFCs. The $Mn^{3+/}Mn^{4+}$ redox couple seems to have good electrochemical reaction kinetics. However, 20% Mn doping in LSC did not show significant improvement of electrode performance. R_p of $La_{0.8}Sr_{0.2}Cr_{0.8}Mn_{0.2}O_3$ was still as high as 50–70 Ω cm^2 in H_2 at 850 ℃ (Vernoux *et al.*, 2001). Surprisingly, good electrochemical performance was achieved by increasing the Mn doping to 50% in LSC, i.e., $La_{0.8}Sr_{0.2}Cr_{0.5}Mn_{0.5}O_3$ (LSCM). LSCM exhibited comparable electrochemical performance to Ni–YSZ cermets. It was stable both in fuel and air conditions and showed stable electrode performance in methane. The electrode polarization resistance approached 0.8 Ω cm^2 at 900 ℃ in wet CH_4 (Tao and Irvine, 2003). Isotopic exchange experiments indicated that the oxygen tracer diffusion coefficient (D^*) of LSCM under oxidising and reducing conditions at 1000 ℃ were 4×10^{-10} cm^2/s and 3×10^{-8} cm^2/s, respectively. Under the same conditions the surface exchange coefficient (k^*) were 5×10^{-8} cm/s and 4×10^{-8} cm/s, respectively (Raj *et al.*, 2006). The electrode performance of LSCM can be further improved via electrode engineering of composite electrodes and the impregnation methods (Jiang *et al.*, 2006a; Jiang *et al.*, 2006b; Lu and Zhu, 2007). One of the

drawbacks of LSCM is its low electronic conductivity. The total conductivity of LSCM in air is less than 30 S/cm and not higher than 1 S/cm in the reducing environment (Jiang *et al.*, 2008). It implies that the current collection comes to be an issue for fuel cells with LSCM anode.

2.4.5.2 Titanate

Titanates that are stable in reducing conditions are another group of potential SOFC anode materials. The most popular parent structure is strontium titanate ($SrTiO_3$). It is n-type conductor when donor-doped (e.g. La^{3+}, Y^{3+}) and/or exposed to reducing atmospheres. La^{3+} is an appropriate donor dopant because of similar ionic radii with Sr^{2+}. The initial electrical conductivity of $La_xSr_{1-x}TiO_3$ (LST) strongly depends on the pO_2 during the sample sintering. The samples sintered in air exhibited an electrical conductivity on the order of magnitude of 10^1 S/cm. In contrast, LST that was sintered in hydrogen at 1650 ℃ showed conductivity in the order of magnitude of 10^2 S/cm under typical SOFC operating temperatures (Marina *et al.*, 2002). LST could be used as the anode support due to the high electronic conductivity (Pillai *et al.*, 2008; Ma *et al.*, 2010). The conductivity of LST increases together with increasing La concentration but levels off at the La content around 0.4. Depending on the percentage of La dopant the conductivity of LST can reach ~10^2 S/cm. At low pO_2 the electronic conduction is reinforced when Ti^{4+} is reduced to Ti^{3+}. Meanwhile, oxygen vacancies are generated because of the electroneutrality. This is the reason why the conductivity LST in reducing conditions is much higher than that in air. LST has been doped with transition metals (Ni, Co, Cu, Cr and Fe) and Ce, among which Ce seems to be the most effective one (Cumming *et al.*, 2011). LST is also compatible to YSZ even when subjected to oxidation/reduction cycling.

LST can also form complex perovskite phases if with oxygen excess. $La_2Sr_4Ti_6O_{19-\delta}$ and its derivatives, which has a unit cell consisting of six ordered perovskite primate cells and with about 1/19 oxygen excess, had been regarded as potential anode for SOFC fed with hydrocarbons. Their conductivities strongly depend on the oxygen stoichiometry. They exhibit n-type conduction behaviour when more Ti^{3+} is generated. While the conductivity was negligible in air, it could be increased to ~10^2 S/cm in 5% H_2/Ar atmosphere at 900 ℃. An anodic R_p of 8.93 Ω cm^2 and P_{max} of 0.02 W cm^2 were

achieved in wet CH_4 when using pure $La_2Sr_4Ti_6O_{19-\delta}$ as anode (Canales-Vazquez *et al.*, 2003). $La_4Sr_{n-4}Ti_nO_{3n+2}$ (n >7) are layered phases and have oxygen planes in the form of crystallographic shears joining octahedron blocks. These planes became more sporadic with increasing n (i.e., decrease of oxygen content) until they were no longer in crystallographic features. It finally resulted in local oxygen-rich defects randomly distributed within a perovskite framework when n>11. Optimized titanates with disordered oxygen defects were proven to be excellent SOFC anode materials. For SOFCs using the engineered $La_4Sr_8Ti_{11}Mn_{0.5}Ga_{0.5}O_{37.5}$, the n=12 member in the $La_4Sr_{n-4}Ti_nO_{3n+2}$ series, as anode, high OCV and very low R_p both in H_2 and CH_4 were reported (Ruiz-Morales *et al.*, 2007).

The electrode performance was greatly improved by replacing 1/12 Ti by Mn in $La_4Sr_{n-4}Ti_nO_{3n+2}$ series (n=12). For SOFCs with $La_4Sr_8Ti_{11}MnO_{38-\delta}$ composite anode, R_p was as low as 0.7 Ω cm^2 in wet CH_4 and at 950 ℃. The overpotential was lower than 0.1 V at a drawn current density of 0.6 A/cm^2 (Ovalle *et al.*, 2006). Comparable cell performance was achieved with a large replacement of Ti with Mn, such as $La_{0.4}Sr_{0.6}Ti_{0.4}Mn_{0.6}O_{3-\delta}$ (Fu *et al.*, 2006). R_p around 0.57 Ω cm^2 at 900 ℃ in CH_4 was achieved by sophisticated doping with Sc or Ga into Ti site (Table 2-3). However, the chemical expansion of these materials is irreversible during the redox cycling, though the expansion itself is not high. This property would restrict their applications in electrolyte-supported and/or small-sized SOFCs, such as the integrated planar-type SOFC.

An unusual increase of electrical conductivity was observed in Y-doped $SrTiO_3$. The electrical conductivity of $Sr_{1-1.5x}Y_xTiO_{3-\delta}$ increased with increasing yttrium level and reached a maximum value of 64 S/cm with x = 0.08 at 800 ℃ (Hui and Petric, 2002a). Its conductivity was influenced by both the oxygen partial pressure of the reducing atmosphere and the saturation level of the dopant. It also underwent a transition from p-type to n-type conduction under decreased pO_2. The conductivity was increased from 64 S/cm for the charge-neutral $Sr_{0.88}Y_{0.08}TiO_{3-\delta}$ composition to a maximum of 82 S/cm for $Sr_{0.86}Y_{0.08}TiO_{3-\delta}$ at 800 ℃. However, cell performance with optimized Y-doped $SrTiO_3$ anodes was still not higher than 0.05 W/cm^2 in wet H_2 (Hui and Petric,

2002b). One of the shortcomings of Y-doped $SrTiO_3$ is that it must be prepared from prolonged reduction at elevated temperatures up to 1500 ℃.

2.4.6 Double perovskite

Double perovskites contain different B-site cations that are ordered. The degree of cation order strongly influences the oxygen self-diffusion in double perovskites such as $GdBaCo_2O_{5+\delta}$ (Parfitt *et al.*, 2011). Early results indicated that $SrCu_{0.4}Nb_{0.6}O_{2.9}$ was not stable in H_2 as metallic Cu precipitated from the double perovskite structure (Tao and Irvine, 2002b). $Sr_2Mn_{0.8}Nb_{1.2}O_{6-\delta}$ had a total conductivity of 0.36 S/cm and exhibited p-type behaviour in low pO_2 (Tao and Irvine, 2002a). Replacing Mn and Nb with Mg and Mo, $Sr_2Mg_{1-x}Mo_xO_{6-\delta}$ (SMMO) seemed to be a good material for hydrocarbon utilization with modest sulphur tolerance. The conductivity of SMMO reached 10 S/cm at 800 ℃ in H_2 and CH_4, and the system gave satisfactory anode performance in H_2 and CH_4 as well as moderate sulphur tolerance (Huang *et al.*, 2006b). With 300 mm-thick LSGM as electrolyte and $SrCo_{0.8}Fe_{0.2}O_{3-\delta}$ as cathode, P_{max} of single cells could reach 0.84 W/cm^2 and 0.45W/cm^2 at 800 ℃ and 700 ℃ in H_2, respectively. P_{max} was around 0.44 W/cm^2 and 0.34 W/cm^2 in dry and wet CH_4 at 800 ℃. The sulphur tolerance of SMMO enabled the use of natural gas as fuel. Single SOFCs with SMMO anodes showed negligible performance degradation up to 50 power cycles (Huang *et al.*, 2006c). La-substituted SMMO, i.e. $Sr_{2-x}La_xMgMoO_{6-\delta}$ ($0.6 \leq x \leq 0.8$), showed better performance than SMMO. Differential scanning calorimetry (DSC) results showed that SMMO underwent phase transition at 275 ℃ in air. The phase transition, however, did not occur if SMMO was exposed to wet H_2 (Marrero-Lopez *et al.*, 2009). One of the issues of Mo-containing oxides is that Mo might easily diffuse to other cell components (Marrero-López *et al.*, 2007). Therefore, the long-term stability of SOFCs using Mo-containing anodes is of concern. In addition, SMMO reacts with the three major SOFC electrolyte materials, i.e. YSZ, GDC, and $La_{0.8}Sr_{0.2}Ga_{0.8}Mg_{0.2}O_{3-\delta}$ above 1000 ℃, among which the reaction with YSZ is most severe (Marrero-Lopez *et al.*, 2010).

Various doping approaches of SMMO had been reported in literature, e.g. Co (Zhang *et al.*, 2011), Fe (Xiao *et al.*, 2010; Liu *et al.*, 2010b), and Ni (Huang *et al.*, 2009) replacing Mg and Mo, La (Ji *et al.*, 2007) and Ca and Ba (Zhang *et al.*, 2010b)

replacing Sr. The electronic conductivity seem to be improved by replacing Mg with Fe in the double perovskite structure. The conductivity of $Sr_2Fe_{1.5}Mo_{0.5}O_{6-\delta}$ (SFM) reached 300–600 S/cm in air and hydrogen. Surprisingly, however, that both positive (Liu *et al.*, 2010b) and negative temperature (Xiao *et al.*, 2010) effects had been observed in Fe-doped SMMO. Generally speaking, the conductivity of SMMO and its derivatives are in the range of several to hundreds of S/cm for various doped SMMO (Table 2-3). $Sr_2Fe_{1.5}Mo_{0.5}O_{6-\delta}$ (Liu *et al.*, 2010b) showed P_{max} around 0.1 W/cm^2 at 850 ℃ in wet CH_4. In comparison, much higher P_{max} had been reported to be 0.55, 0.57, and 0.23, for $Sr_{1.2}La_{0.8}MgMoO_{6-\delta}$ (Ji *et al.*, 2007), $Sr_2CoMoO_{6-\delta}$, $Sr_2NiMoO_{6-\delta}$ at 800 ℃ and in wet CH_4 , respectively. More conductivity and electrode performance results are shown in Table 2-3.

Table 2-3 Conductivity and electrochemical properties of selected conducting oxides as SOFC anodes (Table modified from Ref. (Jiang and Chan, 2004))

Composition	Electrical conductivity (S/cm)		Polarization resistance (Ω cm^2)		Reference
	Temperature /reduced [a]	Temperature/ Oxidized [b]	Temperature/ hydrogen [c]	Temperature/ methane [c]	
Fluorite-zirconia based					
$Y_{0.20}Ti_{0.18}Zr_{0.62}O_{1.90}$	-	-	16.8 (932)	-	(Kelaidopoulou *et al.*, 2001a)
	-	-	-	170 (932)	(Kelaidopoulou *et al.*, 2001b)
$x ZrO_2$–$(1-x)In_2O_3$ ($0.23<x<0.45$)	-	2–10 (1000)	-	-	(Sasaki *et al.*, 1994)
$Y_{0.165}Zr_{0.735}Ti_{0.1}O_{2-x}$	0.303 (900)	0.334 (900)	-	-	(Tietz *et al.*, 2004)
$Y_{0.11}Zr_{0.84}Ti_{0.05}O_{2-x}$	0.462 (900)	0.372 (900)	-	-	
$Y_{0.22}Zr_{0.73}Ti_{0.05}O_{2-x}$	0.715 (900)	0.624 (900)	-	-	
$Y_{0.243}Zr_{0.657}Ti_{0.1}O_{2-x}$	0.159 (900)	0.199 (900)	-	-	
$Y_{0.087}Zr_{0.813}Ti_{0.1}O_{2-x}$	0.246 (900)	0.266 (900)	-	-	
$Y_{0.165}Zr_{0.664}Ti_{0.171}O_{2-x}$	0.134 (900)	0.553 (900)	-	-	
$Y_{0.165}Zr_{0.806}Ti_{0.029}O_{2-x}$	0.070 (900)	0.058 (900)	-	-	
$Ti_xZr_{0.786-x}Y_{0.214}O_{1.89}$ ($0.045<x<0.090$)	0.002~0.005 (900)	-	-	-	(Swider and Worrell, 1996)
Fluorite-ceria based					
$Ce_{0.9}Gd_{0.1}O_2$	0.7 (800)	$10^{-1.7}$~ $10^{-1.3}$ (800)	-	-	(Wang *et al.*, 2000)
$Ce_{0.8}Gd_{0.2}O_2$	0.6 (800)	-	-	-	
$Ce_{0.8}Gd_{0.2}O_{2-\delta}$	0.16 (800)	8.6×10^{-2} (800)	-	-	(Yahiro *et al.*, 1989)
$Ce_{0.6}Gd_{0.4}O_{1.8}$	-	-	0.39 (1000)	-	(Marina *et al.*, 1999)
$Ce_{0.8}Gd_{0.2}O_{1.9}$	~$10^{-0.9}$ (800)	~$10^{-1.3}$ (800)	-	-	(Yahiro *et al.*, 1989)
$Ce_{0.8}Sm_{0.2}O_{1.9}$	~$10^{-0.7}$ (800)	~$10^{-1.1}$ (800)	-	-	
CeO_2	-	1.31×10^{-6} (500)	-	-	(Suda *et al.*, 2006)

$Ce_{0.95}La_{0.05}O_{1.975}$	2.23×10^{-3} (500)	2.10×10^{-3} (500)	-	-	
$Ce_{0.9}La_{0.1}O_{1.95}$	3.71×10^{-3} (500)	3.48×10^{-3} (500)	-	-	
$Ce_{0.8}La_{0.2}O_{1.9}$	2.82×10^{-3} (500)	2.83×10^{-3} (500)	-	-	
$Ce_{0.8}Tb_{0.2}O_x$	0.1 (800)	$\sim10^{-1.8}$ (800)	-	-	(Martinez-Arias *et al.*, 2005)
$Ce_{0.5}Tb_{0.5}O_x$	$\sim10^{-1.9}$ (800)	$\sim10^{-1.7}$ (800)	-	-	
CeO_{2-x}	2 (905)	-	-	-	(Naik and Tien, 1979)
CeO_2- 0.4 m/o Nb_2O_5	3.7 (905)	0.3 (905)	-	-	
Rutile					
NbO_2	~200 (1000)	-	-	-	(Reich *et al.*, 2001)
$Nb_{1-x}Ti_xO_2$ ($0<x<1$)	$\sim10^{1.3}$-10^{3} (997)	-	>500 (762)	>1000 (812)	
$Ti_{1-2x}Cr_xNb_xO_2$ ($0<x<=0.5$)	>20 (900)	$1.5–1.7\times10^{-2}$ (900)	-	-	(Lashtabeg *et al.*, 2009)
$Ti_{0.93}Nb_{0.07}O_2$	~ 50 (400–1000)	-	-	-	(Michibata *et al.*, 2011)
Tungsten bronze					
$Sr_{0.6}Ti_{0.2}Nb_{0.8}O_3$	2.5 (930)	3×10^{-4} (930)	-	-	(Slater and Irvine, 1999a)
$Sr_{0.4}Ba_{0.2}Ti_{0.2}Nb_{0.8}O_3$	2.5 (930)	2×10^{-4} (930)	-	-	
$Sr_{0.2}Ba_{0.4}Ti_{0.2}Nb_{0.8}O_3$	3.2 (930)	2×10^{-4} (930)	-	-	
$Ba_{0.4}Ca_{0.2}Ti_{0.2}Nb_{0.8}O_3$	3.1 (930)	2×10^{-4} (930)	-	-	
$Ba_{0.6}Ti_{0.2}Nb_{0.8}O_3$	3.2 (930)	1×10^{-4} (930)	-	-	
$Ba_{0.6}Mn_{0.067}Nb_{0.933}O_3$	2.2 (930)	4×10^{-4} (930)	-	-	(Slater and Irvine, 1999b)
$Ba_{0.4}La_{0.2}Mn_{0.133}Nb_{0.867}O_3$	0.2 (930)	6×10^{-4} (930)	-	-	
$Ba_{0.4}Sr_{0.2}Mn_{0.067}Nb_{0.933}O_3$	1.8 (930)	4×10^{-4} (930)	-	-	
$Ba_{0.6}Ni_{0.067}Nb_{0.933}O_3$	4.5 (900)	5×10^{-4} (930)	-	-	
$Ba_{0.4}La_{0.2}Ni_{0.133}Nb_{0.867}O_3$	2.4 (930)	2×10^{-4} (930)	-	-	
$Ba_{0.6}Mg_{0.067}Nb_{0.933}O_3$	1.3 (930)	8×10^{-5} (930)	-	-	
$Ba_{0.4}La_{0.2}Mn_{0.133}Nb_{0.867}O_3$	0.5 (930)	2×10^{-5} (930)	-	-	
$Ba_{0.4}La_{0.2}Fe_{0.2}Nb_{0.8}O_3$	1.1 (930)	2×10^{-4} (930)	-	-	
$Ba_{0.5}La_{0.1}Fe_{0.2}Nb_{0.8}O_3$	0.7 (930)	3×10^{-3} (930)	-	-	
$Ba_{0.6}Fe_{0.1}Nb_{0.9}O_3$	3.8 (930)	1×10^{-2} (930)	-	-	
$Ba_{0.4}Ca_{0.2}Fe_{0.1}Nb_{0.9}O_3$	1.2 (930)	3×10^{-3} (930)	-	-	
$Ba_{0.4}Sr_{0.2}Fe_{0.1}Nb_{0.9}O_3$	2.3 (930)	4×10^{-3} (930)	-	-	
$Ba_{0.6}In_{0.1}Nb_{0.9}O_3$	1.0 (930)	1×10^{-4} (930)	-	-	
$Ba_{0.4}Sr_{0.2}In_{0.1}Nb_{0.9}O_3$	1.5 (930)	1×10^{-4} (930)	-	-	
$Ba_{0.4}La_{0.2}In_{0.2}Nb_{0.8}O_3$	0.3 (930)	2×10^{-5} (930)	-	-	
$Ba_{0.6}Cr_{0.1}Nb_{0.9}O_3$	3.6 (930)	2×10^{-3} (930)	-	-	
$Ba_{0.6}Sn_{0.2}Nb_{0.8}O_3$	21 (930)	3×10^{-4} (930)	-	-	
$(Sr_{1-x}Ba_x)_{0.6}Ti_{0.2}Nb_{0.8}O_{3-\delta}$	0.01-1 (930)	~ 10^{-5} (930)	~28 (930)	-	(Kaiser *et al.*, 2000)
Pyrochlore					
$Gd_2(Ti_{0.5}Mo_{0.5})_2O_7$	11 (900)	-	-	-	(Porat *et al.*, 1997b)
$Gd_2(Ti_{0.3}Mo_{0.7})_2O_7$	$\sim10^{1.8}$ (800)	$\sim10^{-1.7}$ (800)	-	-	(Porat *et al.*, 1997a)
$Gd_2(Ti_{0.5}Mo_{0.5})_2O_7$	$\sim10^{1.2}$ (900)	$\sim10^{-1.5}$ (900)	-	-	
$Gd_2(Ti_{0.9}Mo_{0.1})_2O_7$	~0.1(900)	$\sim10^{-3}$ (900)	-	-	
$Gd_2((Mo_{2/3}Mn_{1/3})_{0.1}Ti_{0.9})_2O_7$	$\sim10^{-1.4}$ (1000)	$\sim10^{-2.2}$ (1000)	-	-	(Sprague and Tuller, 1999)
$Gd_2Ti_{1.4}Mo_{0.6}O_7$	-	-	0.2 (950)[f]	-	(Zha *et al.*, 2005a)
$Gd_2(Ti_{0.983}Ti_{0.017})_2O_{7-\delta}$	$\sim10^{-2}$ (900)	$\sim10^{-2.5}$ (900)	-	-	(Kramer *et al.*, 1994)

$Pr_2Ce_{0.4}Zr_{1.6}O_{7\pm\delta}$	0.01 (1000)	3×10^{-4} (1000)	-	-	(Holtappels *et al.*, 2000)
$Pr_2Zr_2O_{7\pm\delta}$	2×10^{-3} (1000)	6×10^{-5} (1000)	-	-	
Single perovskite					
(i) Chromite					
$La_{0.7}Ca_{0.32}CrO_3$	-	-	86 (850)	-	(Primdahl *et al.*, 2001)
$La_{0.75}Ca_{0.25}Cr_{0.9}Mg_{0.1}O_3$	-	-	21 (850)	-	
$La_{0.8}Sr_{0.2}Cr_{0.97}V_{0.03}O_3$	-	-	5 (850)	30 (850)	
$La_{0.7}Mg_{0.3}CrO_3$	0.17 (800)	3.35 (800)	-	-	(Jiang *et al.*, 2008)
$La_{0.75}Sr_{0.25}CrO_3$	7.07 (800)	59.1 (800)			
$La_{0.7}Ca_{0.3}CrO_3$	1.6 (800)	50.1 (800)	-	-	
$La_{0.7}Ba_{0.3}CrO_3$	-	2.69 (800)			
$La_{0.8}Sr_{0.2}Cr_{0.97}V_{0.03}O_3$	-	-	-	28 (850)	(Vernoux *et al.*, 2000)
$La_{0.75}Sr_{0.25}Cr_{0.5}Fe_{0.5}O_3$	-	-	1.15 (850)	1.79 (850)	(Tao and Irvine, 2004c)
$La_{0.7}Sr_{0.3}Cr_{0.5}Ti_{0.5}O_3$	0.02 (800)	-	-	-	(Pudmich *et al.*, 2000)
$La_{0.7}Sr_{0.3}Cr_{0.8}Ti_{0.2}O_3$	-	-	40 (857)	-	
$La_{0.8}Sr_{0.2}CrO_3$	-	-	256 (850)	-	(Vernoux *et al.*, 2001)
$La_{0.8}Sr_{0.2}Cr_{0.8}Mn_{0.2}O_3$	-	-	51(850)	-	
$La_{0.8}Sr_{0.2}Cr_{0.5}Mn_{0.5}O_3$	1.3 (900)	38 (900)	0.26 (900)	0.85 (900)	(Tao and Irvine, 2003)
$La_{0.75}Sr_{0.25}Cr_{0.5}Mn_{0.5}O_3$	-	-	1.4(800)	2.3 (800)	(Lu and Zhu, 2007)
	-	-	2.5 (800)[g]	11 (800)	(Jiang *et al.*, 2006b)
	-	-	-	2.62 (900)[g]	(Jiang *et al.*, 2006a)
	0.22 (800)	28.8 (800)	-	-	(Jiang *et al.*, 2008)
$(La_{0.8}Sr_{0.2})_{0.9}Cr_{0.5}Mn_{0.5}O_3$	-	-	0.18 (900)	-	(Tao *et al.*, 2005)
(ii) Titanate					
$La_{0.7}Ca_{0.3}TiO_3$	2.7 (900) [d]	-	-	-	(Pudmich *et al.*, 2000)
$La_{0.4}Ca_{0.6}TiO_3$	60 (900)	-	-	-	
$La_{0.7}Ca_{0.3}Cr_{0.5}Ti_{0.5}O_3$	0.3 (900)	-	-	-	
$La_{0.7}Ca_{0.3}Cr_{0.8}Ti_{0.2}O_3$	-	-	32 (850)	-	
$La_{0.4}Sr_{0.4}TiO_3$	96 (880)	-	-	-	(Neagu and Irvine, 2010)
$La_{0.1}Sr_{0.9}TiO_3$	3 (1000)	1 (1000)	-	-	(Marina *et al.*, 2002)
$La_{0.1}Sr_{0.9}TiO_3$ [e]	80 (1000)	0.004 (1000)	-	-	
	-	-	510 (800)	-	(Yashiro *et al.*, 2001)
$La_{0.2}Sr_{0.8}TiO_3$	3 (1000)	1 (1000)	-	-	(Marina *et al.*, 2002)
$La_{0.2}Sr_{0.8}TiO_3$ [e]	200 (1000)	0.03 (1000)	-	-	
$La_{0.3}Sr_{0.7}TiO_3$	4 (1000)	1.3 (1000)	-	-	
$La_{0.3}Sr_{0.7}TiO_3$ [e]	200 (1000)	0.01 (1000)	-	-	
$La_{0.4}Sr_{0.6}TiO_3$	16 (1000)	0.004 (1000)	-	-	
$La_{0.4}Sr_{0.6}TiO_3$ [e]	360 (1000)	0.03 (1000)	-	-	
$La_{0.2}Sr_{0.8}TiO_3$ [e]	$\sim10^{2.02}$ (900)	$10^{1.76}$ (900)	-	-	(Huang *et al.*, 2007)
$La_{0.2}Sr_{0.8}TiO_3$ [e]	-	-	350 (800)	-	(Yashiro *et al.*, 2001)
$SrTi_{0.97}Nb_{0.03}O_3$	-	-	700 (800)	-	
$Sr_{0.94}Ti_{0.9}Nb_{0.1}O_3$	-	-	160 (850)[g]	-	(Blennow *et al.*, 2009)
$SrTi_{1-x}Nb_xO_3$ ($0.01<x<0.08$)	9–28 (800)	-	-	-	(Karczewski *et al.*, 2010)
$Sr_{0.895}Y_{0.07}TiO_3$	7–64 (800)	-	-	-	(Vozdecky *et al.*, 2011)

$Sr_{0.85}Y_{0.15}Ti_{0.95}Ca_{0.05}O_3$	37 (800)	-	-	-	(Hui and Petric, 2001)
$Sr_{0.85}Y_{0.15}Ti_{0.95}Co_{0.05}O_3$	45 (800)	-	-	-	
$Sr_{0.85}Y_{0.15}Ti_{0.95}Zr_{0.05}O_3$	13 (800)	-	-	-	
$Sr_{0.85}Y_{0.15}Ti_{0.95}Mg_{0.05}O_3$	6 (800)	-	-	-	
$Sr_{0.88}Y_{0.08}TiO_3$	64 (800)	-	-	-	
$SrTi_{0.99}Nb_{0.01}O_3$	$\sim10^{-0.4}$ (800)	$\sim10^{-1.2}$ (800)	-	-	(Horikiri *et al.*, 2008)
$SrTi_{1.09}Nb_{0.01}O_3$	$\sim10^{-0.8}$ (800)	$\sim10^{-0.8}$ (800)	-	-	
$SrTi_{0.99}Nb_{0.01}O_3$	10–11 (600-900)	-	-	-	(Gross *et al.*, 2009)
$SrTi_{0.95}Nb_{0.05}O_3$	6–10 (600-900)	-	-	-	
$SrTi_{0.8}Nb_{0.2}O_3$	70–90 (600-900)	-	-	-	
$Sr_{0.88}Y_{0.08}TiO_{3-\delta}$	$\sim10^{1.7}$ (800)	~0.1 (800)	-	-	(Hui and Petric, 2002b)
$Sr_{0.85}Y_{0.10}Ti_{0.95}Co_{0.05}O_{3-\delta}$	45 (800)	-	-	-	
$La_{0.4}Sr_{0.6}TiO_{3-\delta}$	1	2×10^{-5} (800)	-	-	(Fu *et al.*, 2006)
$La_{0.4}Sr_{0.6}Ti_{0.8}Mn_{0.2}O_{3-\delta}$	0.1 (800)	2×10^{-2} (800)	-	-	
$La_{0.4}Sr_{0.6}Ti_{0.6}Mn_{0.4}O_{3-\delta}$	0.1 (800)	2 (800)	-	-	
$La_{0.4}Sr_{0.6}Ti_{0.4}Mn_{0.6}O_{3-\delta}$	2(800)	20 (800)	0.35 (855)[g]	0.8 (855)[g]	
$La_xSr_{0.9-x}Ti_{0.6}Fe_{0.4}O_{3-\delta}$ (x=0-0.45)	$10^{-0.55}$~$10^{0.18}$ (800)	$10^{-0.3}$~1 (800)	-	-	(Fagg *et al.*, 2003b)
$Sr_{0.98}Y_{0.02}TiO_3$	-	10 (900)	-	-	(Li *et al.*, 2007b)
$Sr_{0.92}Y_{0.08}TiO_3$	-	65 (900)	-	-	
$Sr_{0.91}Y_{0.09}TiO_3$	-	70 (900)	-	-	
$Sr_{0.88}Y_{0.12}TiO_3$	-	50 (900)	-	-	
$Sr_{0.88}Y_{0.08}TiO_3$	-	-	2.9 (800)[g]	-	(Kurokawa *et al.*, 2007a)
$Sr_{0.9}Ti_{0.8}Nb_{0.2}O_3$ [e]	350 (800)	-	-	-	(Kolodiazhnyi and Petric, 2005)
$Sr_{0.84}Y_{0.04}Ti_{0.8}Nb_{0.2}O_3$ [e]	250 (800)	-	-	-	
$Sr_{0.88}Y_{0.08}TiO_3$ [e]	100 (800)	-	-	-	
$La_2Sr_4Ti_6O_{19-\delta}$	30 (900)	8.5×10^{-4} (900)	2.97 (900)	8.93 (900)	(Canales-Vazquez *et al.*, 2003)
$La_4Sr_8Ti_{11}MnO_{38-\delta}$	-	-	0.3 (950)[g]	0.7 (950)[g]	(Ovalle *et al.*, 2006)
$La_4Sr_8Ti_{11}Mn_{0.5}Ga_{0.5}O_{38-\delta}$	0.5 (900)	10^{-3} (900)	0.2 (900)	0.57 (900)	(Ruiz-Morales *et al.*, 2007)
$La_2Sr_4Ti_{5.7}Sc_{0.3}O_{19-z}$	-	-	0.5 (900)	1.2 (900)	(Canales-Vazquez *et al.*, 2005)
Double perovskite					
$Sr_2Mn_{0.8}Nb_{1.2}O_6$	8×10^{-3} (900)	0.36 (900)	-	-	(Tao and Irvine, 2002b)
$SrMn_{0.5}Nb_{0.5}O_{3-\delta}$	3.1×10^{-2} (900)	1.23 (900)	-	-	(Tao and Irvine, 2002a)
$Sr_2Mg_{1-x}Mo_xO_{6-\delta}$	4-8 (800)	-	-	-	(Huang *et al.*, 2006b; Huang *et al.*, 2006c)
$Sr_2MgMoO_{6-\delta}$	-	-	0.41 (900)	-	(Marrero-Lopez *et al.*, 2010)
	0.19 (800)	7.7×10^{-4} (800)	-	-	(Marrero-Lopez *et al.*, 2009)

$Sr_2CoMoO_{6-\delta}$	1.17 (800)	0.14 (800)	-	-	(Zhang *et al.*, 2011)
$Sr_2Fe_{4/3}Mo_{2/3}O_{6-\delta}$	16 (800)	-	-	-	(Xiao *et al.*, 2010)
$Ca_2FeMoO_{6-\delta}$	416 (800)	-	-	-	(Zhang *et al.*, 2010b)
$Sr_2FeMoO_{6-\delta}$	222 (800)	-	-	-	
$Ba_2FeMoO_{6-\delta}$	25 (800)	-	-	-	
$Sr_2NiMoO_{6-\delta}$	1.11 (800)	0.09	-	-	(Huang *et al.*, 2009)
$Sr_2CoMoO_{6-\delta}$	4.76 (800)	0.20	-	-	

a. Testing in reducing atmosphere (e.g. forming gas)
b. Testing in oxidizing atmosphere (e.g. air)
c. Hydrogen and methane correspond to wet hydrogen and wet methane that are humidified at room temperatures.
d. Temperatures in parentheses are of Celsius degree (℃).
e. Sample sintered or annealing in hydrogen.
f. 10 vol.% H_2S–H_2 fuels.
g. Composite electrode used.

Chapter 3. Synthesis, characterization, and performance of lanthanum strontium vanadate via solid state reactions

3.1 Introduction

Historically, lanthanum strontium vanadate $La_{1-x}Sr_xVO_3$ (LSV, $0 \le x \le 1$) are of interests because of their metal-insulator transition (Sayer *et al.*, 1975) and hence, plausible candidates of high-T_c superconductors (Mahajan *et al.*, 1992). Electrical conductivity of LSV ($0 \le x \le 0.4$) changes from semiconducting to metallic behaviour with strontium content around 0.2. LSV ($x \ge 0.2$) reach 10^2-10^4 S/cm of electronic conductivity in a typical SOFC operating at temperatures between 500 and 1000 ℃ (Sayer *et al.*, 1975; Webb and Sayer, 1976). For the two ends of LSV (i.e. $LaVO_3$ and $SrVO_3$), orthorhombic $LaVO_3$ is a Mott insulator, while cubic $SrVO_3$ is an oxide conductor with metallic behaviour (Inaba *et al.*, 1995).

Both high electrical conductivity and catalytic activity on fuel oxidation are prerequisites for potential SOFC anodes. It was found that vanadium-based oxides had already been widely used in the catalytic industry. Supported vanadia had been investigated extensively because of its technological importance in industrial heterogeneous catalytic processes, such as oxidative dehydrogenation of hydrocarbons like propane (Daniell *et al.*, 2002), toluene (Bulushev *et al.*, 2000) and butadiene (Bond *et al.*, 1979) and selective catalytic reduction of nitrogen oxides (Georgiadou *et al.*, 1998). Complex pyrovanadate, such as La–Mn–V–O (Varma *et al.*, 2001) and La–Fe–V–O (Varma *et al.*, 2003), had been proven to be good catalysts for CO oxidation at temperatures above 200 ℃. $SrVO_3$ had also been attempted as an oxidation catalyst for methanol and benzene, but without success (De and Balasubramanian, 1983). The binary perovskite containing V^{3+} and V^{4+}, exhibiting good catalytic performance on selective oxidation of alcohols has also been reported (Trikalitis and Pomonis, 1995).

Despite the unique properties of vanadate, it has not been widely used in SOFCs. Small proportion of strontium pyrovanadate, $Sr_3(VO_4)_2$, is routinely added into strontium-doped lanthanum chromite to produce high density interconnect materials (Simner *et al.*, 2000). It is only in recent years that vanadate is being explored to be an anode material for SOFC. It was reported that "Strontium doped $LaVO_3$ is stable under SOFC fuel outlet conditions..., however… is unlikely to be useful as anode materials" (Hui and Petric, 2001). However, studies showed that LSV was active in electrochemical H_2S oxidation (Aguilar *et al.*, 2004b; Aguilar *et al.*, 2004a; Cheng *et al.*, 2005; Cheng *et al.*, 2006). SOFC with $La_{0.7}Sr_{0.3}VO_3$ anode is among the best of all reported results, with excellent sulphur tolerance up to percentage level (Aguilar *et al.*, 2004b). Nevertheless, it seems that $La_{0.7}Sr_{0.3}VO_3$ (LSV7030) has low catalytic activity for H_2 and CH_4 oxidation. The polarization resistance at 1000°C is about 5 Ω cm^2 for such cells running on H_2 (Aguilar *et al.*, 2004a). Maximum power density can reach 150 mW/cm^2 for the cell with LSV7030/YSZ (250 μm)/$La_{0.85}Sr_{0.15}MnO_3$ configuration fed with pure H_2 at 900 ℃. Recently, $LaCrO_3$–VO_x–YSZ anode containing 40 wt.% reduced vanadium oxide (VO_x) was tested using tainted syngas derived from coal gasification, but no results on pure fuel gases were reported (Xu *et al.*, 2007). While vanadate has been proven to be excellent in sulphur tolerance, low catalytic activity to fuel oxidation undermines its candidature of SOFC anode.

3.2 Powder synthesis

A literature survey shows that there are four methods employed for synthesizing LSV_{Re}, i.e., (*i*) reduction from LSV_{Ox} (Trikalitis and Pomonis, 1995; Khan *et al.*, 2004); (*ii*) arc melting of reduced raw materials (Sayer *et al.*, 1975; Bordet *et al.*, 1993); (*iii*) annealing of LSV_{Ox} in vacuum (Mahajan *et al.*, 1992; Shinike *et al.*, 1976; Hur *et al.*, 1994); and (*iv*) directly sintering in reducing environment (Inaba *et al.*, 1995; Nakamura *et al.*, 1979). Early researchers synthesized dense polycrystalline LSV_{Re} because of their interests in the electrical and magnetic properties. The corresponding operating temperature was extremely high, i.e., 1400–1800 ℃. Such a high temperature process not only led to equipment complexity, but also reduced the catalytic activity because of increased crystal size and decreased surface area of materials. A modified method (*i*) was used in the present study. This method had been reported in early works on selective isopropanol oxidation (Trikalitis *et al.*, 1998).

A series of LSV ($0 \leq x \leq 1$) powders were synthesized by solid state reactions in air followed by reduction in the forming gas. The raw materials for oxidized LSV (LSV_{Ox}) synthesis were lanthanum (III) oxide, strontium (II) carbonate, and vanadium (V) oxide. La_2O_3 (Advanced Materials, 99.995%) was calcined at 1000 ℃ for 4 h to remove the moisture and carbonaceous compounds. The decomposition of $SrCO_3$ (Advanced Materials, 99.5$^+$%) was carried out at 1000 ℃ for 6 h. V_2O_5 (Sigma-Aldrich, 99.6$^+$%) was firstly ball milled for 10 min and then dried at 300 ℃ for 2 h. Stoichiometric amounts of La_2O_3, decomposed $SrCO_3$, and V_2O_5 were put into a rolling jar. Roll milling was carried out in isopropanol with YSZ media up to 24 h. The slurry was dried at 80 ℃ in air. The dried powders were compacted into pellets with diameter of 24 mm. They were calcined at 600 ℃ for 48 h to minimize vanadium loss. They were finally fired at 800 ℃ for 24 h to form the right phases. Yellowish powders (LSV_{Ox}) were obtained after crushing and milling the sintered pellets in an agate mortar. The reduction experiment of LSV_{Ox} was carried out in a tube furnace. To yield reduced LSV (LSV_{Re}), LSV_{Ox} were compacted into pellets and reduced in forming gas (5% H_2/Ar) at 1000 ℃ for 24 to 48 h with intermediate grinding. The pellets were crushed into powders after reduction. There are two reasons why forming gas rather than pure H_2 was used in this project. The first reason is the stringent safety regulation in Singapore. The second reason is to ensure the stability of the material in reducing atmosphere. p_{O2} is not always low at SOFC anode chamber, especially under high current loading operation conditions where a lot of steam is generated. If LSV_{Ox} cannot be reduced in forming gas, it will definitely fail under practical SOFC operating conditions. La-rich LSV_{Re} are black and Sr-rich LSV_{Re} are black with bluish tint.

3.3 Structural and thermal gravimetric characterization

LSV powders were pressed onto a specially designed XRD sample holder for XRD characterization. Phase screening of LSV was carried out with X-ray diffraction (XRD, Philips PW1830). Another diffractometer, Shimadzu 6000 with Cu Kα radiation, was used for phase identification. The step size was 0.02 ° with a scan rate of 0.5 °/min. Profile refinement was carried out with the commercial Jade 5 software. To check the thermal stability of LSV, LSV_{ox}–YSZ mixture was calcined at 1300 ℃ for 3 h for XRD characterization.

Light yellow $LaVO_4$ is monoclinic (Monazite type), and yellowish $Sr_2V_2O_7$ is triclinic (Figure 3-1 and Table3-1). Figure 3-2a shows the XRD patterns of as-synthesized LSV_{Ox}. Single phase can be obtained at the two ends of LSV_{Ox}. LV_{Ox} and SV_{Ox} are hard to dissolve in each other due to their distinct crystalline structures. Not surprisingly, any attempt to achieve a single phase LSV_{Ox} ($0 < x < 1$) will fail. As shown in Fig. 3-2a, trace of $LaVO_4$ is visible even in $LSV0595_{Ox}$. In present study LSV_{Ox} ($0 < x < 1$) are treated as a mixture of $LaVO_4$ and $Sr_2V_2O_7$. In Fig. 3-2b, single phase can be readily synthesized for slightly Sr-doped LV_{Re}. LSV_{Re} ($0 \leq x \leq 0.1$) are refined as orthorhombic, with increasing cell volume when more Sr^{2+} (1.44 Å) replace La^{3+} (1.36 Å) (Shannon, 1976). $LSV5050_{Re}$ profile could be fitted to cubic $(La_{0.50}Sr_{0.50})VO_{2.95}$ (PDF#33-1343). With caution, it can be orthorhombic because the differences in lattice parameters are very close to each other, as in the case of $LaVO_3$. $LaVO_3$ was once believed to be cubic, but Bordet *et al.* noticed the distorted VO_6 octahedral network and thus classified it as orthorhombic $GdFeO_3$ type (Bordet *et al.*, 1993). As shown in Fig. 3-2b, the peak width at half height of $LSV5050_{Re}$ is quite large. Such a peak broadening can be ascribed to lattice disorder or fine grain size down to nano-scale. It seems impossible that powders prepared from solid state reaction are nano-sized. Thus the peak broadening is empirically ascribed to random occupation of strontium and lanthanum in the perovskite A-site lattice. Unlike LSV_{Re} (x= 0, 0.05, 0.1) and $LSV5050_{Re}$, LSV_{Re} (x= 0.2, 0.3, 0.4) are binary phase structure between $LaVO_3$ and $(La_{0.50}Sr_{0.50})VO_{2.95}$.

For the Sr-rich LSV_{Re}, it is futile to eliminate the impurities from LSV_{Re} ($0.8 \leq x \leq 1$) even with repeated grinding and firing. Impurities are identified as $Sr_3(VO_4)_2$-, $Sr_6V_6O_{19}$-, or $Sr(V_6O_{11})$-like phases. Figure 3-3 shows a typical XRD pattern of SV_{Re}, the toughest composition within the LSV category. Even after a 1000 ℃ reduction for 2 days with intermediate grinding, $Sr_3(VO_4)_2$ is still the dominant phase while almost no $SrVO_3$ diffraction peaks were detected. It is not easy to identify the other peaks in the Fig. 3-4, noting that there are at least 29 La–Sr–V oxides in the standard powder diffraction (PDF) files. The valence of vanadium is 5+ in $Sr_3(VO_4)_2$, which implies that it may be impossible to obtain vanadate with V^{3+}/V^{4+} for the conditions used here. In contrast to $SrVO_3$, $LaVO_3$ is much easier to be prepared. This is possibly because the V^{4+} state is less stable than the V^{3+} state. Nakamura *et al.* prepared $LaVO_3$ by reducing V_2O_5 and La_2O_3 at 1200 ℃ for 12 h in a CO_2/H_2 gas ($PO_2 = 10^{-10}$ bar)

(Nakamura *et al.*, 1979). It is believed that $LaVO_3$ can also form in the present experimental conditions, i.e., 1000 ℃ for 24 h in 5% H_2/Ar, noting that PO_2 is around 10^{-21} bar for 5% H_2/Ar at 900 ℃ (Tao and Irvine, 2004a).

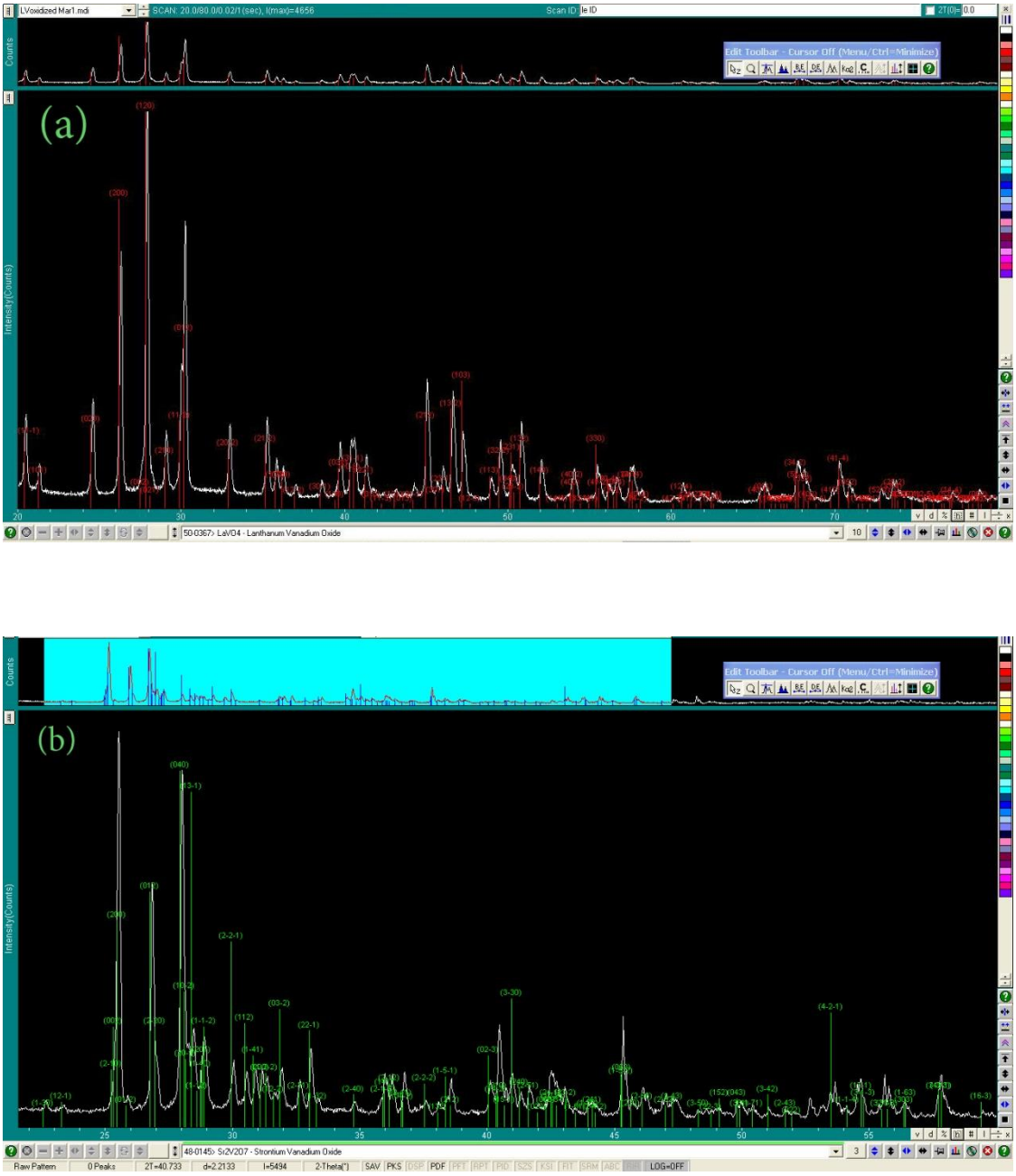

Figure 3-1 XRD patterns of (a) $LaVO_4$ (LV_{Ox}) and (b) $Sr_2V_2O_7$ (SV_{Ox}) fitted in Jade® 5.

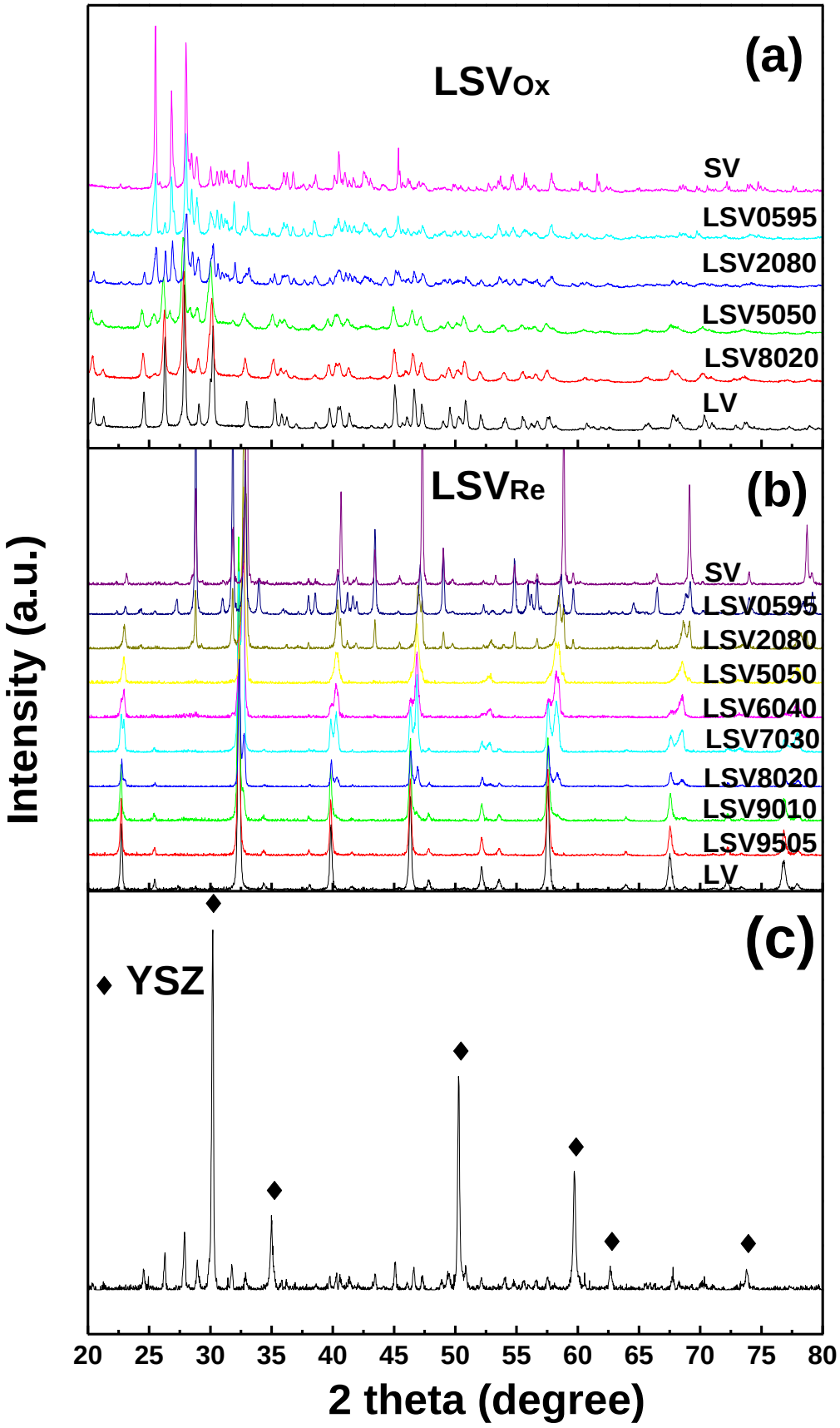

Figure 3-2 XRD patterns of (a) LSV_{Ox}, (b) LSV_{Re}, and (c) mixture of $LSV7030_{Ox}$ and YSZ fired at 1300 ℃ for 3 h, with a 50:50 weight ratio.

Table 3-1 Fitted unit cell parameters of LSV

Composition	Lattice setting	Lattice parameters
LV_{Ox}	Monoclinic	a = 7.019(4) Å, b = 7.260(3) Å, c = 6.714(3) Å, β = 104.878(1) ° V = 330.62 Å^3, Z = 4
SV_{Ox}	Triclinic	a = 7.087(5) Å, b = 12.964(1) Å, c = 7.044(4) Å, α = 93.806(1) ° β = 90.925(3) ° γ = 99.384(1) ° V = 636.84 Å^3, Z = 4
LV_{Re}	Orthorhombic	a = 5.513(2) Å, b = 7.883(1) Å, c = 5.537(1) Å, V = 239.14 Å^3, Z = 4
$LSV9505_{Re}$	Orthorhombic	a = 5.545(3) Å, b = 7.834(1) Å, c = 5.521(1) Å, V = 239.82 Å^3, Z = 4
$LSV9010_{Re}$	Orthorhombic	a = 5.545(5) Å, b = 7.835(2) Å, c = 5.528(9) Å, V = 240.16 Å^3, Z = 4
$LSV5050_{Re}$	Cubic	a = 3.869(1) Å, V = 57.93 Å^3, Z = 1

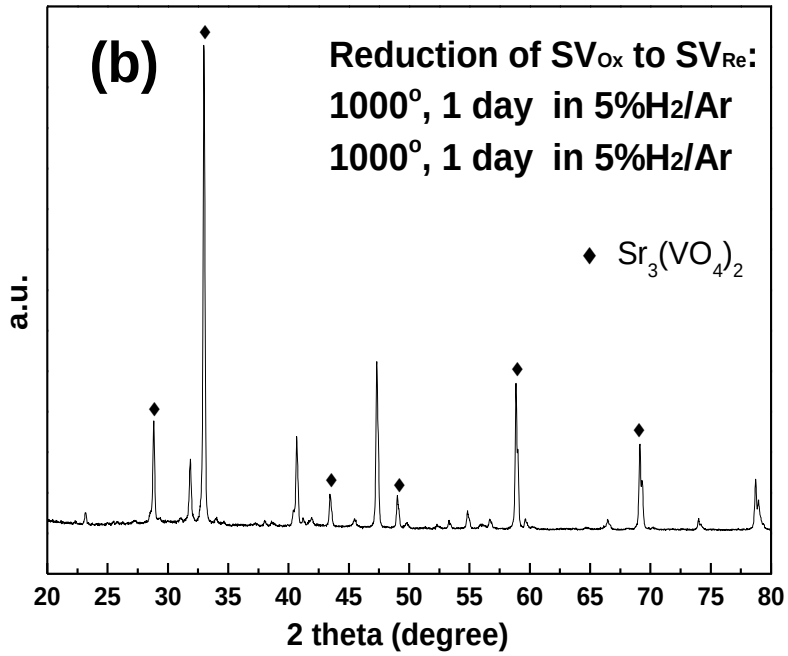

Figure 3-3 XRD patterns of reduced strontium vanadate (SV_{Re}). Note that the powders are sintered two days with intermediate grinding (1 day+ 1day route).

$SrVO_3$ can be reduced from $Sr_2V_2O_7$ at 1250 ℃ in 7% H_2–Ar. At 800 ℃, it is stable only when $PO_2 < 10^{-10}$ bar (Hui and Petric, 2001). With arbitrary single phase of Sr-rich LSV_{Re} is thought to be impossible at present conditions, i.e., 1000 ℃ in 5% H_2/Ar. This is different from the reported results that single phase can be obtained for the whole range of LSV($0 \leq x \leq 1$) via 1500°C vacuum annealing and arc-melting (Mahajan *et al.*, 1992). It seems that the pyrovanadate impurities are not detrimental to the catalytic activities of LSV_{Re}. Trikalitis *et al.* obtained LSV_{Re} as a mixture of $LaVO_3$, $SrVO_3$ and $Sr_3V_2O_8$, which were quite active for isopropanol selective oxidation (Trikalitis *et al.*, 1998). As our objective is to select some materials for catalytic fuel oxidation in SOFC, any pursuits on single phase materials and detailed investigation on phase structure are beyond the scope of the present study. To study the chemical compatibility of LSV with YSZ, LSV was mixed with YSZ powder in 50:50 wt. % and fired at 1300 ℃ for 3 h in air. One of the XRD patterns of LSV-YSZ after calcination is shown in Fig. 3-2c. No Bragg peaks were observed other than the expected peaks arising from LSV_{Ox} and YSZ. This indicates that no significant reactions had occurred between the two materials, at least within XRD detection limitations.

The oxidation behaviour of LSV_{Re} was investigated by thermal gravimetric analysis (TGA) via TGA 2950 (TA Instruments). 15 mg of LSV_{Re} was put into the Pt pan. N_2 was purged into the thermobalance chamber with a flow rate of 80 sccm. The TGA system was heated up from room temperature to 1000 ℃ in air at a scan rate of 5 ℃/min. Figure 3-4 shows the oxidation behaviour of LSV_{Re} in air. It can be seen in Fig. 3-4 that the onset temperature (T_{onset}) of oxidation strongly depends on the composition. T_{onset} of slightly Sr-doped LSV is around 340–360 ℃, and it is around 486 ℃ for the oxidation of $LSV5050_{Re.}$ As shown in the Fig. 3-4, only a single step is observed in all the TGA curves. It is assumed that the vanadate (III) is completely oxidized to vanadate (V). The oxidation seems to complete at 600 ℃. After that no noticeable weight change is observed. The weight gain between 300 to 600 ℃ is attributed to the vanadate oxidation. The oxygen non-stoichiometry parameter δ is calculated as:

$$LaVO_{3-\delta} + \frac{1+\delta}{2} O_2 \rightarrow LaVO_4 \qquad \text{(Equation 3-1)}$$

$$La_{0.95}Sr_{0.05}VO_{3-\delta} + \frac{0.975+\delta}{2}O_2 \rightarrow La_{0.95}Sr_{0.05}VO_{3.975} \quad \text{(Equation 3-2)}$$

$$La_{0.8}Sr_{0.2}VO_{3-\delta} + \frac{0.9+\delta}{2}O_2 \rightarrow La_{0.8}Sr_{0.2}VO_{3.9} \quad \text{(Equation 3-3)}$$

$$La_{0.5}Sr_{0.5}VO_{3-\delta} + \frac{0.75+\delta}{2}O_2 \rightarrow La_{0.5}Sr_{0.5}VO_{3.75} \quad \text{(Equation 3-4)}$$

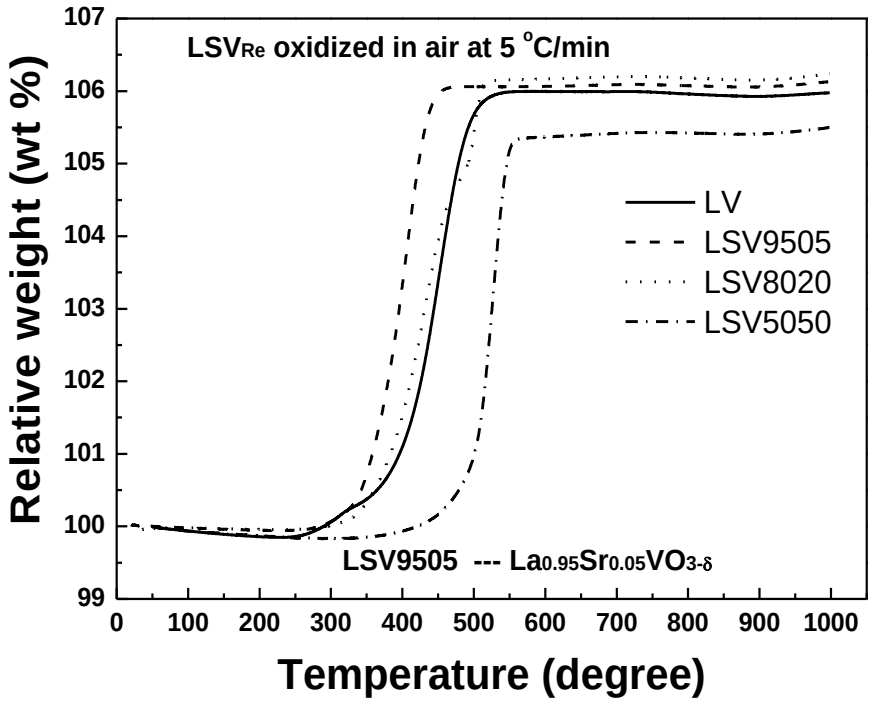

Figure 3-4 TGA curves for the oxidation of reduced $La_{1-x}Sr_xVO_{3-\delta}$ (LSV_{Re}) with x= 0, 0.05, 0.2, 0.5. Note that the final products after TGA measurement were assumed to pyrovanadate, i.e., vanadium in V^{5+}.

Table 3-2 TGA data listing of LSV_{Re} oxidation. δ is the oxygen non-stoichiometry parameter in the $La_{1-x}Sr_xVO_{3-\delta}$.

Sample	T_{onset} (℃)	T_{offset} (℃)	Weight increase (wt. %)	δ
LV_{Re}	364	494	6.127	-0.084
$LSV9505_{Re}$	342	439	6.184	-0.062
$LSV8020_{Re}$	348	513	6.202	-0.017
$LSV5050_{Re}$	486	547	5.658	4.06×10^{-4}

The δ values of LSV_{Re} are given in Table 3-2. The obtained δ values scatter from -0.084 to 4.06×10^{-4}. The large discrepancy of δ might be due to the system error of the low-accuracy TGA instrument. Whether LSV_{Re} is of oxygen-deficient or oxygen-excess is, therefore essentially unknown. Literature results showed that LSV was predominantly of oxygen-deficient. Hur *et al.* obtained $LaVO_{2.92}$ (δ = 0.08) via 1600 ℃ vaccum annealing of raw mixed V_2O_3 and La_2O_3 powders (Hur *et al.*, 1994). Mahajan *et al.* showed that δ of LV_{Re}, $LSV8020_{Re}$, and $LSV5050_{Re}$ were 0.02, 0.01, and -0.05, respectively (Mahajan *et al.*, 1992).

With caution, it can be inferred that the oxygen nonstoichiometry of LSV is non-negligible. The ionic conductivity (σ_i) of LSV_{Re}, though not measured in this study, might not be low. While little ionic conductivity data had been reported in literature, the electronic conductivity (σ_{el}) of LSV_{Re} was reported to be high. In a typical SOFC temperature range, LSV_{Re} ($0 \leq x \leq 0.2$) shows the semiconductor behaviour with conductivity around 0.1-1 S/cm. For the case of LSV_{Re} ($0.2 \leq x \leq 0.4$), σ_{el} is in the order of 10^2-10^4 S/cm (Webb and Sayer, 1976). The increased conductivity results from the introduction of V^{4+} together with the Sr^{2+} in LSV_{Re}. The electronic transfer of V^{3+}/V^{4+} redox couple should contribute to the high conductivity of $LSV_{Re}(0.2 \leq x)$.

3.4 Half-cell performance of LSV anodes

3.4.1 Experimental procedures

Electrode performance of LSV anodes was evaluated by electrochemical impedance spectroscopy (EIS) and dc polarization. A schematic illustration of the three-electrode configuration is shown in Fig. 3-5. This kind of configuration had been proven in minimizing the artefacts arisen from the electrode misalignment. It had been used in our group for many years. The YSZ electrolyte in this configuration was 18 mm in diameter and 1 mm in thickness. LSV_{Ox} and YSZ were mixed in a 50:50 weight ratio, and the LSV_{Ox}–YSZ paste was screen printed onto YSZ electrolyte. It was fired at 1180°C for 2h to form an anode layer with thickness of 30 μm. A "just cover" Pt current collection layer was brush-painted onto the LSV–YSZ anode. As Pt is susceptible to be catalytically active, gold paste (Fuel Cell Materials, USA) was also used as current collector. Pt was used as the counter and reference electrodes (CE and

RE, respectively) on the opposite side of YSZ, where the gap between CE and RE is at least 4 mm. The active area of the working surface was 0.46 cm^2. The cell was sealed onto an alumina tube using a ceramic sealant (Ceramabond 552, Aremco). It was cured at 90 ℃ and 200 ℃ for 2 h each. A gas-tight pre-test was carried out by passing N_2 with very slow flow rate. During the electrochemical testing, the anode side was fed with either pure H_2 or wet CH_4. The fuel flow rate was 50 sccm. The opposite side, i.e. the side with CE and RE, was exposed to ambient air. LSV anode was in situ reduced for 2 h at 900 ℃. Electrochemical testing was carried out between 800 to 1000 ℃, with a heating and cooling rate of 2 ℃/min.

EIS was carried out using a Solartron 1255B frequency response analyzer coupled to a 1287 electrochemical interface. The impedance spectra were recorded at open-circuit voltage (OCV) with 10 mV ac amplitude over the frequency range 10^5-10^{-2} Hz. Ohmic resistance of the electrochemical cell, R_Ω, was estimated from the high frequency (high-f) intercept on the impedance curves. Electrode polarization resistance, R_p, was extracted from the difference between its low-f and high-f intercepts. Potential dynamic polarization was carried out by sweeping from OCV to 0.8 V anodic biases at a scan rate of 1 mV/s. Microstructure of the anodes was inspected by scanning electron microscopy (SEM, JEOL JSM-6340F). The impedance data and potentiodynamic polarization data were analyzed by commercial Zview and Corrview software, respectively.

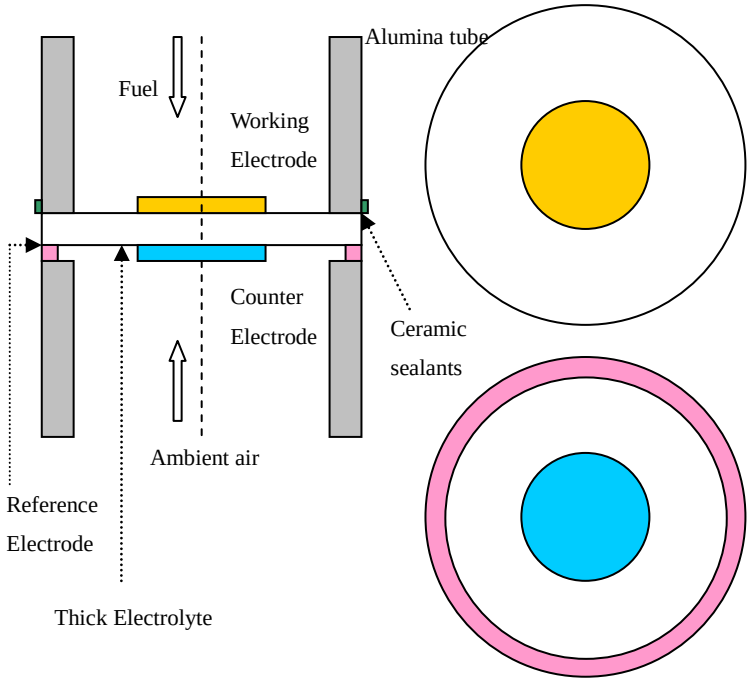

Figure 3-5 Schematic illustration of the half-cell configuration. Note that the scale of all components is only a guide for the eyes.

3.4.2 LSV–YSZ anodes fed with pure H_2

Steele proposed several criteria decades ago for oxide anodes attempting to complete methane oxidation (Steele *et al.*, 1990). The first given rule was "Good electronic conductivity (preferably > 10^2 S/cm) at anode operating potentials (-0.7 to -0.9 V). Probably n-type behaviour preferable." LSV_{Re} is metallic (Webb and Sayer, 1976) and slightly n-type (Hui and Petric, 2001). At a typical temperature range of SOFC (600 to 1000 ℃), the dc conductivity of $LSV8020_{Re}$ was $10^{1.9}$-$10^{2.2}$ S/cm while around $10^{1.5}$ S/cm for $LSV9010_{Re}$ (Webb and Sayer, 1976). LSV_{Re} ($x < 0.2$) were ruled out as far as electronic conductivity was concerned. Recalling the discussion in Section 3.3, Sr-rich LSV_{Re} were also unfavourable due to its chemical instability in oxidizing environment. For these reasons, only LSV_{Re} ($0.2 \leq x \leq 0.5$) were chosen for electrochemical testing LSV is good electronic conductor but its ionic conductivity is assumed to be negligible. The three phase boundaries (TPBs) are thus confined to LSV–YSZ interface if pure LSV anode is used. TPB is the place where the electronic component, ionic component, and fuel meet and electrochemical reactions take place. Initial efforts on fabricating pure LSV anodes had failed because they delaminated from YSZ electrolyte during *in situ* reduction. The reason is that LSV undergoes considerable lattice shrinkage during reduction, when orthorhombic $LaVO_4$ and triclinic $Sr_2V_2O_7$ release lattice oxygen to

form LSV_{Re}. Experimental results showed that the use of composite anodes of LSV and YSZ alleviated the delamination problem. The YSZ component in LSV–YSZ composite anodes provided a rigid skeleton to withhold the LSV component. In addition, the TEC mismatch between LSV and YSZ was minimized. Furthermore, the TPB was extended from 2D interface to 3D reaction zones once LSV–YSZ composite anodes were employed. The detailed investigation on three phase boundaries (TPBs), both experimental and theoretical, will be discussed in Chapter 4.

Electrode engineering is a complex that at least includes particle size, particle size ratio, firing history, electrode composition, conductivity, porosity, thickness, and fuel compositions. In this chapter, the effects of electrode composition and firing history on the electrochemical performance of LSV–YSZ composite electrodes are investigated. Modelling works pertaining to electrode optimization was again given in Chapter 4. Unreasonably large R_p and R_Ω were observed in LSV[1] (70 wt. %)–YSZ and LSV(80 wt.%)–YSZ. R_p of LSV–YSZ anodes with LSV contents at 40 wt.%, 50 wt.%, and 60 wt.% are 1.2, 0.38, 0.35 $\Omega\ cm^2$, respectively (Fig. 3-6). The delamination problem of LSV (60 wt.%)–YSZ is occasionally observed. It appears that LSV (50 wt.%)–YSZ is the best composition. Figure 3-7 shows the impedance responses of LSV6040 (50 wt. %)–YSZ anodes sintered at different temperatures. The ohmic resistance, R_Ω, varied significantly with the anode sintering temperatures. R_Ω is the lumped resistance at least consisting of electrolyte ohmic resistance, electrode ohmic resistance, and various contact resistances. Based on the conductivity of YSZ from literature (Ciacchi *et al.*, 1994), the ohmic resistance of 1 mm thick YSZ should be around 0.54 $\Omega\ cm^2$. For LSV6040–YSZ anode sintered at 1100 ℃, R_Ω was more than 2 $\Omega\ cm^2$ at 1000 ℃ (Fig. 3-7). A sintering temperature of 1100 ℃ was thus too low. Increasing the sintering temperature to 1150 ℃ readily reduced R_Ω to 1.4 $\Omega\ cm^2$. R_Ω is further decreased to 0.5 $\Omega\ cm^2$ in the sintering temperature range of 1180 to 1200 ℃ (Fig. 3-7).

[1] LSV in LSV-YSZ are not marked explicitly as LSV_{Ox} or LSV_{Re}. Note that LSV is LSV_{Ox} during electrode preparation and it is LSV_{Re} during electrochemical testing after in situ reduction.

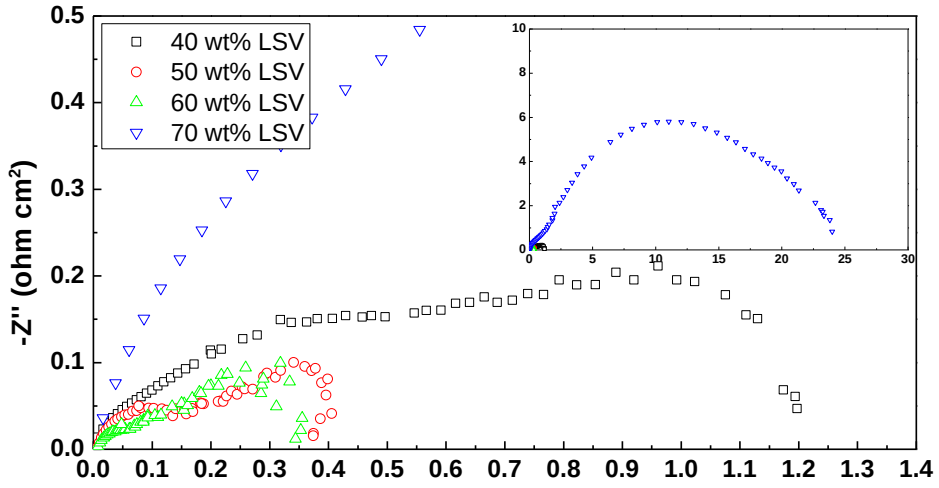

Figure 3-6 Impedance curves of the LSV6040 (40 wt.%)–YSZ, LSV6040 (50 wt.%)–YSZ, LSV6040 (60 wt.%)–YSZ, LSV6040 (70 wt.%)–YSZ composite anodes in pure H_2 at 1000 ℃. Note that LSV6040 (70 wt.%)–YSZ anode layer peels off from YSZ electrolyte, leading to unreasonably large impedance.

Figure 3-8a shows the impedance spectra of a typical LSV-YSZ anode ($LSV6040_{Re}$-YSZ) in pure H_2 and under the OCV condition. The corresponding R_p is in the range from 1.31 to 0.34 Ω cm^2 between 800 to 1000 ℃. As reported by Tao and Irvine, LSCM anode showed a R_p of 0.47 Ω cm^2 in wet H_2 (3% H_2O-H_2) at 925 ℃ (Tao and Irvine, 2004a). Our early works also demonstrated that R_p of LSCM-YSZ (50:50 wt.%) composite anode reached 2.4 Ω cm^2 at 800 ℃ in wet H_2 (Jiang *et al.*, 2006a) . Doped tertiary titanates were also reported as potential anode materials. At the operating temperature of 900 ℃ in wet H_2, R_p reached 0.3 Ω cm^2 for $LaSrTiMnO_x$ (Ovalle *et al.*, 2006; Fu *et al.*, 2006), while 0.5 Ω cm^2 for $La_2Sr_4Ti_{6-x}Sc_xO_{19-z}$ (Canales-Vazquez *et al.*, 2005). LSV–YSZ was thus considered as comparable to these more well-established oxide anode materials. Low-*f* arcs at a characteristic frequency of 0.1 Hz were shown in Fig. 3-8a. These arcs were tentatively ascribed to gas conversion impedance. The low-*f* arcs at 1 Hz were reported to the gas conversion impedance between H_2 and H_2O, in the case of hydrogen oxidation in cermet anodes fed with H_2/H_2O mixture (Brown *et al.*, 2000). Due to the imperfect ceramic sealant, gas conversion also exists in present material system, though pure H_2 instead of wet H_2 was used. Based upon the measured OCV and employing Nernst equation, it was estimated that H_2O can reach as high as 7 % in the vicinity of anode. The assumption of gas conversion is supported by the observed low-*f* arcs up to 1000 ℃, as gas conversion was usually more significant at high temperature due to the more water produced. This is

because the ceramic sealants become more and more leaking at elevated temperatures. Intermediate-*f* arcs peaked around 20–100 Hz were clearly visible at 800 ℃ and 850 ℃, while they fade away at temperatures higher than 900 ℃. Impedance arcs peaked around 10–100 Hz were classified as the diffusion over a stagnant gas layer, in the case of H_2 oxidation in Ni-based cermet anodes (Primdahl and Mogensen, 1999). The intermediate-*f* arcs here observed are tentatively regarded to thermal-activated gas diffusion induced impedance. Unobvious high-*f* arcs that peaked around several kHz were consistently observed in the spectra. Its real axis part was smaller than the gas conversion arc (low-*f* arc) and diffusion arc (intermediate-*f* arc).

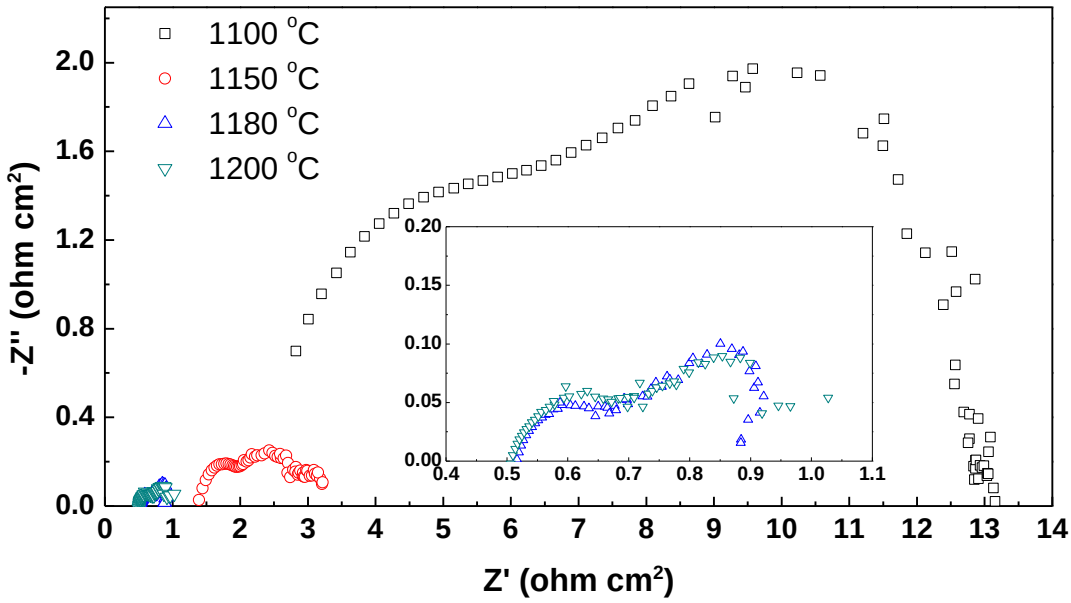

Figure 3-7 Impedance curves of LSV6040 (50 wt.%)–YSZ (50 wt.%) composite anodes sintered at 1100 ℃, 1150 ℃, 1180 ℃, and 1200 ℃. All impedance spectra were collected at 1000 ℃ in pure H_2.

As shown in Fig. 3-9a, as-fired LSV anode is fine and uniform with particle size in the range of 0.5-2 μm but the porosity is low. The porosity has been increased by in situ reduction from LSV_{ox} to LSV_{Re}. Good adhesion and thermal compatibility between the LSV_{Re} and YSZ electrolyte is shown in the inset of Fig. 3-9b, in consistent with the low contact resistance shown in Fig. 3-8a. It seemed difficult to sinter a well-contact LSV_{Re}–YSZ interface at 1000 ℃ (Aguilar *et al.*, 2004b, Aguilar *et al.*, 2004a), as the melting point of LSV_{Re} is as high as 2050 ℃ (Sayer *et al.*, 1975). In contrast, the melting point of LSV_{Ox} components, such as $Sr_2V_2O_7$, is not higher than 1200 ℃, thus enabling good sinterbility in the samples investigated in this study. Taken in account the ionic conductivity of YSZ (Ciacchi *et al.*, 1994), R_Ω shown in Fig. 3-8a is reasonable

for half-cells with 1 mm thick YSZ electrolyte. The ohmic resistance of electrode and the contact resistance between the electrode and the electrolyte contribute 0.1 Ω cm^2 to the total ohmic resistance at 900°C, but this value become negligible at 1000 ℃. The low contact resistance is the reason for small high-*f* arcs obtained in this study (Fig. 3a).

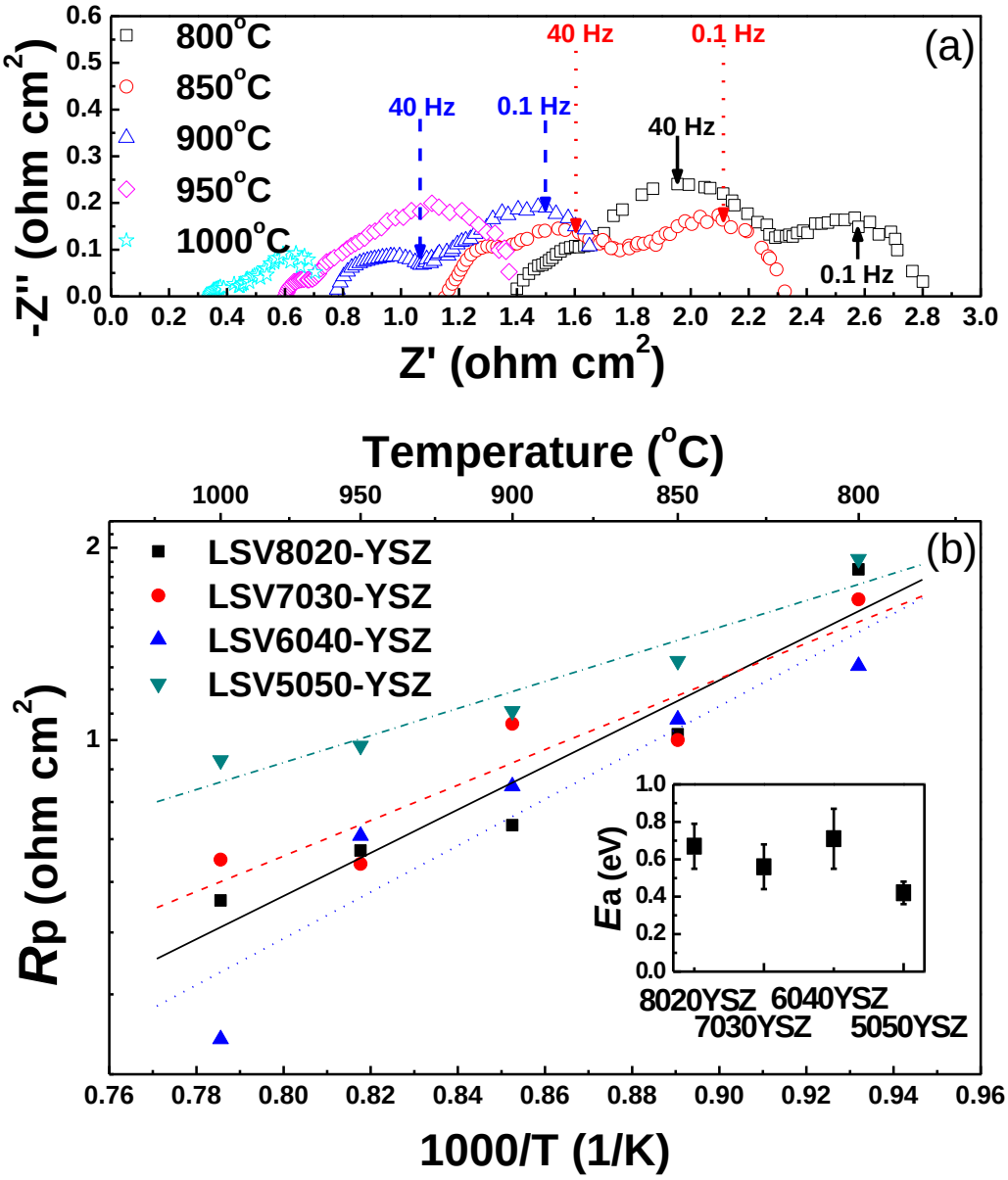

Figure 3-8 (a) OCV impedance responses in pure H_2 for $LSV6040_{Re}$–YSZ (50:50 wt. %) composite anode. (b) Arrhenius plot for LSV_{Re} (x = 0.2, 0.3, 0.4, 0.5)–YSZ composite anodes. Inset of (b) shows the corresponding fitted E_a estimated from 800–1000 ℃.

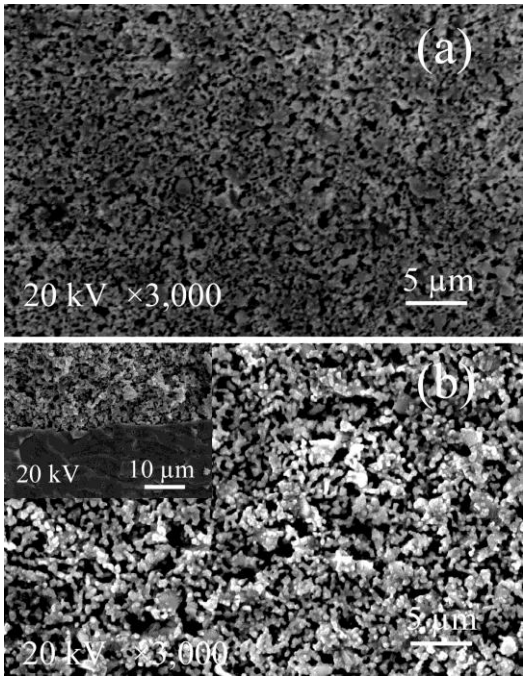

Figure 3-9 SEM images of LSV6040-YSZ composite anode (a) as-fired in air at 1180 ℃ for 2 h; (b) *in situ* reduced of (a) in pure H_2 at 900 ℃ for 2 h. Inset of (b) shows the cross-section profile of $LSV6040_{Re}$-YSZ with YSZ electrolyte.

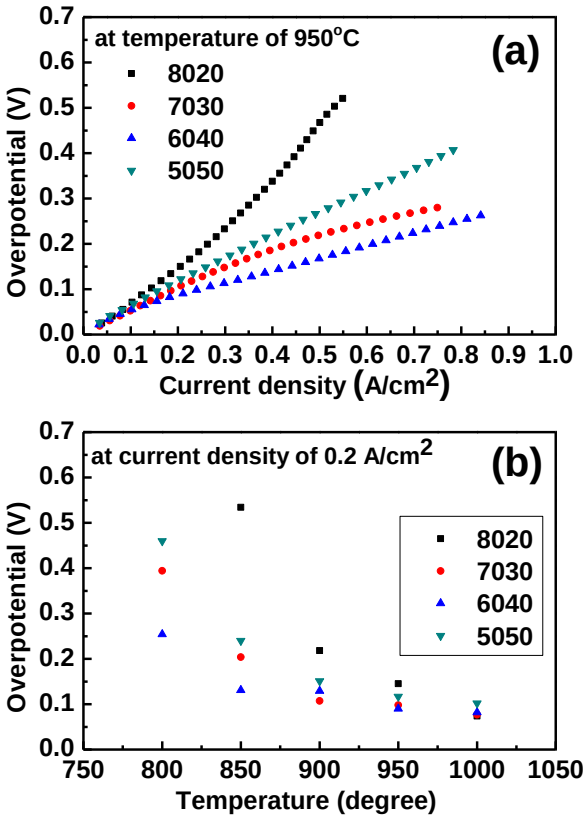

Figure 3-10 Anodic overpotential dependencies for LSV_{Re} (x = 0.2, 0.3, 0.4 0.5)-YSZ (50:50 wt. %) on (a) current density at temperature of 950 ℃, and (b) temperature at current density of 0.2 A/cm^2 in pure H_2. Note that $LSV5050_{Re}$-YSZ cannot reach 0.2 A/cm^2 at 800 ℃ under the potential bias of 0.8 V (maximum bias applied in this study).

As shown in Figs. 3-8 and 3-10, LSV_{Re} (x = 0.2, 0.3, 0.5)–YSZ (50:50 wt.%) are of inferior but comparable performance as compared to that of x = 0.4. R_p of LSV_{Re}(x = 0.5)–YSZ, the weakest in this category, decreases from 1.92 Ω cm^2 at 800°C to 0.92 Ω cm^2 at 1000 ℃. R_p of the four examined anodes are fitted to the Arrhenius equation. The apparent activation energies (E_a) range from 0.42 to 0.71 eV (inset of Fig. 3-10b). A wide spread values of E_a had been reported in the literature for the state-of-the-art Ni-based anodes. Anodes with fine structure such as Ni film and fine cermet, usually have low E_a, e.g. 0.49 eV (Nakagawa *et al.*, 1995) and 0.5 eV (Brown *et al.*, 2000). Large E_a was reported in coarse cermet (1.2 eV) and Ni felt electrodes (1.2-1.6 eV) (Brown *et al.*, 2000). In literature, usually only thermal-dependent impedance arcs were used to abstract E_a. In contrast, in this study E_a is estimated from the total polarization resistance. Preliminary analysis shows coarse powders and hence coarse microstructure (coarsening YSZ powder at 1200 ℃ for 1 hour) has higher E_a. For example, E_a of LSVRe(x = 0.4)–YSZ (coarsened) with 50:50 weight ratio is 0.85 eV, which is higher than the fine microstructure of E_a = 0.71 eV (inset of Fig. 3-10b). Though there might be other factors contributing to the activation energy, it is believed that a fine microstructure of LSV–YSZ contributes to low E_a.

Figure 3-10a shows the polarization behavior of LSV_{Re} (x = 0.2, 0.3, 0.4, 0.5)–YSZ (50:50 wt. %) in pure H_2 at 950 ℃. The anodic overpotential of LSV_{Re}(x = 0.4)–YSZ, the best of the four materials, is 0.2 V for a current density of 0.64 A/cm^2. For all the four materials, the overpotential is not higher than 0.15 V at a current density of 0.2 A/cm^2 at 950 ℃ (Fig. 3-10b). When drawing a current density of 0.2 A/cm^2, the overpotential of LSCM-YSZ (50:50 wt. %) was reported to 0.38 V (Jiang *et al.*, 2006a) and 0.18 V (Ye *et al.*, 2008). The polarization performance of LSV is considered to be better than that of LSCM at 950 ℃.

Before moving to discussions on wet CH_4, it is necessary to diagnose the catalytic effort of Pt. It is surmised that Pt is catalytically active while Au is not. Figure 3-11 shows the impedance spectra of half cells with Pt and Au current collectors (cc). It is surprisingly to note that the whole impedance (R_Ω+R_p) are almost the same. This result

indicates that the catalytic effect of Pt is negligible for LSV–YSZ anodes. A fatal disadvantage of Au cc is the high R_Ω, which is 0.62 Ω cm^2 and 0.09 Ω cm^2 larger than Pt cc (Fig. 3-11). Actually the Au paste peels off from the electrode very easily during sample preparation (Bek, 2009). Hereafter in this study Pt instead of Au is used as current collector.

3.4.3 LSV–YSZ anodes fed with wet CH_4

One of the advantages of SOFC is its capability of utilizing hydrocarbon as fuel, in contrast to PEMFC where only extremely pure H_2 can be used. The dominant paraffin in fossil fuel is the natural gas. Natural gas consists of methane together with small amount of ethane, propane, butane, and pentane, as well as traces of carbon dioxide, nitrogen, helium and hydrogen sulphide. From the thermodynamic point of view, methane is more reluctant to be reduced than other alkenes. It is also least prone to carbon deposition because of the stable structure and high hydrogen-to-carbon ratio. According to BP's annual report on world energy, the reserves-to-production (R/P) ratio is 62.8 (British Petroleum, 2010). Natural gas is extensively used in Singapore for power generation and residential utilization.

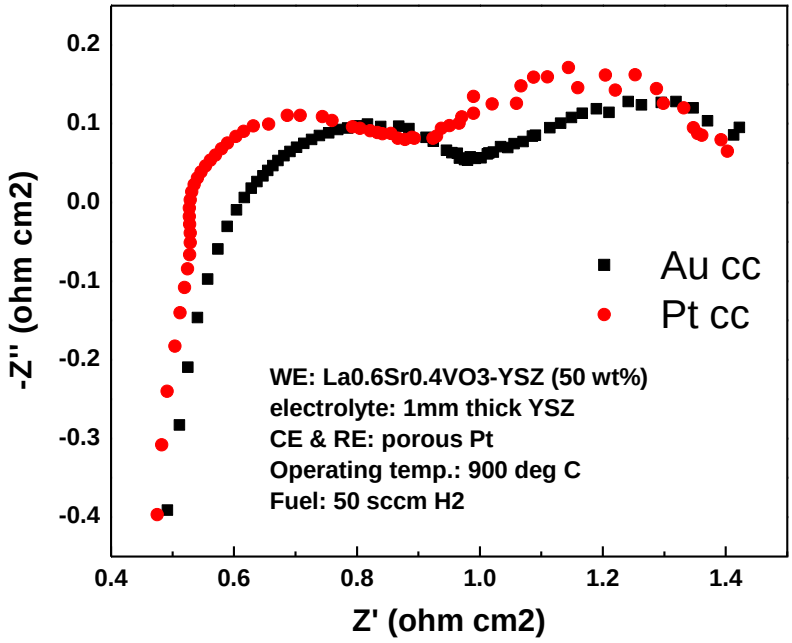

Figure 3-11 Impedance responses of $La_{0.6}Sr_{0.4}VO_3$ –YSZ (50:50 wt. %) with Au and Pt as current collectors.

Figure 3-12 shows the impedance responses of LSV6040 (50 wt.%)–YSZ anodes fed with pure CH_4. R_p at 900 ℃, 950 ℃, and 1000 ℃ are found to be 13.5 Ω cm^2, 11.5 Ω cm^2, and 4.8 Ω cm^2, respectively, at OCV conditions. The R_p in pure CH_4 is about 14 times larger than that in pure H_2, indicating the large energy barrier of CH_4 oxidation. Nevertheless, the R_p plunges under polarized conditions and shows significant dependency on temperature. At the operating temperature of 900 ℃, a 52 % drop of R_p is observed under only 100 mV bias. The drop reaches 74 % as the temperature is increased to 1000 ℃. The activation under potential biases indicates that LSV is a potential candidate for CH_4 oxidation, though the reaction resistance is rather large.

Weakly humidified CH_4 instead of pure CH_4 is routinely used in SOFCs. The incorporation of steam helps in reforming CH_4 into CO and H_2 rich gases. The reforming effect is, nevertheless, less pronounced when CH_4 is only weakly humidified and the fuel flow rate is high. Steam incorporation may play both physical and chemical roles. From the physical aspect, steam improves the adsorption of CH_4 onto the TPB–usually the rate-limiting step in the whole fuel oxidation pathways. From the chemical aspect, absorbed steam on TPBs facilitates fuel dissociation and various spillover reactions. It may also accelerate surface diffusion of the intermediates. All these proposed mechanisms are similar to the case in humidified H_2 fuel. With the absence of direct and in-situ investigation tools, the exact reaction pathways of steam-aided reaction mechanisms are still uncertain. Open circuit voltage (OCV) is the electromotive force, which indicates to what extent energy can be drawn from electrochemical systems. Practical cell potential at open circuit conditions, i.e OCV, is always much lower than the Nernst potential. For example, the Nernst potential of wet CH_4 oxidation in typical SOFC temperatures was in the range from 1.2 to 1.4 V (Jiang *et al.*, 2006b). In contrast, OCV was just about 0.8 to 1.1 V using LSCM–YSZ composite anodes (Jiang *et al.*, 2006b). It is possibly due to incomplete CH_4 oxidation to CO/CO_2 and H_2/H_2O. Experiments showed that it took nearly 30 minutes for the system to become stable when the fuel is shifted from H_2 and CH_4, vice versa.

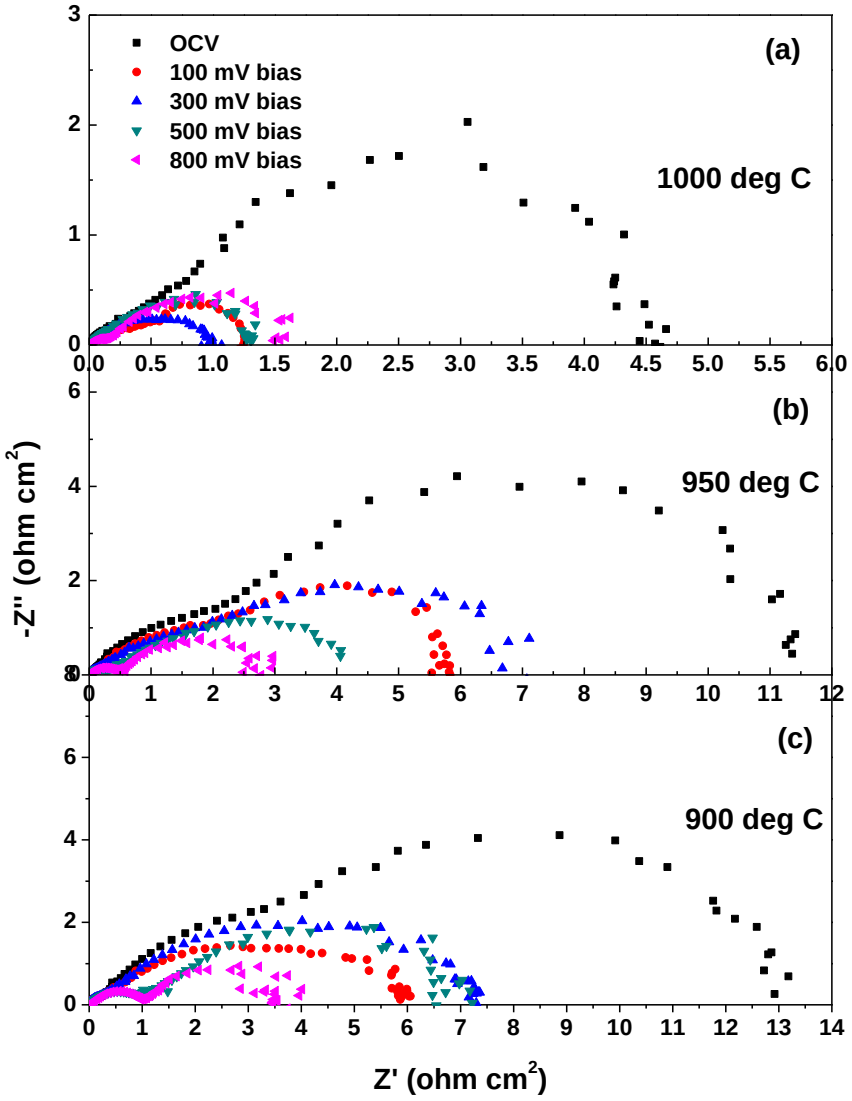

Figure 3-12 Impedance curves of LSV6040 (50 wt.%)-YSZ anode in pure CH_4 at (a) 1000 ℃, (b) 950 ℃, and (c) 900 ℃.

Figure 3-13 shows the OCV of $LSV6040_{Re}$–YSZ (50:50 wt. %) anode fed with wet CH_4 at temperatures between 800 to 1000 ℃. The OCV is dependent on the operating temperature. It increases from -0.91 V at 800 ℃ to -1.09 V at 1000 ℃. Some glitches consistently appear in the OCVs between 800 ℃ to 850 ℃, and occasionally at temperatures higher than 850 ℃. These glitches are likely related to reversible surface oxidation/reduction of LSV species during methane conversion, either internal reforming or direct oxidation. Significant potential oscillation under dc bias was observed in Ni–YSZ fed with CO/CO_2 fuel (Holtappels *et al.*, 1999). It was ascribed to periodic carbon deposition and removal on Ni surface. Naked-eye observations on the

tested LSV–YSZ anodes did not find any trace of carbon deposition, thus a surface reconstruction model based on carbon deposition is unlikely relevant to present study. Early works demonstrated that LSCM (Jiang *et al.*, 2006b; Wang *et al.*, 2008) and LSCM–YSZ (Wang *et al.*, 2008) also showed OCV oscillation when fed with wet CH_4. It was phenomenally ascribed to CH_4-H_2O interaction and creation/annihilation of surface oxygen vacancy (Wang *et al.*, 2008) . It was plausible since most conducting oxide, like LSCM and LSV_{Re}, are thought to be poor ionic conductors.

As shown in Fig. 3-13b, R_p of $LSV6040_{Re}$–YSZ (50:50 wt. %) anodes are 3.53, 1.91, 1.44, 1.17, 1.07 Ω cm^2 from 800 ℃ to 1000 ℃ with a temperature increment of 50 ℃. Figure 3-13c shows the corresponding polarization curves. While the limiting current was observed for the case of 800 ℃ and 850 ℃, the potential-current curve at 1000 ℃ indicated signs of activation at large polarized conditions. As practical fuel cells are operated under polarized rather than OCV conditions, such kind of kinetic activation of $LSV6040_{Re}$–YSZ (50:50 wt. %) anodes is promising. For half-cells tested in wet CH_4 at 900 ℃, R_p of engineered LSCM–YSZ were around 0.85 Ω cm^2 (Tao and Irvine, 2004a) and 2.6 Ω cm^2 (Jiang *et al.*, 2006b). LSV_{Re}–YSZ is thus thought to be comparable to LSCM-related materials.

It is believed that the impedance curves in H_2, before switched to and after switched back from wet CH_4, should be the same if LSV–YSZ anode is not coked by deposited carbon. Otherwise, the deposited carbon from CH_4 pyrolysis carbon will block the reaction sites thus rendering larger R_p. Figure 3-14 shows the three impedance curves in initial H_2, wet CH_4, and again H_2 after switching back from the exposure in wet CH_4 after sufficient time. It was fairly normal for the larger R_p in wet CH_4 than that in H_2. What of interest is that the R_p of the two impedance curves in H_2, before and after CH_4 exposure, are almost the same, albeit slightly different at high frequency regions. It is evident that the LSV anodes are carbon-resistant. While the low-frequency impedance arc is almost unchanged, the high-frequency arc distinctly different. This change of high-frequency impedance, which is most probably related to interfacial charge transfer, indicates subtle alternation of the anode/electrolyte interfaces.

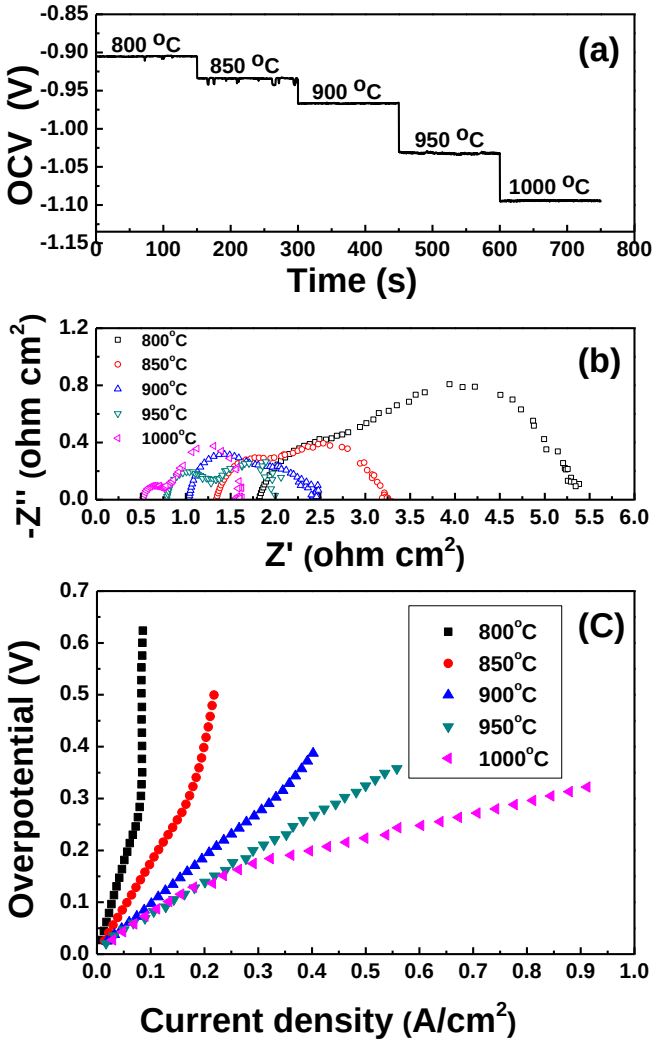

Figure 3-13 (a) OCV curves (b) impedance spectra (c) anodic overpotential of $LSV6040_{Re}$-YSZ (50:50 wt. %) in wet methane.

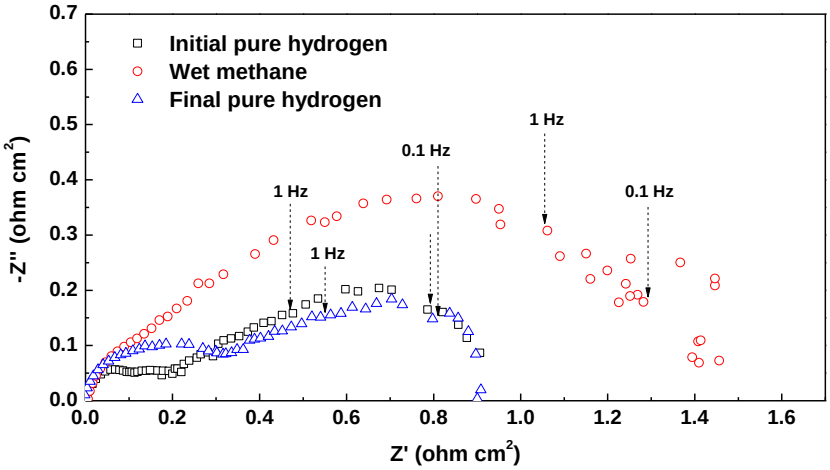

Figure 3-14 OCV impedance responses of LSV6040 (50 wt.%)-YSZ anode at 900 ℃ in pure H_2 and wet CH_4. Legend description: "Initial pure hydrogen", OCV impedance in H_2 (just before gas shifting to wet CH_4); "wet methane", OCV impedance in wet methane; "final pure hydrogen", impedance in pure H_2.

3.5 YSZ-supported single cells with LSV anodes

In this section electrolyte-supported single cells were fabricated and tested. Modest single cell performance had been demonstrated. These preliminary but promising results pave the way for practical SOFCs with LSV-based anodes. The cathode material is chosen from well-established materials. In this study it is LSM. LSM is routinely used for high temperature SOFC with the operating temperature higher than 800 ℃. To reduce the ohmic losses, the most effective way is to use thin film electrolyte instead of thick electrolyte support, as long as the contact of the SOFC components is already good enough. In this preliminary stage, thin YSZ-supported single cells with LSV anodes were constructed and evaluated.

3.5.1 Fabrication of YSZ-supported single cells

The electrolyte was prepared from YSZ (Tosoh, Japan) by a ceramic route as given in Section 3.4. The thickness of as-sintered YSZ disc is around 500 μm. It was mechanically polished down to 300 μm. The LSV–YSZ composite powders were prepared identical to that described in Section 3.4. The cathode powders, $La_{0.85}Sr_{0.15}MnO_3$, are commercially available from Nextech (the USA). Our early work showed that A-site deficient LSM had much better catalytic activity than stoichiometry LSM (Leng *et al* ., 2004; Leng *et al* ., 2006). To produce 10% A-site deficiency, say $(La_{0.85}Sr_{0.15})_{0.9}MnO_3$, $La_{0.85}Sr_{0.15}MnO_3$ was mixed with the appropriate amount of $MnCO_3$ and calcined at 900 ℃ for 1 hour. $(La_{0.85}Sr_{0.15})_{0.9}MnO_3$ (LSM)–YSZ composite cathode with 50 wt.% LSM was used as the cathode. LSM added with 10 wt.% graphite powders were applied used as current collection. All the powders are mixed with ink vehicle (Fuel Cell Materials, the USA) to form the corresponding electrode inks.

The two-electrode configuration was used in single cell performance evaluation. It was modified from the three-electrode configuration mentioned in Section 3.4 by shorting the RE and CE. LSV6040–YSZ ink was screen-printed onto the YSZ disc and sintered at 1180 ℃ for 2 hours. The cathode, LSM–YSZ, was subsequently screen-printed to the opposite side of YSZ disc and baked at 600 ℃ for 1 h. A LSM current collection layer with 10 wt.% graphite was applied onto the cathode side. The LSM–YSZ and

LSM were co-sintered at 1150 ℃ for 2 h. Pt meshes were used on both sides for current collection. Pt paste was applied onto anode surface to form a "just cover" fine layer, to ensure good current collection between the anode and Pt mesh. The experimental setup was similar to that mentioned in Section 3.4. They are omitted herein for the sake of simplicity.

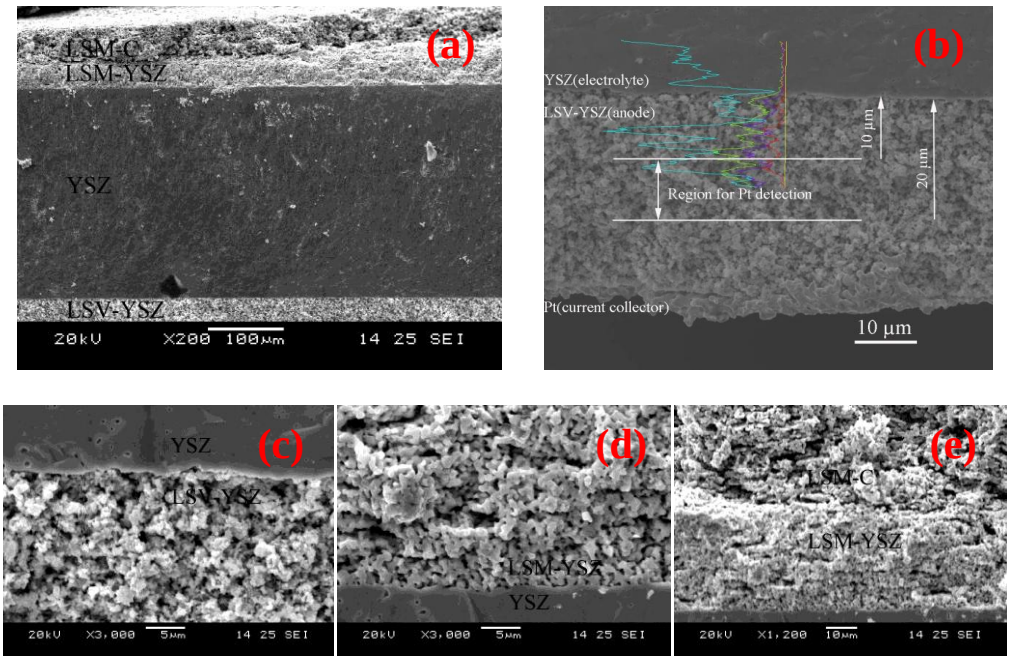

Figure 3-15 SEM images of a dismantled single cell after running in pure H_2 and wet CH_4: (a) holistic view of the single cell; (b) EDX Linescan crossing YSZ (electrolyte) and LSV-YSZ (anode) interface, and for the lines: Zr $L_{\alpha 1}$ (turquoise); V $K_{\alpha 1}$ (bright green); La $L_{\alpha 1}$ (purple); O $K_{\alpha 1}$ (red); (c) YSZ and LSV-YSZ interface; (d) YSZ and LSM-YSZ (cathode) interface; and (d) LSM-YSZ and LSM (current collector at cathode side) interface.

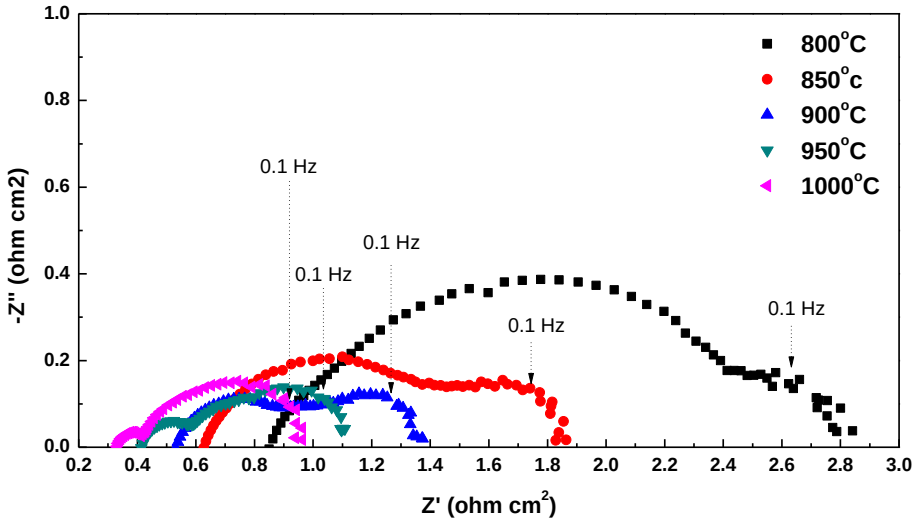

Figure 3-16 Impedance curves of a cell with configuration LSV6040–YSZ /YSZ/(LSM–YSZ/LSM) when exposed to pure H_2.

3.5.2 Microstructure

The single cell with configuration of LSV–YSZ/YSZ (300 μm)/ LSM–YSZ/LSM was run on pure H_2 and wet methane for more than two days. To visualize how a single cell was constructed, SEM observation was taken after the single cell was disassembled. A holistic view of the single cell is shown in Fig. 3-15a, where the four component layers are clearly visible. The thickness of LSV–YSZ, LSM–YSZ, and LSM layers were 30 μm, 30 μm, and 40 μm, respectively. Good adherence between the neighbouring layers was confirmed by the enlarged SEM images, as shown in Figs. 3-15c, 3-15d, and 3-15e. The pores in the LSV–YSZ anode are homogeneously distributed. Within the detection limit, the energy dispersive X-ray spectroscopy (EDX) analysis is not able to discriminate the ionic (YSZ) and electronic parts (LSV or LSM) of the electrodes. For the LSV–YSZ anode, EDX mapping analysis shows that vanadium is uniformly distributed on the whole surface. The porosity of LSM current collector was higher than LSM–YSZ, because 10 wt. % carbon was added into LSM for mitigating mass transportation problems. The anodic current collector was platinum. Compositional analysis was used to check whether Pt had penetrated into TPB regions. As already discussed in Section 3.4, the thickness of TPB was normally less than 10 μm even for good MIECs. Thus the region that stretched from 10 μm to 20 μm away from the anode-electrolyte interface was probed (Fig. 5-1b). The line-scan and mapping analysis did not detect any Pt in regions adjacent to the YSZ electrolyte. Exhaustive EDX point analysis on more than 10 points in the Pt detection region also did not reveal any Pt. It is concluded that Pt does not penetrate to the Pt detection region, not to mention the TPB regions.

3.5.3 Single cell performance in H_2 and wet CH_4

High OCV values in the range of -1.14 V to -1.17 V are observed for the single cell fed with H_2. This indicates that the sealing condition of the test rig is satisfactory. The temperature dependency of the impedance curves are shown in Fig. 3-16. It gives an activation energy of 0.67 eV, which is comparable to E_a=0.62 eV of LSV6040–YSZ anode measured from a three-electrode configuration (Section 3.4.2). It should be emphasized that the impedance curves were collected in a two-electrode configuration. Thus, so-obtained R_Ω and R_p were a combination of the impedance from all cell components: YSZ electrolyte support, LSV–YSZ anode, LSM–YSZ cathode, current

collectors, etc. In the present study, the fuel utilization is still below 9% even at the maximum current density of 1.2 A/cm^2 (See Chapter 9 of Ref. (EG&G Services, 2004) for related tutorials of these calculations). Figure 3-17 shows the current-voltage (*I-V*) responses for a 300-μm thick YSZ-supported SOFC consisting of LSV6040–YSZ composite anode and LSM–YSZ/LSM bi-layer cathode. The fuel used is pure H_2 and its flow rate is 50 sccm. No signs of activation polarization at low *I* and mass-transport limited polarization at high *I* are observed in Fig. 3-17. The OCV, R_Ω, R_p, and P_{max} at various temperatures are listed in Table 3-3. P_{max} are 0.12, 0.19, 0.28, 0.39, 0.52 W/cm^2 for temperatures at 800 ℃, 850 ℃, 900 ℃, 950 ℃, and 1000 ℃, respectively. To the best of the author's knowledge, such kind of performance is among the best of single cells employing vanadate anodes with 300-μm YSZ electrolyte support.

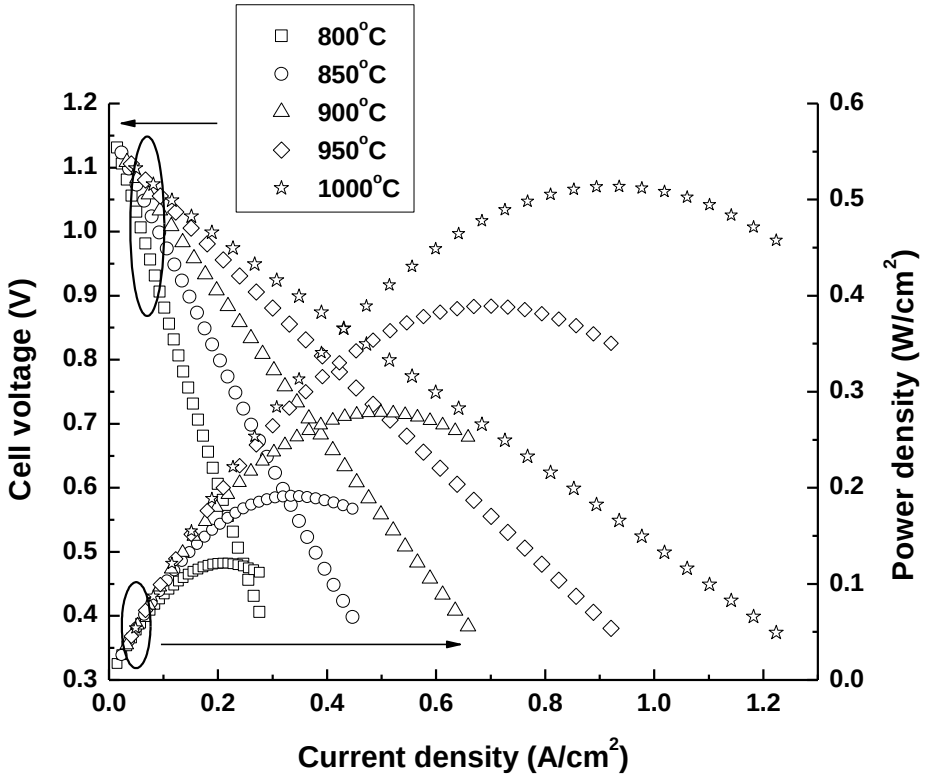

Figure 3-17 Cell voltage (open symbols) and powder density (closed symbols) with relation to current density for a cell with configuration LSV6040-YSZ /YSZ/(LSM-YSZ/LSM-C). The fuel was pure H_2 and its flow rate is 50 sccm.

The impedance spectra of the single cell exposed to wet CH_4 are shown in Fig. 3-18. R_p is much higher in wet CH_4 than that in H_2, though R_Ω is similar in both fuels. At 900 ℃, R_p from wet CH_4 is 1.22 Ω cm^2, in comparison to 0.84 Ω cm^2 in H_2. It indicates that LSV, like most anode materials, has much higher electrochemical activity in H_2 than in

wet CH_4. The exact oxidation mechanisms of CH_4 oxidation are still unclear because of the complex reaction pathways. In literature two reaction pathways for CH_4 oxidation in SOFCs had been proposed: (*i*) indirect oxidation, i.e. cracking of the methane on the anode followed by the electro-oxidation of the cracked species (Mogensen and Kammer, 2003); (*ii*) direct oxidation, i.e. directly electro-oxidizing the methane to CO, CO_2 and H_2O (Steele *et al.*, 1988; Steele *et al.*, 1990). The OCV at 850 ℃, 900 ℃, and 950 ℃ are found to be -0.919 V, -0.951 V, and -0.989 V, respectively. Thermodynamic equilibrium analysis indicates that OCV should be in the range from -1.2 V to -1.4 V at temperatures from 850 ℃ to 950 ℃. Direct oxidation mechanism seems implausible in the case of LSV anodes, as reflected from the low OCVs observed here.

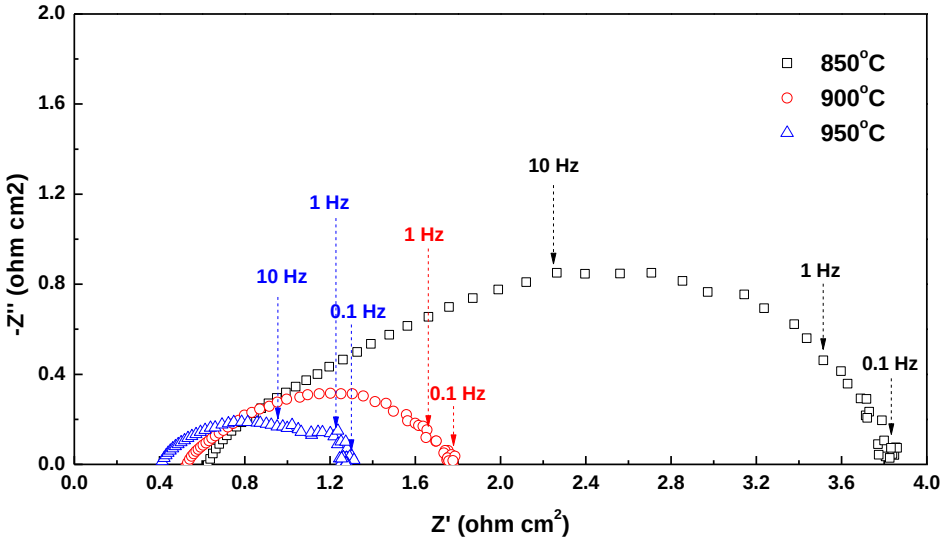

Figure 3-18 Impedance curves of a cell with configuration LSV6040–YSZ /YSZ/(LSM–YSZ/LSM) when exposed to wet CH_4 (CH_4 with 3% H_2O).

Table 3-3 Data listing of single cell with configuration of LSV6040–YSZ /YSZ/(LSM–YSZ/LSM)

	H_2				Wet CH_4 (3 % H_2O CH_4)			
	R_Ω (Ω cm^2)	R_p (Ω cm^2)	OCV (V)	P_{max} (W/cm^2)	R_Ω (Ω cm^2)	R_p (Ω cm^2)	OCV (V)	P_{max} (W/cm^2)
800 ℃	0.85	1.99	-1.173	0.12	---	---	---	---
850 ℃	0.63	1.24	-1.165	0.19	0.64	3.19	-0.919	0.05
900 ℃	0.54	0.84	-1.153	0.28	0.53	1.22	-0.951	0.13
950 ℃	0.42	0.70	-1.147	0.39	0.41	0.90	-0.989	0.18
1000 ℃	0.32	0.65	-1.143	0.52	0.34	---*	-1.005	0.25

* R_p at 1000 ℃ in wet CH_4 was not shown because of severe distortion in the low-*f* impedance arc.

Figure 3-19 shows the DC polarization curves of the single cell in wet CH_4. P_{max} at 850 ℃, 900 ℃, and 950 ℃ are 0.05, 0.13, and 0.18 W/cm^2, respectively. Relatively low cell performance of LSV anodes in wet CH_4 calls for further anode engineering. Though still inferior to Ni-cermet based SOFCs, the single cell performance achieved in this study has been quite encouraging. Table 3-4 lists a brief literature survey of single cell performance using vanadate anodes. It can be seen that vanadate anodes are active in electrochemical H_2S oxidation (Aguilar *et al.*, 2004a; Aguilar *et al.*, 2004b; Cheng *et al.*, 2005; Cheng *et al.*, 2006). SOFC with $La_{0.7}Sr_{0.3}VO_3$ anode was of excellent sulphur tolerance up to percentage level (Aguilar *et al.*, 2004b). Nevertheless, it seems that $La_{0.7}Sr_{0.3}VO_3$ (LSV7030) has low catalytic activity towards H_2 and CH_4 oxidation. Polarization resistance at 1000 ℃ was as large as 5 Ω cm^2 for such cells running on H_2 (Aguilar *et al.*, 2004a). P_{max} reaches 150 mW/cm^2 for the cell with LSV7030/YSZ (250 μm)/$La_{0.85}Sr_{0.15}MnO_3$ configuration fed with pure H_2 at 900 ℃. Recently, $LaCrO_3$-VO_x-YSZ anode containing 40 wt.% reduced vanadium oxide (VO_x) was tested using tainted syngas derived from coal gasification (Xu *et al.*, 2007). All of these works did not report the performance results on clean CH_4 fuel oxidation. Vanadate had been reported to be excellent in sulphur tolerance. In this chapter, LSV is also proved to have promising performance both in pure H_2 and wet CH_4.

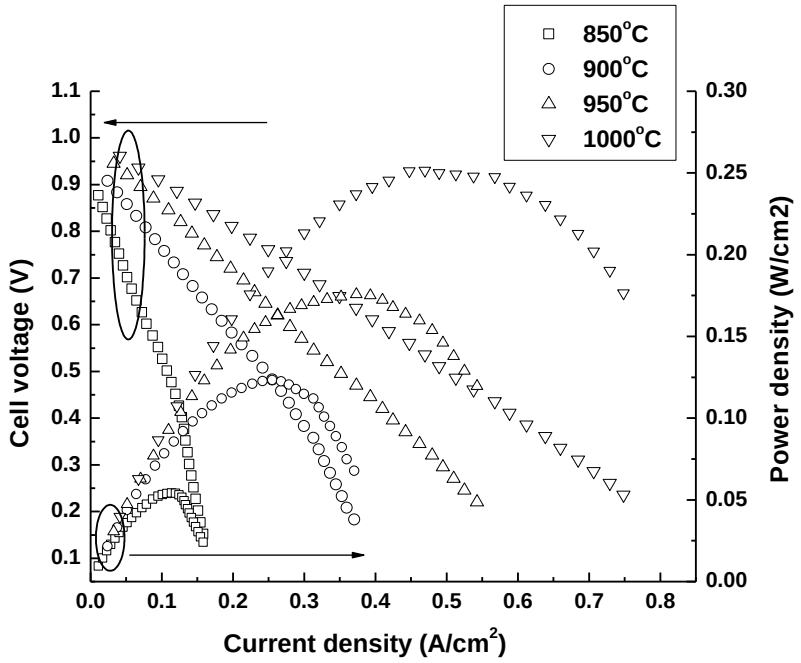

Figure 3-19 Cell voltage (open symbols) and powder density (closed symbols) with relation to current density for a cell with configuration LSV6040–YSZ /YSZ/(LSM–YSZ/LSM). The fuel was wet CH_4 (CH_4 with 3% H_2O) and its flow rate is 50 sccm.

Table 3-4 Comparison of cell performance of SOFC using vanadate oxides.

Half cell anode performance (R_p from EIS)		Single cell Performance		References
		Cell configuration	Maximum power density (W/cm^2)	
0.70 (H_2, 950 ℃); 0.90 (wet CH_4, 950 ℃)		LSV6040-YSZ/YSZ (300 μm)/(LSM-YSZ/LSM-C)	0.52(H_2, 1000 ℃); 0.25 (wet CH_4, 1000 ℃)	This work
-		LSV7030 /YSZ (250 μm)/LSM-YSZ	0.28 (5% H_2S-CH_4, 950 ℃)	(Aguilar *et al.*, 2004b)
~ 9 (H_2, 950 ℃)	~2 (10 % H_2S-H_2, 950 ℃)	LSV7030-YSZ/YSZ (250 μm)/SSC-GDC	0.14 (5% H_2S-CH_4, 950 ℃)	(Aguilar *et al.*, 2004a)
8.5 (H_2, 950 ℃)	6.3 (3 % H_2S-H_2, 950 ℃)	LSV7030/YSZ (250 μm)/LSM-YSZ	0.11 (5% H_2S-H_2, 950 ℃)	
2.3 (wet H_2, 1000 ℃)	1.0 (wet 10% H_2S-H_2, 1000 ℃)	LSV7030/YSZ (250 μm)/LSM-YSZ	-	(Cheng *et al.*, 2005)
~12 (0.5 % H_2S-H_2, 900 ℃)		$LaCrO_3$-VO_x-YSZ (300 μm)/ Pt	0.17 (0.5 % H_2S-H_2, 900 ℃)	(Xu *et al.*, 2007; Xu *et al.*, 2010)
~ 5.5 (H_2, 800 ℃)	~8.3 (syngas,800 ℃)	LSV7030 /YSZ (120 μm)/LSM-YSZ	~.1 (H_2, 800 ℃)	(Cooper *et al.*, 2010)

3.6 Summary

Research works on crystalline structure, electrical conductivity and magnetic behaviour of LSV can be dated back to a half century ago. Extension of LSV into catalytic application was, however, little reported. In this chapter, $La_{1-x}Sr_xVO_3$ (LSV) with x = 0.0, 0.05, 0.1, 0.2, 0.3, 0.4, 0.5, 0.8, 0.9, 0.95, 1.0 were synthesized by solid state reactions, either in oxidized or reduced form. LSV_{Ox} was regarded as a mixture of $LaVO_4$ and $Sr_2V_2O_7$. Single phase can be obtained only for LSV_{Re} (x = 0, 0.05, 0.1) and $LSV5050_{Re}$, and LSV_{Re} (x = 0.2, 0.3, 0.4) was a binary phase structure between $LaVO_3$ and $(La_{0.50}Sr_{0.50})VO_{2.95}$. Chemical compatibility with YSZ had been confirmed at least up to 1300 ℃. The TGA analysis showed that the oxygen vacancy in LSV_{Re} is non-negligible.

Composite anodes of LSV_{Re} (x=0.2, 0.3, 0.4, 0.5) with YSZ showed comparable electrode performance with more well-studied oxide anodes such as LSCM. Electrode engineering was carried out by means of sintering temperature and electrode

composition. LSV anodes were not able to be sintered satisfactorily below 1150 ℃. Composite anodes with LSV more than 70 wt.% peeled off from YSZ electrolyte when exposed to pure H_2. Composite anodes with LSV less than 40 wt.% failed to form a percolation network for electron transfer. In this study LSV6040 (50 wt. %)–YSZ was used for electrode performance evaluation. LSV–YSZ anodes achieved R_p of 0.7–1.1 Ω cm^2 in pure H_2 at 900 ℃ for 2h. The anodic overpotential was lower than 0.2 V when drawing a current density of 0.2 A/cm^2. Apparent activation energies were in the range from 0.42 to 0.71 eV for the four LSV_{Re} (x= 0.2, 0.3, 0.4, 0.5)–YSZ anodes. Preliminary study indicated that LSV–YSZ anodes, at least $LSV6040_{Re}$–YSZ, were active for CH_4 oxidation. For half cells fed with 3% H_2O–CH_4 at 900 ℃, polarization resistance of $LSV6040_{Re}$–YSZ anode reached 1.4 Ω cm^2 at open circuit conditions. Polarization curves showed that the current density can reach 0.2 A/cm^2 with the anodic overpotential less than 0.2 V.

Electrolyte-supported single cells with configuration of LSV6040–YSZ/YSZ (300 μm)/LSM–YSZ/(LSM) were constructed. Satisfactory single cell performance had been demonstrated. When fed with pure H_2 and operated at 900 ℃, R_p of the single cell was 0.84 Ω cm^2 and P_{max} was 0.28 W/cm^2. When the fuel gas was switched to 3% H_2O humidified CH_4, polarization resistance was 1.22 Ω cm^2 and the P_{max} was 0.13 W/cm^2. Single cell performance achieved in this study was among the best results of SOFCs employing vanadate anodes. The single cell exhibited great temperature dependency in H_2 and wet CH_4. Further electrode engineering is desirable in order to achieve high performance. These preliminary but promising results paved the way for further exploration on high performance SOFCs with LSV-based anodes.

Chapter 4. Impedance responses and the double layer structure of LSV anodes via citric route

4.1 Impedance identification of LSV anode in H_2–H_2O–He atmosphere

Lanthanum strontium vanadate (LSV) had been attempted to be a plausible SOFC anode material since 2001 (Hui and Petric, 2001). LSV suffers phase transformation between cubic and low symmetric forms under redox cycling. The steep lattice change thus incurred might render LSV an unsuitable candidate. Later, LSV anodes were found with excellent sulphur tolerance but rather modest catalytic activity in clean fuels (Aguilar *et al.*, 2004a, Aguilar *et al.*, 2004b, Cheng *et al.*, 2005, Cheng *et al.*, 2006). In Chapter 3, the lattice mismatch problem was alleviated by in situ reduction of LSV–YSZ composite— the same strategy applied to the state-of-the-art Ni cermet anodes (Ge and Chan, 2009b). With that recipe we demonstrated salient electrode performance of LSV–YSZ composite anodes in pure H_2 and wet methane. To understand this kind of anodes further, fundamental works regarding to fuel oxidation mechanism had been carried out. In this study, the impedance behaviour was investigated via electrochemical impedance spectroscopy (EIS). A series of impedance spectra were collected in deliberately designed H_2–He–H_2O ternary atmosphere. The impedance arcs were identified as reaction impedance at high frequencies, concentration impedance at medium-to-low frequencies, and occasionally inductive loops at extremely low frequencies.

4.1.1 Powder synthesis, half-cell preparation, and impedance spectroscopy

LSV powders were synthesized successfully from three soft chemistry methods, i.e. glycine nitrate combustion and two citric routes. All LSV powders mentioned in this chapter are 20 at % strontium doped lanthanum vanadate ($La_{0.8}Sr_{0.2}VO_3$, or simply LSV). $La_{0.8}Sr_{0.2}VO_3$ is preferred based on a trade-off of catalytic activity and redox stability. They were prepared via a citric route with lanthanum nitrate, strontium nitrate, ammonium metavanadate, and citric acid as starting materials. The

as-prepared LSV powders were annealed stepwise to 600 ℃ for 12 hours. They were then mixed thoroughly with YSZ (Tosoh, Japan) in a 50:50 weight ratio. The anodic ink composed of LSV–YSZ and commercial ink vehicle (Fuel Cell Materials, USA). It was screen-printed onto YSZ electrolyte disc (1 mm thick). It was fired for 2 hours at 1210 ℃ to form an anode layer. Its geometric area was 0.46 cm^2 and its thickness was 30 μm. Pt paste was brush-painted to the opposite side and sintered at 900 ℃ for 30 minutes as counter and reference electrodes.

The electrochemical testing was carried out in the same test rig as given in Chapter 3. A small amount of Pt paste was applied to improve the "point" current collection on the anode side. Both the counter and reference electrode were exposed to air. The fuel gas, consisting of H_2 and He, was modulated from the corresponding pure gases via a Brooks® multi-channel mass flow controller. To yield the H_2–He–H_2O tertiary gas, H_2–He was channelled through a humidifier with temperature control of ± 0.1 ℃. The half-cell was heated to 950 ℃ at 3 ℃/min and hold for 4 hours before electrochemical testing. EIS was carried out using a Solartron 1255B frequency response analyzer coupled to a Solartron 1287 electrochemical interface. The impedance spectra were recorded with 10 mV ac amplitude over the frequency range of $10^5 – 10^{-2}$ Hz, under 0–500 mV anodic dc bias. Before the collection of impedance spectra, the half-cell was subjected to potentiostatic polarization at the desired dc bias for 20 minutes. The potential transients were obtained by chronoamperometry undergoing potential step from open circuit voltage (OCV) to 500 mV anodic bias, with a sampling rate of 30 points/sec.

4.1.2 Impedance spectra, equivalent circuit, and double layer capacitance

Figure 4-1 shows the XRD patterns of $La_{0.8}Sr_{0.2}VO_3$ (LSV in short hereafter in this chapter) prepared from solid state reactions and citric route. As mentioned in Chapter 3, LSV prepared from solid state reactions contains ineradicable impurities. In contrast, XRD analysis shows that (Shimadzu 6000, Cu Kα radiation) the LSV prepared from citric route is of single phase after reduction in H_2 at 900^{o}C for 12 hours. This indicates that citric route yields more homogenous and catalytically active LSV particles.

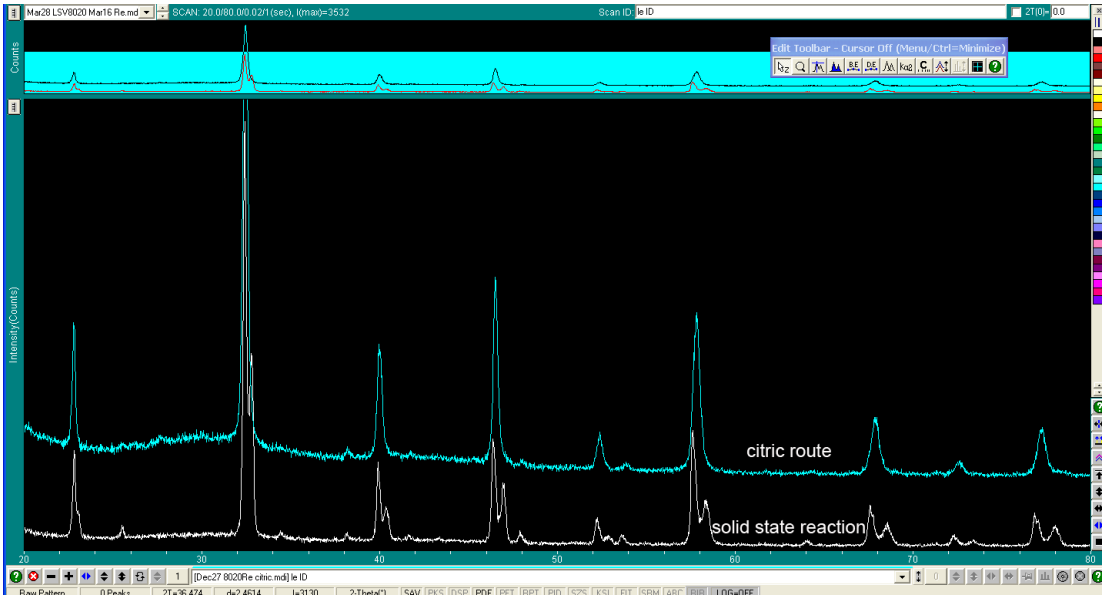

Figure 4-1. XRD patterns of $La_{0.8}Sr_{0.2}VO_3$ as prepared from solid state reactions and citric route, as demonstrated in Jade® 5.

The OCV impedance spectra recorded in pure H_2 generally contain two depressed and poorly separated arcs, besides the parasitic inductance caused by the lead wires at extremely high frequencies (Fig. 4-2a). The high frequency arc, Arc 1, peaks around 500 to 2000 Hz (i.e., relaxation frequency at 500–5000 Hz). Such kind of impedance arcs usually correspond to reaction steps with fast kinetics, such as double layer charging, spillover reaction, charge transfer, and surface adsorption/desorption. Relaxation frequency of the middle-to-low frequency arc, Arc 2, scatters around 0.5 to 2 Hz. With regard to SOFC anodes, middle and low frequency arcs are usually ascribed to gas diffusion in the porous electrode and gas channels, gas conversion, and OCV modulation due to the change of gas compositions. It can be called as concentration impedance. For impedance spectra collected under biases larger than 250 mV, small inductive loops, Arc 3, begin to emerge at extremely low frequencies below 0.1 Hz. This sluggish phenomenon can be either a potential-driven or an activation process from adsorbate intermediates, especially water that is generated in considerable quantity under large dc biased conditions.

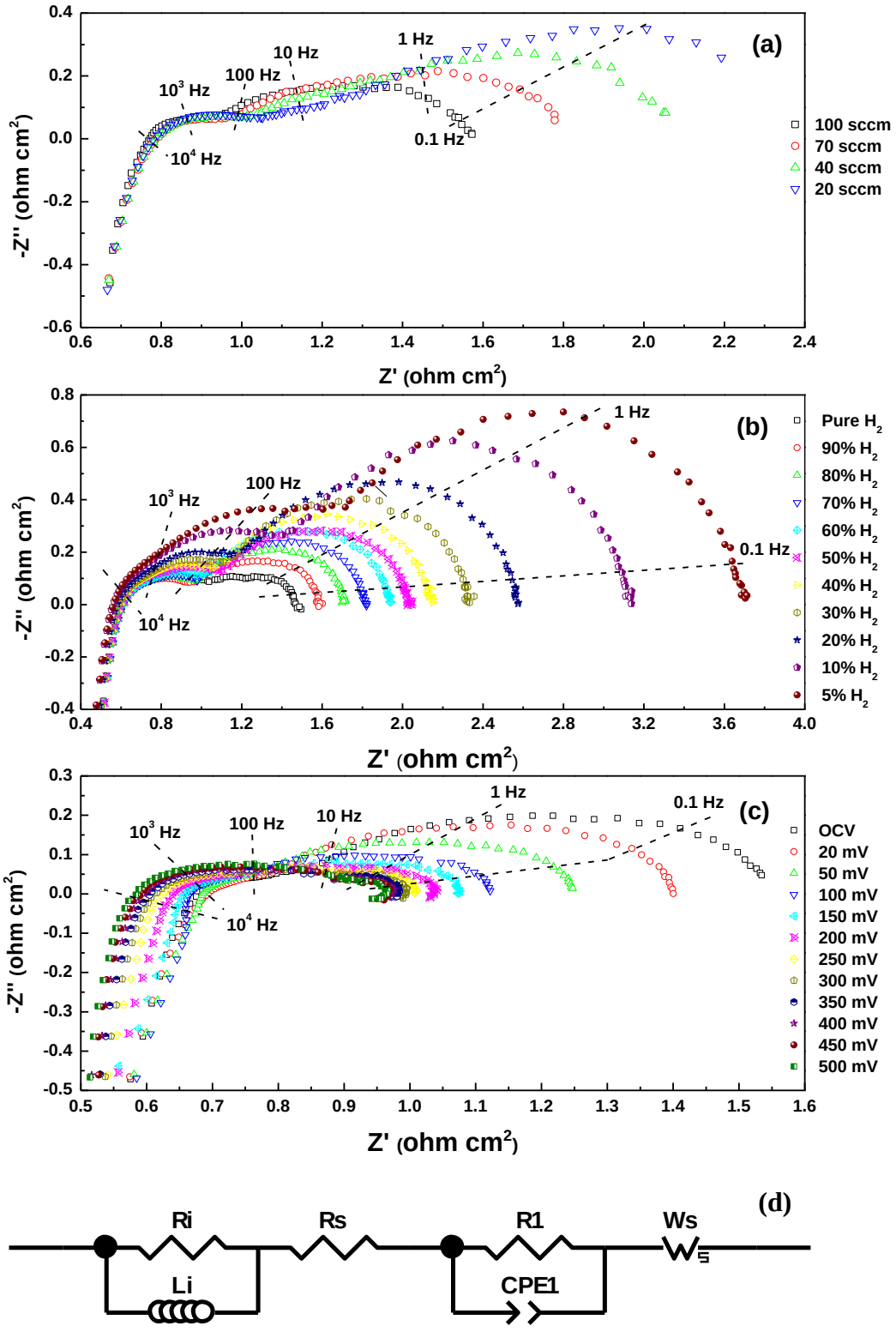

Figure 4-2 Impedance responses of LSV–YSZ anode in (a) pure H_2 under different flow rate and (b) H_2-He binary gases, both under OCV conditions, and (c) pure H_2 under different dc bias. The equivalent circuit is shown in (d). The fuel flow rate was 100 sccm. The testing temperature was 950 ℃.

While too early to draw a conclusion on the physical causes of Arc 3, it is not trivial to do an analogy with other energy conversion systems also with low frequency inductive loops. Such phenomenon had been observed in "all solid" secondary battery (Kahil *et al.*, 1986) and polymer fuel cells (Roy *et al.*, 2007; Schneider *et al.*, 2008). Arc 3 is also fairly common in SOFC cathodes. While it might be due to enhanced electronic conductivity of electrolyte surface (Schouler and Kleitz, 1987), theoretic investigations on oxygen reduction on Au/YSZ interface indicated that Arc 3 may be aroused from stepwise multi-electron transfer with adsorbed intermediates (Vanhassel *et al.*, 1991). Besides the mechanism mentioned above, for LSM-YSZ cathode it may also due to the improved interface structure after current passage. In terms of more relevant Ni anodes, Arc 3 was seldom found in Ni pattern anodes but not uncommon in Ni paste and Ni cermet anodes. Controversy still exists: Bieberle claimed no inductive loops (Bieberle and Gauckler, 2001; Bieberle, 2000) while Boer observed Arc 3 in Ni pattern anodes (Boer, 2000). Generally, Arc 3 only exists in porous anodes with low electrode impedance.

After this rather qualitative discussion on the shapes and possible contributions, impedance spectra are fitted to certain equivalent circuits. A subset of inductance and negative resistance in parallel, L_i/R_i, describes the parasitic inductance aroused from Pt lead wires at extremely high frequencies. Arc 1 is simulated routinely by a *R*/CPE subset. The high frequency part of Arc 2 is generally of linear relationship. In contrast, the low frequency part is somewhat a depressed arc— typical appearance of O element, which is also named as finite length Warburg or porous bounded Warburg element (Consultrsr.com, 2011). O element is used extensively to depict the impedance of rotating disk electrode (RDE), where the reactants simply diffuse through the Nernst Diffusion Layer (NDL). In our gas channel design the inlet gases are supplied perpendicular to the anode surface, which produces similar fluid flow field to RDE. Fig. 4-2a shows the impedance responses of the LSV–YSZ anode with different H_2 flow rate. With the decreasing flow rate, it is worth noting how Arc 2 changes from finite length Warburg to some symptoms of infinite Warburg while Arc 1 almost remains unchanged. Arc 2 is also reduced significantly with increasing dc biases (Fig. 4-2c), which may be due to the compacted NDL or buffering effect of the generated water. The change of fuel flow rate only alters the hydrodynamic force, i.e., the NDL thickness. In contrast, fuel dilution not only changes NDL thickness

but also the H_2 partial pressure on the NDL surface. Both Arc 1 and Arc 2 are increased due to fuel dilution (Fig. 4-2b), implying that H_2 concentration in NDL affects the fuel oxidation reactions. Arc 3 is not included in the equivalent circuit because its physical nature is still undetermined. Impedance curves are deconvoluted through a (L_i/R_i) R_s (R_1/CPE$_1$) W_s equivalent circuit, where R_s is the series resistance and W_s is an O element.

All electrochemical reactions must take place at the electrified interface, the double layer. The nature of double layer at LSV–YSZ interface and the magnitude of its capacitance are the keystones to understand the anode behaviour towards H_2 oxidation. In this section the double layer capacitance (C_{dl}) is obtained from two methods: one is EIS method and the other is transient method. In the EIS method, each impedance curve is fitted to an equivalent circuit and the C_{dl} is assigned to be the capacitance (C) calculated from (R_1/CPE$_1$). The relationship between C, impedance Z, and angular relaxation frequency ω_{max} of (R_1/CPE$_1$) can be described by

$$C = \frac{\sqrt[n]{R_1 T_1}}{R_1} = T_1 \omega_{\max}^{n-1} \qquad \text{(Equation 4-1)}$$

$$Z = \frac{1}{T_1 (i\omega)^n} \qquad \text{(Equation 4-2)}$$

where R_1 is the resistance, T_1 (CPE1-T) and n (n equivalent to CPE1-P) are parameters of constant phase element #1 in ZView©, ω is the angular frequency, and i is the imaginary unit. The circuit used in transient method, R_u (C_{dl}/R_p), includes uncompensated resistance (R_u), double layer capacitance (C_{dl}), and the polarization resistance (R_p). Though sometimes the values of parameters obtained from the two methods are quite similar (e.g., R_u to R_s and R_p to R_1), it is worth to highlight that their physical meanings are always different. For current transients responding to a potential step, C_{dl} can be obtained from integration, i.e.

$$C_{dl} = \frac{\Delta Q}{\Delta U} = \frac{\int_{t=0}^{t=t_s} \left[i_{(t)} - i_s \right] dt}{\Delta U} \qquad \text{(Equation 4-3)}$$

where ΔU is the difference between the OCV and applied potential step, t_s is the time interval, and i_s is the current density where the current decay saturates. C_{dl} can also be estimated from non-linear fitting. If a potential step U is applied to the system at $t = 0$, the current transient fulfils

$$C_{dl}R_u\frac{di_{(t)}}{dt}+(1+\frac{R_u}{R_p})i_{(t)}=\frac{U}{R_p},i_{(0)}=\frac{U}{R_u} \quad . \qquad \text{(Equation 4-4)}$$

Solve Eq. 4-4 to yield its analytical solution,

$$i_{(t)}=\frac{e^{-\frac{t(R_p+R_u)}{C_{dl}R_pR_s}}U\left(R_p+e^{\frac{t(R_p+R_u)}{C_{dl}R_pR_s}}R_u\right)}{R_u(R_p+R_u)} \quad . \qquad \text{(Equation 4-5)}$$

With certain initial conditions on the R_u and R_p, C_{dl} is easily available from commercial tools like Wolfram Mathematica© 7.

The nominal C_{dl} obtained from EIS method ranges from 0.3 to 0.7 mF/cm^2 (Fig. 4-3a). The large fitting error of C_{dl} calculated from Arc 1 is resulted from the overlapped impedance arcs, noting that the magnitude of Arc 1 is 2 to 4 times smaller than that of Arc 2. A pattern of n – C_{dl} dependency appears to exist but is still within the fitting error. In the transient method, this problem is even more severe because of the nature of current transients. The current signals oscillate all through the experiment (Fig. 4-4). It is surprising that C_{dl} varies almost 2 orders of magnitude from different methods— 0.5 ± 0.2, 4.3 ± 0.3, and 18.3 ± 1.6 mF/cm^2 for EIS method (Fig. 4-3a), non-linear fitting (Fig. 4-3c), and integration (Fig. 4-3c), respectively. Typical C_{dl} for solid state electrodes, especially Ni cermet SOFC anodes, are in the order of 10^{-1} mF/cm^2 (Gewies *et al.*, 2007; Robertson and Michaels, 1991; Primdahl and Mogensen, 1997). C_{dl} from the EIS method may be envisaged to be "correct" double layer capacitance, which will be discussed in Sections 4.2 to 4.4 in detail. It is, however, necessary to explain why so large discrepancy is observed in the three methods. One explanation is that C_{dl} obtained from the transients is tainted by pseudo-capacitance that is resulted from bulk phenomena. For gas diffusion within the porous electrode,

it could contribute to a capacitance in the order of 10^1 mF/cm^2 (Primdahl and Mogensen, 1999). Its relaxation frequency is generally around several Hz, equivalent to a time constant in the order of 10^{-1} s ($\tau = 1/(2\pi f)$). Other bulk phenomena, such as gas conversion, give even larger values ca 10^3 mF/cm^2 (Primdahl and Mogensen, 1998). As shown in Fig. 4-4, the time constants of transient experiments are around 1–2 seconds, a value large enough to trigger phenomena other than double layer charging, such as gas diffusion and gas conversion.

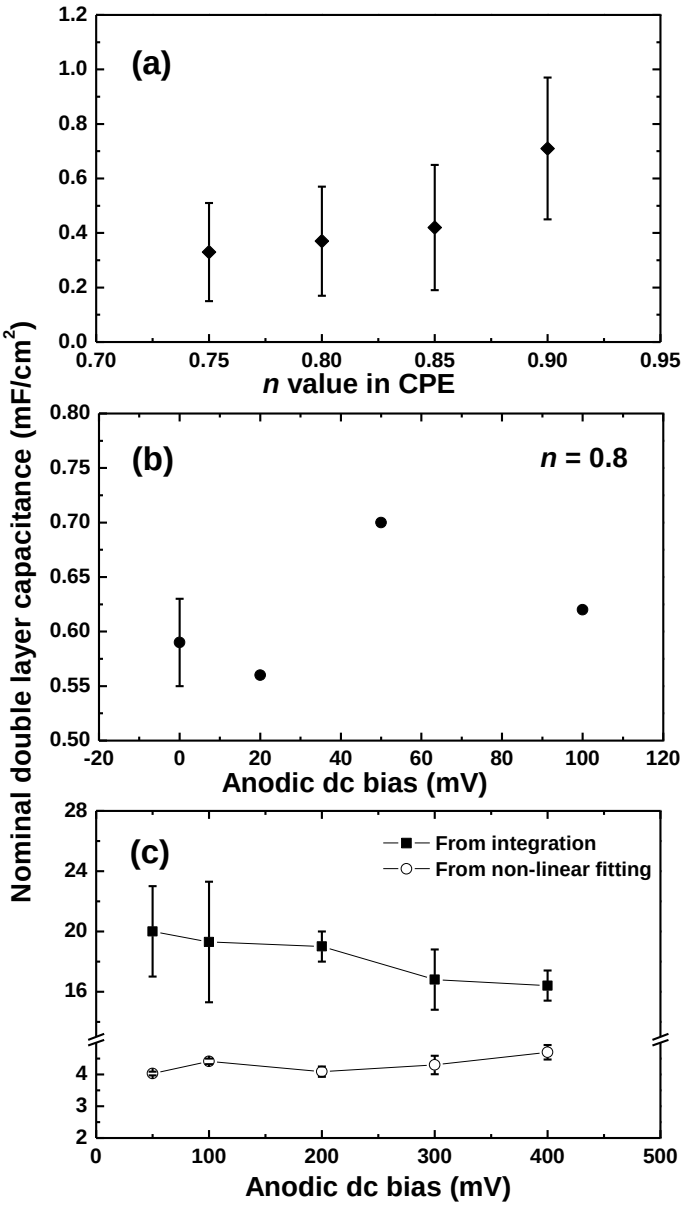

Figure 4-3 Nominal double layer capacitance of LSV–YSZ anode obtained from EIS (a, b) and transients (c), as a function of *n* value in CPE of R_1/CPE$_1$ (a) and under small anodic dc biases (b, c). The H_2 flow rate was 100 sccm. The testing temperature was 950 ℃.

With some confidence on the C_{dl} values around 0.3 to 0.7 mF/cm^2, here the double layer structure is briefly discussed. Most researchers adopt the Helmholtz-Perrin theory to explain double layer capacitance in SOFC anodes. This theory treats the double layer to a parallel-plate capacitor. Area-specific C_{dl} is thus represented as

$$C = \frac{\Delta Q}{\Delta U} = \frac{\varepsilon \varepsilon_0}{d} \quad , \qquad \text{(Equation 4-6)}$$

where d is the distance between the oHp and YSZ surface, ε is the relative permittivity of the material in-between, and ε_0 is the permittivity of free space. Eq. 4-6 implies constant C_{dl} with no dependency on voltage. However, C_{dl} of LSV–YSZ anode does change with different dc biases (Fig. 4-3b). Reliable and ubiquitous C_{dl}–U relationship is yet to be identified. In literature, positive C_{dl} –U dependency had been reported (Bieberle *et al.*, 2001). Helmholtz-Perrin theory also predicts unrealistic small double layer distance. Some modification must be applied to the theory. At least, the diffusive nature of the electrified layer, exact charged species, and extension of three phase boundary (TPB) should be taken into account. More works should be addressed on these problems.

4.1.3 Impedance behaviour under H_2–H_2O–He ternary atmosphere

Fig. 4-5 shows the fitted results of elements in (L_i/R_i) R_s (R_1/CPE$_1$) W_s equivalent circuit. For Arc 1 simulated by (R_1/CPE$_1$), both R_1 and C_{dl} increase with increasing H_2 content in H_2–He atmosphere. Strong dependency of R_1 to H_2 content implies that surface adsorption or dissociation of H_2 onto LSV surface could be the rate determining step in H_2 oxidation. The nominal C_{dl} rises slightly with increasing H_2 content, indicating an extension of the reaction sites or accumulation of charged species on LSV side of TPB. It is not clear whether the fuel dilution effect is of chemical or physical nature, bearing in mind how it can alter LSV surface structure and gas diffusivity. Arc 2 is described by an O element, Generalized Finite Warburg element (GFW, W_s), whose impedance is

$$Z = R \frac{\tanh(i\omega T)^P}{(i\omega T)^P} \quad , \qquad \text{(Equation 4-7)}$$

where R (W_s-R), T (W_s-T) and P (W_s-P) are the parameters of GFW in ZView©. The Warburg resistance R increases significantly from 0.8 Ω cm^2 to 1.8 Ω cm^2 but T decreases consistently for almost 25%, when the fuel composition changes from 10 vol. % He to 90 vol. % He. While the increase of R is straightforward to understand, it is confusing for the decreasing T. In the diffusion interpretation, T stands for

$$T = \frac{L^2}{D_{eff}} = \frac{\tau L^2}{D_{AB}\varphi} \quad , \qquad \text{(Equation 4-8)}$$

where L is the NDL thickness, τ is the tortuosity, φ is the porosity, and D_{AB} is the binary diffusion coefficient. T should increase according to fuel dilution, with the assumption of constant effective diffusion coefficient (D_{eff}). Anyway, an order-of-magnitude evaluation of the L value should still be meaningful. In present experiments L is estimated to be around 5–10 mm, with the assumption of $0.25 < \tau < 0.35$ (Williford *et al.*, 2003), $0.3 < \varphi < 0.5$ (this study), and $11\times10^{-4} < D_{H2\text{-}He} < 13\times10^{-4}$ m^2/s (McCourt *et al.*, 2005).

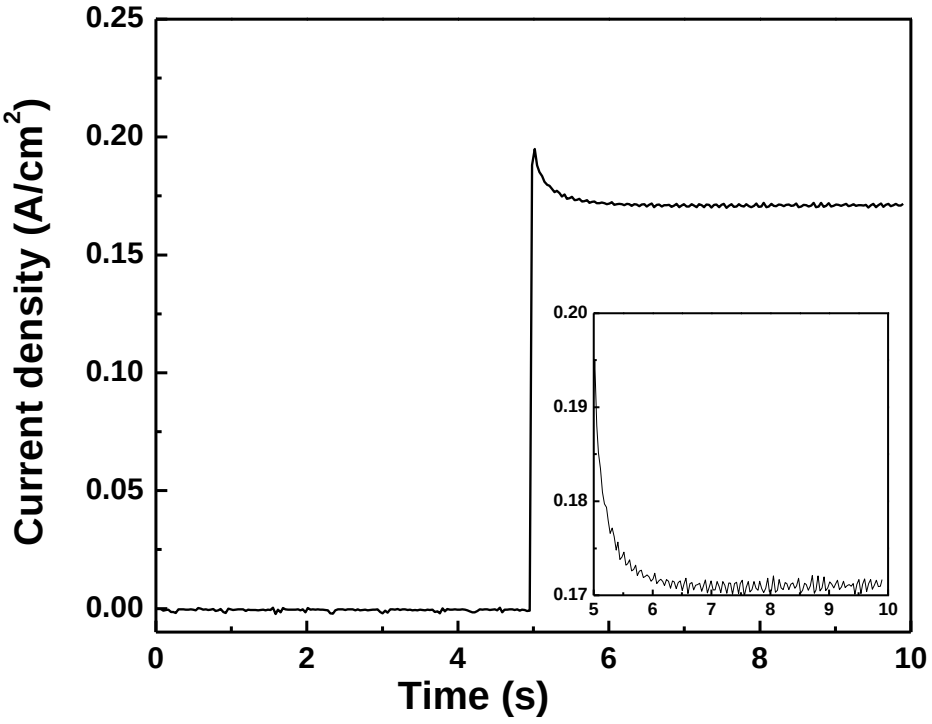

Figure 4-4 Current transient of LSV–YSZ anode subjected to a 200 mV potential step. The H_2 flow rate is 100 sccm. The testing temperature is 950 ℃.

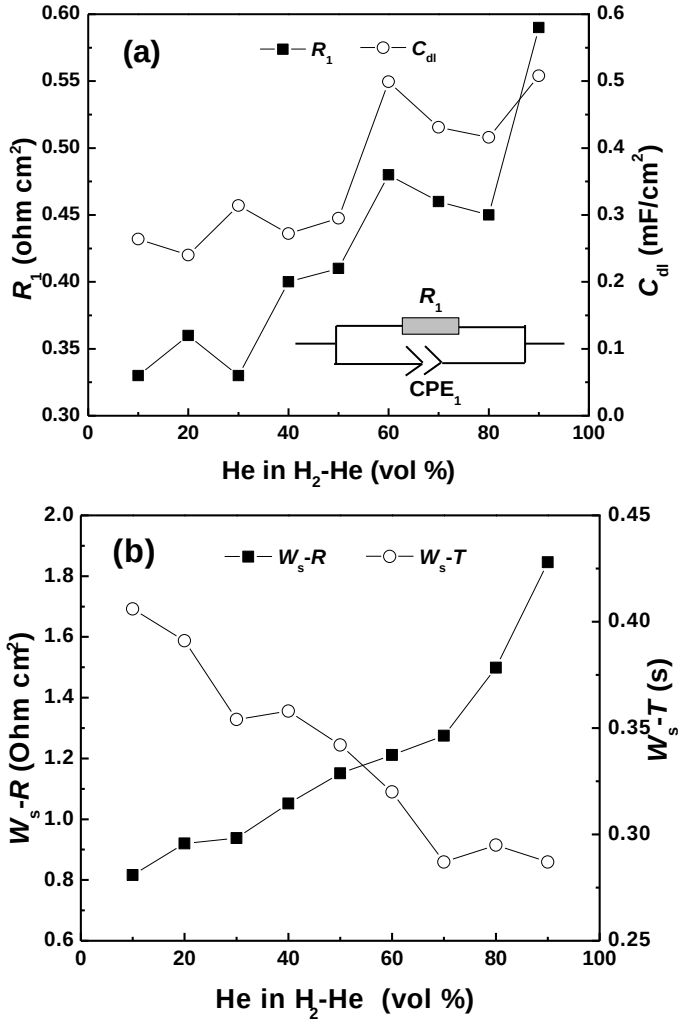

Figure 4-5 Equivalent circuit values of LSV–YSZ anode exposed to H_2-He binary atmosphere: (a) R_1 and nominal C_{dl} in (R_1CPE$_1$), and (b) W_s-R and W_s-T in W_s, with W_s-P fixed at 0.36. Note that in (a), only three in the five parameters in the (R_1CPE$_1$) subset are independent (see Eq.1).

Impedance spectra of LSV–YSZ anodes recorded in wet atmosphere (H_2-H_2O gases) are distinct to their counterparts in dry atmosphere. The impedance points collapse below 1 Hz. Arc 1 dominates and Arc 2 appears to die out. The grouped polarization resistance, R_p, is comparable to that in dry H_2. The whole spectra cannot be fitted to relevant equivalent circuit given in Figure 4-2d. The ω_{max} of Arc 1, 200–600 Hz, is one order lower and the corresponding reaction resistance, R_1, is however larger than that in pure H_2. H_2 oxidation is somewhat retarded but the gas diffusion problem is alleviated significantly. This detrimental steam effect on Arc 1 emerges even with a small addition of water. It continues at least up to 15 vol. % H_2O, as shown in Fig. 4-6. To incorporate small amount of steam into fuels has been a common practice for SOFCs with Ni-cermet anodes. A beneficial water effect is

with little controversy for most SOFC anodes. It is rather impressive for the detrimental water effect as observed in LSV–YSZ anodes. It seems little to do with the change of electrode conductivity, as far as the negligible variation of R_s is concerned (Fig. 4-6). As steam facilitates the surface conduction of YSZ (Sakai *et al.*, 2003), the water effect of LSV–YSZ anodes must come from the subtle alternation of LSV surface structure but not that of YSZ. Much works on the interfacial structure of LSV have to be carried out.

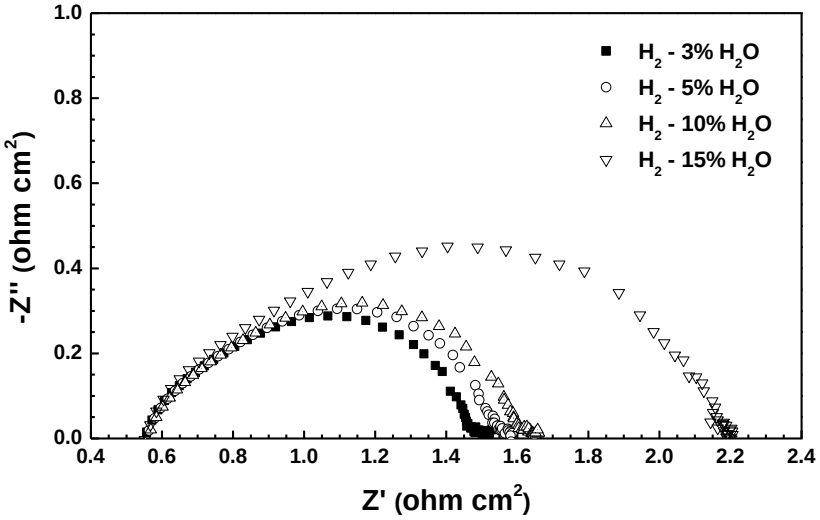

Figure 4-6 Impedance responses of LSV–YSZ anode in H_2–H_2O atmosphere.

Fig. 4-7 exhibits how the LSV–YSZ anode responses under both water and fuel dilution effects. For impedance spectra recorded at wet atmosphere (here "wet" means H_2 humidified at room temperature, i.e. 3 vol. % H_2O–H_2), all the spectra are not able to be fitted to equivalent circuit given in Figure 4-2d. Any discussions relying on equivalent circuit, like capacitance, are thus not meaningful. When the fuel is shifted to wet atmosphere, with caution it is assumed that Arc 1 remains and Arc 2 converges at low frequencies. With this assumption the resistance values are roughly estimated from the corresponding impedance spectra. Comparing the spectrum obtained from wet H_2 to that from the dry H_2, R_s is identical (0.67 Ω cm^2) and R_1 slightly increases from 0.13 $\pm$ 0.02 to 0.15 $\pm$ 0.03 Ω cm^2 (Fig. 4-7a and 4-7b). The R_2 slumps from 0.73 to 0.09 Ω cm^2, an impressive result exhibiting on how only 3 % H_2O almost eliminates the dominant diffusion impedance in dry atmosphere. In the case of fuel dilution of wet H_2, the relaxation frequency shows a decreasing trend and is one order lower than that in dry atmosphere, indicating more sluggish reaction

kinetics at low hydrogen partial pressure atmosphere (Fig. 4-7c). Furthermore, R_1 increases nearly three times when wet H_2 relinquishes gradually to (10H_2–90He)–3 % H_2O (Fig. 4-7b), comparing to only one time increase of dry H_2–He atmosphere in that case (Fig. 4-5). High electrode degradation rate in wet fuels may be due to its oxidizing atmosphere. Note that the oxygen partial pressure jumps 2–3 three orders to 10^{-15}– 10^{-18} bar with the introduction of only 3 % H_2O.

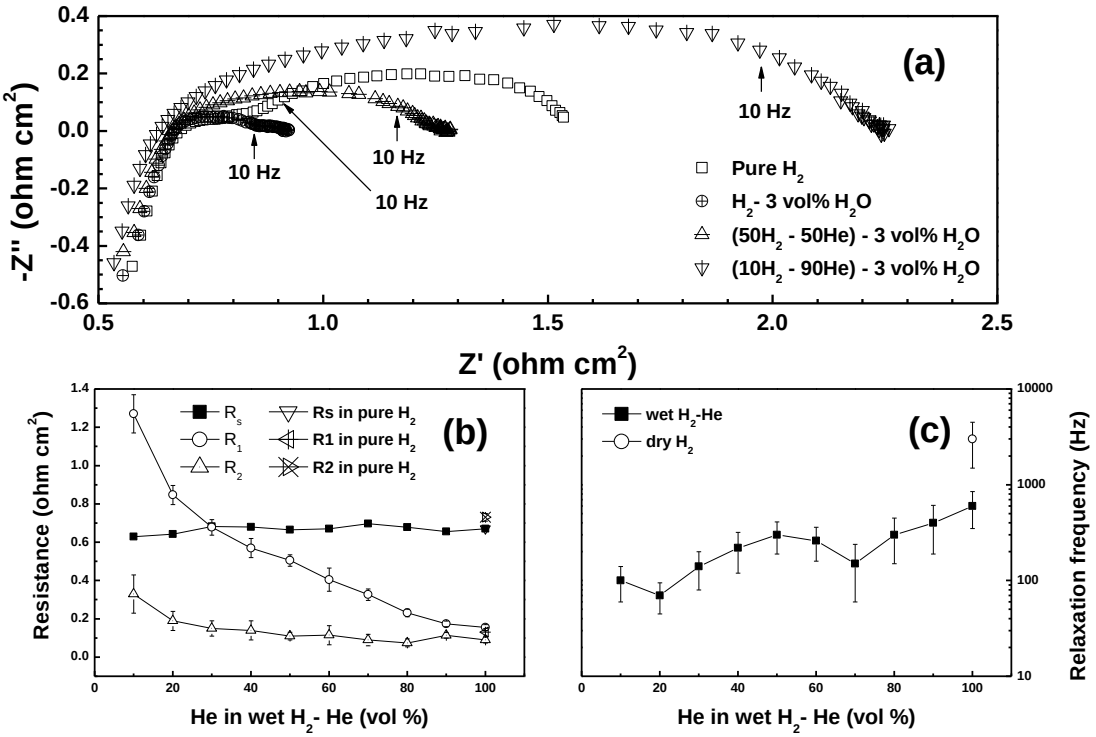

Figure 4-7 (a) Impedance responses of "Arc 1", (b) estimated resistance values, and (c) relaxation frequencies of LSV-YSZ anode in H_2–H_2O–He atmosphere.

4.1.4 Brief summary

The impedance behaviour of composite anodes of 20 at % strontium doped lanthanum vanadate (LSV) and yttria-stabilized zirconia (YSZ) was investigated in H_2–H_2O–He atmosphere. Impedance spectra in H_2-He binary atmosphere mostly contain two depressed and poorly separated arcs, and occasionally inductive loops at extremely low frequencies under biased conditions. The high frequency arc, Arc 1, was ascribed to reaction resistance. The middle-to-low frequency arc, Arc 2, was identified to concentration impedance in the porous electrode or gas channels. Small inductive loops, Arc 3, begin to emerge for dc biases larger than 250 mV. Significant efforts were contributed to obtain the double layer capacitance. The EIS method might have given "correct" capacitance in the order of 10^{-1} mF/cm^2. The capacitance

obtained from the transient method is contaminated and its value is 1–2 orders higher than normal double layer capacitances. In wet atmosphere, the impedance spectra still include Arc 1 but Arc 2 collapses together at low frequencies. A detrimental water effect that seldom observed in most SOFC anodes was identified up to 15 vol. % H_2O.

4.2 Double layer structure in solid oxide fuel cell anode/electrolyte interfaces: a Monte Carlo study

Solid oxide fuel cells (SOFCs) are high temperature energy conversion devices owning the advantages of high efficiency and fuel flexibility (McIntosh and Gorte, 2004; Goodenough and Huang, 2007). The electrochemical fuel oxidation is believed to occur around three phase boundaries (TPBs), influenced at least by materials properties, fuel composition, operating conditions, impurities (Hansen *et al.*, 2004), and water (Sakai *et al.*, 2003). The reaction mechanisms can thus be fairly complicated. Some reaction paths have been proposed but the underlying mechanisms are hitherto still unclear (Raz *et al.*, 2001; Mogensen *et al.*, 2007). Surprisingly, little attention has been paid to the double layer of anode/electrolyte interfaces. The double layer plays a fundamental role in determining the electrode kinetics and has attracted broad interests in various electrochemical systems (Pajkossy and Kolb, 2007; Rufford *et al.*, 2009). A clear understanding on the double layer structure should be helpful in elucidating the interfacial structures and reaction processes in SOFCs. This work was dedicated to provide a quantitative picture of the double layer in SOFC anode/electrolyte interfaces. A case study was carried on lanthanum strontium vanadate ($La_{0.8}Sr_{0.2}VO_3$, LSV)/8 mol % yttria-stabilized zirconia (YSZ) interfaces. LSV is a highly conducting oxide and has great potential to be SOFC anode fed with tainted fuels (Ge and Chan, 2009b).

The solid electrolyte interface usually has a more compact double layer than the liquid electrolyte interface. Furthermore, charged particles in solid crystalline electrolytes are mobile only in certain directions. The primitive model method initially proposed by Torrie and Valleau (Torrie and Valleau, 1979), which successfully describes the Gouy–Chapman (G–C) layer in liquid electrolytes (Wang and Ma, 2010a; Fedorov *et al.*, 2010), therefore seems insufficient to depict the whole double layer in solid electrolyte

interfaces. Generally speaking, solid electrolyte interfaces are conceptually simpler than their liquid counterparts due to confined lattice ions and diminished ion-dipole interactions. These kinds of simplifications enabled us to simulate the oxygen vacancy distribution in YSZ as the stochastic evolution of randomized charged particles on well-defined lattices.

This work simulated 2-dimensional double layer structure of LSV/YSZ interfaces in LSV–YSZ(H_2)|YSZ|Pt(air) half cells at 950 ℃, with an open circuit voltage (OCV) of -1.18 V. The electrons on the LSV side were aligned compactly along the LSV/YSZ interface. The oxygen vacancy distributions on the YSZ side of the interface were simulated by the Markov chain Monte Carlo (MCMC) technique. The square grid ($L \times L$) was subsumed to (400) planes of YSZ. The grid size L was assigned as 40, as a trade-off of computing time and adequate description of the double layer. The normalized distance (z) away from the LSV/YSZ interface was in unit of the nearest neighbouring distance among oxygen vacancies (0.257 nm, PDF #30–1468). Impenetrable walls at $z = 0$ and $z = L$ represented the LSV/YSZ interface and the bulk YSZ, respectively. The $L \times L$ grid was translated with periodic boundary conditions in the direction perpendicular to the LSV/YSZ interface. The Hamiltonian of canonical ensemble comprises (*i*) the attraction between the reference particle and the charged line ($H_{\text{p-l}}$) and (*ii*) the repulsion due to neighbouring particles ($H_{\text{p-p}}$). $H_{\text{p-l}}$ is due to the long-range Coulombic attractions between the electron reservoirs at the LSV side and the reference oxygen vacancy in the YSZ side of the LSV/YSZ interfaces,

$$H_{\text{p-l}} = \sum_{k}^{N} \left[-\frac{q\lambda}{2\pi\varepsilon_0\varepsilon_{\text{r}}} \ln \frac{L + \sqrt{L^2 + 4z_k^{\,2}}}{z_k} \right] , \qquad \text{(Equation 4-9)}$$

where N is the total numbers of oxygen vacancies, λ the line charge density, q the charge of oxygen vacancy (q=2e), ε_0 the vacuum permittivity, and ε_{r} the relative static permittivity. $H_{\text{p-p}}$ is simply due to the Coulombic repulsions among oxygen vacancies,

$$H_{\text{p-p}} = \sum_{k}^{N} \sum_{l}^{N} \frac{q^2}{4\pi\varepsilon_{\text{r}}\varepsilon_0 r_{kl}} , \qquad \text{(Equation 4-10)}$$

where r_{kl} is the distance between a k and a l oxygen vacancies. Let the probability of a transition from state i to j is $p_{i,j}$ ($i \neq j$), of a trial realizing this transition is $q_{i,j}$, and of an

acceptance of this trial is $f_{i,j}$. It is then found that

$$p_{i,j} = q_{i,j} f_{i,j} \quad . \qquad \text{(Equation 4-11)}$$

The $q_{i,j}$ fulfils the uniform distribution. In this study, the $f_{i,j}$ is according to the Metropolis algorithm,

$$f_{i,j} = \min\left\{1, \alpha \exp\left[-\frac{\left(1-\beta\theta^2\right)\Delta H_{\text{p-l},ij} + \Delta H_{\text{p-p},ij}}{kT}\right]\right\} , \qquad \text{(Equation 4-12)}$$

where θ is the coverage rate of the outer Helmholtz plane (oHp), α a factor related to the effective double layer thickness, β ($0 < \beta < 1$) a degenerated factor accounting for the driving force decay, k the Boltzmann constant, T the absolute temperature. The rapid prototyping was implemented on Mathematica® 7. All MCMC simulations were run at 1×10^6 iterations, which had been proved to be sufficient to reach the invariant distribution. It took nearly 40 hours to run the code on a Hewlett–Packard® Z400 workstation.

Figure 4-8 shows a typical oxygen vacancy diagram in the YSZ side of LSV/YSZ interfaces under OCV condition. Oxygen vacancies in the first several charged sheets seem to be strongly attracted by the interface. The oxygen vacancy distribution gradually becomes stochastic along the direction towards the bulk YSZ. Figure 4-9 shows the three-dimensional visualization and the density plot constructed by superimposing 16 such diagrams that are generated from the same code. As shown in Fig. 4-9, the oxygen vacancies exhibit no catastrophic agglomerations and are uniformly distributed at places far away from the interface ($z > 10$). It is worth to highlight that the oxygen vacancy concentrations adjacent to the interface is one order of magnitude larger than that in the bulk YSZ, mostly probably due to the double layer charging effect. This interfacial accumulation of oxygen vacancies should be incorporated into any analyses on electrode kinetics and reaction mechanisms around TPBs (e.g. adsorption, spillover, and desorption). The double layer region extends about 6 to 8 sheets (i.e. 1.5 to 2.1 nm), beyond which the background concentration is reached. The border between the double layer and the bulk YSZ is nevertheless very obscure.

The inset of Fig. 4-10 gives the one-dimensional relative oxygen vacancy density (ρ/ρ_0)

profile of the corresponding diagram. ρ/ρ_0 is defined as the ratio of summed oxygen vacancy densities of each sheet (ρ) over the background density (ρ_0). ρ/ρ_0 of the first five sheets, as shown in Fig. 4-8, are 12.32, 6.02, 4.17, 2.32, and 1.58. Comparing to the cases of liquid electrolyte interfaces (Fawcett, 2009) (Torrie and Valleau, 1980), these ρ/ρ_0 values are comparable but the ρ/ρ_0 profile decays much faster. Figure 4-10 shows the ρ/ρ_0 profiles of polarized LSV/YSZ interfaces under anodic biases (E_{bias}) from 0 to 150 mV. Each profile is averaged from 7 independent MCMC runs. The ρ/ρ_0 profiles of heavily biased interfaces are "steeper" than those of lightly biased interfaces. The inset of Fig. 4-10 shows listed fitting results of the ρ/ρ_0 profiles according to an exponential decay, $\rho/\rho_0=1+a*\exp(-k*z)$. a and k are in the ranges from 22.9–23.1 and 0.71–0.73, respectively. Both of them exhibit descendent behaviours towards the increase of E_{bias}, implying the gradual relaxations of the double layer. This phenomenon roots in the dwindling Volta potential difference of LSV/YSZ interfaces, Ψ_{YSZ}^{LSV}, when the interfaces are subjected to changing E_{bias}. The effect of E_{bias} on Ψ_{YSZ}^{LSV} is nontrivial and deserves the electrochemical potential analysis on half cells.

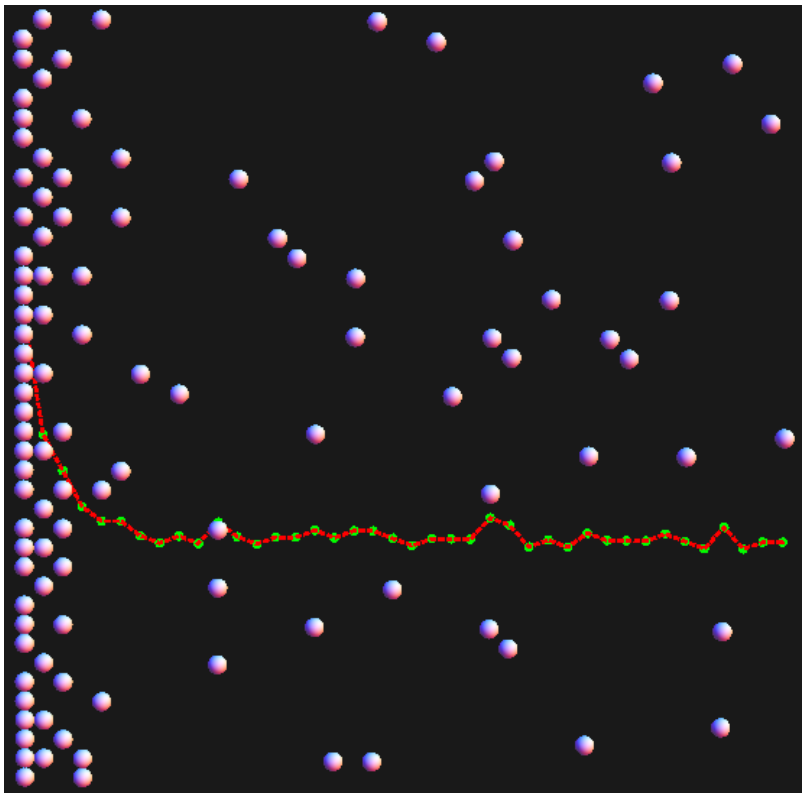

Figure 4-8 Oxygen vacancy distribution diagram in the YSZ that is adjacent to the LSV/YSZ interface, under OCV condition. The inset shows the corresponding relative oxygen vacancy density profile.

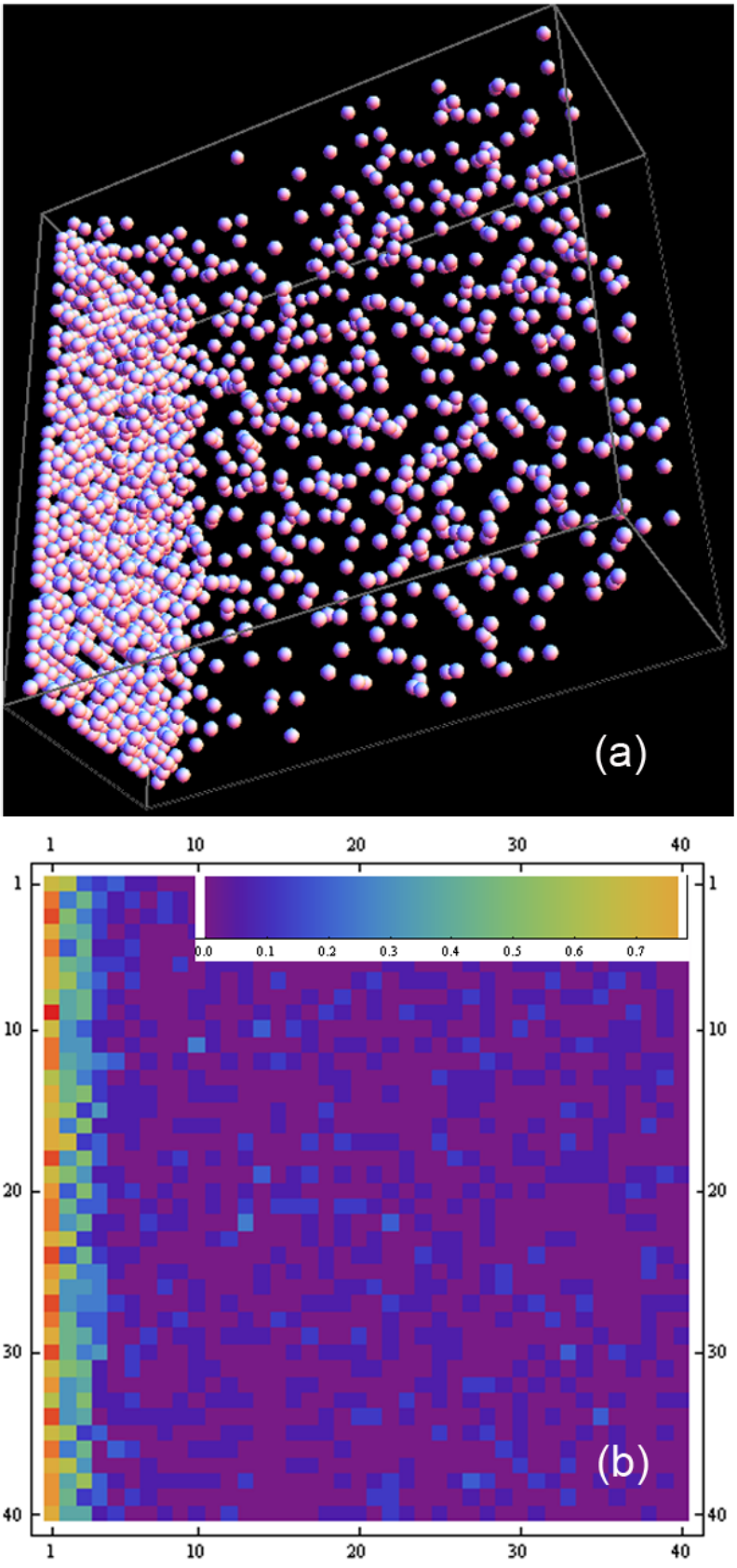

Figure 4-9 (a) Three-dimensional visualization and (b) density plot of oxygen vacancies in the YSZ side of LSV/YSZ interfaces under OCV condition.

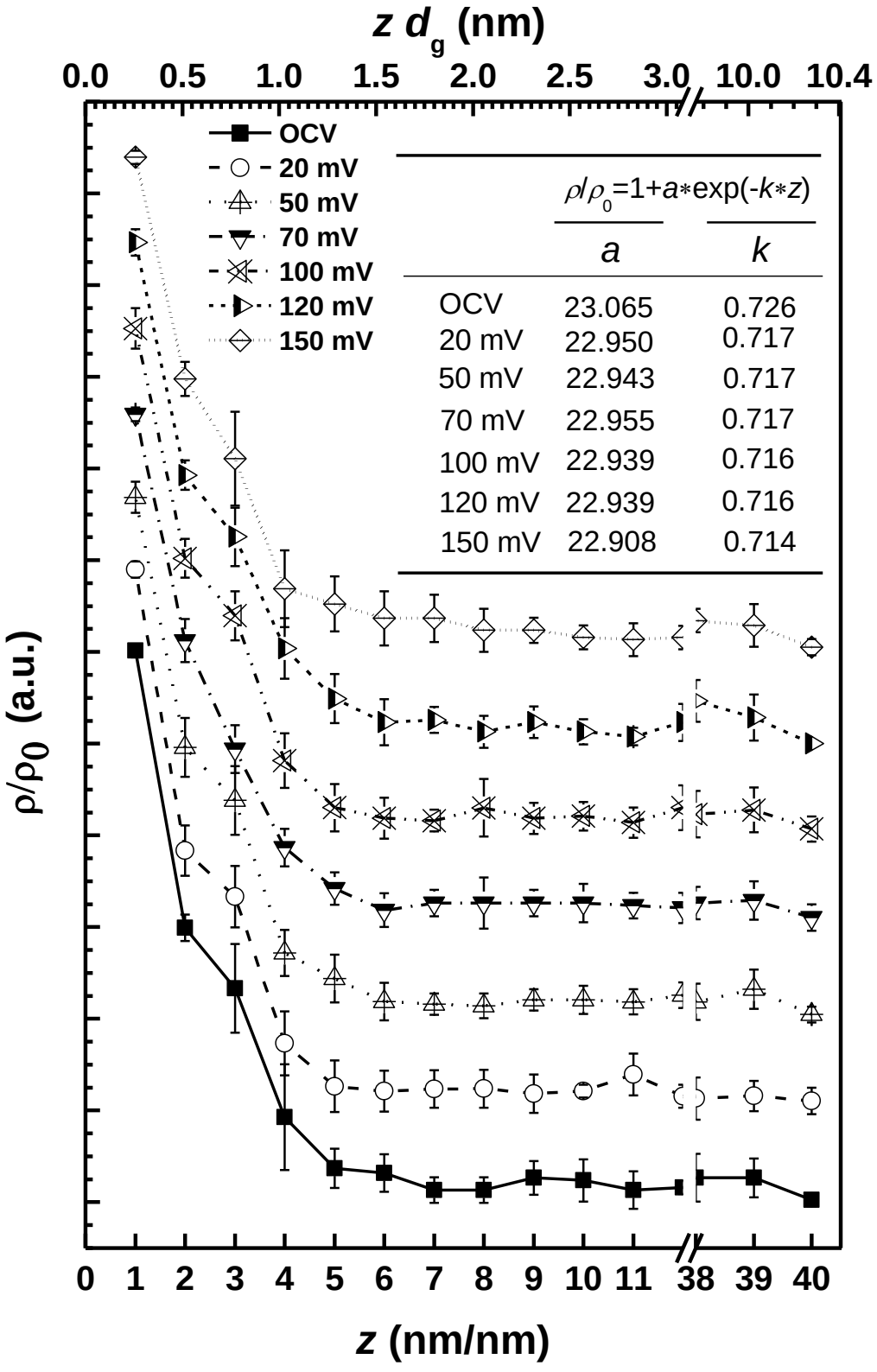

Figure 4-10 Relative oxygen vacancy density profiles in the YSZ side of polarized LSV/YSZ interfaces under anodic biases from 0 to 150 mV. The profiles are shifted vertically merely for illustration purpose.

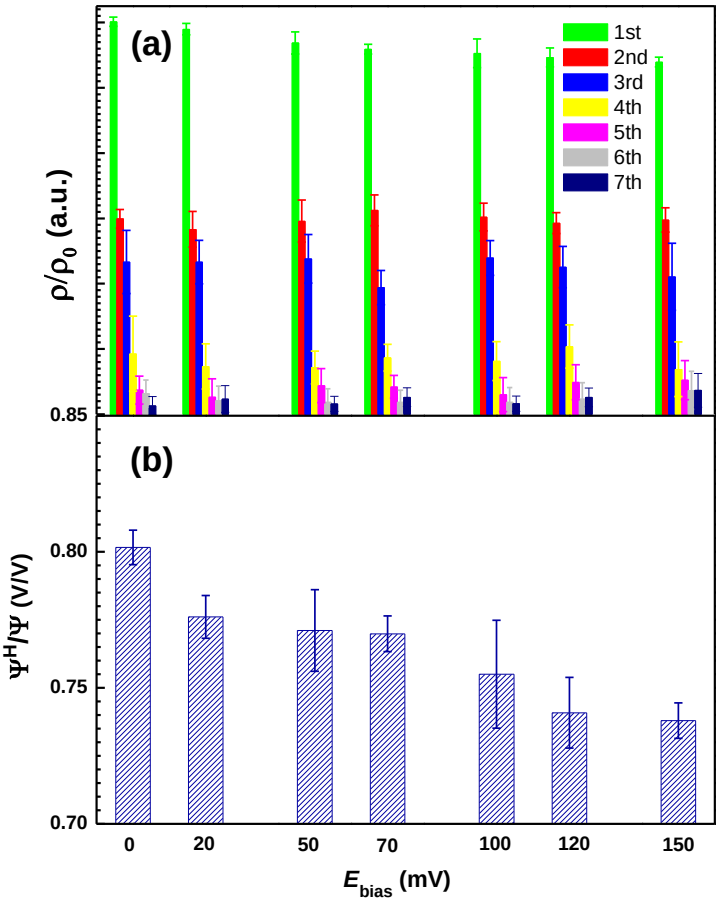

Figure 4-11 (a) Relative oxygen vacancy densities of the first seven charged sheets and (b) the Volta potential portion of the H–P layer in the YSZ side of polarized LSV/YSZ interfaces.

The separation of the Helmholtz–Perrin (H–P) layer and the G–C layer has an important application on calculating the Volta potential distributions across polarized interfaces. It is however difficult to pinpoint the "boundary" between the two layers. It might only be conceptually separable because the charge distribution is continuous even around the boundary. To present the double layer clearly, Fig. 4-11a shows the ρ/ρ_0 values of the charged sheets that are supposed within the double layer region. In this study, the first two charged sheets are tentatively regarded to compose the H–P layer. The Volta potential portion of the H–P layer over the whole double layer ($\Psi_H / \Psi_{YSZ}^{LSV}$) are thus found to be 0.80±0.01, 0.77±0.01, 0.77±0.02, 0.77±0.01, 0.76±0.02, 0.74±0.01, and 0.74±0.01, under E_{bias} of 0, 20, 50, 70, 100, 120, and 150 mV, respectively (Fig. 4-11b). A typical double layer structure therefore looks like: 70–80% of oxygen vacancies are immobilized in the outer Helmholtz plane, with a distance of 0.5–0.8 nm away from the LSV/YSZ interface; 20–30% of oxygen vacancies decay stochastically into thermal

disarray, with an effective region that extends about 2 nm into the bulk YSZ. Further work on the effects of dielectric mismatch (Jho *et al.*, 2008; Wang and Ma, 2010b), temperature, and fuel atmosphere will be considered in future to establish a complete understanding of SOFC anode/electrolyte interfaces.

4.3 Double layer capacitance of anode/solid-electrolyte interfaces

Solid electrolytes have been widely used in solid state energy conversion systems like batteries and fuel cells. Among various energy conversion systems, solid oxide fuel cells (SOFCs) own the advantages of high efficiency and fuel flexibility. The interfacial reaction mechanisms across the electrolyte and the electrode in SOFCs, however, are still in controversy (Mogensen *et al.*, 2007; Bessler *et al.*, 2010). One of the reasons may be the insufficient understanding on the double layer under SOFC operating conditions.

The double layer consists of an electron layer on the electrode and an oxygen vacancy layer on the electrolyte. One of the most-studied descriptors of the double layer is the double layer capacitance (C_{dl}). The electrocapillary technique represents the most classic method of measuring C_{dl} in mercury/solution interfaces (Grahame, 1947). Direct-current measurements of C_{dl} in solid electrode/ liquid electrolyte interfaces became feasible after the invention of potentiostat (Hickling, 1942). These dc voltammetry methods are, however, limited to low sensitivity and poor resolution. For example, our previous work demonstrated that they failed to resolve C_{dl} from various pseudo-capacitances (Ge and Chan, 2009a). *In situ* characterization techniques, including infrared spectroscopy (Ashley *et al.*, 1991), Raman spectroscopy (Macomber *et al.*, 1982), atomic force microscopy (Wang and Bard, 2001), neutron diffraction (Williams *et al.*, 1998), and various synchrotron radiation methods (Tikhonov, 2006; Luo *et al.*, 2006), had been used to investigate the double layer in recent years. Recently, encouraging works on *in situ* Raman and infrared spectroscopy had been carried out in SOFCs (Pomfret *et al.*, 2008; Lu *et al.*, 2002).

Impedance spectroscopy has hitherto been very popular on measuring C_{dl} in various interfaces. Impedance responses of SOFC electrode/electrolyte interfaces are always

severely depressed due to the frequency dispersion of electrochemical reactions. The frequency dispersion rarely occurs in homogeneous and clean interfaces, *e.g.* adsorbate-free mercury (Grahame, 1947) and single crystal surfaces (Eberhardt *et al.*, 1996). It is largely ascribed to inhomogeneity: (*i*) fractal disorder (Pajkossy, 2005), including surface roughness (Jarzabek and Borkowska, 1997), electrode porosity (Hitz and Lasia, 2001), and atomic scale irregularity (Kerner and Pajkossy, 1998); (*ii*) non-uniform potential and current distribution (Jorcin *et al.*, 2006); and (*iii*) anion adsorption (Pajkossy and Kolb, 2007). The frequency dispersion has been fairly common in SOFCs because of their porous electrodes and corrugated electrode/electrolyte interfaces. The constant phase element (CPE) is a non-intuitive circuit element that can be used to describe depressed impedance spectra. The frequency dispersion makes the CPE exponent (n) difficult to be obtained from impedance spectra, because the constant phase angle of CPE (θ) becomes ambiguous due to the overlapping of impedance arcs. This might be one of the reasons why diverse C_{dl} values have always been reported. Take the Ni–yttria-stabilized zirconia cermet, a typical high temperature SOFC anode, as an example. Primdahl and Mogensen reported that C_{dl} of Ni–8-mol% yttria-stabilized zirconia (YSZ[‡]) anodes was in the range from 200 to 700 μF/cm^2 in 3% H_2O–H_2 and at 1000 ℃ (Primdahl and Mogensen, 1997). Jiang and Badwal noted that C_{dl} of Ni–3-mol% yttria-stabilized zirconia anodes at 1000 ℃ was *ca* 100 μF/cm^2, slightly increasing with the increase of H_2 concentration in 2% H_2O–H_2–N_2 atmosphere (Jiang and Badwal, 1999). Holtappels *et al.* showed that C_{dl} of Ni–YSZ anodes was of several tens of μF/cm^2 from 725 to 890 ℃ but could jump to several hundred μF/cm^2 at 950 ℃, exhibiting complex dependencies on temperature and fuel composition (H_2 balanced with H_2O and Ar) (Holtappels *et al.*, 1999). The extrapolated C_{dl} at 1000 ℃ appears to be in the capacitance range given in Ref. (Primdahl and Mogensen, 1997). Besides the frequency dispersion, it is worth noting that the differences in SOFC architectures could also be responsible for the reported discrepancies. As shown in Ref. (Jiang and Badwal, 1999), C_{dl} of 80% Ni–zirconia anodes could be 30% and 150% larger than the anodes containing 70% of Ni and pure Ni, respectively. These results imply that the double layer of SOFC anode/electrolyte interfaces is fairly complicated. The underlying mechanism is still unclear and relevant capacitance models are yet to be developed.

C_{dl} can also be evaluated theoretically according to Stern's method (Stern, 1924),

consisting of the Helmholtz model (Helmholtz, 1853) and Gouy–Chapman model (Gouy, 1910; Chapman, 1913). In this work, the experimentally measured and theoretically obtained C_{dl} are hereafter denoted as C_{dl}^{app} and C_{dl}^{int}, respectively. The derivation of the Gouy–Chapman capacitance (C_G) is the most critical task in calculating C_{dl}^{int}. Firstly, it involves an investigation on the potential distributions across electrode/electrolyte interfaces. Then, the Helmholtz–Perrin layer (the H–P layer) and the Gouy–Chapman layer (the G–C layer) must be separated.

It is worth noting that C_{dl}^{app} of SOFC electrode/electrolyte interfaces are always much larger than those involving liquid electrolytes (Brett and Brett, 1994; Kisza, 2006). In addition, conventional capacitance models, *e.g.* the parallel-plate condenser model, predicate unrealistically small thicknesses of the double layer. Furthermore, they fail to account the changing capacitance behaviour of polarized SOFC interfaces. To address these problems, a case study was carried out on lanthanum strontium vanadate (LSV)/YSZ interfaces exposed in SOFC anodic environment. LSV is a conducting oxide and has great potential to be robust SOFC anodes (Ge and Chan, 2009b). In this study, C_{dl}^{app} was obtained from impedance spectroscopy and C_{dl}^{int} was evaluated via Stern's method. The numeric inconsistency between C_{dl}^{app} and C_{dl}^{int} was discussed.

$La_{0.8}Sr_{0.2}VO_x$ (LSV) powders were synthesized via a citric route with $La(NO_3)_3\ 6H_2O$ (Fluka, 99.0%), $Sr(NO_3)_2$ (Fluka, 99.0%), NH_4VO_3 (Sigma-Aldrich, 99.5%), and $C_6H_8O_7\ H_2O$ (Fluka, 99.5%) as starting materials. Mixed raw materials were dissolved in deionised water. The solution was then heated at 70 ℃ and under magnetic stirring. A dark blue gel was obtained after dissipating excess water. It was dehydrated overnight at 100 ℃ and carefully grounded in an agate mortar. The precursor was baked stepwise to 800 ℃ for 12 hours in order to match the particle size of YSZ (Tosoh). Anodic inks were formed by mixing LSV–YSZ powders (50:50 by weight) together with the ink vehicle (Fuel Cell Materials). Green anodes were fabricated by screen-printing the ink onto a 1-mm-thick YSZ disc. LSV–YSZ composite anodes were sintered at 1200 ℃ for 2 hours. LSV is of single phase after reduction in H_2 at 900 ℃ for 12 hours, as checked by X-ray powder diffraction (Shimadzu 6000, Cu Kα radiation). The geometric area of anodes was 0.46 cm^2. Pt paste was brush-painted on

the other side of YSZ and sintered at 900 ℃ for 30 minutes. The test rig configuration had been given in Ref. (Ge and Chan, 2009b). The operating temperature was 950 ℃. The H_2 flow rate was 100 sccm. The open circuit voltage of half cells was -1.18 V.

Half cells were polarized potentiostatically at desired anodic biases until the system became stable. The anodic biases selected in this study were 0, 20, 50, 70, 100, 120, and 150 mV. Impedance responses were recorded via a Solartron 1255B frequency response analyzer coupled to a 1470E electrochemical interface. The frequency range was 100,000–0.05 Hz. The sampling rate was 10 points/decade of frequency. For a given equivalent circuit, the complex nonlinear least squares (CNLS) fitting algorithm was used to fit in the complex impedance plane (Macdonald *et al.*, 1982). Impedance spectra were fitted via Zview® 3.2c. Under each given anodic bias, impedance spectra were collected in batches with a batch size of 10. The whole batch was discarded and re-recorded unless the Chi-squared (χ^2) of every fitting result is lower than 3×10^{-4}. In this study, impedance spectra of four samples prepared from the same batch, Samples A to D, were recorded.

Electrons in the LSV side of LSV/YSZ interfaces were assumed to be uniformly distributed and compactly aligned. Oxygen vacancies in the YSZ side followed Stern's picture: the H–P layer locating on the outer Helmholtz plane (oHp) and the G–C layer decaying continuously along the direction towards the bulk YSZ. The Volta potential difference across the LSV/YSZ interface was evaluated from its relationship with the electrochemical potential and the work function. The H–P layer was described by a parallel–plate condenser model. The G–C layer was depicted by a modified Poisson–Boltzmann theory (Appendix A).

4.3.1 Apparent double layer capacitance

Figure 4-12 shows typical impedance spectra of polarized LSV/YSZ interfaces at 950 ℃ and under H_2 atmosphere, comprising an inductive impedance arc at high frequencies and two severely depressed and overlapped capacitive impedance arcs at intermediate and low frequencies. The high-frequency impedance arc (high-*f* arc) is triggered by Pt lead wires. The intermediate-*f* arc, of great interest in this study, results from two concurrent phenomena: the double layer charging and the faradaic reaction.

The low-*f* arc is attributed to gas diffusion and conversion processes. (Primdahl and Mogensen, 1998) (Primdahl and Mogensen, 1999) All impedance spectra were fitted to a Voigt-type equivalent circuit $(R_i/L_i)R_s(R_1/CPE_1)(R_2/CPE_2)$ (MacDonald, 1987). In the equivalent circuit, (R_i/L_i), R_s, (R_1/CPE_1), and (R_2/CPE_2) represent the high-*f* arc, the lumped ohmic resistance, the intermediate-*f* arc, and the low-*f* arc, respectively. Impedance spectra collected under small applied anodic biases (E_{bias} < 150 mV) are highly reproducible (Fig. 4-12). Once the E_{bias} is larger than 150 mV, however, the low-*f* arcs become so unstable that they cannot be fitted satisfactorily. As indicated in Fig. 4-12, polarization resistance of the intermediate-*f* arc (R_1) ranges from 0.15 to 0.20 Ω cm^2 and is somewhat independent on E_{bias}. It implies that the interfacial reaction mechanism remains unchanged under these E_{bias}. In contrast, polarization resistance of the low-*f* arc (R_2) ranges from 0.4 to 0.9 Ω cm^2 and has a negative dependency on E_{bias}. Such behaviours are mostly due to the water effect in gas transport phenomena (Primdahl and Mogensen, 1998). Detailed discussions on the water effect of LSV–YSZ anodes have given in Section 3.1 and are beyond the scope of the present section (Ge and Chan, 2009a).

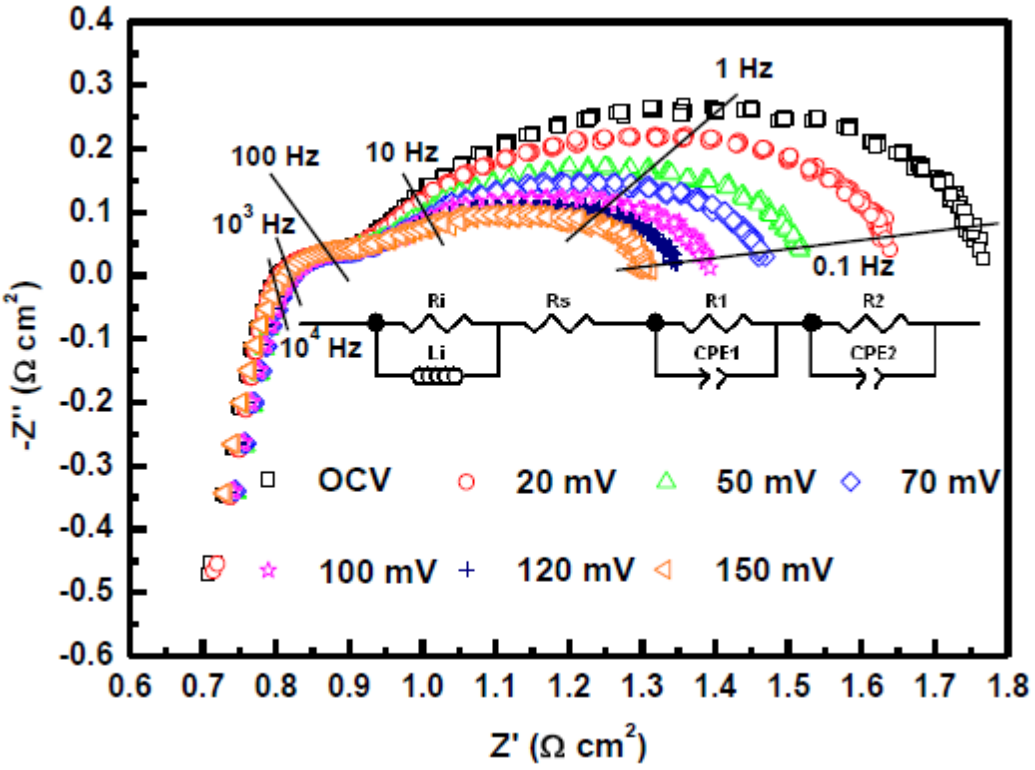

Figure 4-12 Nyquist plots of typical impedance responses of polarized LSV/YSZ interfaces. Ten impedance spectra are recorded at each potential bias. The inset shows the equivalent circuit used throughout this study.

The CNLS fitting results with unrestricted parameters indicate that n_1 of CPE_1 are approximately 0.60. For the sake of mechanistic consistency, all CNLS fitting procedures were therefore carried out with fixed n_1 of 0.60. C_{dl}^{app} can be expressed as

$$C_{dl}^{app} = \frac{\sqrt[n_1]{R_1 Q_1}}{R_1} \quad , \qquad \text{(Equation 4-13)}$$

by using Eq. 3 in Ref. (Hsu and Mansfeld, 2001), where Q is the CPE parameter together with n that define CPE ($Z_{CPE}=Q^{-1}(j\omega)^{-n}$). Figure 4-13 shows the fitting results of four samples produced from the same batch, among which sample A corresponds to the one shown in Fig. 4-12.

Figures 4-13a and 4-13b show R_1 and Q_{CPE1} as a function of E_{bias}, respectively. Figure 4-13c shows the corresponding C_{dl}^{app} that are converted according to Eq. 4-13. C_{dl}^{app} of LSV/YSZ interfaces, taking sample A as an example, are 171±13, 240±10, 218±11, 178±6, 172±8, 165±10, and 165±20 μF/cm^2 under E_{bias} of 0, 20, 50, 70, 100, 120, and 150 mV, respectively. These C_{dl}^{app} values of LSV/YSZ interfaces are in the same order of magnitude as those of metal(air)/YSZ interfaces (Hendriks *et al.*, 2002a; Robertson and Michaels, 1991), an order of magnitude higher than those of interfaces with aqueous (Brett and Brett, 1994) or supercritical organic electrolytes (Abbott and Harper, 1999), and two orders of magnitude higher than those of metal/non-aqueous electrolyte interfaces *e.g.* molten salts (Kisza, 2006), ionic liquids (Lockett *et al.*, 2010; Costa *et al.*, 2010), and organic electrolytes (Feng *et al.*, 2010). The occurrence of such large C_{dl}^{app} values is not thought to be experimental artefacts mainly from two reasons. Firstly, consistent results had been observed for all the four samples investigated in this study (samples A to D, Fig. 4-13). Secondly, such occurrence is not uncommon: many high temperature SOFC anodes also had been reported to exhibit large C_{dl}^{app} values (Holtappels *et al.*, 1999; Primdahl and Mogensen, 1997; Jiang and Badwal, 1999).

The pronounced feature of all $C_{dl}^{app} - E_{bias}$ curves is their right-skewed volcano (or called "capacitance surge") patterns. These bump-shaped patterns peak around E_{bias}=20 mV and gradually restore after E_{bias}=100 mV. Samples A to D exhibit similar

trends, albeit with different C_{dl}^{app} values (Fig. 4-13c). The poor reproducibility of C_{dl}^{app} is well-known for electrochemical systems involving solid electrolytes, *e.g.* silver halides (Armstron and Mason, 1973) and YSZ (Hendriks *et al.*, 2002b). As the curves in Fig. 4-3c are somewhat reproducible, these patterns are thought to own some intrinsic merits rather than merely experimental errors. C_{dl}^{app} had been reported to be positively dependent on E_{bias} in lithographically patterned (Bieberle *et al.*, 2001) and point-contact (Kek *et al.*, 2001) Ni/YSZ interface. The exact mechanism of the "capacitance surge" phenomenon is still under investigation. The possibilities of charging microstructure and electrode failure are excluded since the impedance spectra are reversible and reproducible. The results, nevertheless, imply that double-plate condenser models, predicting constant capacitance regardless of applied biases, are insufficient.

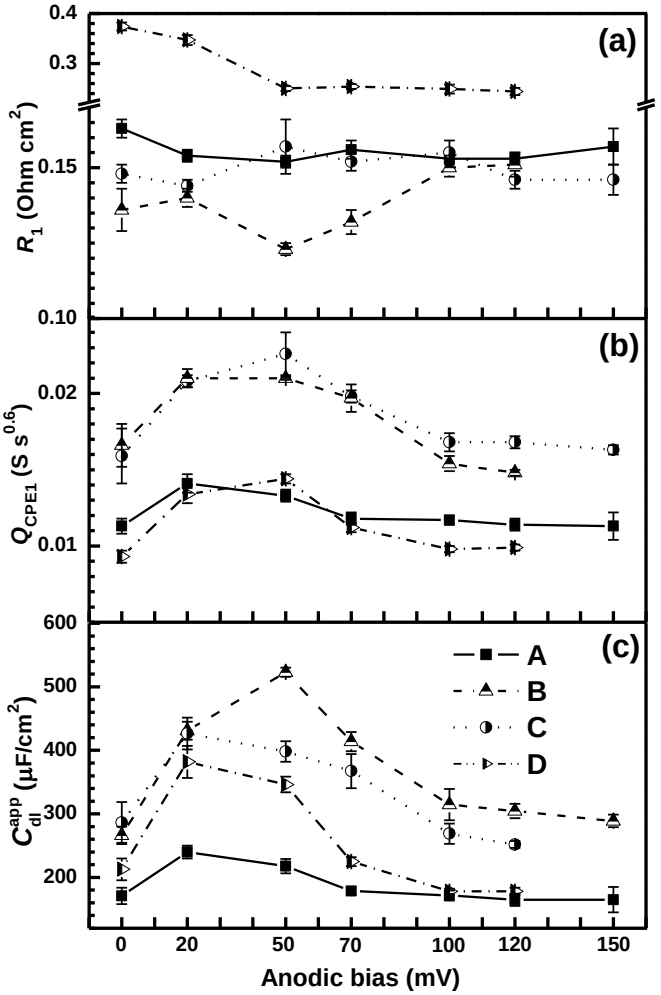

Figure 4-13 Equivalent circuit fitting results of (a) polarization resistance (R_1), (b) the CPE parameter (Q_{CPE1}), and (c) apparent double layer capacitance (C_{dl}^{app}) of the R_1/CPE_1 subset. Sample A (filled square, solid line) of the four samples (A to D) corresponds to the one in Figure 1. Each error bar is generated from 10 consecutive impedance spectra.

4.3.2 Analytical description of the Gouy–Chapman layer

The double layer of LSV/YSZ interfaces is formed by closely packed electrons on the LSV side and oxygen vacancies on the YSZ side. The oxygen vacancies can be further divided into two sub-layers: the compact H–P layer and the diffusive G–C layer (Fig. 4-14a). The Volta potential of LSV/YSZ interfaces ($\Psi_{\mathrm{YSZ}}^{\mathrm{LSV}}$) is the Volta potential difference between LSV and YSZ,

$$\Psi_{\mathrm{YSZ}}^{\mathrm{LSV}} = \Psi^{\mathrm{LSV}} - \Psi^{\mathrm{YSZ}}, \qquad \text{(Equation 4-14)}$$

where Ψ^{LSV} and Ψ^{YSZ} are the Volta potential in the LSV side and the YSZ side, respectively. All the terms in Eq. 4-15 are negative as the interface is exposed in anodic environment. Away from the interface, Ψ^{YSZ} increases linearly within the oHp and asymptotically approach zero from the oHp to the bulk YSZ (Fig. 4-14b). The portion of Ψ^{YSZ} in the G–C layer is denoted as Ψ_{G}. The spatial variation of Ψ_{G} fulfils a modified Poisson–Boltzmann equation,

$$\frac{\mathrm{d}^2\Psi}{\mathrm{d}z^2} = -\frac{4e_0 n_{V_O^{\cdot\cdot}}^0}{\varepsilon_{\mathrm{r,G}}\varepsilon_0}\sinh\left(\frac{e_0\Psi}{kT}\right)\exp\left(-\frac{e_0\Psi}{kT}\right), \qquad \text{(Equation 4-15)}$$

where z is the distance away from the LSV/YSZ interfaces, e_0 the elementary charge, ε_0 the vacuum permittivity, $\varepsilon_{\mathrm{r,G}}$ the relative static permittivity of YSZ in the G–C layer, $n_{V_O^{\cdot\cdot}}^0$ the free oxygen vacancy concentration of YSZ, k the Boltzmann's constant, and T the absolute temperature. Reduce Eq. 4-15 to first-order,

$$\left(\frac{\mathrm{d}\Psi}{\mathrm{d}z}\right) = \sqrt{\frac{2n_{V_O^{\cdot\cdot}}^0}{\varepsilon_{\mathrm{r,G}}\varepsilon_0}}\sqrt{kT\left[\exp\left(-\frac{2e_0\Psi}{kT}\right)-1\right]+2e_0\Psi} \quad . \qquad \text{(Equation 4-16)}$$

According to the Gauss's law of electrostatics the surface charge density in the G–C layer (σ_{G}) is given by

$$\sigma_{\mathrm{G}} = \sqrt{2\varepsilon_{\mathrm{r,G}}\varepsilon_0 n_{V_O^{\cdot\cdot}}^0}\sqrt{kT\left[\exp\left(-\frac{2e_0\Psi_{\mathrm{G}}}{kT}\right)-1\right]+2e_0\Psi_{\mathrm{G}}} \quad . \qquad \text{(Equation 4-17)}$$

Differentiating σ_{G} against Ψ gives the Gouy–Chapman capacitance (C_{G}),

$$C_{\mathrm{G}} = e_0\left[\exp\left(-\frac{2e_0\Psi_{\mathrm{G}}}{kT}\right)-1\right]\sqrt{\frac{2\varepsilon_{\mathrm{r,G}}\varepsilon_0 n^0_{V_O^{\cdot\cdot}}}{kT\left[\exp\left(-\frac{2e_0\Psi_{\mathrm{G}}}{kT}\right)-1\right]+2e_0\Psi_{\mathrm{G}}}}\quad . \qquad \text{(Equation 4-18)}$$

Mathematical derivations that lead to Eqs. 4-15 to 4-18 are given in Appendix A.

Figure 4-15 shows the relationship between C_{G} and Ψ_{G} with Eq. 4-18 solved numerically, by substituting reasonable values of $\varepsilon_{\mathrm{r,G}}$ and $n^0_{V_O^{\cdot\cdot}}$. C_{G} increases with the increasing absolute value of Ψ_{G}. In reality, the singularity shown in the inset of Fig. 4-15 never occurs because the Volta potential develops in any electrode/electrolyte interfaces. As a rough evaluation, C_{G} ranges from 300 to 700 μF/cm^2 in a typical Ψ_{G} range of most SOFC materials (*e.g.* 100 to 200 mV). Note that C_{G} is distinct to $C_{\mathrm{dl}}^{\mathrm{app}}$, though their numerical values seem similar. The occurrence of large values of C_{G} might be attributed to the solid structure of YSZ, which results in a more compact G–C layer than that in aqueous electrolytes.

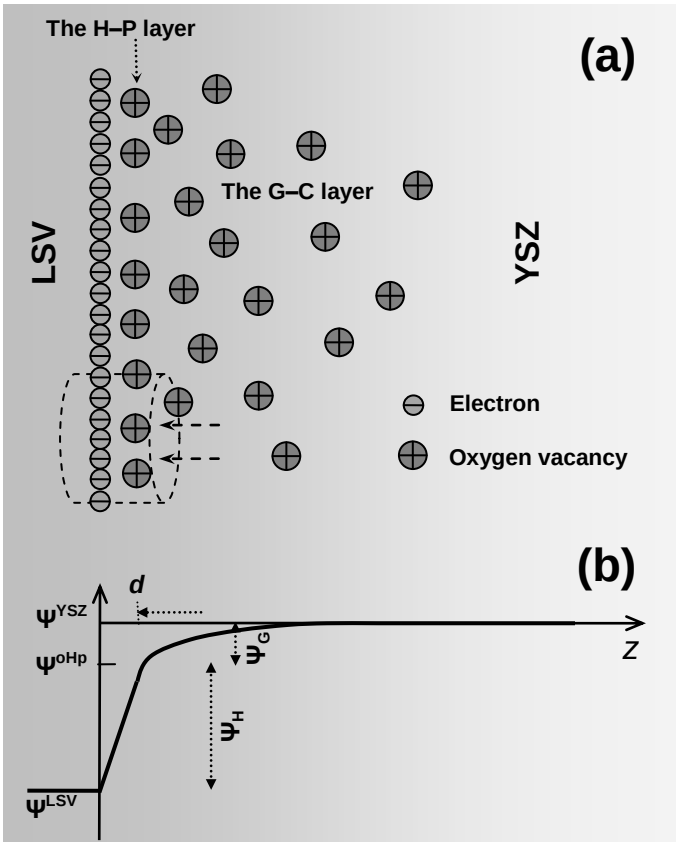

Figure 4-14 Schematic illustrations of the double layer developed across the LSV/YSZ interface: (a) microscopic structure; (b) the Volta potential distribution.

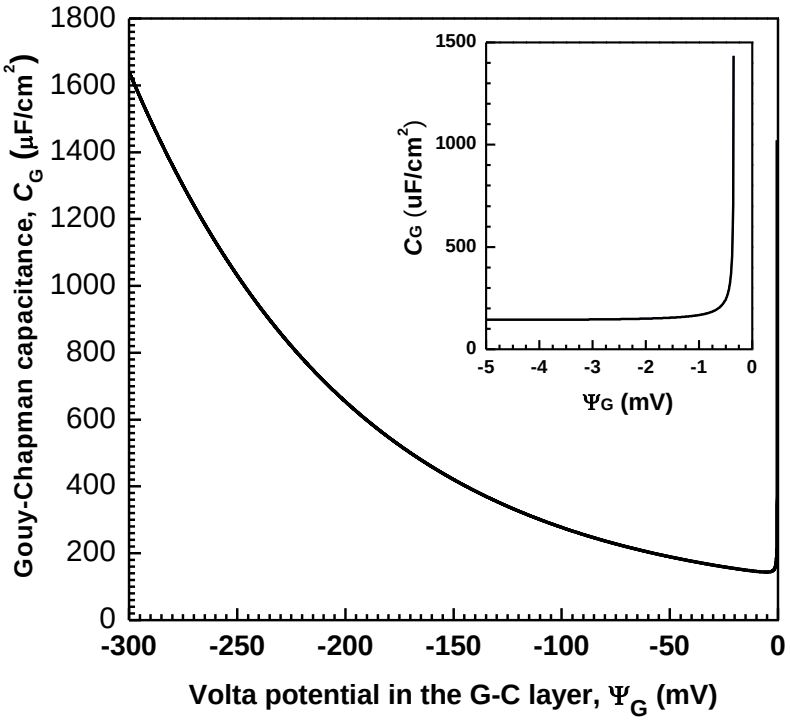

Figure 4-15 (a) Gouy–Chapman capacitance versus the Volta potential of the Gouy–Chapman layer. The inset shows the magnified figure near the zero potential, where the singularity occurs according to Eq. 4-16.

4.3.3 Interfacial variation of the Volta potential

Deterministic C_G values, however, are still unavailable from Eq. 4-18 unless Ψ_{YSZ}^{LSV} is known and Ψ_G is separated from the Volta potential in the H–P layer (Ψ_H). As shown in Fig. 4-14b, Ψ_{YSZ}^{LSV} comprises Ψ_G and Ψ_H,

$$\Psi_{YSZ}^{LSV} = \Psi_G + \Psi_H . \qquad \text{(Equation 4-19)}$$

The problem of determining Ψ_G therefore consists of two sub-problems: (*i*) how to obtain Ψ_{YSZ}^{LSV} under given polarized conditions and (*ii*) how to split Ψ_{YSZ}^{LSV} into Ψ_G and Ψ_H.

To obtain Ψ_{YSZ}^{LSV} under given polarized conditions (the problem *i*), first consider the LSV/YSZ interface under the OCV condition. As shown in the inset of Fig. 4-16a, Ψ_{YSZ}^{LSV} is related to the Galvani potential ϕ, the outer potential χ, the chemical potential μ, the electrochemical potential $\tilde{\mu}$ (*i.e.* the Fermi level E_F), and the work function Φ.

Detailed explanations are omitted here for simplicity. Interested readers are recommended with thorough works on metal/aqueous (Trasatti, 1974; Trasatti, 1982; Trasatti, 1990), semiconductors (Reiss, 1985; Reiss, 1988), metal/solid electrolyte (Riess, 1997; Riess and Vayenas, 2003), and ionic solid interfaces (Nowotny, 1997). In this work Ψ is expressed by $\tilde{\mu}$ and Φ, both of which are experimentally measurable (Schindler *et al.*, 1989; Tsiplakides *et al.*, 2007; Tsiplakides and Vayenas, 2001; Tsiplakides and Vayenas, 2002; Frantzis *et al.*, 2000; Nowotny *et al.*, 1989; Nowotny and Sloma, 1991). $\Psi_{\mathrm{YSZ}}^{\mathrm{LSV}}$ is thus given by

$$\Psi_{\mathrm{YSZ}}^{\mathrm{LSV}} = -\frac{\tilde{\mu}_{e,\mathrm{YSZ}}^{\mathrm{LSV}} + \Phi_{\mathrm{YSZ}}^{\mathrm{LSV}}}{e_0} \quad , \qquad \text{(Equation 4-20)}$$

where $\tilde{\mu}_{e,\mathrm{YSZ}}^{\mathrm{LSV}}$ and $\Phi_{\mathrm{YSZ}}^{\mathrm{LSV}}$ are the electrochemical potential difference and work function difference between LSV and YSZ across the LSV/YSZ interface, respectively. As the electrochemical state of the bulk YSZ is set as the reference state, Eq. 4-20 is simplified to

$$\Psi^{\mathrm{LSV}} = -\frac{\tilde{\mu}_{e,\mathrm{YSZ}}^{\mathrm{LSV}} + \Phi^{\mathrm{LSV}}}{e_0} \quad , \qquad \text{(Equation 4-21)}$$

For LSV–YSZ(H_2)|YSZ|Pt(air) half cells investigated in this study, $\tilde{\mu}_e^{\mathrm{LSV}}$ is experimentally given by

$$e_0 E_{\mathrm{emf}} = -\left(\tilde{\mu}_e^{\mathrm{LSV}} - \tilde{\mu}_e^{\mathrm{Pt}}\right) \quad , \qquad \text{(Equation 4-22)}$$

where E_{emf} is the electromotive force (Fig. 4-16a).

A brief literature survey was conducted on the electrochemical potential and the work function of YSZ, Pt, and LSV. The absolute potential of standard YSZ oxygen electrode was 5.07 ± 0.05 V at 400 ℃ and under oxygen partial pressure (p_{O_2}) of 1.2×10^{-2} bar (Riess and Vayenas, 2003; Tsiplakides and Vayenas, 2001; Tsiplakides and Vayenas, 2002; Vayenas, 2000; Vayenas *et al.*, 2001). A rudimentary evaluation considering atmospheric effect from the Nernst equation and temperature effect from Ref. (Riess and Vayenas, 2003) suggests $\tilde{\mu}_e^{\mathrm{YSZ}}$ =-5.23 eV at 950 ℃ and in air. $\tilde{\mu}_e^{\mathrm{Pt}}$ is

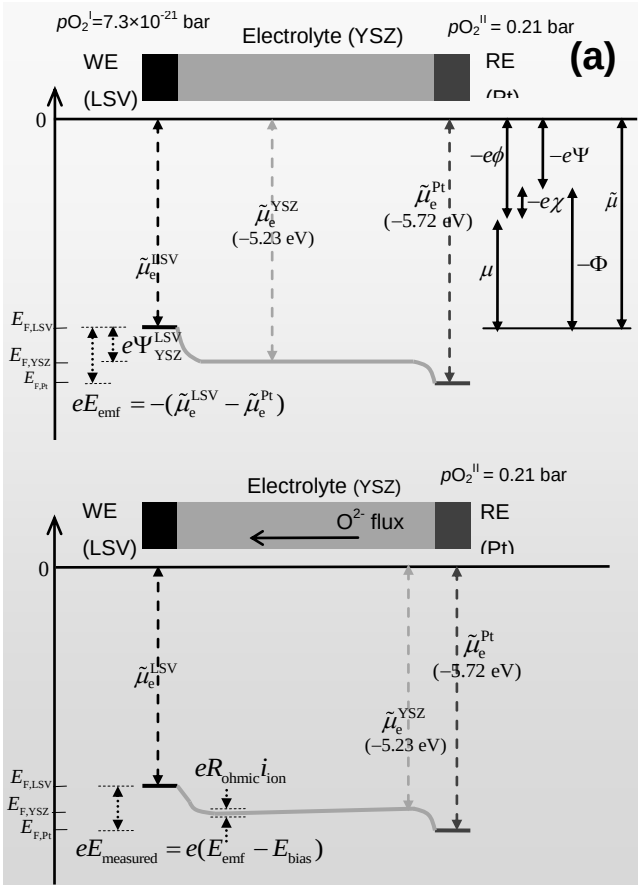

Figure 4-16 Schematic representations of the energy-level diagrams in LSV–YSZ(H_2)|YSZ|Pt(air) half cells under: (a) open circuit voltage, and (b) anodically polarized conditions. The right inset in (a) shows the correlations among ϕ, Ψ, χ, μ, $\tilde{\mu}$, E_F, and Φ. Note that all the interfacial variations are exaggerated merely for illustration purpose.

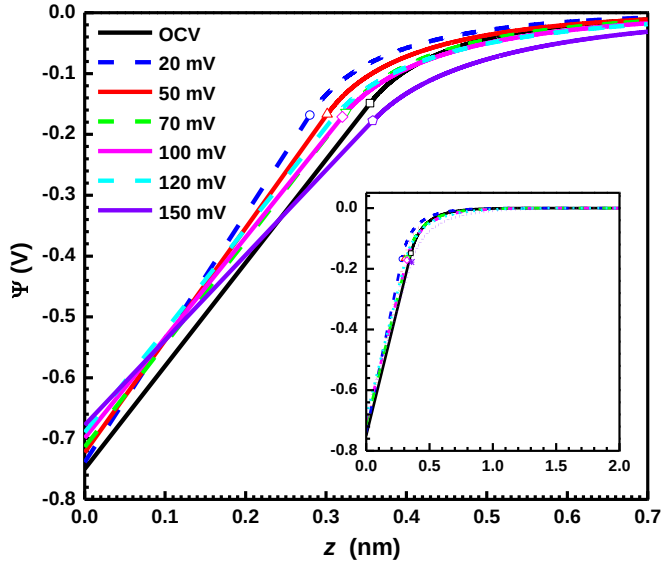

Figure 4-17 Spatial variations of the Volta potential across the polarized LSV/YSZ interfaces. Junctions between the Helmholtz–Perrin layer and the Gouy–Chapman layer are labelled by embedded symbols. The inset shows a holistic view of such curves from the interface to the bulk YSZ.

estimated to be -5.72 eV at 950 ℃ and in air, based on work function data of Pt (p_{O_2} =1.2×10^{-2} bar)|YSZ|Ag(p_{O_2} =1.2×10^{-2} bar) electrochemical cells (Tsiplakides and Vayenas, 2002; Tsiplakides and Vayenas, 2001), and temperature coefficients given in Ref. (Seely, 1941). Φ^{LSV} is evaluated to be 3.79 eV at 950 ℃ and in reducing environment, with temperature and atmospheric coefficients bought from Refs. (Kurtz and Henrich, 1983; Smith and Henrich, 1990; Egdell *et al.*, 1984). According to Eqs. 4-21 and 4-22, Ψ_{YSZ}^{LSV} under the OCV condition is thus found to be -0.75 V.

When half cells are polarized and subjected to non-negligible faradaic currents, $\tilde{\mu}$ throughout the bulk YSZ becomes no longer uniform (Fig. 4-16b). The measured potential difference (E_m) is given by

$$E_m = E_{emf} + E_{bias} = -\frac{\tilde{\mu}_e^{LSV} - \tilde{\mu}_e^{Pt}}{e_0} \quad . \qquad \text{(Equation 4-23)}$$

Note that in Eq. 4-23 E_m and E_{emf} are negative but E_{bias} is positive. Ψ_{YSZ}^{LSV} with non-negligible faradaic currents is thus given by

$$\Psi_{YSZ}^{LSV} = -\frac{\tilde{\mu}_{e,YSZ}^{LSV} + \Phi_{YSZ}^{LSV}}{e_0} + R_\Omega i_{ion} \quad , \qquad \text{(Equation 4-24)}$$

where R_Ω is the ohmic resistance and i_{ion} is the ionic current across the bulk YSZ ($i_{ion} \geq 0$). R_Ω and i_{ion} were obtained from impedance spectroscopy and potentiostatic polarization, respectively. Typical Ψ_{YSZ}^{LSV} values, taking sample A as an instance, are -0.750, -0.739, -0.723, -0.714, -0.699, -0.690, and -0.678 V, under E_{bias} of 0, 20, 50, 70, 100, 120, and 150 mV, respectively. It is worth to highlight that the exertion of E_{bias} on LSV/YSZ interfaces leads to reduced Ψ_{YSZ}^{LSV}, and consequently, the loosened double layer.

To split Ψ_{YSZ}^{LSV} into Ψ_G and Ψ_H (the problem *ii*), the microscopic structure of the H–P layer and the G–C layer must be analysed. In a simplified Monte Carlo simulation, the oxygen vacancies on the YSZ side of the LSV/YSZ interfaces is described as the evolving charged particles on *a priori* defined lattices. The Hamiltonian of canonical

ensemble comprises (*i*) the attraction between oxygen vacancies in YSZ and the electrons in LSV (*ii*) the repulsion among nearest neighbouring oxygen vacancies in YSZ. The jump frequencies and acceptance rules are based on the Metropolis algorithm (Shonkwiler and Mendivil, 2009). The Monte Carlo simulation results indicated that the Volta potential portion of the H–P layer over the whole double layer ($\Psi_H / \Psi_{YSZ}^{LSV}$) were 0.80±0.01, 0.77±0.01, 0.77±0.02, 0.77±0.01, 0.76±0.02, 0.74±0.01, and 0.74±0.01, under E_{bias} of 0, 20, 50, 70, 100, 120, and 150 mV, respectively. Note that the Volta potential portion of the G–C layer over the whole double layer ($\Psi_G / \Psi_{YSZ}^{LSV}$) is complementary to $\Psi_H / \Psi_{YSZ}^{LSV}$.

Finally, the spatial variation of Ψ_G can be obtained by solving Eq. 4 numerically, after both the two problems *i* and *ii* answered. On the other hand, the spatial variation of Ψ_H is linear because the H–P layer has been modelled as a double-plate capacitor. Figure 4-17 shows the spatial variations of Ψ_{YSZ}^{LSV} of polarized LSV/YSZ interfaces by utilizing the continuous and derivable boundary conditions near Ψ^{oHp} (Appendix A, Eqs. A10–1 and A10–2). The $\Psi_{YSZ}^{LSV} - z$ curves of various polarized LSV/YSZ interfaces exhibit similar patterns: a linear increase that accounts for about 70–80% of Ψ_{YSZ}^{LSV} and an asymptotical increase to zero potential. A structural relaxation of the double layer is evident when the LSV/YSZ interfaces are subjected to increasing E_{bias} (Fig. 4-17).

4.3.4 Intrinsic double layer capacitance

Every $\Psi_{YSZ}^{LSV} - z$ curve in Fig. 4-17 incorporates a separator between the H–P layer and the G–C layer. The separators are obtained after solving Eq. 4-16 with initial and boundary conditions from Eq. A10. Thicknesses of the H–P layer (d_H) of polarized LSV/YSZ interfaces are thus known as 0.355±0.003, 0.280±0.003, 0.302±0.006, 0.325±0.003, 0.320±0.008, 0.306±0.005, 0.358±0.003 nm, under E_{bias} of 0, 20, 50, 70, 100, 120, and 150 mV, respectively. These d_H values are equivalent to 2.0–2.6 times of the ionic radius of oxygen ions in YSZ ($r_{O^{2-}}$) (Shannon, 1976). If the cut-off where the double layer ceases is 100 μV, thicknesses of the G–C layer (d_G) are 1.10, 1.23, 1.26, 1.32, 1.48, 1.64, and 1.88 nm, respectively (Table 4-1). In other words, typical values of d_H and d_G are equivalent to 1.1–1.4 and 5.7–8.7 times of the lattice spacing of (400) planes of YSZ (PDF #30–1468), respectively. The double layer thickness, *i.e.* d_H+d_G,

increases monotonically with E_{bias}. Under an E_{bias} of 150 mV, d_H+d_G is almost 50% larger than that under the OCV condition. It is surprising to note that the double layer has such a compact structure and it is significantly sensitive to external stimuli.

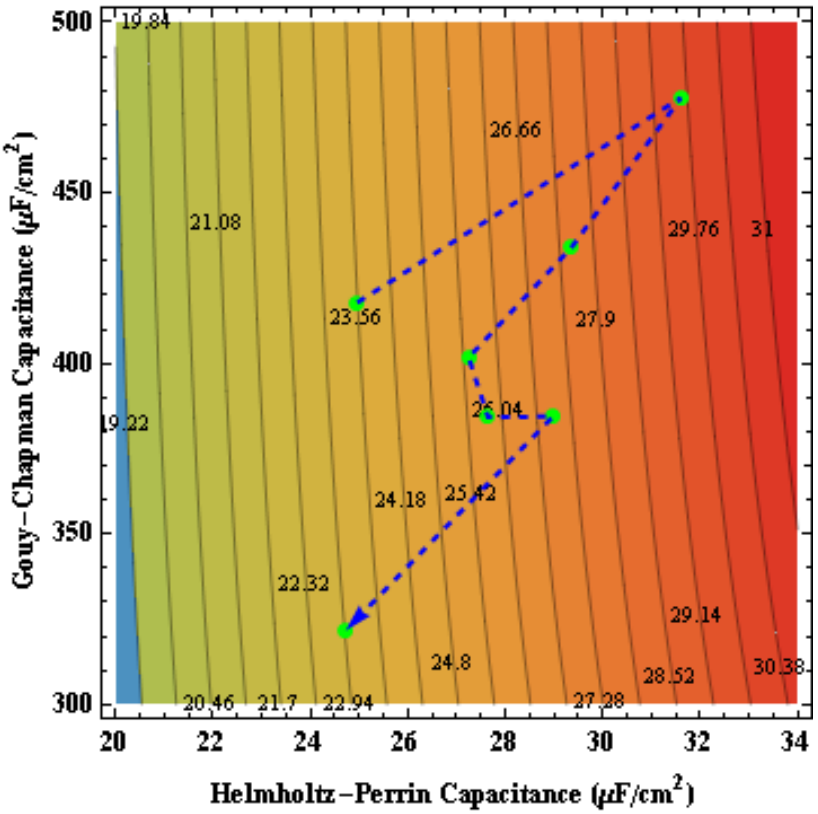

Figure 4-18 Contour plots of intrinsic double layer capacitance comprising the Helmholtz–Perrin capacitance and the Gouy–Chapman capacitance. Along the direction of the arrow, the embedded points consecutively represent the intrinsic double layer capacitance of the LSV/YSZ interfaces under anodic biases of 0, 20, 50, 70, 100, 120, and 150 mV, as shown in Table 1. The dashed line is merely a trend line.

The intrinsic double layer capacitance (C_{dl}^{int}) consists of C_H and C_G connected in series (Stern, 1924),

$$\frac{1}{C_{dl}^{int}} = \frac{1}{C_H} + \frac{1}{C_G} \quad . \qquad \text{(Equation 4-25)}$$

C_G is potential dependent and has been given in Eq. 4-18. In contrast, C_H is potential independent and is routinely expressed as (Helmholtz, 1853)

$$C_H = \frac{\varepsilon_{r,H}\varepsilon_0}{d_H} \quad , \qquad \text{(Equation 4-26)}$$

where $\varepsilon_{r,H}$ is the relative static permittivity of YSZ in the H–P layer. For LSV/YSZ interfaces subjected to 0, 20, 50, 70, 100, 120, and 150 mV, C_H are 24.9, 31.6, 29.3, 27.2, 27.6, 28.9, and 24.7 μF/cm^2, respectively (Eq. 4-16); C_G are 417.8, 477.8, 433.9, 401.7, 384.3, 384.4, and 321.6 μF/cm^2, respectively (Eq. 4-18); and finally C_{dl}^{int} are 23.5, 29.6, 27.4, 25.5, 25.7, 26.9, 22.9 μF/cm^2, respectively (Eq. 4-25, inset of Fig. 4-18). Figure 4-18 shows contour plots of C_{dl}^{int} as functions of C_H and C_G, indicating the dominant role of C_H on C_{dl}^{int}. The relative difference between C_H and C_{dl}^{int}, defined as $(C_H - C_{dl}^{int})/C_{dl}^{int}$, is less than 8%. The whole rationale should still be adopted whenever C_H is used as the estimator of C_{dl}^{int}. The reason is that d_H heavily depends on the Volta potential difference and the thickness of the double layer. Table 4-1 summarizes the parameters, *i.e.* the Volta potential, thickness, and capacitance, which describe the H–P layer, the G–C layer, and the double layer of polarized LSV/YSZ interfaces.

Table 4-1 Listing of parameters pertinent to the double layer of LSV/YSZ interfaces in LSV–YSZ(H_2)|YSZ|Pt(air) half cells at 950 ℃.

Applied anodic biases (mV)	The compact layer			The diffusive layer		The double layer	
	Volta potential portion $\Psi_H / \Psi_{YSZ}^{LSV}$ (mV/mV)	Thickness d (nm)	Helmholtz–Perrin capacitance C_H (μF/cm^2)	Thickness d (nm)	Gouy–Chapman capacitance C_G (μF/cm^2)	Intrinsic double layer capacitance C_{dl}^{int} (μF/cm^2)	Apparent double layer capacitance C_{dl}^{app} (μF/cm^2)
0	0.802±0.006	0.3547±0.028	24.9	1.10	417.8	23.5	170.9±12.8
20	0.772±0.008	0.2802±0.029	31.6	1.23	477.8	29.6	240.0±10.0
50	0.769±0.015	0.3016±0.059	29.3	1.26	433.9	27.4	217.7±11.2
70	0.771±0.007	0.3250±0.028	27.2	1.32	401.7	25.5	178.5±5.6
100	0.755±0.020	0.3203±0.084	27.6	1.48	384.3	25.7	171.6±7.8
120	0.741±0.013	0.3056±0.054	28.9	1.64	384.4	26.9	164.8±9.8
150	0.737±0.006	0.3583±0.032	24.7	1.88	321.6	22.9	165.0±20.1

4.3.5 Double layer capacitance: apparent versus intrinsic

The $C_{dl}^{app} - E_{bias}$ curves show a right-skewed volcano pattern that peaks around 20–50 mV (Fig. 4-13c). Surprisingly, the $C_{dl}^{int} - E_{bias}$ curves also exhibit a "capacitance surge" at small E_{bias} (Fig. 4-18). It is of great interest to note that the theoretical approaches have satisfactorily depicted the changing double layer capacitance behaviours of polarized LSV/YSZ interfaces. Generally speaking, the "capacitance surge" phenomenon results from the Volta potential variations and the changing double layer structure. When half cells are subjected to a small E_{bias}, oxygen vacancies once trapped at oHp become relaxed and permeate towards the bulk YSZ. The LSV/YSZ interfaces therefore undergo a minute decrease of Ψ_{YSZ}^{LSV} and accordingly a slight relaxation of the double layer. These effects lead to an expansion of the G–C layer and an increase of $\Psi_G / \Psi_{YSZ}^{LSV}$. Note that the increase of $\Psi_G / \Psi_{YSZ}^{LSV}$ counteracts the decrease of Ψ_{YSZ}^{LSV} that leads to it. In other words, it competes with the loosened H–P layer that is resulted from the dwindling coulombic attractions. These two counterbalancing effects results in a local maximum in C_{dl}–E_{bias} curves. The exact position of the local maximum, however, is currently unknown due to insufficient data explored in this study. To locate the local maximum, sophisticated materials characterization techniques that measure the surface states (and therefore, the Volta potentials) of on-running SOFCs must be involved. It is of great interest to note that *in situ* ambient-pressure X-ray photoelectron spectroscopy (APXPS) has been adopted recently, which successfully measures the surface states in ceria/YSZ/Pt single chamber cells under H_2–H_2O atmosphere and at 750 ℃ (DeCaluwe *et al.*, 2010; Zhang *et al.*, 2010a). The rationale of the Volta potential analysis could be tested and verified, if APXPS is employed to obtain the electrochemical states of electrode/solid-electrolyte interfaces.

Notwithstanding similar E_{bias} effects on C_{dl}^{app} and C_{dl}^{int}, C_{dl}^{app} are basically one order of magnitude larger than C_{dl}^{int} (Table 4-1). This discrepancy roots in the inconsistent surface areas that are used in the two approaches: C_{dl}^{app} adopts the geometric area (A_{geo}) but C_{dl}^{int} embraces the real area (A_{real}). The relationship between C_{dl}^{app} and C_{dl}^{int} can be simply connected by

$$C_{dl}^{app} = k\ C_{dl}^{int} = \frac{A_{real}}{A_{geo}} C_{dl}^{int} \quad , \qquad \text{(Equation 4-27)}$$

where k is the area normalizing factor. Typical k values, take sample A as an example, are 7.3 ± 0.5, 8.1 ± 0.4, 7.9 ± 0.4, 7.0 ± 0.2, 6.7 ± 0.3, 6.1 ± 0.4, 7.2 ± 0.9, under E_{bias} of 0, 20, 50, 70, 100, 120, and 150 mV, respectively. It is surprisingly to find that A_{real} is about 6–8 times of A_{geo}, at least for the case of LSV–YSZ composite anode exposed in H_2 at 950 ℃. Historically, models pertinent to A_{real} rely on assumptions about charge transfer and electrode microstructure, involving parameters that are notoriously difficult to determine and verify. A_{real} represents the area where electrochemical fuel cell reactions take place. These reactions occur only at three phase boundaries (TPBs) where gas (fuel or oxygen), electrode (anode or cathode), and electrolyte meet. If a composite electrode is used, as the case of LSV–YSZ anode, only the TPBs that are not far away from the anode–electrolyte interface contribute to the reactions. An active layer therefore exists and the remainder of the composite electrode merely functions as current collector and gas diffusion layer. Apparently, A_{real} is composed of the TPBs within the active layer. In other words, *in situ* detection and monitoring of A_{real} become feasible by merely recording the impedance responses of on-running SOFCs and utilizing the apparent and intrinsic double layer capacitance analysis, even without *a priori* knowledge on the electrode microstructure and the conductivity of electrode and electrolyte materials.

This work describes a combined experimental and modelling study of the electrochemical characteristics associated with the double layer in high temperature SOFCs via a case study on LSV/YSZ interfaces. Impedance responses of electrode/solid-electrolyte interfaces are recorded. C_{dl}^{app} is obtained by appropriate fitting processes to the impedance spectra. To fully understand the capacitive behaviour of the interfaces, modelling works decouple contributions from the two different regions of the double layer— the tightly bound H–P layer and the more diffuse G–C layer. As a result of the modelling efforts, C_{dl}^{app} is found to be around 1 order of magnitude higher than C_{dl}^{int} that the models predict. This difference is ascribed to differences between the anode's electrochemically active area and the anode's two-dimensional geometric footprint. To fully generalize this rationale, the double

layer of SOFCs operated under various fuel atmospheres and lower operating temperatures needs to be addressed. The fuel atmosphere exerts pronounced influences on the impedance responses and the C_{dl}^{app} consequently obtained from impedance spectra. The fuel composition effect had been widely observed in, *e.g.* Ni cermet anodes with H_2–H_2O atmosphere (Jiang and Badwal, 1999; Matsui *et al.*, 2007; Kim *et al.*, 2009) and LSV–YSZ anodes with H_2–H_2O–He atmosphere (Ge and Chan, 2009a). Fundamentally, the change of fuel atmosphere alters χ, Φ, and $\tilde{\mu}$ of the electrocatalysts. The variation of $\tilde{\mu}$ can be easily measured for SOFCs in half cell configurations, provided that the electrochemical states of the reference electrode are readily known. In contrast, detecting the variations of χ and Φ of SOFC components is challenging because of the high operating temperatures, fuel atmospheres, and the difficulty of attaching probes across each component. χ and Φ could possibly be measured by *in situ* APXPS (Zhang *et al.*, 2010a; DeCaluwe *et al.*, 2010). As the alternation of surface states due to the change of fuel atmosphere varies from case to case, no general rules about the fuel composition effect on C_{dl}^{int} can be drawn.

The decrease of operating temperature would result in sluggish electrochemical fuel cell reactions. As reflected in impedance spectra, the impedance arc pertinent to electrochemical reactions is enlarged and the time constant of the arc increases. The C_{dl}^{app} of anode/electrolyte interfaces at low temperatures should thus be smaller than those at high temperatures. This trend has been observed in Ni–YSZ cermet anodes (Holtappels *et al.*, 1999), and had also been reported in point-contact metal (Ni, Pt, Au)/ 9 mol% yttria-doped zirconia single crystal interfaces (Bieberle *et al.*, 2001). This effect, however, might not be obvious for electrodes with low thermal activation energy and complex electrode architecture. To determine C_G and C_H at low temperatures, the temperature effects of $\varepsilon_{r,G}$, $\varepsilon_{r,H}$, $n^0_{V_O^{\cdot\cdot}}$, Ψ, Ψ_G/Ψ, Φ, and $\tilde{\mu}$ must be known, as indicated in Eqs. 4-18 to 4-26. Take the LSV/YSZ interfaces under the OCV condition as an example. The change of Φ_{YSZ}^{LSV} might be insignificant for operating temperatures down to 800 ℃, mainly because of the small temperature dependency of Φ (Langmuir, 1936; Potter, 1940; Smith, 1949). $\tilde{\mu}_e^{LSV}$ is experimentally measurable according to Eq.10, where E_{emf} fulfils the Nernst equation. The Nernst equation predicts increased OCVs at

lower temperatures. To summarize and according to Eqs. 4-20 to 4-22, Ψ_{YSZ}^{LSV} is somewhat increased if SOFC operating temperatures are decreased. The G–C layer has also been enlarged because of less oxygen vacancies in YSZ are freely mobile at lower temperatures, resulting in the increase of Ψ_G/Ψ (in other words, the decrease of Ψ_H/Ψ). Therefore, Ψ_G definitely becomes larger due to the increases of Ψ_{YSZ}^{LSV} and Ψ_G/Ψ. In contrast to Ψ_G, the changing behaviour of Ψ_H is unable to be predicated unambiguously, noting that Ψ_{YSZ}^{LSV} has been increased but Ψ_H/Ψ has been decreased. It should bear in mind that C_{dl}^{int}, as indicated in Table 4-1 and Fig. 4-18, is controlled by the property of the H–P layer. Therefore, the behaviour of C_{dl}^{int} at low temperatures is difficult to predict due to the uncertainty of Ψ_H. The complete capacitance and Volta potential analyses, as proposed in Section 3.2 to 3.5, should be adopted to resolve this ambiguity.

4.3.6 Brief summary

The double layer capacitance of solid electrode/solid-electrolyte interfaces was investigated via a case study on LSV/YSZ interfaces in SOFC anodic environment. The magnitude of apparent double layer capacitance was of several hundreds of $\mu F/cm^2$. Under anodic polarized conditions, it exhibited a right-skewed volcano pattern that peaks around 20 to 50 mV. The intrinsic double layer capacitance exhibited similar "capacitance surge" behaviour. The phenomenon was ascribed to mutual competitions between the loosened H–P layer and the increase of Volta potential in the G–C layer. The numeric values of intrinsic double layer capacitance were, however, almost one order of magnitude lower than the apparent. Such kind of discrepancy was ascribed to the inconsistent areas that were used in the two cases. The capacitance analysis enables *in situ* detection of active areas and TPBs of composite electrode–electrolyte interfaces in various solid state electrochemical systems.

4.4 Three phase boundaries and electrochemically active zones in solid oxide fuel cell anode/electrolyte interfaces

Solid oxide fuel cells (SOFCs) are highly efficient energy conversion devices with advantages of fuel flexibility and long-term stability. Electrochemical fuel cell reactions in SOFC electrodes take place around three phase boundaries (TPBs), where

gas, electrode, and electrolyte meet. Numerous analytical (Costamagna *et al.*, 1998; Chan and Xia, 2001), numerical (Abbaspour *et al.*, 2010; Martinez and Brouwer, 2008), and experimental (Wilson *et al.*, 2006; Shearing *et al.*, 2010) works on TPBs had been reported. Avoiding the structural complexity of porous and composite electrodes, some characteristics of TPBs have been obtained from unitary, dense, and two-dimensionally patterned electrodes (Bieberle and Gauckler, 2000; Mizusaki *et al.*, 1994). The microstructure and TPBs of composite electrodes had been reported to be quantified by stereological measurements (Zhao *et al.*, 2001). In the case of composite electrodes, only those TPBs adjacent to the electrode/electrolyte interface contribute to electrochemical reactions. An active electrode layer therefore exists (Fukunaga *et al.*, 2007; Sakamoto *et al.*, 1996; Abudula *et al.*, 1996; Nakamura *et al.*, 2008; Menzler and Haanappel, 2010). The remainder above the active electrode layer merely functions as current collectors and gas diffusion layers. When SOFCs are subjected to external loads (i.e. in polarized conditions), this scenario becomes more complicated because the active TPBs fluctuate in accordance with the applied stimulus. Meanwhile, studying solid electrode/solid electrolyte interfaces by in situ techniques is difficult because of these systems' opaque and sealed geometries. Several in situ techniques on SOFCs have been developed recently (Pomfret *et al.*, 2010; DeCaluwe *et al.*, 2010). These in situ techniques are, however, constrained to the characterization on materials' surface states. Any fuel cell reaction paths beneath the sintered electrode/electrolyte interfaces are still difficult to be detected.

TPBs instead of electrochemically active zones (EAZs) have long been attributed to the places where fuel cell reactions occur. This argument appears especially plausible for composite electrodes comprising purely ionic and electronic components. Generally speaking, three-dimensional EAZs are generated by the out-of-plane extensions of the corresponding one-dimensional TPB lines. The extent of such extensions depends on the materials properties of electrodes and electrolytes, gas atmosphere, operating temperature, external loads, etc. Electrochemical reactions thus take place in three-dimensional EAZs beyond one-dimensional TPBs. The cross-sections of EAZs, to some extent, represent the interfaces where the electrochemical double layer develops. Surprisingly, the correlation between TPBs and EAZs has hitherto been poorly known.

This work is dedicated to investigate the relationship between TPBs and EAZs, by

employing the electrode microstructural modelling and the apparent and intrinsic double layer capacitance analysis. The TPBs of composite anodes are obtained from the microstructure models of virtually sintered packing beds. On the other hand, the capacitance analysis provides the real reaction areas of on-running SOFCs (Ge *et al.*, 2011), which are regarded as the cross-section areas of EAZs. To fully demonstrate the rationale, a case study was carried out on half-cells with lanthanum strontium vanadate (LSV)–yttria-stabilized zirconia (YSZ) as composite anode and YSZ as electrolyte. LSV is a conducting oxide and has great potential to be robust SOFC anodes (Ge and Chan, 2009b). The rationale is thought to be suitable for various parametric analyses on TPBs and EAZs, though only the electrical potential effect has been discussed herein.

4.4.1 Materials and characterization

$La_{0.8}Sr_{0.2}VO_x$ (LSV) powders were synthesized via a citric route as described in Section 4.3. The sample preparation and half cell testing procedures had been given in Ref. (Ge and Chan, 2009b) and are omitted for simplicity. To prepare samples for particle size measurement, firstly the powders were ultrasonically dispersed in isopropanol. The suspension was then dripped onto clean Si wafer and dried in air. Hundreds of particles were counted from scanning electron microscopy (SEM, JEOL JSM-6340F) images. The particle sizes are fitted to a normal distribution function. The mean of the normal distribution function is used as the mean particle size of the corresponding particles. A home-built Mathematica® 7 code interpreted SEM surface morphology images of sintered LSV–YSZ anodes and provided the two-dimensional porosity. A standard calibration sample with large surface area, known electrode thickness and composition, was used to convert the two-dimensional porosity into three-dimensional porosity. The anode thickness was obtained from the cross-section profiles via SEM.

The LSV–YSZ green anode was described analytically as a binary random loose particle aggregate. The packing bed was constructed geometrically based on a set of experimental inputs, consisting of particle size, particle size ratio, powder composition, and packing density. The particles were supposed to be distributed in the packing bed homogeneously and statistically. The coordination numbers of particles in the packing bed were analyzed on the basis of geometric arguments. Finally, the green packing bed was sintered according to a particle-to-plate sintering model.

4.4.2 Virtual packing

Table 4-2 lists the parameters describing the LSV–YSZ composite anode, comprising electrode thickness, electrode composition, electrode porosity, particle size, and particle density. These parameters serve as the initial inputs in establishing the packing bed. The particle size distributions of LSV and YSZ are shown in the Figs. 4-19 and 4-20, respectively. The LSV and YSZ powders have similar particle sizes and both of them exhibit the normal distribution behaviour. Note that the spread of particle sizes are not considered in this simplified packing model. Figure 4-21 shows the cross-section profile of the LSV–YSZ/YSZ interface, from which the anode layer thickness is readily known. The mass loss due to the reduction of LSV provides a precise way of determining the composition of LSV–YSZ anode. The two-dimensional packing density (η_{2D}) is calculated from surface morphology images as those shown in Fig. 4-22. η_{2D} is converted to the three-dimensional packing density (η_{3D}) because practical SOFC anodes are three-dimensional. A linear relationship is assumed to exist between η_{3D} and η_{2D},

$$\eta_{3D} = k_{2D\rightarrow 3D}\eta_{2D} \quad , \qquad \text{(Equation 4-28)}$$

where $k_{2D\rightarrow 3D}$ is the packing density coefficient. $k_{2D\rightarrow 3D}$ was obtained from a calibration sample with deliberated large surface area. It is worth to mention that the exact microstructure beneath the electrode surface is poorly known. η_{3D}, which is determined by simply measuring the weight and dimensions, could have slightly overestimated the open porosity of the electrodes. The η_{3D} given in Table 4-2 was averaged from five samples produced from the same batch with the one shown in Fig. 4-22.

Table 4-2 Listing of characteristic parameters of the LSV–YSZ composite anode.

Parameters	Values
Anode layer thickness, h	23.0 μm
Particle size of LSV, d_{LSV}	0.23 ± 0.04 μm
Particle size of YSZ, d_{YSZ}	0.27 ± 0.05 μm
Density of reduced LSV, ρ_{LSV}	6.606 g/cm^3
Density of YSZ, ρ_{YSZ}	5.942 g/cm^3
Geometric surface area of LSV–YSZ composite anodes, A_{geo}	0.46 cm^2
Two-dimensional packing density, η_{2D}	0.79 ± 0.03 cm^2/cm^2
Packing density coefficient, $k_{2D\rightarrow 3D}$	0.67
Three-dimensional packing density, η_{3D}	0.53 cm^3/cm^3
Volume fraction of LSV (void exclusive), f^V_{LSV}	0.42 cm^3/cm^3
Number fraction of LSV (void exclusive), f^n_{LSV}	0.54 particles/particles
Area fraction of LSV (void exclusive), f^A_{LSV}	0.46 cm^2/cm^2

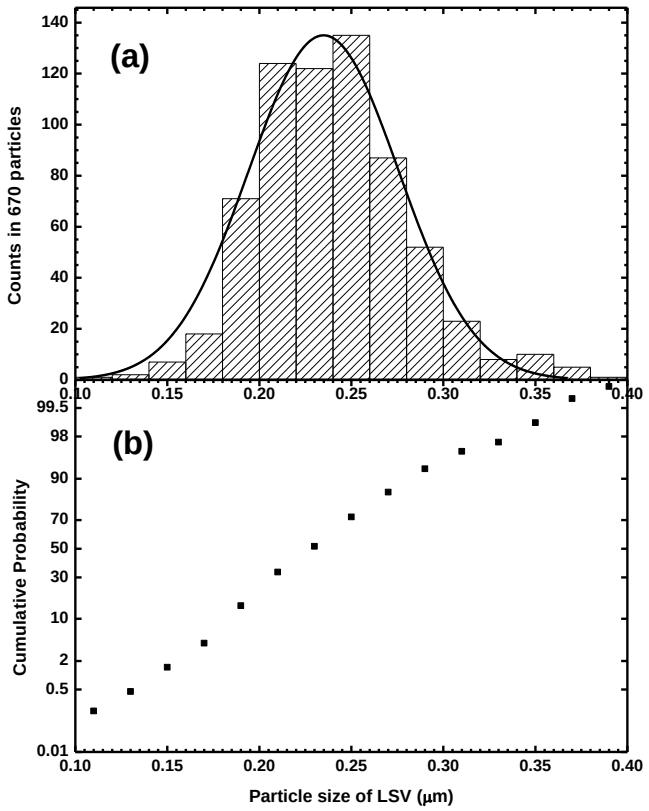

Figure 4-19 (a) Particle size distribution and (b) cumulative probability of LSV particles.

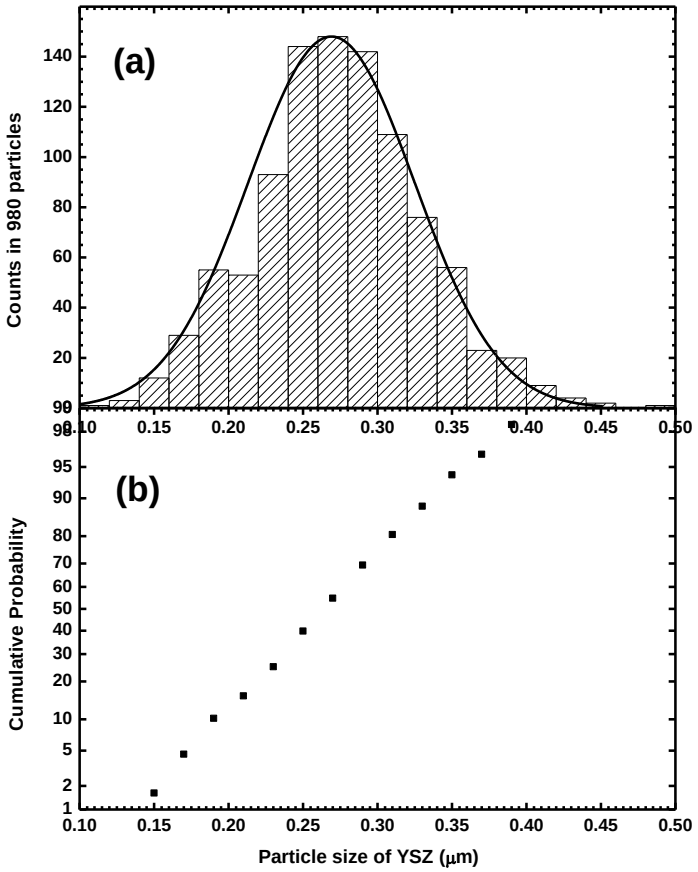

Figure 4-20 (a) Particle size distribution and (b) cumulative probability of YSZ particles.

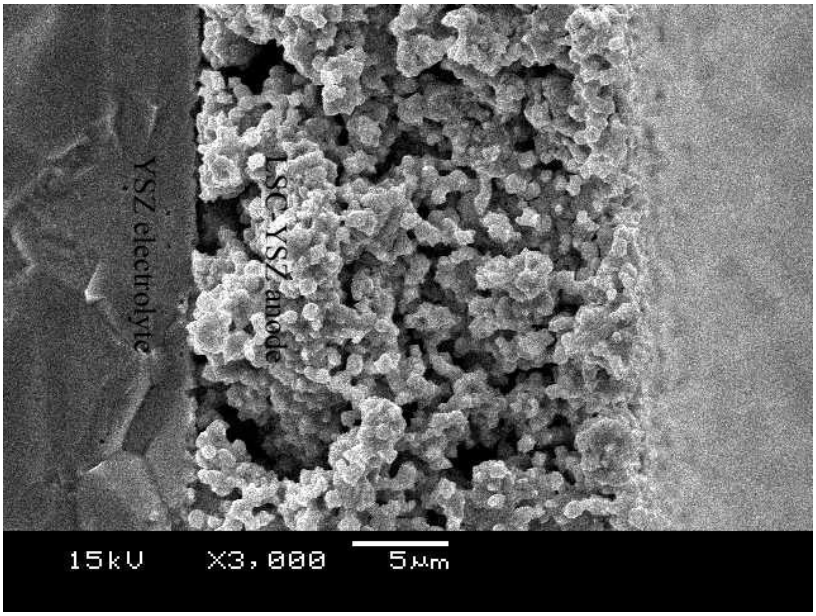

Figure 4-21 SEM image of the cross-section profile of a LSV–YSZ composite anode sintered onto YSZ electrolyte. The apparent poor adhesion may be incurred during the preparation of the fractured sample.

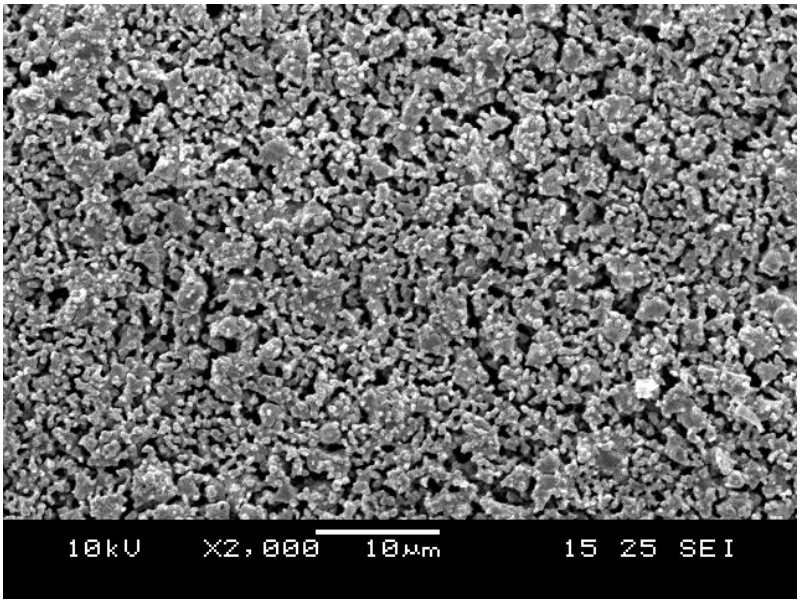

Figure 4-22 SEM surface morphology image of an as-reduced LSV–YSZ composite anode. The sporadic black regions represent voids while the others symbolize particle aggregates. The two-dimensional packing density of this anode is 0.78 cm^2/cm^2. The corresponding three-dimensional packing density, obtained from the image analyses by implementing home-build Mathematica® 7 codes, is 0.52 cm^3/cm^3.

Among various packing modes the random loose packing seems most relevant (Jaeger and Nagel, 1992), as the void fraction (ε=1-η_{3D}) of LSV–YSZ anodes is as high as 0.47 (Table 4-2). It considers how many randomized LSV and YSZ particles can be accommodated, i.e. coordination numbers, around a specific particle. The coordination numbers of a reference particle rely on the relative particle size (r_p) and the area fraction (f^A) in packing beds (Suzuki and Oshima, 1983). Without loss of generality, take LSV as the reference particle. The total coordination numbers of a LSV reference particle (N^b_{LSV}) is the sum of that in contact with LSV particles ($N^b_{LSV,LSV}$) and that in contact with YSZ particles ($N^b_{LSV,YSZ}$),

$$N^b_{LSV} = N^b_{LSV,LSV} + N^b_{LSV,YSZ} \quad . \qquad \text{(Equation 4-29)}$$

In Eq. 4-29, $N^b_{LSV,LSV}$ is given by coordination numbers in the corresponding monosized LSV packing bed ($N^m_{LSV,LSV}$, or simply N^m) weighted by the area fraction of LSV (f^A_{LSV}),

$$N^{b}_{\mathrm{LSV,LSV}} = f^{A}_{\mathrm{LSV}} N^{m} \quad . \qquad \text{(Equation 4-30)}$$

N^m is 6.50 as η_{3D} is 0.53 in this work, as shown in Table 4-2 (Suzuki, 2007). Note that in Eq. 4-30 the particle segregation behaviours are not considered. f^{A}_{LSV} is related with the number fraction of LSV (f^{n}_{LSV}) as

$$f^{A}_{\mathrm{LSV}} = \frac{f^{n}_{\mathrm{LSV}} r_{\mathrm{p}}^{2}}{f^{n}_{\mathrm{LSV}} r_{\mathrm{p}}^{2} (r_{\mathrm{p}}^{2} - 1) + 1} \quad . \qquad \text{(Equation 4-31)}$$

In Eq. 4-31, r_{p} is the particle size ratio of LSV over YSZ,

$$r_{\mathrm{p}} = \frac{d_{\mathrm{LSV}}}{d_{\mathrm{YSZ}}} \quad , \qquad \text{(Equation 4-32)}$$

where d_{LSV} and d_{YSZ} are particle sizes of LSV and YSZ, respectively. $N^{b}_{\mathrm{LSV,YSZ}}$ is obtained in the same manner with $N^{b}_{\mathrm{LSV,LSV}}$,

$$N^{b}_{\mathrm{LSV,YSZ}} = (1 - f^{A}_{\mathrm{LSV}}) N^{m}_{\mathrm{LSV,YSZ}} \quad , \qquad \text{(Equation 4-33)}$$

where $N^{m}_{\mathrm{LSV,YSZ}}$ is the coordination numbers of a reference LSV particle embedded in the YSZ packing bed. $N^{m}_{\mathrm{LSV,YSZ}}$ is related with r_{p} and N^m as

$$N^{m}_{\mathrm{LSV,YSZ}} = \frac{2\alpha}{1 - \dfrac{(r_{\mathrm{p}}^{2} + 2r_{\mathrm{p}})^{1/2}}{1 + r_{\mathrm{p}}}} \quad , \qquad \text{(Equation 4-34)}$$

where α is a geometric factor directly proportional to N^m,

$$\alpha = \frac{2 - \sqrt{3}}{4} N^{m} \quad . \qquad \text{(Equation 4-35)}$$

The coordination numbers of YSZ can be obtained via the same arguments as that of LSV. Table 4-3 lists the coordination numbers of LSV and YSZ particles in the LSV–YSZ packing bed. It can be found in Table 4-3 that larger particles always have bigger coordination numbers, albeit with sophisticated and non-linear interdependences.

Table 4-3 Coordination numbers in the simulated LSV–YSZ packing bed.

Coordination numbers	Values (contacts/particle)
$N^{m}_{\mathrm{LSV,\,YSZ}}$	5.50
$N^{b}_{\mathrm{LSV,\,LSV}}$	2.99
$N^{b}_{\mathrm{LSV,\,YSZ}}$	2.97
N^{b}_{LSV}	5.96
$N^{m}_{\mathrm{YSZ,\,LSV}}$	7.78
$N^{b}_{\mathrm{YSZ,\,YSZ}}$	3.51
$N^{b}_{\mathrm{YSZ,\,LSV}}$	3.58
N^{b}_{YSZ}	7.09

For any correctly–designed composite anodes, both the electronic and ionic components must form electrical percolating networks. For binary packing beds composed of purely electronic (e.g., LSV) and ionic (e.g., YSZ) particles, the formation of percolating networks solely depends on whether the coordination numbers of homogenous particles ($N^{b}_{i,i}$) are larger than the percolation threshold ($N^{*}_{i,i}$). $N^{*}_{i,i}$ is defined as the minimum coordination numbers that render particles long-range interconnected. It was reported to be $(D^2+D)/(2D-1)$ for the rigid particle aggregates, where D is the dimension (Kuo and Gupta, 1995). Generally speaking, larger particles involve smaller number fraction (f^{n}) to render $N^{b}_{i,i} > N^{*}_{i,i}$. Figure 4-23 shows contour plots of $N^{b}_{\mathrm{LSV,YSZ}}$ together with the percolating regions of LSV and YSZ, as functions of f^{n}_{LSV} and r_{p}. The whole region is divided into three sub-regions by the two contours of $N^{b}_{\mathrm{LSV,LSV}}$ and $N^{b}_{\mathrm{YSZ,YSZ}}$, viz. the non-percolating region of LSV (light gray), the percolating region of both LSV and YSZ (rainbow), and the non-percolating region of YSZ (pastel violet). The largest percolating region obviously occurs when a monosized packing bed (i.e. $r_{\mathrm{p}} = 1$) with equal amount of LSV and YSZ particles (i.e. $f^{n}_{\mathrm{LSV}} = 0.5$) forms. The percolating region shrinks when particle aggregates deviate

from r_p = 1 and $f_{LSV}^n = 0.5$. Accordingly, the percolating region shown in Fig. 4-23 is merely a small portion of the whole crescent-shaped percolating region. As can be seen in Table 4-3 and Fig. 4-22, both LSV and YSZ situate within the percolating region. Fig. 4-23 also implies that r_p and f^n should not deviate strongly from 1 and 0.5, respectively. Otherwise, the risk of obtaining non-percolating composite electrodes is high because the percolating region becomes too narrow to manipulate. Contour plot diagrams like Fig. 4-23 are useful in designing and evaluating coordination numbers and percolation thresholds of binary particle aggregates.

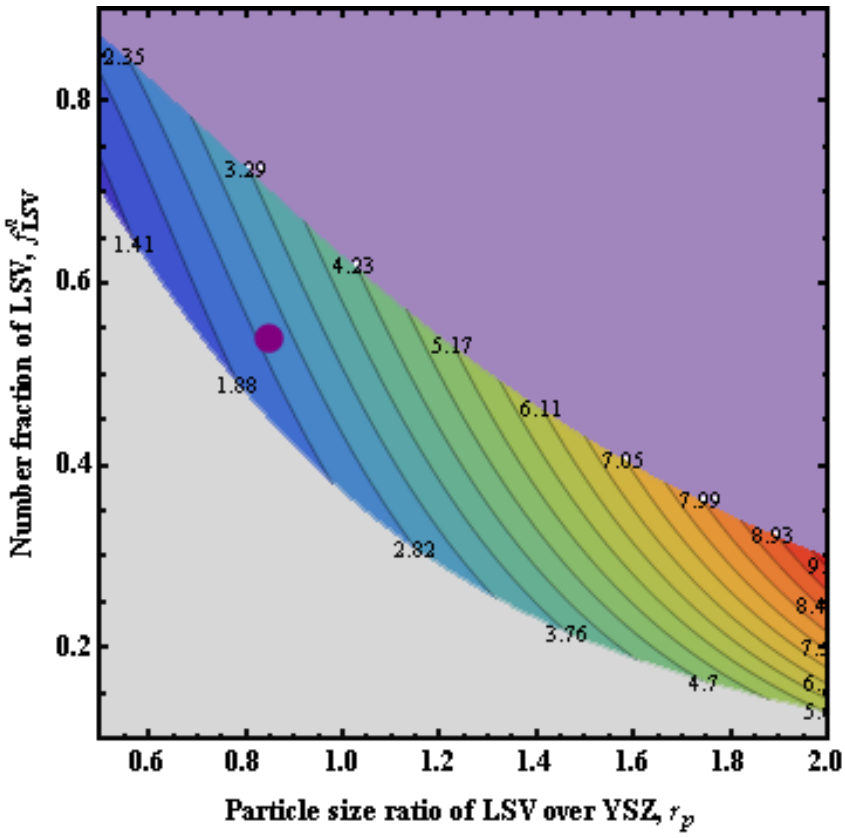

Figure 4-23 Contour plots of $N_{LSV,YSZ}^b$ as functions of f_{LSV}^n and r_p. The light gray zone and the pastel violet zone are the non-percolation regions of LSV and YSZ, respectively. The rainbow zone is the percolating region of both LSV and YSZ. The embedded purple dot represents the simulated LSV–YSZ composite anode under investigation.

Packing beds constructed by coordination number theories were largely based on Bouvard and Lange's method (Chan *et al.*, 2004; Jeon *et al.*, 2006; Janardhanan *et al.*, 2008; Mori *et al.*, 2008; Chen *et al.*, 2011). Their packing method involves an implicit assumption that the coordination number of monosized packing beds (N^m) is exactly 6

(Bouvard and Lange, 1991). Unlike Bouvard and Lange's method, the void fraction effect on N^{m} has been incorporated in our packing model. As summarized by Suzuki (Suzuki, 2007), N^{m} is in principle a monotonically decreasing function on the void fraction ε.

4.4.3 Virtual sintering

The necks among heterogeneous particles in the packing bed represent the sintering necks among electronic and ionic particles in realistic SOFC composite anodes. In contrast, the necks among homogeneous particles are of little interests as long as percolating networks have already formed. This work therefore considers the LSV−YSZ necks under the conditions of percolating LSV−LSV and YSZ−YSZ networks. The neck formation between two LSV and YSZ particles is considered from: (*i*) adhesion at room temperature and (*ii*) sintering at elevated temperatures. The adhesion of contacting LSV and YSZ particles occurs in order to minimize the surface energy. The surface energy of both particles should be quite low because of organic surface films. The lower limit of the radius of adhesion necks (x_0) formed by Van der Waals forces is given by

$$x_0 = \left(\frac{r_s a^2}{10\mu} \right)^{1/3} , \qquad \text{(Equation 4-36)}$$

where γ_s is the surface energy, a the particle radius, and μ the shear modulus of LSV particles (Ashby, 1974). According to Eq. 4-36, the normalized radius of adhesion necks (x_0/a) is 0.04.

This lightly (i.e. 4%) contacting LSV–YSZ particle aggregate is subsequently sintered in the initial sintering stage, thus preventing abnormal particle growth and maintaining considerable electrode porosity (Figs. 4-22 and 4-25). The YSZ should be inert as the electrode sintering temperature (1200 ℃) is significantly lower than its melting point. Note that the constrained sintering between the YSZ substrate and the thin electrode and the free surface sintering are not considered in this study. A sphere-to-plate model that considers a LSV sphere sintered to YSZ plate should be reasonable, because the effective curvature of inert YSZ is almost zero. The normalized curvature difference (K) for diffusion from a surface source (e.g., surface diffusion and lattice diffusion) is

$$K = \left(\frac{1}{\rho} - \frac{1}{x} + \frac{2}{a}\right)\left(1 - \frac{x}{a}\right) \quad , \qquad \text{(Equation 4-37)}$$

where ρ is the radius of curvature of the sintering neck and x is the radius of the sintering neck (inset of Fig. 6) (Ashby, 1974). By simple geometry,

$$\rho = \frac{x^2}{2(a-x)} \quad . \qquad \text{(Equation 4-38)}$$

Under quasi steady state conditions, the grow rate of sintering necks controlled by lattice diffusion (dx_{latt}/dt) is

$$\frac{dx_{latt}}{dt} = \frac{2D_v\gamma_s\Omega K^2}{kT} \quad , \qquad \text{(Equation 4-39)}$$

where D_v and Ω are the lattice diffusion coefficient and the ionic volume of LSV, respectively (Kuczynski, 1949; Wilson and Shewmon, 1966). In contrast, the surface diffusion leads to a sintering neck grow rate (dx_{surf}/dt) given by

$$\frac{dx_{surf}}{dt} = \frac{2D_s\delta_s\gamma_s\Omega K^3}{kT} \quad , \qquad \text{(Equation 4-40)}$$

where D_s and δ_s are the surface diffusion coefficient and the effective surface thickness of LSV, respectively (Kuczynski, 1949; Wilson and Shewmon, 1966). The diffusion coefficients in Eqs. 4-39 and 4-40 fulfil the Arrhenius behaviour,

$$D_i = D_0^i \exp\left(-\frac{Q_0^i}{RT}\right), \ i = \mathrm{v,s} \qquad \text{(Equation 4-41)}$$

where D_0^i and Q_0^i are the pre-exponential factor and the activation energy for the specific diffusion mode, respectively. Table 4-4 lists the sintering parameters of LSV. Figure 4-24 shows the normalized radius of sintering necks (x/a) in function of sintering time. The neck growth is quite fast in the first 10 minutes but relatively sluggish after 3 hours. x/a is 0.14 for a sintering time of 2 hours if the sintering is lattice diffusion controlled. In comparison, x/a is 0.54 if the sintering is surface diffusion controlled. It is thus inferred that the sintering of LSV–YSZ particle aggregate is dominated by the surface diffusion.

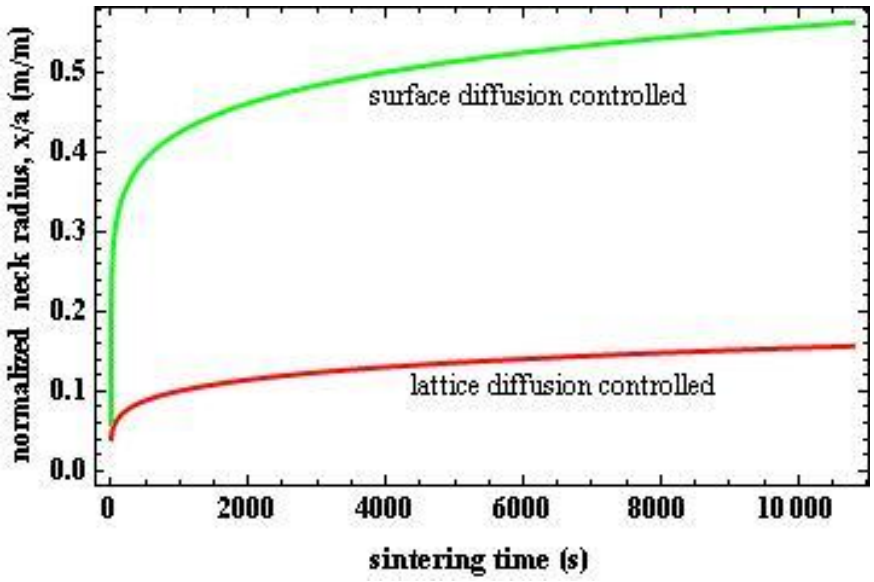

Figure 4-24 Numerical sintering curves of the LSV–YSZ packing bed at 1200 ℃, controlled either by surface diffusion (green) or lattice diffusion (red) of LSV from surface sources. The inset illustrates the neck formation during the initial sintering stage. *x* and *a* are the radiuses of the sintering neck and the LSV particle, respectively.

Table 4-4 Listing of parameters of LSV for the sintering model.

Parameters	Values
Atomic volume, Ω	9.24×10^{-23} cm^3
Melting point, T_m	1953 K
Density, $\rho_{LSV\text{-}ox}$	4.89 g/cm^3
Surface energy, γ_s	700 mJ/m^2
Effective surface thickness, δ_d	7×10^{-8} cm
Pre-exponential factor for lattice diffusion, D_o^v	3.2×10^2 cm^2/s
Activation energy for lattice diffusion, Q_0^v	378 kJ/mol
Pre-exponential factor for surface diffusion, D_0^s	2×10^3 cm^2/s
Activation energy for surface diffusion, Q_0^s	370 kJ/mol
Sintering temperature, T	1473 K
Sintering time, t	7200 s

In literature, the description on TPBs of SOFC electrodes was mostly modelled by the intersection of two overlapping heterogeneous particles (Abbaspour *et al.*, 2010; Golbert *et al.*, 2008; Kenney *et al.*, 2009; Nishida and Itoh, 2011; Sanyal *et al.*, 2010). To the best of our knowledge, Costamagna and coworkers first proposed this particle-overlapping method (Costamagna *et al.*, 1998). The method involves a priori knowledge on the extent of particle overlapping. In addition, the role of materials properties in the neck formation has been somewhat overlooked. Numerical sintering models had also been proposed for externally compacted SOFC composite electrodes (Schneider *et al.*, 2006). In contrast, the analytical sintering model used in this work is free of external pressure.

4.4.4 Three phase boundaries and electrochemically active zones

Figure 4-25 shows a schematic configuration of the half-cell consisting of YSZ electrolyte, LSV–YSZ composite anodes, and enlarged EAZs of two sintered LSV and YSZ particles. It is worth noting that EAZs are, in principle, the sum of numerous tiny and discontinuous active zones around the sintering necks. As sketched in Fig. 7, the dimensions of EAZs are defined by three length scales, viz. the length specific TPB length (l_{TPB}), the in-depth TPB penetration of electrocatalysts (w), and the distance away from the interface between the LSV–YSZ anode and the YSZ electrolyte, i.e. LSV−YSZ/YSZ interface (l). Without loss of generality, let LSV be the reference particle. The length specific l_{TPB} is thus given by

$$l_{\mathrm{TPB}} = sN^{b}_{\mathrm{LSV,YSZ}}\rho^{l}_{\mathrm{LSV}} \ , \qquad \text{(Equation 4-42)}$$

where s is the perimeter of sintering necks of two as-sintered LSV and YSZ particles ($s = 2\pi x$) and ρ^{l}_{LSV} is the line density of LSV along the direction away from the LSV−YSZ/YSZ interface. Unless addressed explicitly, the TPB length used all through this study is length specific, which is the TPB length normalized to the direction away from the composite electrode-electrolyte interface. The s and ρ^{l}_{LSV} of the LSV–YSZ anodes are 0.4 μm/contact and 1.53×10^{13} particles/cm, respectively. The corresponding l_{TPB} is thus found to be 1.8×10^{9} cm/cm, equivalent to a volume-specific TPB length of 3.9×10^{9} cm/cm^3. The TPB length reported herein is one order of

magnitude larger than those experimentally determined values (Wilson *et al.*, 2006). This discrepancy might be because LSV particles are much finer than NiO particles. Furthermore, the particle agglomeration, particle segregation, and dead-sintered interfaces have not been considered in this study.

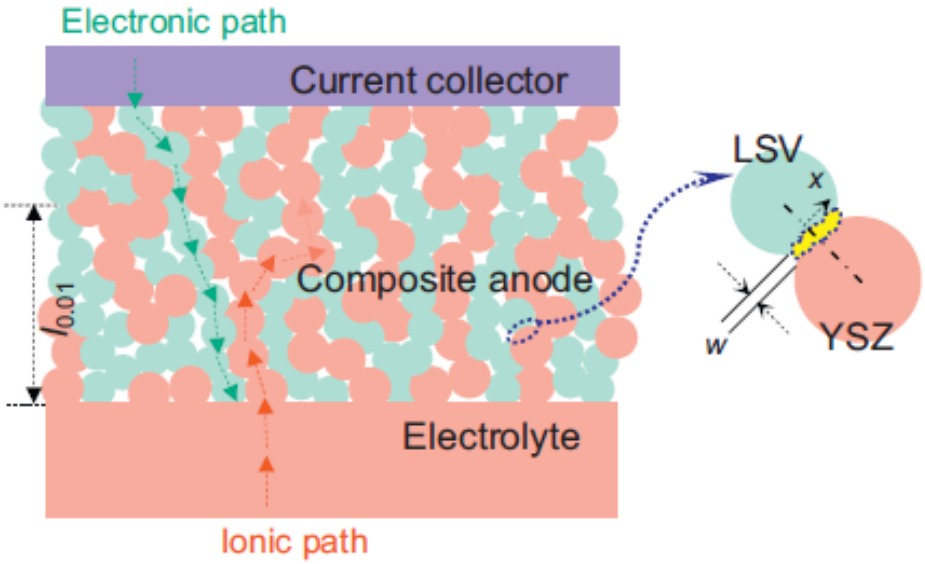

Figure 4-25 Schematic illustration of the microstructure and sintering necks of LSV–YSZ composite anodes. In the figure, x, w, and $l_{0.01}$ are the radius of the sintering necks, the in-depth TPB penetration of electrocatalysts, and the active electrode thickness, respectively.

w is assumed to decay exponentially along l,

$$w = w_0 \exp(-\kappa l) \quad , \qquad \text{(Equation 4-43)}$$

where w_0 is the w at the LSV–YSZ/YSZ interface and k is a proportionality factor that fulfils

$$\kappa l_{0.01} = \ln 100 \quad . \qquad \text{(Equation 4-44)}$$

In Eq. 44, $l_{0.01}$ is defined empirically as the l where w decays 99%. It is worth to mention that the selection of 99% decay is arbitrary. To some extent, $l_{0.01}$ could be regarded as the active electrode thickness, beyond which fuel cell reactions become so sluggish that w is negligible. In summary, the cross-section area of EAZs (A_{EAZ}) is given by integrating l_{TPB}, w, and l from the LSV–YSZ/YSZ interface ($l = 0$) to the active electrode thickness ($l = l_{0.01}$),

$$A_{\mathrm{EAZ}} = \int_0^{l_{0.01}} l_{\mathrm{TPB}} f_c w_0 e^{-\kappa l} \mathrm{d}l \quad , \qquad \text{(Equation 4-45)}$$

where f_c = 1.15 is a correction factor that accounts for particle coarsening on the basis of cumulative distribution functions (Suzuki, 2007). The ratios of A_{EAZ} over A_{geo} of the LSV–YSZ composite anode had been known to be 7.3 ±0.5, 8.1 ±0.4, 7.9 ±0.4, 7.0 ±0.2, 6.7 ±0.3, 6.1 ±0.4, 7.2 ±0.9, under anodic biases (E_{bias}) of 0, 20, 50, 70, 100, 120, and 150 mV, respectively (Ge *et al.*, 2011). The A_{EAZ} of polarized LSV–YSZ composite anodes can thus be readily known. Except w_0 and $l_{0.01}$, the parameters in Eqs. 15–18 have been known from the virtual packing and sintering data (Tables 4-2 and 4-3).

The magnitude of w_0 has been rarely reported in literature. Nakagawa et al. observed no performance changes of Ni films ranging from 0.8 μm to 12.9 μm (Nakagawa *et al.*, 1995). They thus inferred that the EAZs of Ni–YSZ cermet anodes were less than 1 μm away from the Ni–YSZ/YSZ interface. Horita et al. examined active sites of cathodically polarized $La_{0.9}Sr_{0.1}MnO_3$(LSM)/YSZ interfaces under $^{16}O/^{18}O$ atmosphere. They concluded with caution that the length scale of the active sites for O_2 reduction was less than 1 μm (Horita *et al.*, 1998). While the experiments largely delimit the upper bound that is around 1 μm, the lower bound of w_0 might have to be simulated. Adler et al. discussed

The cathodic behaviours of mixed ionic and electronic conductors (MIECs) and found that the penetration depth of poor ionic conductors (e.g. LSM) was essentially less than 100 atomic unit cells (Adler *et al.*, 1996). By analyzing electrochemical potential distributions of patterned MIEC cathodes, Fleig found that the ionic current density dropped by 80% at a distance of several nanometres away from TPBs (Fleig, 2002). Generally speaking, w_0 of SOFC cathodes depends on the oxygen ionic conductivity and oxygen surface exchange rate. If the same argument also applies to SOFC anodes, w_0 of LSV particles should not be larger than 16 nm (Fleig, 2002; Liu, 1998). In this work w_0 is thus thought to be in the order of magnitude of 10^0 nanometres.

An empirical way on estimating $l_{0.01}$ is to examine the electrode thickness effect on fuel cell performance. Take the state-of-the-art Ni cermet anodes as an example. It is interesting to note that most experimental results advocate $l_{0.01}$ in two categories: 100 μm (Fukunaga *et al.*, 2007; Abudula *et al.*, 1996) and 10μm (Sakamoto *et al.*, 1996;

Menzler and Haanappel, 2010; Brown *et al.*, 2000; Primdahl and Mogensen, 1999). Our previous works suggested an optimal anode thickness around 100 μm for submicron-sized particle aggregates (Chan and Xia, 2001). As it tackled with the mass transport behaviour in porous media and was irrelevant to interfacial chemistry, that "optimal" anode thickness might not be the active anode thickness. In contrast, Zhu and Kee stated charge transfer regions extending over a distance of 10−20 μm away from electrolyte surfaces (Zhu and Kee, 2008). Jiang et al. simulated equal-sized and equal-composition LSM–YSZ cathodes and reported the effective thickness of 10–20 μm (Jiang *et al.*, 2010). In this work, $l_{0.01}$ is tentatively regarded to be in the order of magnitude of 10^1 μm.

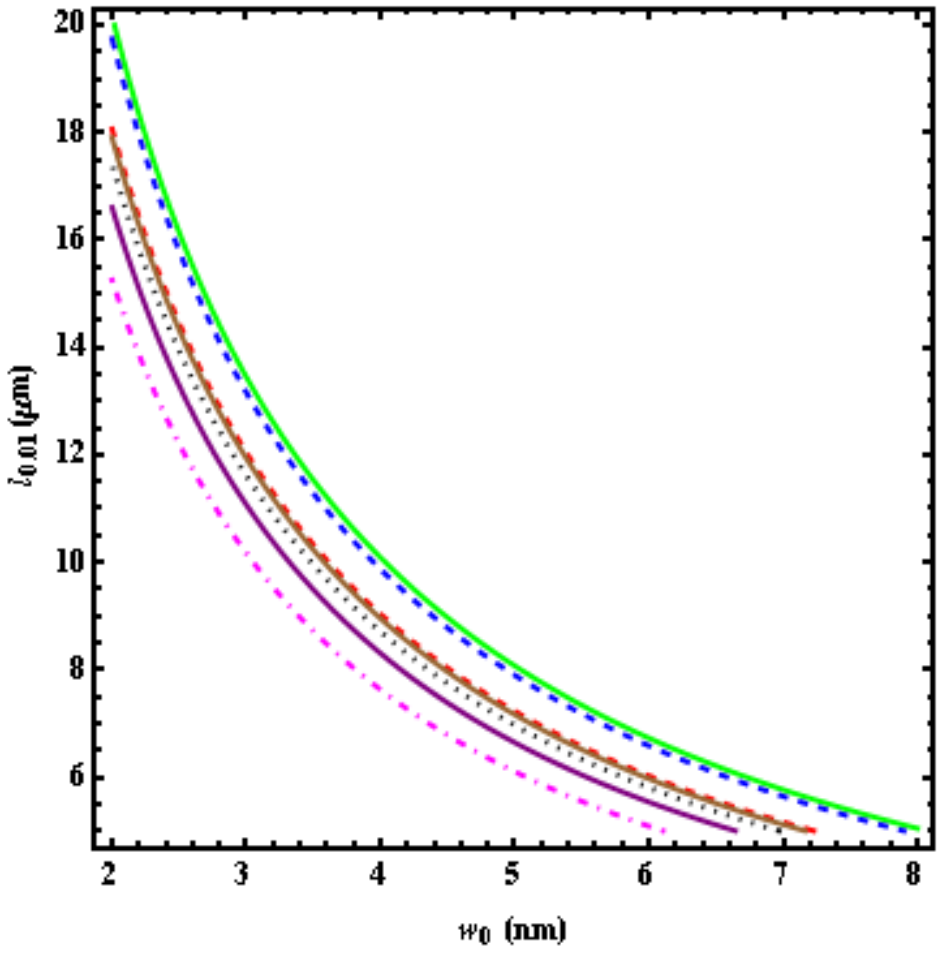

Figure 4-26 Contour plots of A_{EAZ} of LSV–YSZ composite anodes as functions of w_0 and $l_{0.01}$. The A_{EAZ} values of sample A are 3.34 (red, dashed), 3.73 (green, solid), 3.65 (blue, dashed), 3.22 (black, dotted), 3.07 (purple, solid), 2.82 (magenta, dot-dashed), and 3.31cm^2 (brown, solid), under anodic biases of 0, 20, 50, 70, 100, 120, and 150 mV, respectively.

Figure 4-26 shows the contour plots of A_{EAZ} as functions of w_0 and $l_{0.01}$ after solving Eq. 4-35 numerically. It should be borne in mind that in Fig. 4-26 w_0 and $l_{0.01}$ are treated as two independent parameters, although the exact interrelationship between w_0 and $l_{0.01}$ is hitherto unknown. In addition, exact values of w_0 and $l_{0.01}$ are unable to be obtained within the scope of the present study. Notwithstanding these limitations, it is still meaningful to discuss the behaviours of EAZs in polarized LSV–YSZ anodes. For instance, under the open circuit voltage (OCV) condition w_0 is 3.61 nm if $l_{0.01}$ is given as 10 μm, vice versa. If w_0 is assigned as 5 nm and it remains constant under polarized conditions, $l_{0.01}$ are 7.23, 8.07, 7.90, 6.96, 6.64, 6.10, and 7.16 μm, under E_{bias} of 0, 20, 50, 70, 100, 120, 150 mV, respectively. On the other hand, $l_{0.01}$ would be 12.04, 13.45, 13.16, 11.61, 11.07, 10.17, 11.94 μm, respectively, if w_0 was 3 nm instead of 5 nm (Fig. 8). SOFCs are certainly operated under more sophisticated conditions with either independent or interrelated w_0 and $l_{0.01}$. Unfortunately, this kind of uncertainty has not been able to be minimized without convincing experimental evidences. This work therefore merely provides some technical guidelines on these hard-to-measure interfacial parameters (Fig. 4-26). It is worth to highlight that either the active electrode thickness or the TPB length, which has been used extensively in literature, is not sufficient in describing the reactive regions in on-running SOFCs alone.

To summarize, the rationale on establishing the relationship between TPBs and EAZs, though derived based on LSV–YSZ composite anodes in SOFCs, is suitable for various solid state electrode/electrolyte interfaces, e.g. fuel cells with solid electrolytes, solid state electrolytic cells, oxygen sensors, and batteries. Besides purely academic interests, it is thought to be useful for technical designs on electrodes and electrode/electrolyte interfacial structures. $l_{0.01}$ represents the optimized thickness of the functional layer in SOFC anodes. Note that the use of functional layers has been very popular in Ni-cermet supported SOFC stacks. In addition, w_0 sets the design target on the shell thickness of (inert) core-(active) shell structures. These kinds of structures have being used extensively in polymer electrolyte membrane fuel cells (PEMFCs) (Wang *et al.*, 2010). Notwithstanding with these merits, the theory should be judged critically on some inherent assumptions and limitations. A fundamental assumption, albeit made tacitly, is that the electrocatalyst is purely electronic and the electrolyte is purely ionic. The whole theory needs further corrections in order to be suitable for MIECs. The significance of MIECs should not be overlooked, as they have

been quite common in intermediate and low temperature SOFCs. Furthermore, the virtual packing neglects problems like particle segregation and particle size distribution. These problems become significant if r_p strongly deviates from the unity. This work could be further improved by employing in situ techniques to characterize the electrode microstructure (Wilson *et al.*, 2006; Shearing *et al.*, 2010; Bouvard and Lange, 1991; Kanno *et al.*, 2011). Sophisticated materials characterization techniques (e.g. in situ Raman spectroscopy (Cheng *et al.*, 2007), in situ X-ray photoelectron spectroscopy (DeCaluwe *et al.*, 2010; Zhang *et al.*, 2010a), and synchrotron X-ray scattering (Nagy and You, 2009) should also be involved in order to measure w and $l_{0.01}$ experimentally.

4.4.5 Brief summary

The interrelationship between TPBs and EAZs was investigated via a case study on LSV–YSZ composite anodes in SOFCs. The TPB lengths were calculated from a virtually packed and sintered particle aggregate. The packing and sintering methods were suitable for the optimization of SOFC composite electrodes. The length specific TPB length was 1.8×10^9 cm/cm, equivalent to a volume-specific TPB length of 3.9×10^9 cm/cm^3. The cross-section area of EAZs was basically 6 to 8 times of the geometric area. Empirical correlations among EAZs, TPBs, active electrode thickness, and in-depth penetration of electrocatalysts were established. Under the circumstance of polarized LSV–YSZ anodes, the active electrode thickness and in-depth penetration of electrocatalysts were typically in the range of 5–20 μm and 2–8 nm, respectively.

4.5 Summary

The double layer and electrochemically active zones of solid state electrode/solid-electrolyte interfaces were investigated via a case study on LSV/YSZ interfaces in solid oxide fuel cell anodic environments. A comprehensive theory had been elaborated by addressing the double layer structure, the double layer capacitance, and the electrochemically active zones. The double layer structure was described by a modified Poisson–Boltzmann theory and Monte Carlo simulations. The apparent double layer capacitance was obtained from impedance spectroscopy. Its magnitude was of several hundreds of μF/cm^2. The Helmholtz–Perrin capacitance was ca 22 to 30 μF/cm^2 while the Gouy–Chapman capacitance was ca 320 to 480 μF/cm^2. The intrinsic double layer capacitance was dominated by the Helmholtz–Perrin capacitance.

Thicknesses of the compact layer were around 0.28 to 0.36 nm; thicknesses of the diffusive layer were around 1.1 to 1.9 nm. Under anodic biases from 0 to 150 mV, the "capacitance surge" phenomenon was ascribed to mutual competitions between the loosened compact layer and the increase of Volta potential in the diffusive layer. Synergic capacitance analyses enabled in situ detections of electrochemically active zones. With electrode microstructures described by the sintered LSV−YSZ particle packing beds, correlations among electrochemically active zones, three phase boundaries, in-depth penetration of electrocatalysts, and effective anode thickness were established.

Chapter 5. Sulphur tolerant and carbon resistant solid oxide fuel cells with LSV anodes

5.1 Importance and current status of sulphur-tolerant and carbon-resistant SOFC anodes

The international commitment on sustainable society and low-carbon future demands green energy conversion technologies (International Energy Agency, 2010). In an idealized scenario, primary energy sources are converted to secondary energy sources, mostly in electrical energy, with high energy conversion efficiency and low carbon footprint. Such kinds of energy conversion devices are thought to be incorporated into smart grids, in order to improve the system efficiency and stability towards demand fluctuations and intermittent electrical sources. Currently available technologies, *e.g.* wind (Li, 2010), nuclear (Muradov and Veziroglu, 2008), solar (Pagliaro *et al.*, 2010), metal hydrides (Aguey-Zinsou and Ares-Fernandez, 2010), and batteries (Baker, 2008) largely fail to meet at least one of the key targets including cost, reliability, flexibility, efficiency, and large scale deployment. One of the technologies that generally fulfil these requirements is SOFC. SOFC has been extensively studied since the last three decades (Minh, 1993; Jacobson, 2010). Distinctive advantages of SOFCs are the high energy conversion and storage efficiency and the fuel flexibility. SOFC electrical efficiencies ranging from 40% (simple and small systems) to 50% (hybrid systems) had been demonstrated, and the theoretical efficiency is projected up to 60% (Energy, 2004). SOFCs employing robust hydrogen electrodes can be fed with H_2, CO, syngas, gasified reformates from natural gas, coal, and heavy hydrocarbons. Direct hydrocarbon fed SOFCs had also been demonstrated (McIntosh and Gorte, 2004).

The fuel flexibility, however, has been somewhat constrained by the lack of carbon resistance and sulphur tolerance. The state-of-the-art Ni–cermet electrodes are prone to carbon filament precipitation (Toebes *et al.*, 2002), dusting, and dry corrosion when exposed to hydrocarbon fuels. Ni–cermets are also known to be poisoned by parts per million (ppm) levels of H_2S, though they can be regenerated when exposed to low concentrations and temporarily high concentrations of H_2S (Matsuzaki and Yasuda, 2000; Zha *et al.*, 2007). In literature, various mitigation approaches on Ni–cermet

SOFC anodes had been proposed, including the addition of water (Lakshminarayanan and Ozkan, 2011; Yang *et al.*, 2010) or low melting point metals (Marina *et al.*, 2011) into fuels, and decoration of NiO particles with ceria (Kurokawa *et al.*, 2007b; Yun *et al.*, 2010; Lohsoontorn *et al.*, 2008) or niobia (Choi *et al.*, 2008). Sulphide (Pujare *et al.*, 1987; Yates and Winnick, 1999; Liu *et al.*, 2003) and oxide (Mukundan *et al.*, 2004; Aguilar *et al.*, 2004a; Zha *et al.*, 2005a; Xu *et al.*, 2007; Lu and Zhu, 2008; Danilovic *et al.*, 2009; Zha *et al.*, 2005b; Cooper *et al.*, 2010) anodes had also been explored extensively. Many practical SOFC feedstocks, *e.g.* natural gas, coal gas, syngas, town gas, biogas, and reformed military fuels, contain several to thousands ppm of H_2S. In this chapter, lanthanum strontium vanadate-based SOFCs are tested and they exhibit salient catalytic activity and long-term stability when exposed to various feedstocks out of the H_2–H_2O–CO–CO_2–CH_4–H_2S system.

5.2 Experimental

In this chapter $La_{0.6}Sr_{0.4}VO_x$ (LSV) was used because of its higher catalytic activity than $La_{0.8}Sr_{0.2}VO_x$. LSV powders were synthesized via a citric route. The starting materials were $La(NO_3)_3\,6H_2O$ (Fluka, 99.0%), $Sr(NO_3)_2$ (Fluka, 99.0%), NH_4VO_3 (Sigma-Aldrich, 99.5%), and $C_6H_8O_7\,H_2O$ (Fluka, 99.5%). The molar ratio of total metal ions over citric acid was 2:3. Stoichiometric amounts of the raw materials were dissolved in deionised water. The solution was heated at 70 ℃ under magnetic stirring. A dark blue gel was obtained after dissipating excess water. It was dehydrated overnight at 100 ℃ and carefully ground in an agate mortar. The precursor was baked at 600 ℃ for 2 hours in a pristine alumina crucible (Coorsteck, the USA). The LSV powers were re-ground in the agate mortar. The LSV powers were further baked at 600 ℃ for 2 hours and at 800 ℃ for 6 hours. The YSZ powders (Tosoh, Japan) were used as-received.

Right amounts of LSV and YSZ powders were roll-milled overnight in isopropanol with YSZ balls. Subsequently, the slurry was dried at 80 ℃ in ambient air to obtain a homogeneous LSV–YSZ mixture. The powder mixture was added with ink vehicles (Fuel Cell Materials, the USA) and ground in the agate mortar to form the electrode paste. Green electrodes were prepared by screen-printing the ink onto 1-mm-thick YSZ electrolyte substrates. The geometric area of electrodes was 0.46 cm^2. The

electrochemically catalytic layer, LSV (50 wt.%)–YSZ, were sintered at 1215 ℃ for 2 hours. The gas diffusion layer, LSV (70 wt.%)–YSZ, was screen-printed onto the catalytic layer and sintered at 1205 ℃ for another 2 hours. A piece of Au gauze (Alfa Aesar, 52 mesh woven from 0.102 mm diameter wire, 99.99% metal basis) with a small amount of Pt paste in discrete dots was pressed onto the electrode to improve the contact quality. The Pt paste was also applied on the opposite side of YSZ substrate to represent the counter and the reference electrodes. All the Pt layers were sintered at 900 ℃ for 30 minutes.

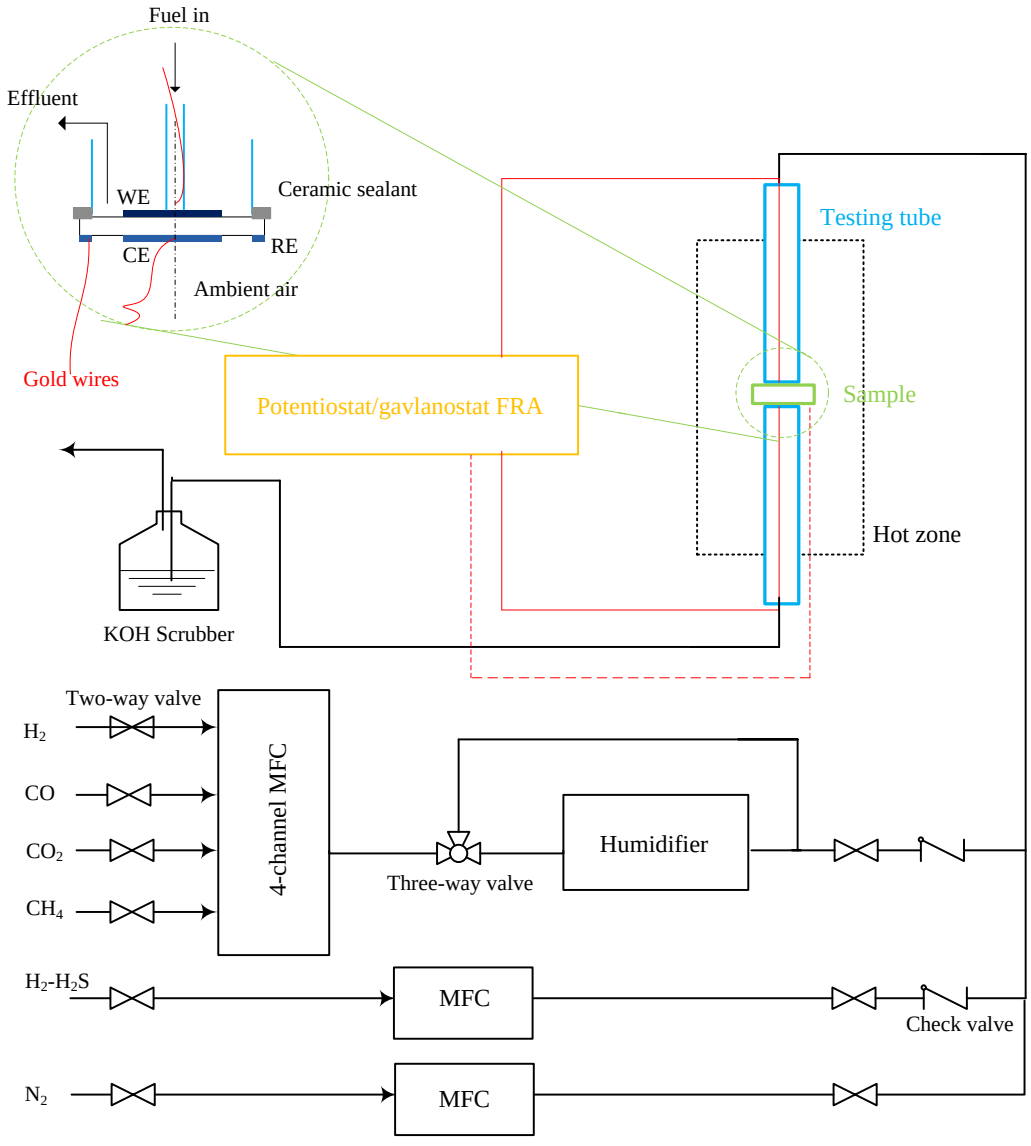

Figure 5-1 Schematic diagram of the flow channel, test rig, and half cell configuration.

The half cell configuration is given in Fig. 5-1. The lead wires on the hydrogen electrode side are made of Au (Alfa Aesar, 0.5 mm diameter, 99.9985% metal basis). The lead wires on the oxygen electrode side are made of Pt (Alfa Aesar, 0.5 mm diameter, annealed, 99.95% metal basis). The half cell was sealed onto an alumina tube with ceramic paste (Aremco 552, the USA). The testing tube was cured at 120 ℃ for 2 hours. Both the counter and reference electrodes are exposed to ambient air. After purging with N_2, the test rig was heated up in H_2 with a ramping rate of 2 ℃/min. The operating temperature was 900 ℃. At the hydrogen electrode side, the H_2S-free feedstock was modulated from the corresponding pure gases via Brooks® 4-channel mass flow controller (MFC). H_2S was introduced to the feedstock by using a certified gas blend of H_2S and H_2 (1000 ppm H_2S balanced with H_2). To obtain H_2O-containing feedstock, the gas blend was channelled through a humidifier with temperature control of ±0.1 ℃. The wet gas blend was further mixed with 1000ppm H_2S–H_2 to get the desired composition. The total flow rate of feedstock was maintained at 100 sccm.

Impedance responses were recorded under given anodic biases via a Solartron 1255B frequency response analyzer coupled to a 1470E electrochemical interface. The frequency range was 100,000–0.05 Hz. The sampling rate was 10 points/decade of frequency. Impedance spectra were fitted via Zview® 3.2c according to complex nonlinear least squares (CNLS) algorithm. Quasi-steady state polarization was performed by sweeping from -0.3 V (vs OCV) to 0.6 V (vs OCV), with a ramping rate of 0.1 mV/s and a sampling rate of 1 point/mV. Long-term stability tests were performed by chronopotentiometry, i.e. monitoring the electric potentials under given current densities. The sampling rate was 0.2 points/sec.

The X-ray diffraction pattern was recorded on a Shimadzu 6000 with Cu Kα radiation. The step size was 0.02 º. The scan rate was 2 º/min. Low vacuum scanning electron microscopy (SEM, JEOL JSM–6360) and field-emission SEM (FESEM, JEOL 7600F) were used for low and high magnification surface morphology observations, respectively. Qualitative element detection in the electrodes was carried out via the energy-dispersive X-ray spectroscopy (EDX, Oxford Instruments X-Max), which are coupled to the JEOL JSM–6360.

5.3 Structure and microstructure

Figure 5-2 shows the XRD pattern of LSV powders that were reduced at 900 ℃ in pure H_2 for 5 hours. The single phase LSV is well fitted to cubic structure, with a = 3.8815(6) Å, V = 58.48 Å^3, and space group Pm-3m. It is stated that LSV is of "pseudo" cubic perovskite structure. The reason is that it might be of orthorhombic structure but with very similar lattice parameters (Bordet *et al.*, 1993; Ge and Chan, 2009b). As shown in Chapter 3, LSV prepared from solid state reactions contains eradicable impurities. In contrast, LSV synthesized via citric route is of single phase (Fig. 5-2). This is possibly attributed to the better reactivity of finer LSV powders.

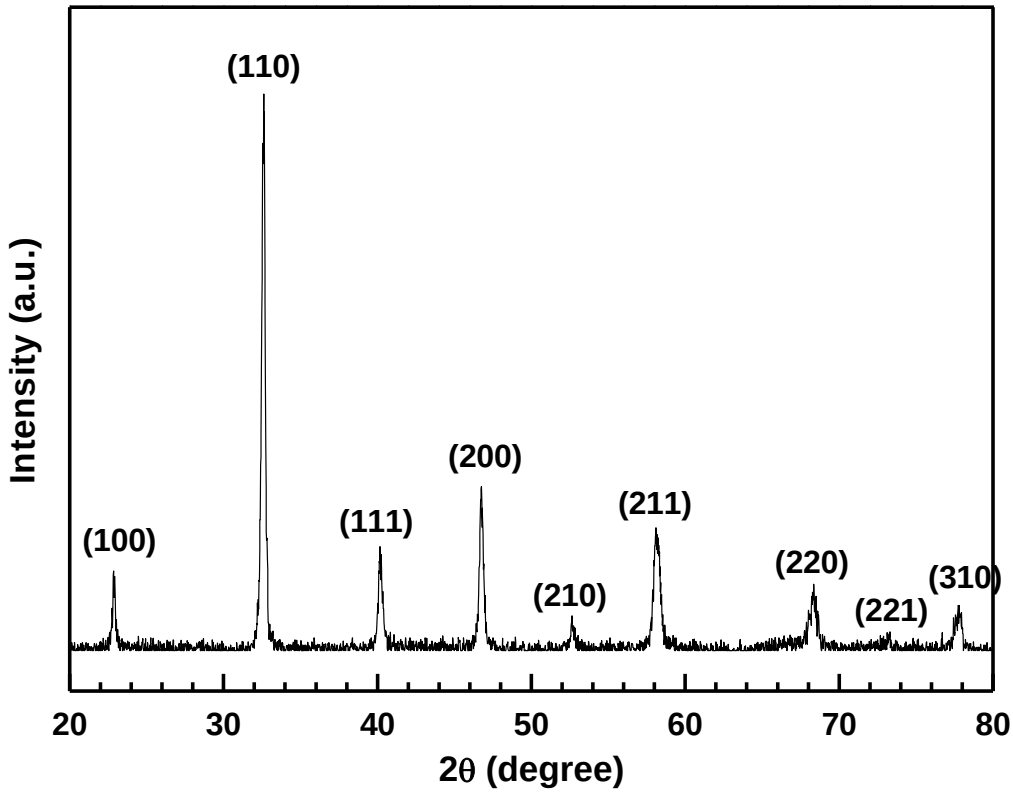

Figure 5-2 X-ray diffraction pattern of $La_{0.6}Sr_{0.4}VO_x$ (LSV) that is reduced in pure H_2 at 900 ℃ for 5 hours.

Figure 5-3 shows the electrode performance of LSV–YSZ anodes in the effect of LSV contents. The high-frequency resistances represent the ohmic resistances of LSV–YSZ anodes. The difference between the low-frequency resistance and the high-frequency resistance is the polarization resistance (R_p). As seen in Fig. 5-3, the lowest R_p occurs when the LSV content is 50 wt. %. The microstructure of graded LSV anodes is shown

in Fig. 5-4. The catalytic layer and the gas diffusion layer are 30 μm and 15 μm, respectively. Good adhesion between the electrolyte substrate and the catalytic layer and between the catalytic layer and the gas diffusion layer is evident.

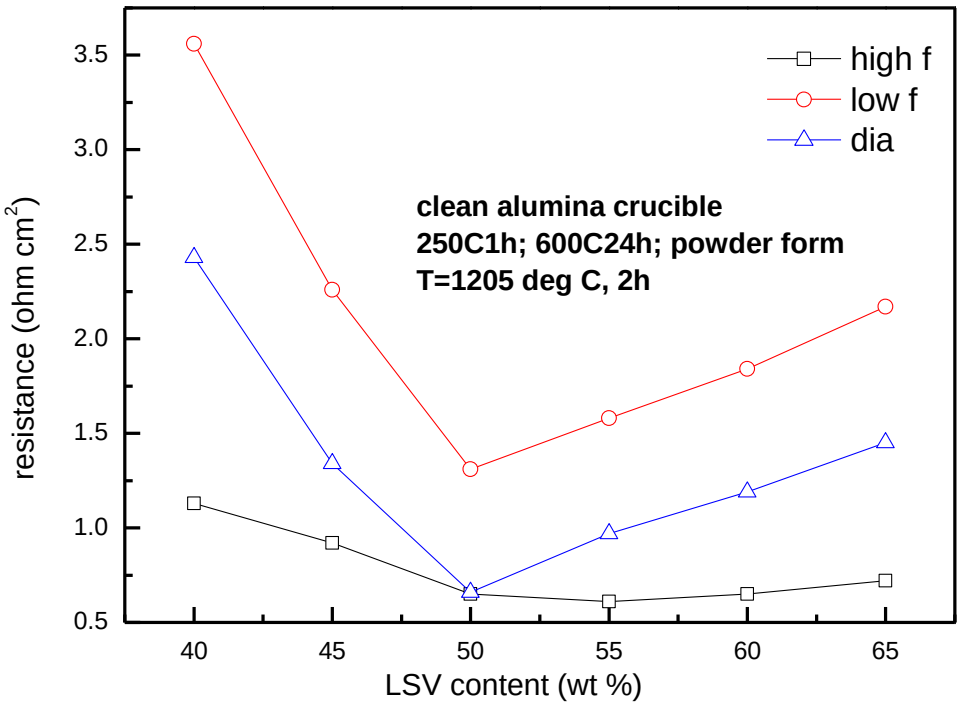

Figure 5-3 Effect of composition of LSV–YSZ anodes on high-frequency resistance ($R_{h\text{-}f}$), low frequency resistance ($R_{l\text{-}f}$), and the polarization resistance ($R_p = R_{h\text{-}f} - R_{l\text{-}f}$).

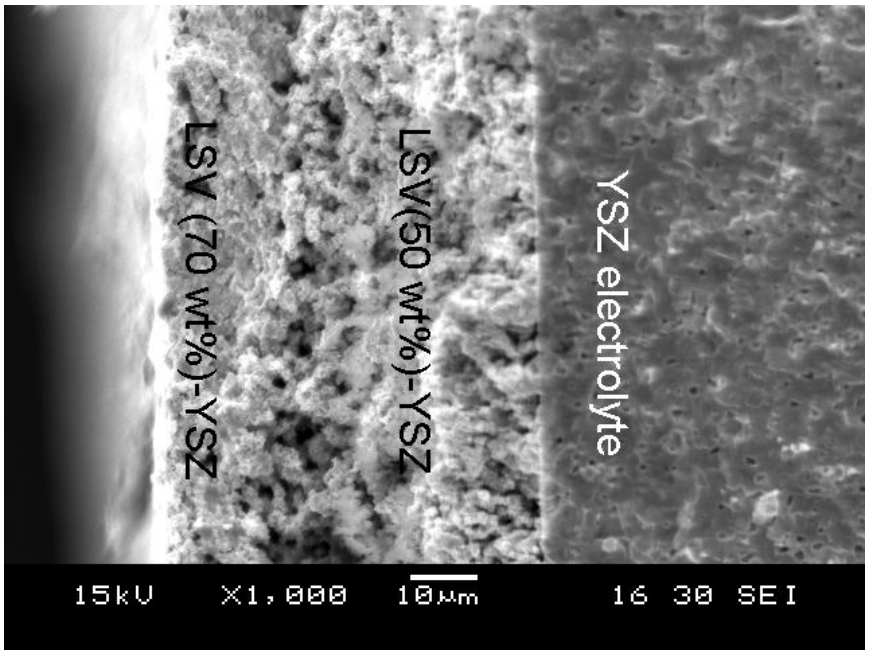

Figure 5-4 Cross-section profile of the fractured LSV–YSZ electrode.

5.4 Impedance spectroscopy and polarization of LSV anodes in clean fuels

Impedance spectroscopy shows good electrode performance of the LSV anodes. The polarization resistances (R_p) of the LSV electrode in H_2 are 0.54, 0.43, 0.44 Ω cm^2 under the potential biases (E_{bias}) of -100, 0, and 100 mV, respectively (Fig. 5-5a). The high R_p under E_{bias}=-100 mV is due to the severe starvation of H_2O. With the H_2O content of the feedstock increased to 9 vol.% (Table 5-1), R_p are 0.11, 0.22, 0.44, 0.56 Ω cm^2 under E_{bias} of -300, -100, 0, 100 mV, respectively (Fig. 5-5b). These results indicate that LSV seems to be of higher catalytic activity as electrolyser than fuel cell. Under the open circuit voltage (OCV) condition, the $La_{0.75}Sr_{0.25}Cr_{0.5}Mn_{0.5}O_3$ (LSCM) and $La_4Sr_8Ti_{11}Mn_{0.5}Ga_{0.5}O_{37.5}$ SOFC anode showed R_p of 0.47 (Tao and Irvine, 2003) and 0.20 (Ruiz-Morales *et al.*, 2006) Ω cm^2 in $97H_2$–$3H_2O$ at 900 ℃, respectively. LSV is thought to be comparable to these more well-established SOFC oxide anode materials. In contrast, only a few half cell results were reported for oxide solid oxide electrolysis cell (SOEC) negative electrodes. Based on a rough comparison with the single cell result of LSCM (Yang and Irvine, 2008; Jin *et al.*, 2011) and symmetric cell result of $Sr_2Fe_{1.5}Mo_{0.5}O_{6-\delta}$ (Liu *et al.*, 2010a), LSV could be regarded as one of the best oxides for SOEC negative electrodes. It is worth to mention that only the fuel cell operations are discussed in this chapter, as SOEC is beyond the scope of this PhD project.

Typical polarization curve of LSV anode with IR compensation are given in Fig. 5-6. The ohmic resistance used in the IR compensation was obtained via impedance spectroscopy at OCV conditions. It can be found that the reaction kinetics is strongly affected by only incorporating 9 vol.% H_2O into the feedstock. As indicated in Fig. 5-6, the polarization behaviour of LSV anodes seems asymmetric between the cathodic and the anodic side. The exchange current density (i_0), obtained from the low overpotential ranges near the OCV, are given in the inset of Fig. 5-6. It is surprisingly to find that i_0 at the anodic side ($i_{0\text{-a}}$) is always larger than that in the cathodic side ($i_{0\text{-c}}$). This is in contradiction with the impedance results shown in Fig. 5-5. One of the plausible reasons may be that the absorbed water impedes fuel cell reactions. The exact mechanism is, however, still unknown. Figure 5-7 shows the chronopotentiometry

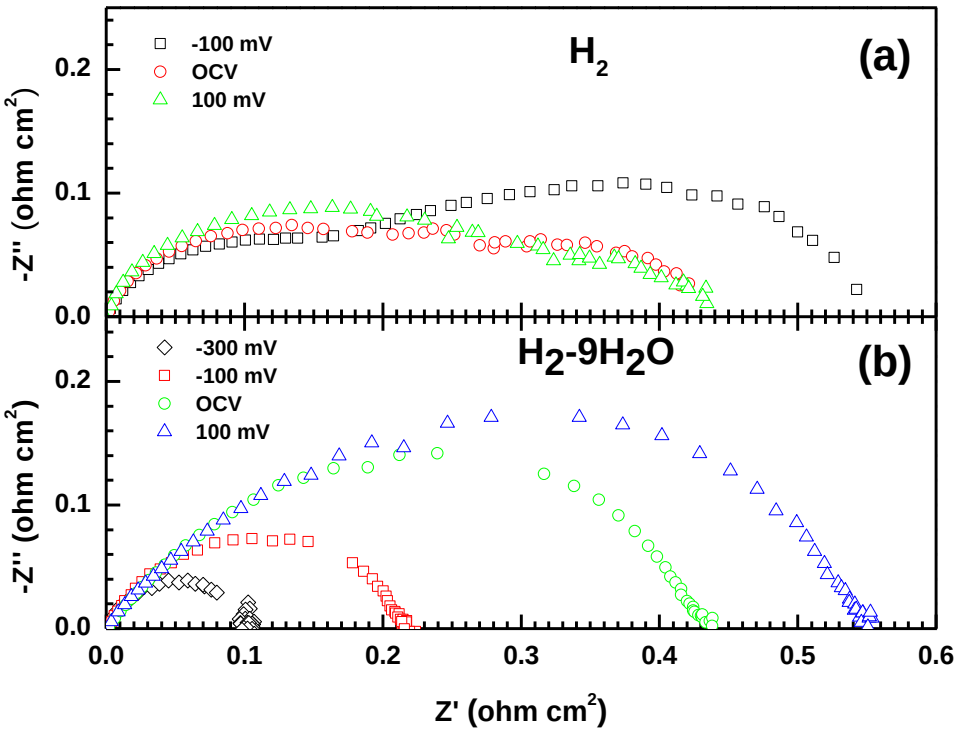

Figure 5-5 Impedance spectra of the LSV electrode as mentioned in Fig. 4a: (a) the freshly prepared electrode in pure H_2 and (b) the electrode after 70-hour fuel cell polarization and in the $70H_2$–30CO–50ppm H_2S atmosphere.

Table 5-1 Composition and tendency of carbon formation of gases addressed in Chapter 5. The operating temperature is 900 ℃. The carbon formation is predicted by assuming the thermodynamic equilibrium of the gas species.

Feedstock (100 sccm in total)						Carbon formation	Remarks
H_2	H_2O	CO	CO_2	CH_4	H_2S		
100	-	-	-	-	-	-	-
91	9	-	-	-	-	-	-
36	9	-	55	-	-	No	H_2-rich biogas (humidified)
73	9	-	18	-	-	No	H_2-rich biogas with low CO_2 concentration (humidified)
10	-	-	35	55	-	Yes	CH_4-rich biogas
80	-	-	20	-	-	No	H_2-rich biogas with local CO_2 concentration
55	-	30	15	-	-	No	Coal gas from hydrogasification
100	-	-	-	-	50 ppm	-	-
70	-	30	-	-	-	Yes	Syngas; desulphurized town gas
70	-	30	-	-	50 ppm	Yes	town gas
65	-	30	5	-	50 ppm	No	Coal gas
75	-	-	25	-	50 ppm	No	H_2-rich biogas with low CO_2 concentration
60	-	-	20	20	50 ppm	Yes	Mixture of H_2-rich biogas and CH_4-rich biogas
97	3	-	-	-	50 ppm	-	-

curves of the LSV electrode in pure H_2 and $91H_2$–$9H_2O$, where the half cell is polarized under anodic current density of 0.2 A/cm^2. The fresh LSV electrode has the overpotential (η) of 89 mV in H_2 and a degradation rate (κ) of 0.023%/hour (h). A potential drop can be seen in Fig. 5-7 when the fuel gas is shifted from H_2 to $91H_2$–$9H_2O$. This potential drop is mostly due to the reduction of OCV. Potential oscillation is observed after 2-hour exposure to $91H_2$–$9H_2O$. This phenomenon might be due to the surface reconstruction of LSV under oxidising environment.

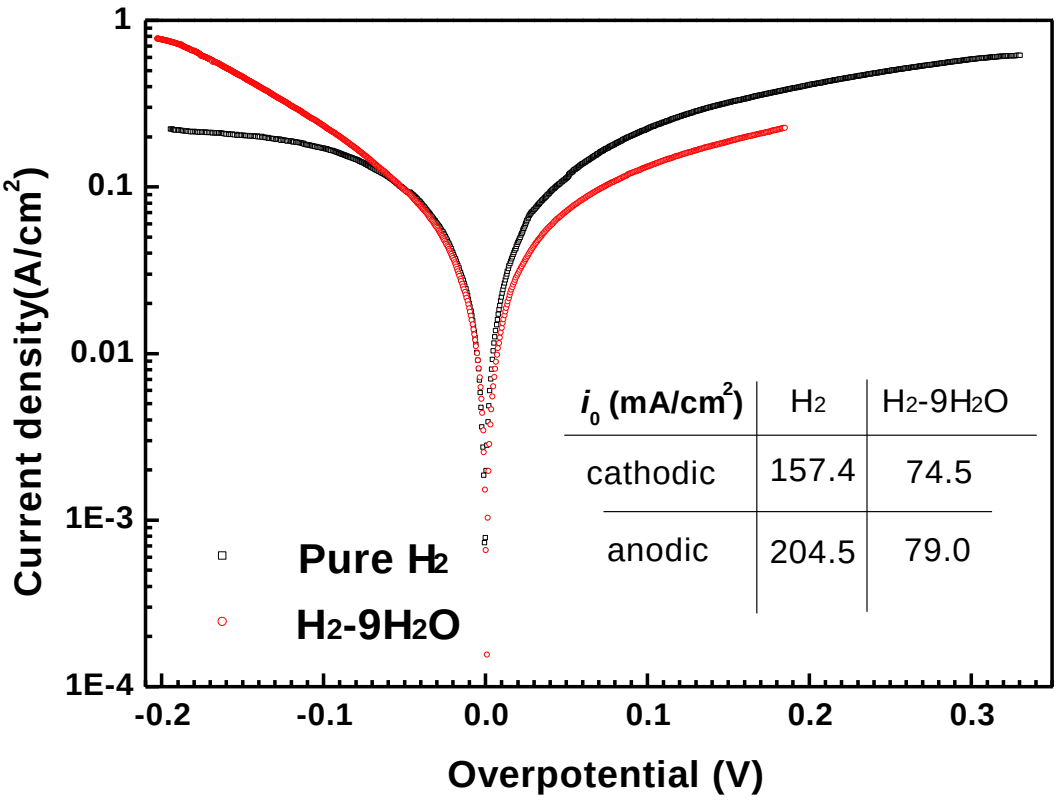

Figure 5-6 IR-compensated polarization curve of LSV anode in pure H_2 and H_2–$9H_2O$ at 900 ℃. The inset table shows the corresponding exchange current densities.

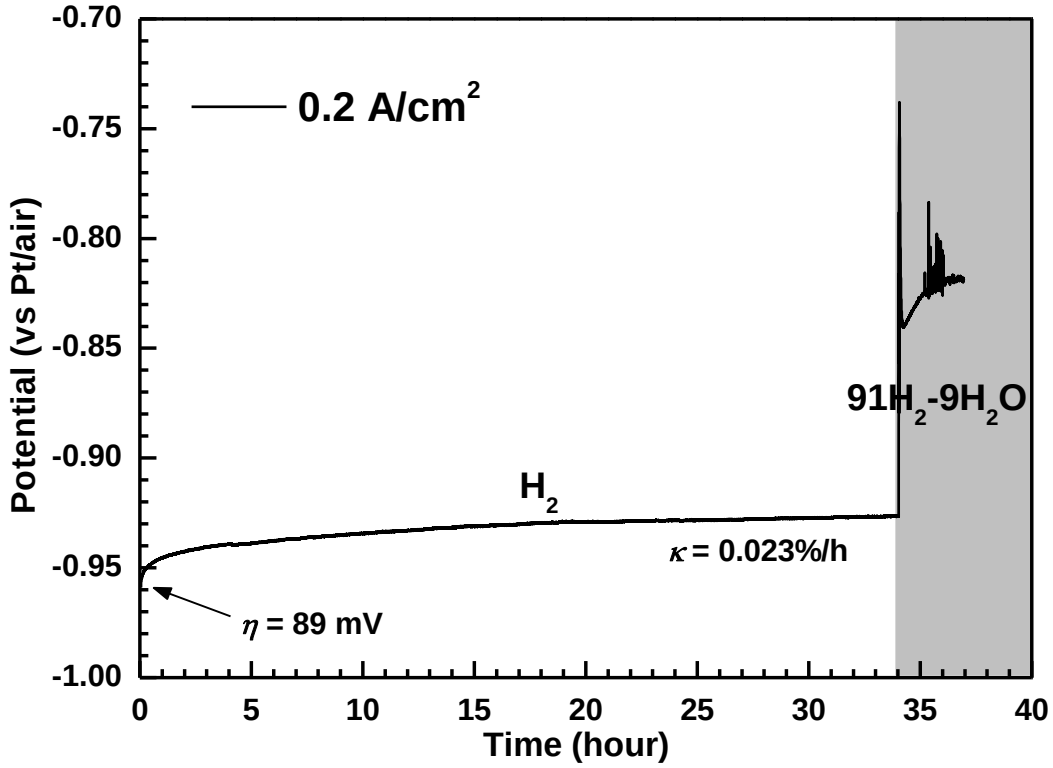

Figure 5-7 Long-term chronopotentiometry of the LSV anodes exposed to pure H_2 and $91H_2$–$9H_2O$ under anodic current density of 0.2 A/cm^2.

5.5 LSV anodes exposed to simulated practical fuels: syngas, biogas, and coal gas

50 ppm H_2S was added to H_2 to test the sulphur tolerance of LSV. Figure 5-8 shows the electrode behaviour under a current density of 0.2 A/cm^2. η suddenly jumps from 91 mV to 102 mV when the H_2 fuel is tainted by 50 ppm H_2S. This fast electrode degradation is most probably related to the H_2S adsorption onto LSV, which consequently blocks the electrochemical reaction sites. This type of degradation lasts for 3 h and results in the η change of 1 mV, where the adsorption/desorption equilibrium of H_2S has been established. The LSV electrode undergoes a performance improvement of 0.012%/h (i.e. κ = -0.012%/h), rather than degradation, in the following 112 h. η finally reaches 97 mV after the 130h fuel cell operation, which is only 6 mV higher than that in pure H_2. The salient long-term stability is also evident in the microstructural analysis. As can be seen in Figs. 5-9a and 5-9b, little change of the microstructure has been observed for the microstructure between the freshly prepared

electrode and the electrode subjected to 130h polarization. It is of great interest to note that LSV is catalytically active in H_2–50ppm H_2S and has being continuously improved at least up to a few hundred hours.

To further demonstrate the suitability of LSV towards practical gases, it is subjected to a continuous testing on simulated town gas, biogas, and coal gas with 50 ppm H_2S (Table 5-1). The LSV electrode exhibits non-negligible performance degradation (κ = 0.090%/h) under the circumstance of fuel cell polarization in 70H_2–30CO (Fig. 5-10a), a typical composition of syngas. Interestingly, the LSV electrode enjoys performance improvement (κ = -0.003%/h) merely by adding the feedstock with 50 ppm H_2S. After the 52h fuel cell operation, R_p of this syngas is only 0.07 Ω cm^2 larger than that of the freshly made electrode in H_2 (Fig. 5-11). A coal gas composition is simulated by replacing 5% of H_2 with CO_2 in the previous feedstock, *i.e.* 65H_2–30CO–5CO_2–50 ppm H_2S. η of the electrode exposed to this coal gas is -68 mV. It decreases to -61 mV after the 10-h electrolysis (Fig. 5-10a). After 3h standby exposure to H_2–50 ppm H_2S the LSV electrode is subjected to fuel cell polarization in H_2–50 ppm H_2S and then 75H_2–25CO_2–50 ppm H_2S, a typical H_2–rich biogas with low CO_2 concentration. η and R_p in H_2–50 ppm H_2S is almost unchanged as comparing to fresh electrodes exposed to H_2 (*cf.* Figs. 5-10a and 5-10b for η; *cf.* Figs. 5-11 and 5-12 for R_p). The LSV electrode exhibits slight activation through the following 12 h, with κ of -0.087%/h in H_2–50 ppm H_2S and -0.069%/h in 75H_2–25CO_2–50 ppm H_2S (Fig. 5-10b). The results indicate that LSV SOFC anode performs satisfactorily in practical gases where carbon deposition can hardly occur, even with intermittent electrolysis processes.

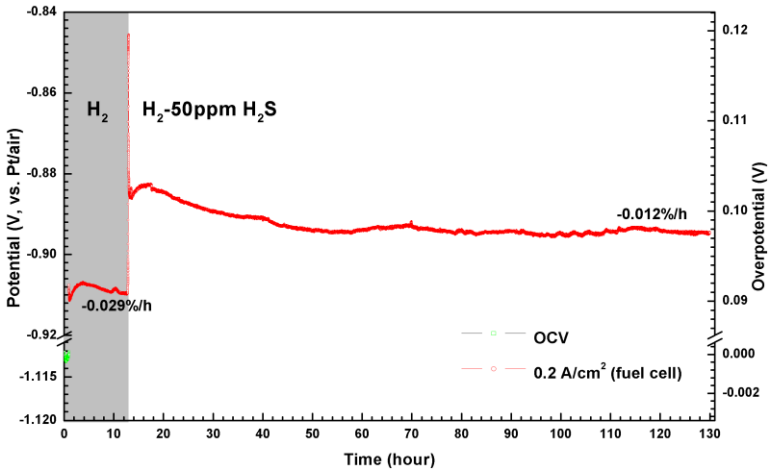

Figure 5-8 Long-term chronopotentiometry of the LSV electrodes under 0.2 A/cm^2 (fuel cell mode), with response to the gas shift from pure H_2 to H_2-50 ppm H_2S.

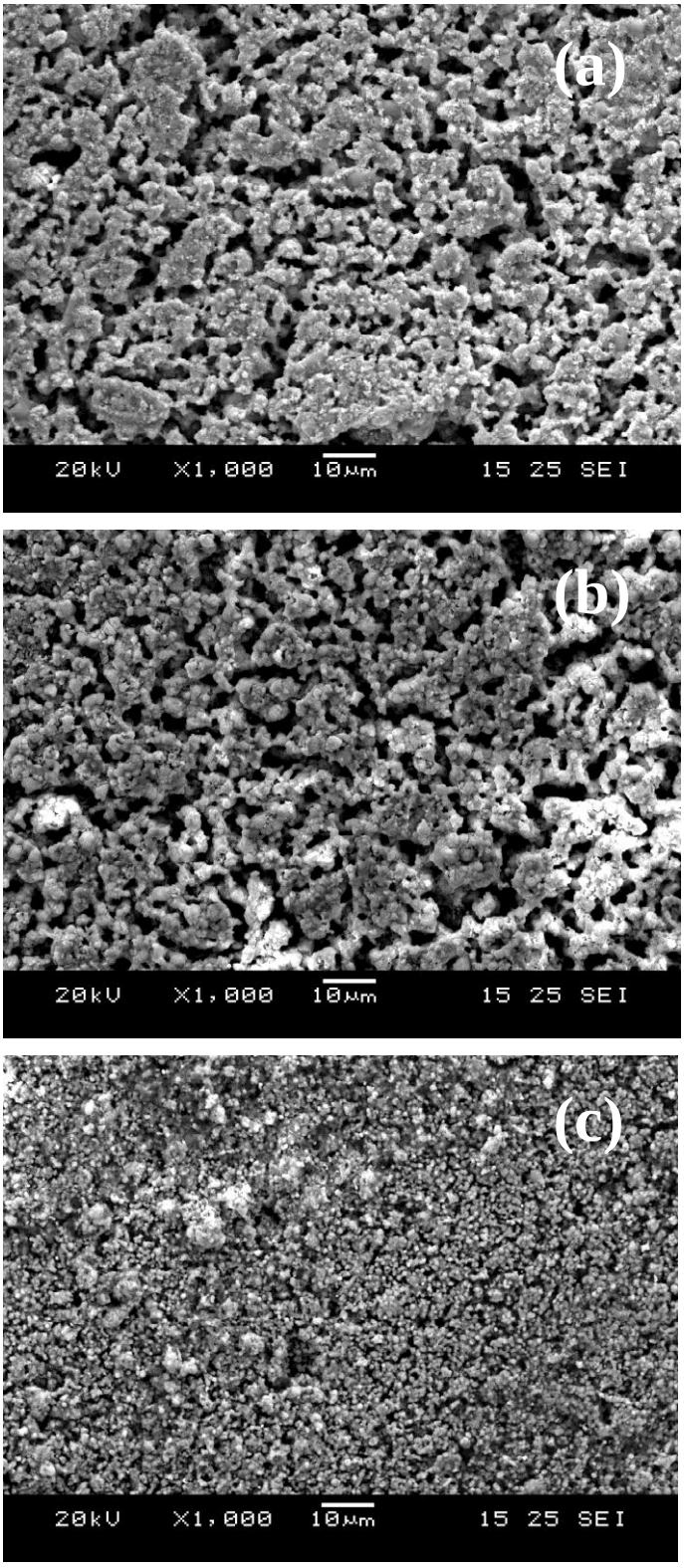

Figure 5-9 Typical low-magnification SEM images of LSV electrodes: (a) freshly reduced (a), operated in fuel cell mode and in H_2–50 ppm H_2S for 127 hours (b), and operated under alternating fuel cell and electrolyser modes and various H_2S-tainted and carbon-forming feedstocks according to Fig. 4 (c).

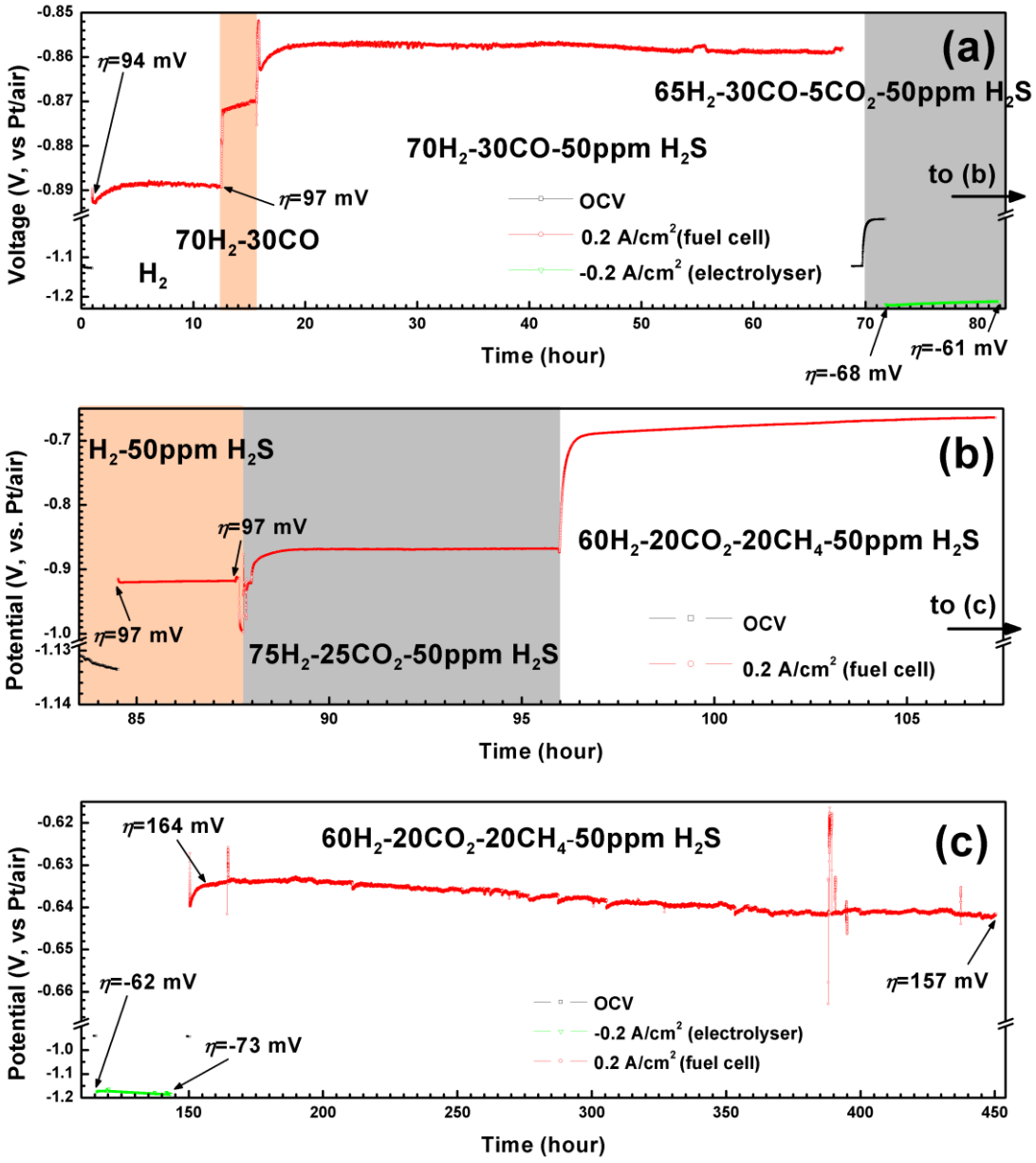

Figure 5-10 Long-term chronopotentiometry of the LSV electrodes exposed to H_2S-tainted feedstocks. The whole figure is divided into (a) to (d) merely for the clear illustration purpose.

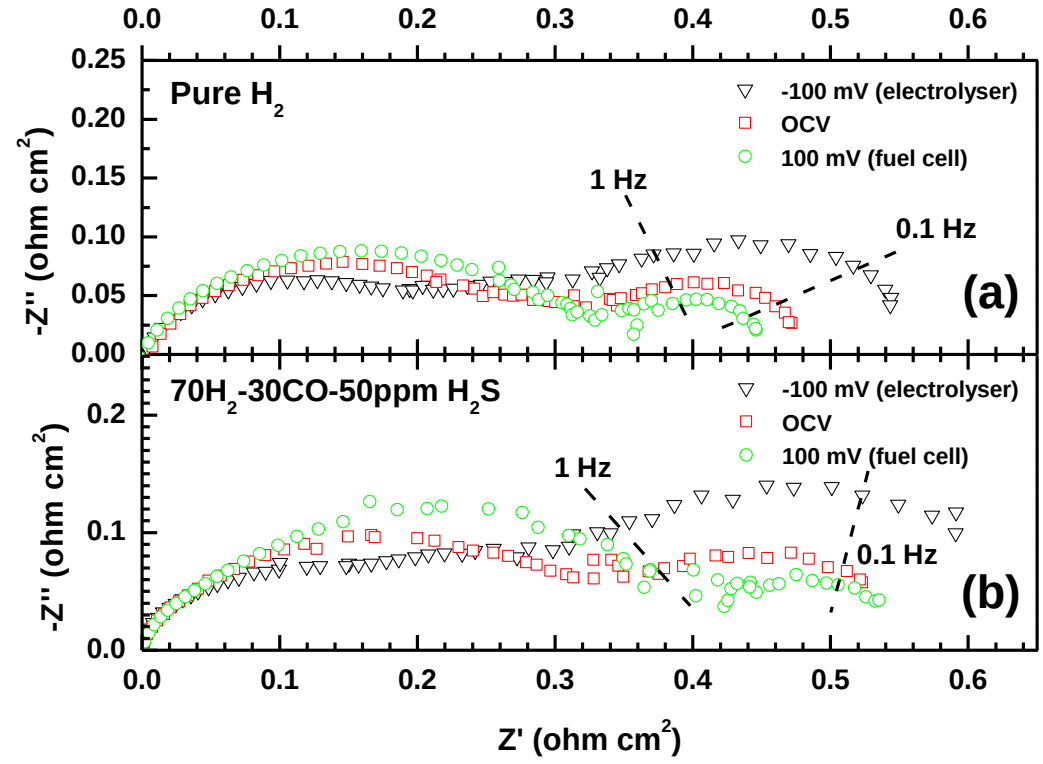

Figure 5-11 Impedance spectra of the LSV electrode as mentioned in Fig. 5-10a: (a) the freshly prepared electrode in pure H_2 and (b) the electrode after 70-hour fuel cell polarization and in the 70H_2–30CO–50ppm H_2S atmosphere.

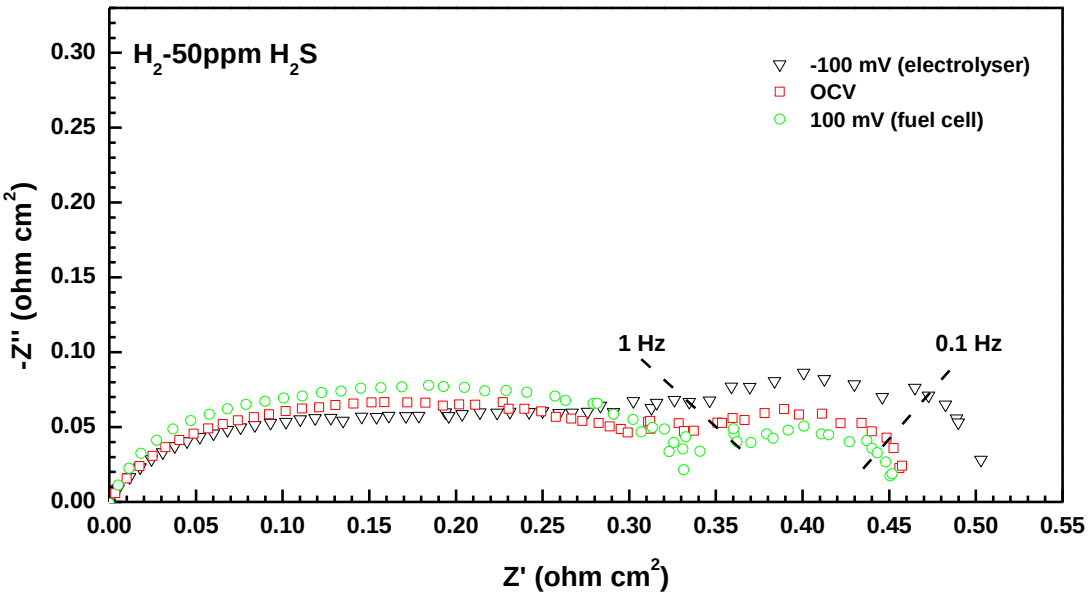

Figure 5-12 Impedance spectra of the LSV electrode exposed to H_2–50ppm H_2S, as mentioned in Fig. 5-10b.

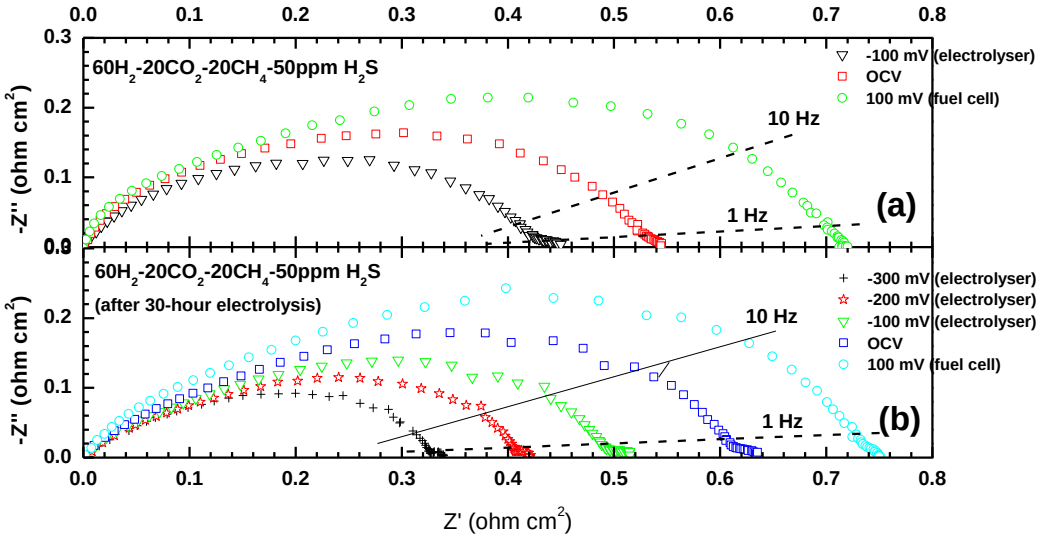

Figure 5-13 Impedance spectra of the LSV electrode exposed to $60H_2$–$20CO_2$–$20CH_4$–50 ppm H_2S as mentioned in Fig. 5-10c: (a) before electrolysis and (b) after the 30-hours electrolysis.

Once the feedstock is shifted to $60H_2$–$20CO_2$–$20CH_4$–50 ppm H_2S, a simulated gas blend of H_2-rich and CH_4-rich biogases that is prone to carbon formation, the electrode potential is suddenly increased from -0.868 V to -0.692 V. This is mainly due to the OCV reduction after the gas shifting. Nevertheless, large k of 0.377%/h has been observed during the 12h fuel cell polarization (Fig. 4-9b). Two degradation mechanisms might exist: (*i*) carbon coking of electrodes and (*ii*) surface oxidation of LSV. To eliminate the ambiguity, the LSV electrode is subsequently subjected to electrolysis for 25 h. The dry reforming of CH_4 by CO_2 is suppressed because CO_2 is reduced to CO during the electrolysis. Therefore, CH_4 pyrolysis dominates and the carbon deposition is more remarkable in electrolyser than that in fuel cell. If the degradation is controlled by the carbon coking mechanism, the electrode degradation after the 25h electrolysis should be more serious than that before the electrolysis. In contrast to this prediction, the electrode potential and R_p have been little changed before and after the electrolysis (-0.664 V vs -0.639 V, *cf.* Fig. 4-9b and Fig. 4-9c; R_p in Fig. 5-13). More distinctively and interestingly, continuous electrode activation with k = -0.05%/h has been observed in the 300h fuel cell operation (Fig. 4-9c). These results clearly rule out the carbon coking mechanism. The most probable mechanism is that the "oxidized" LSV surface has been reconstructed by the reducing environment that is created by electrolysis. Table 5-2 shows the exchange current densities of LSV anodes

exposed to various atmospheres. In line with the results shown in Fig. 5-6, $i_{0\text{-a}}$ is systematically larger than $i_{0\text{-c}}$ in all the fuels. It is surprising to note that the i_0 from the Levenburg–Marquardt (LEV) Tafel fitting method is several times larger than that from traditional Tafel fitting. The underlying reasons are unknown of this moment.

Improved microstructure could be a plausible reason for the continuous electrode activation. It is, however, difficult to explain why both electrodes are activated but their microstructures are distinct for two LSV electrodes that are addressed in Figs. 5-8 and 5-10. The "fine" microstructure of the electrode exposed to carbon-forming gases might be the artefact from deposited carbon particles (*cf.* Figs. 5-9b and 5-9c; *cf.* Figs. 5-14 and 5-15). The exact mechanism of the electrode activation is currently unknown. These promising results, nevertheless, demonstrate that LSV performs satisfactorily at least up to a few hundreds of hours even with the presence of carbon deposition.

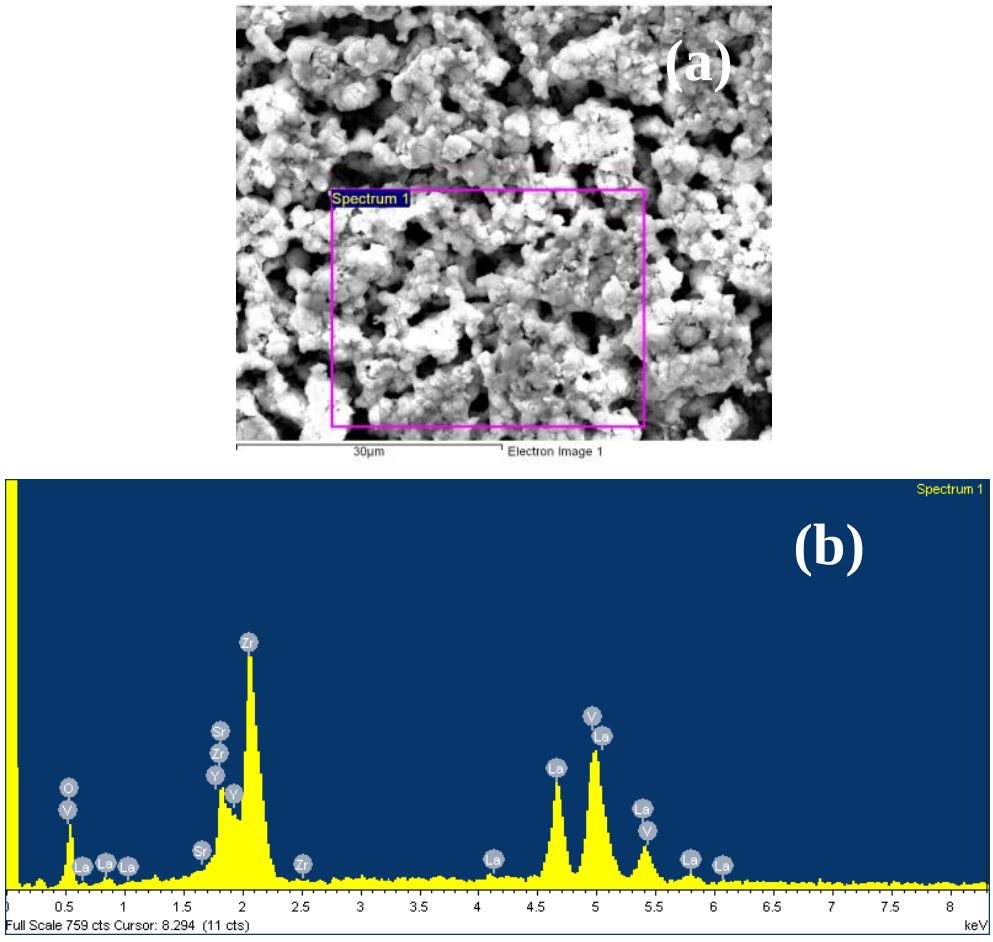

Figure 5-14 The selected area (a) and the corresponding EDX spectrum (b) of the LSV electrode after the fuel cell operation in H_2–50 ppm H_2S for 127 hours. No sulphur is found within the detection limit of EDX.

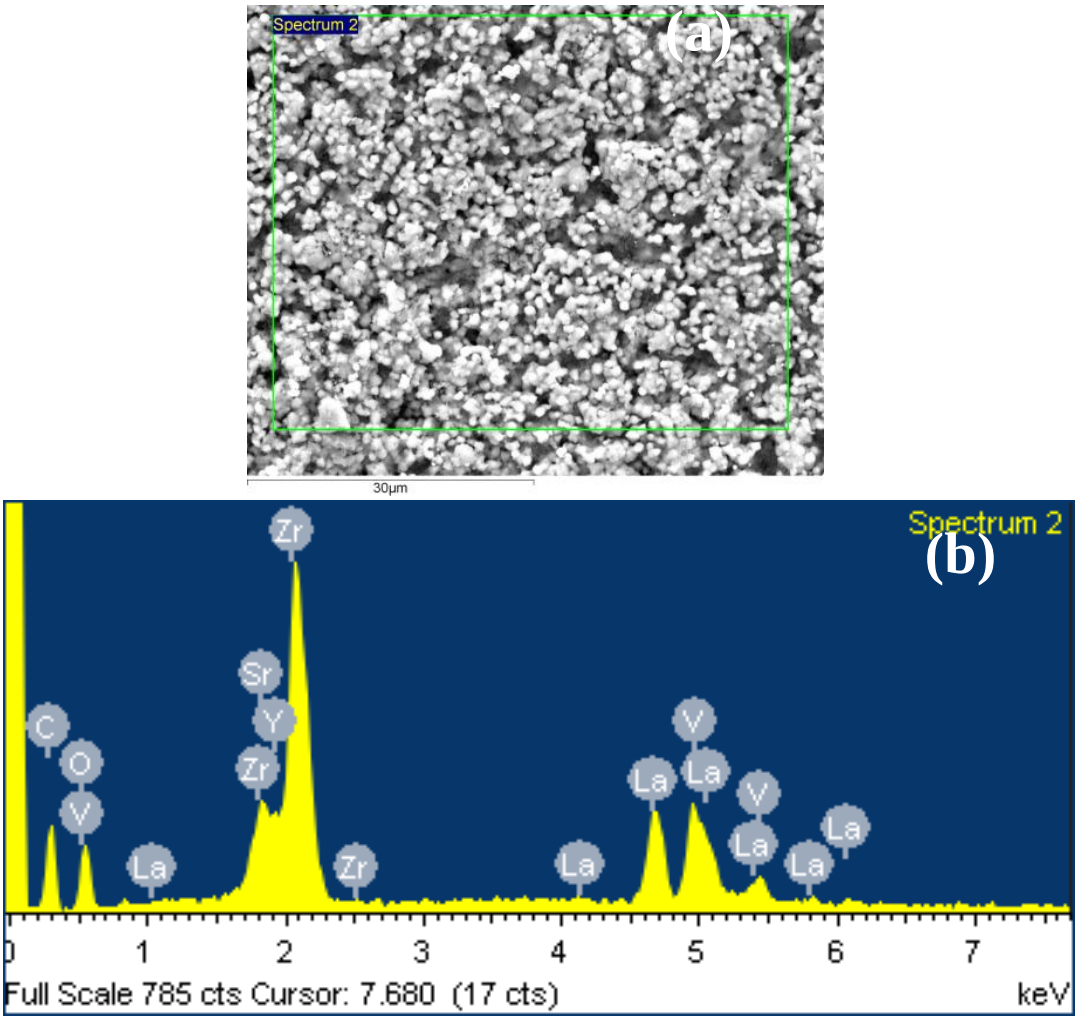

Figure 5-15 The selected area (left) and the corresponding EDX spectrum (right) of the LSV electrode, under alternating fuel cell and electrolyser modes and various H_2S-tainted and carbon-forming feedstock atmospheres for 498 hours, as illustrated in Fig. 5-10. Significant amount of carbon is observed. No sulphur is detected within the detection limit of EDX.

Table 5-2 Exchange current density of LSV anodes exposed to various atmospheres as addressed in Chapter 5.5.

Fuel	Cathodic i_0 $i_{0\text{-c}}$ (A/cm^2)	Anodic i_0 $i_{0\text{-a}}$ (A/cm^2)	LEV	
			i_0 (A/cm^2)	χ^2
H_2	0.108	0.122	0.525	9.339
30CO–70H_2–50ppm H_2S	0.113	0.153	0.755	47.74
20CO_2–20CH_4–60H_2–50 ppm H_2S	0.069	0.102	0.257	0.266
20CO_2–20CH_4–60H_2–50 ppm H_2S	0.058	0.090	0.152	0.486
H_2–50ppm H_2S	0.091	0.129	0.572	46.24
97H_2-3H_2O-50ppm H_2S	0.060	0.132	0.223	0.343

While LSV is excellent in carbon resistance, it is still not clear why it is activated, instead of poisoned, by H_2S-containing feedstock. Scanning electron microscopy (SEM) analyses show negligible contributions of H_2S on modifying electrode microstructure (Figs. 5-9a and 5-9b). This is conceivable because the H_2S concentration is only 50 ppm and most sulphur-containing species, e.g. S, CS_2, are volatile at 900℃. One of the possible mechanisms is the formation of metal sulphides that are catalytically active for fuel cell and electrolysis reactions. Figures 5-16a, 5-16b, and 5-16c show high-resolution surface morphology images of LSV electrodes that are freshly prepared, exposed to H_2–50 ppm H_2S as corresponding to Fig. 5-8, and various feedstocks as corresponding to Fig. 5-9, respectively. No fine structures are observed in the freshly prepared electrode (Fig. 5-16a). Modest amount of nanoparticles are observed in the electrode with 120-h exposure to H_2S (Fig. 5-16b). Large quantity of relatively uniform-sized nanoparticles, with diameter of 5.5 ± 0.9 nm (Fig. 5-17), exists on electrode surfaces that were exposed to H_2S for 510 h (Fig. 5-16c). The nanoparticles are tentatively regarded as certain metal sulphides. The matrix of these nanoparticles should be LSV, as vanadium-based oxides have good affinity to H_2S while YSZ is essentially inert towards H_2S. The concentration of these nanoparticles is still below the detection limit of energy-dispersive X-ray spectroscopy (EDX, Figs. 5-14 and 5-15). In literature, various vanadium-based sulphides had been reported with high electrical conductivity (Kijima *et al.*, 1996) and catalytic activity towards H_2S oxidation (Li *et al.*, 1996). These nanoparticles may lead to enlarged reaction areas and enhanced reaction kinetics, *e.g.* adsorption/desorption, dissociation, and spillover of surface species.

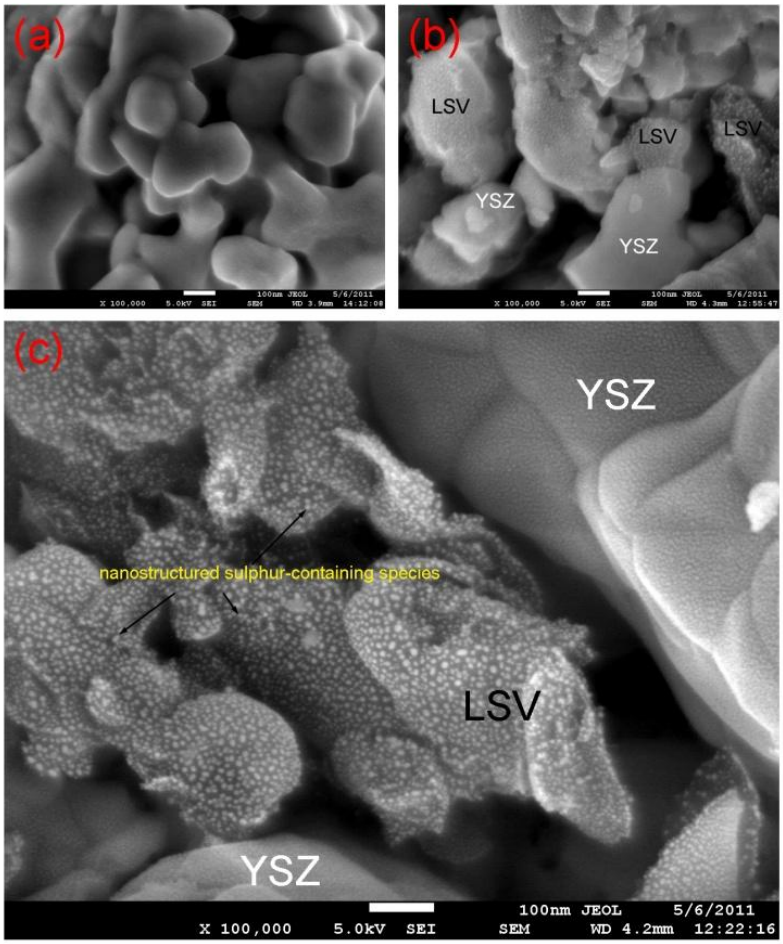

Figure 5-16 Field-emission SEM images of LSV electrode surfaces: (a) freshly reduced, (b) after the fuel cell testing in H_2– 50 ppm H_2S for 120 hours (Fig. 5-8), and (c) after the long term testing as given in Fig. 5-10.

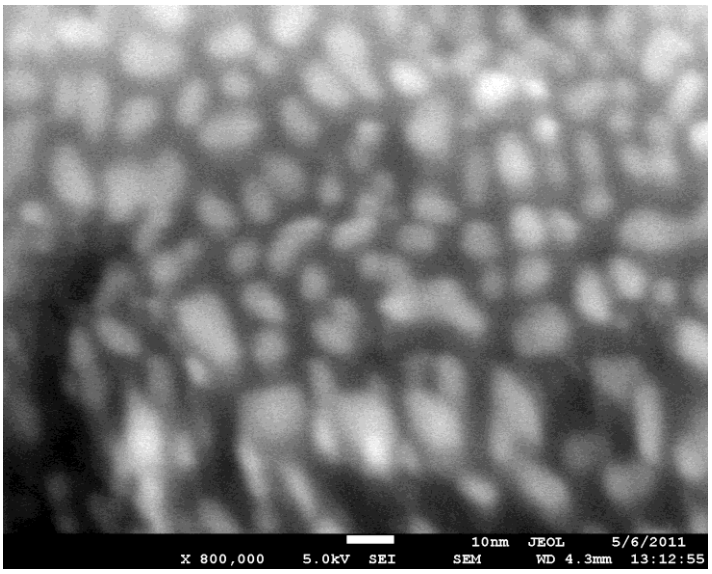

Figure 5-17 High magnification surface morphology images of LSV surfaces, after the 510-h operation according to Fig. 5-10. For the deposited particles, the mean size is 5.5 nm and the standard deviation is 0.9 nm.

To some extent, the nanoparticle decoration on LSV surface is very similar to the extensively-studied impregnation method (Jiang, 2006). The ultimate goal of impregnation is to decorate the electrocatalyst surfaces with highly active nanoparticles. One of the fatal disadvantages of impregnated nanoparticles is their thermal instability. In contrast, the *in situ* "sulphur-decorated" nanoparticles that precipitate on LSV surfaces seem to be very stable for more than 500 hours. The nanoparticles are generated continuously by interactions between LSV and H_2S during the course of high temperature SOFC operation. This is in distinct contrast to impregnated nanoparticles under elevated temperatures, which are largely eliminated due to particle sintering. This approach represents a novel route for fabricating nanostructured electrodes in high temperature energy and conversion devices.

5.6 Summary

The feasibility of SOFCs fed with practical feedstocks has been proven by utilizing LSV-based hydrogen electrodes. LSV is catalytically active in various gases, *e.g.* H_2, syngas, biogas, town gas, and coal gas, under fuel cell and electrolyser modes. LSV electrodes are not coked by deposited carbon when exposed to carbon-forming gases. More interestingly, LSV undergoes continuous activation, rather than poisoning, when exposed to gases containing 50 ppm H_2S. The beneficial H_2S effect is probably due to the nanostructured sulphur compounds that are in situ generated by interactions between LSV and H_2S. LSV-based reversible SOCs, operated under fuel cell and electrolyser modes, have been demonstrated with negligible performance degradation in carbon-forming and H_2S-containing gases for more than 500 hours.

Chapter 6. Conclusions and recommendations

6.1 Conclusions

The objective of this project is to explore satisfactory anodes for SOFCs fed with hydrocarbon fuels and to investigate the interfacial properties of anode/electrolyte junctions in SOFCs. Based on the results and discussion of this project, the following conclusions can be drawn:

- $La_{1-x}Sr_xVO_3$ (LSV) with x = 0.0, 0.05, 0.1, 0.2, 0.3, 0.4, 0.5, 0.8, 0.9, 0.95, 1.0 were synthesized by solid state reactions, both in oxidized and reduced form. LSV_{Ox} was regarded as a mixture of $LaVO_4$ and $Sr_2V_2O_7$. Single phase can be obtained only for LSV_{Re} (x = 0, 0.05, 0.1) and $LSV5050_{Re}$. LSV_{Re} (x = 0.2, 0.3, 0.4) was a binary phase structure between $LaVO_3$ and $(La_{0.50}Sr_{0.50})VO_{2.95}$. Chemical compatibility with YSZ had been confirmed at least up to 1300 ℃. TGA analysis indicated non-negligible oxygen nonstoichiometry of LSV_{Re}. Impedance spectroscopy indicated the necessity of incorporating ionic components into LSV in order to extend the TPBs from the anode/electrolyte interface.

- LSV_{Re} (x= 0.2, 0.3, 0.4, 0.5)–YSZ Composite anodes showed comparable electrode performance to those more well-studied conducting oxide anodes, such as LSCM. Electrode engineering was conducted by means of sintering temperature and electrode composition. LSV anodes were not able to be sintered satisfactorily below 1150 ℃. Once exposed to pure H_2, composite anodes with more than 70 wt.% of LSV peeled off from the YSZ electrolyte substrate. Composite anodes with LSV less than 40 wt.% failed to form an electronically percolating network. LSV6040 (50 wt. %)–YSZ anodes achieved R_p of 0.7–1.1 Ω cm^2 in pure H_2 at 900 ℃. The anodic overpotential was lower than 0.2 V when drawing a current density of 0.2 A/cm^2. The apparent activation energies were in the range from 0.42 to 0.71 eV for the four LSV_{Re} (x= 0.2, 0.3, 0.4, 0.5)–YSZ anodes. Good thermal stability had been achieved. Preliminary studies indicated that LSV–YSZ anodes, at least LSV6040 (50 wt. %)–YSZ, were active for CH_4 oxidation. For half-cells fed with 3% H_2O saturated CH_4 at 900 ℃, polarization resistance of LSV6040 (50

wt. %)–YSZ anode reached 1.4 Ω cm^2 at the open circuit condition. Polarization curves showed that the current density reached 0.2 A/cm^2 with the anodic overpotential less than 0.2 V.

- Modest single cell performance, with the configuration of LSV6040–YSZ/YSZ (300 μm)/LSM–YSZ/(LSM), had been demonstrated. When fed with pure H_2 and operated at 900 ℃, R_p of the single cell was 0.84 ohm cm^2 and P_{max} was 0.28 W/cm^2. When the fuel gas was switched to 3% H_2O humidified CH_4, R_p was increased to 1.22 ohm cm^2 and P_{max} was 0.13 W/cm^2. Single cell performance achieved in this study was among the best of SOFCs using vanadate anodes. Whatever the fuels were the cell performance, nevertheless, showed great temperature dependencies.
- Impedance behaviours of LSV8020(50 wt. %)–YSZ composite anodes, with LSV8020 synthesized from citric route, were investigated in H_2–H_2O–He atmosphere. Impedance spectra in H_2–He binary atmosphere mostly contained two depressed and poorly separated impedance arcs, and occasionally inductive loops at extremely low frequencies and under large potential biases. The high frequency arc, Arc 1, was ascribed to the reaction resistance. The middle-to-low frequency arc, Arc 2, was identified as the concentration impedance due to the porous electrodes or gas channels. Small inductive loops, Arc 3, came to emerge when dc potential biases were larger than 250 mV. Great efforts were paid to the double layer capacitance. The EIS method gave "correct" capacitance in the order of 10^{-1} mF/cm^2. In contrast, capacitance obtained from the transient methods was contaminated by the double layer charging phenomenon. For impedance spectra collected in wet fuel atmosphere, Arc 1 was still maintained but Arc 2 collapsed together at low frequencies. A detrimental water effect, which had been seldom observed in most SOFC anodes, was identified up to 15 % H_2O.
- Two-dimensional oxygen vacancy distributions in the YSZ side of polarized LSV/YSZ interfaces had been successfully constructed via Markov Chain Monte Carlo simulations. The oxygen vacancy concentration directly adjacent to the interface was one order of magnitude larger than that in the bulk YSZ. The spatial ρ/ρ_0 profile could be empirically modelled as an exponential decay. The thickness of the H–P layer was in the range of 0.5 to 0.8 nm. The double

layer region extended about 2 nm into the bulk YSZ. The oxygen vacancy diagrams and ρ/ρ_0 profiles indicated the H–P layer accommodates 70–80% of the oxygen vacancies.

- The double layer capacitance of solid electrode/solid-electrolyte interfaces was investigated via a case study on LSV/YSZ interfaces in SOFC anodic environment. The magnitude of apparent double layer capacitance was of several hundreds of $\mu F/cm^2$. Under anodic polarized conditions, it exhibited a right-skewed volcano pattern that peaks around 20 to 50 mV. The intrinsic double layer capacitance exhibited similar "capacitance surge" behaviour. The phenomenon was ascribed to mutual competitions between the loosened H–P layer and the increase of Volta potential in the G–C layer. The numeric values of intrinsic double layer capacitance were, however, almost one order of magnitude lower than the apparent. Such kind of discrepancy was ascribed to the inconsistent areas that were used in the two cases. The capacitance analysis enabled in situ detection of active areas and TPBs of composite electrode/electrolyte interfaces in various solid state electrochemical systems.
- The interrelationship between TPBs and EAZs was investigated via a case study on LSV–YSZ composite anodes in SOFCs. The TPB lengths were calculated from a virtually packed and sintered particle aggregate. The packing and sintering methods were suitable for the optimization of SOFC composite electrodes. The length specific TPB length of LSV–YSZ composite anodes was 1.8×10^9 cm/cm, equivalent to a volume-specific TPB length of 3.9×10^9 cm/cm^3. The cross-section area of EAZs was basically 6 to 8 times of the geometric area. Empirical correlations among EAZs, TPBs, active electrode thickness, and in-depth penetration of electrocatalysts were established. Under the circumstance of polarized LSV–YSZ anodes, the active electrode thickness and in-depth penetration of electrocatalysts were typically in the range of 5–20 μm and 2–8 nm, respectively.
- The feasibility of SOFCs fed with practical fuels had been proven by utilizing LSV-based anodes. LSV was catalytically active in various gases, e.g. H_2, syngas, biogas, town gas, and coal gas. The polarization resistances were typically smaller than 0.4 $\Omega\ cm^2$ in these fuel atmospheres. LSV anodes were not coked by deposited carbon when exposed to carbon-forming gases. More interestingly, LSV undergone continuous activation, rather than poisoning, when

exposed to gases containing 50 ppm H_2S. The beneficial H_2S effect was probably due to the nanostructured sulphur compounds that were in situ generated by the reactions between LSV and H_2S. LSV-based reversible SOCs had been demonstrated with negligible performance degradation in carbon-forming and H_2S-containing gases for more than 500 hours.

6.2 Major achievements

- ❖ Proof-of-concept demonstration of LSV anodes, synthesized via either solid state reactions and citric route, as competitive candidates for SOFC anodes.
- ❖ Mechanistic investigation of impedance responses of LSV anodes in fuel dilution and high water content environment.
- ❖ Markov Chain Monte Carlo simulation of anode/solid electrolyte interfaces
- ❖ Modified Poisson–Boltzmann theory and the Volta potential analysis of the anode/solid electrolyte interfaces
- ❖ Established interrelationship between three phase boundary and electrochemically active zones
- ❖ Demonstration of the suitability of LSV anodes in practical hydrocarbon fuels.

6.3 Recommendations

- Integrating the double layer structure and reaction kinetics of anode/solid oxide interfaces. In this project, significant efforts had been paid to the interfacial structures, mainly the double layer structure, of anode/electrolyte interfaces via Monte Carlo simulation and analytical Poisson–Boltzmann theory. The ultimate merits of these kinds of interfacial analysis rely on the integration of them with interfacial reaction kinetics. This integration is of great importance simply by noting that practical fuel cells are operated under loading conditions. Such integration calls for the knowledge of electron transfer electrodics and relevant analysis on the gas diffusion and conversion phenomena.
- Expanding the series: doping into V-site of LSV. LSV can be further improved, in terms of structural stability, redox stability, and catalytic activity, by sophisticated and systematic tailoring. The priority goes to two of these issues: one is cell performance and the other is redox stability. To improve the cell

performance, a small amount of precious metals can be doped into V-site. Ruthenium, an economically competitive noble metal, may be able to be incorporated into V-site because of similar ionic radii with $V^{3+/}V^{4+}$. Some alternative dopants are transition metals. Fe, Co, and Ni are not in consideration because of their chemical instability in reducing atmosphere. The effects of Mn should be similar to Ru (i.e., to improve the catalytic performance), as some manganite (e.g., LSM and LSCM) are well-known to be catalytically effective. On the other hand, several titanates and chromites have been proved to be conductive and stable in SOFC anodic environments, as introduced in Chapter 2. Doping Ti and Cr into V sites could stabilize the LSV structure at oxidising environments.

- Electrode-supported SOFCs with LSV anodes. Decreasing electrolyte thickness is critical to minimize the overall cell losses. Thin electrolyte cells can be anode-supported, cathode-supported, interconnector-supported, or inert porous substrate supported. LSM-supported single cells with thin YSZ electrolyte and vanadate anodes seem most relevant. Alternatively, dual tape-casted YSZ electrolyte supported by porous YSZ substrate and impregnated electrodes can be used.
- The sulphur-tolerant mechanism. It is currently unknown whether the excellent sulphur tolerance of LSV anodes is of chemical or of electrochemical nature, though the formation of metal sulphide appears to be quite possible. Chemically speaking, metal sulphide could improve the conducting percolation networks or the adsorption/desorption behaviours of gas species. Electrochemically speaking, metal sulphide might have better charge transfer kinetics than LSV. Synergic chemical, electrochemical, and materials structure investigations should be carried out to resolve the ambiguity.

Appendix A: Gouy–Chapman capacitance of the LSV–YSZ interfaces

The Volta potential difference of the Gouy−Chapman (G–C) layer is divided into two parts: one is the linear part starting from the electrode/electrolyte interface to outer Helmholtz plane (oHp), and the other is the non-linear part decaying asymptotically into bulk electrolyte (Fig. 4-13a). While the linear part is described by the double-plate condenser model, the non-linear part calls for a Debye and Hückel's treatment. Main assumptions in this study are: (*i*) charge cloud approximation. Some oxygen vacancies are immobilized on the outer Helmholtz plane (oHp). The others beyond the oHp are smeared into continuous thermal disarray, thus creating a charge cloud from oHp to the bulk YSZ; (*ii*) continuum. The bulk YSZ is treated as a continuous dielectric medium; (*iii*) one dimension. The charge distribution is uniform in directions parallel to the LSV/YSZ interface; (*iv*) time-invariant. All treatments are in steady state conditions. Transient states with electric-magnetic interactions are not taken into account; (*v*) negligible electron and hole effects. Electron and hole concentrations are in orders lower than that of oxygen vacancies. The electroneutrality is maintained by $Y_{Zr}^{'}$ and $V_O^{\bullet\bullet}$.

For the sake of mechanistic lucidity we start from the derivation of Poisson's equation. Consider a Gaussian pillbox with radius *r* and length *l* (Fig. 3a). One of its two lateral surfaces situates in the LSV side and the other locates in the YSZ side. At a distance *x* away from oHp we denote the volumetric net charge density as $\rho_{(z)}$ and the Volta potential difference as

$$\Delta\Psi_{(z)} = \Psi_{(z)} - \Psi^{YSZ} \quad , \qquad \text{(A1)}$$

where $\Psi_{(z)}$ and Ψ^{YSZ} are the Volta potential at position *z* and the bulk YSZ ($z \to \infty$), respectively. In this study the Volta potential of the bulk YSZ is set to zero. $\Delta\Psi_{(z)}$ is therefore reduced to $\Psi_{(z)}$. The relationship between $\rho_{(z)}$ and $\Psi_{(z)}$ is derived from the Gauss's law of electrostatics,

$$\sum_{\mathrm{i}}\Phi_{\mathrm{i}}=\oiint_{\mathrm{S}}E_{\mathrm{G}}\mathrm{d}S=\frac{q_{\text{enclosed}}}{\varepsilon_0\varepsilon_{\mathrm{r}}}\rightleftharpoons\Phi_{E_{\mathrm{G}},\text{face-left}}+\Phi_{E_{\mathrm{G}},\text{face-right}}+\Phi_{\text{side}}=\frac{\rho_{(z)}\mathrm{d}V}{\varepsilon_0\varepsilon_{\mathrm{r}}}$$
$$\rightleftharpoons\pi r^2E=\pi r^2\left(-\frac{\mathrm{d}\Psi_{(z)}}{\mathrm{d}z}\right)=\frac{1}{\varepsilon_0\varepsilon_{\mathrm{r}}}\int_l^{l+\Delta z}\rho_{(z)}\pi r^2\mathrm{d}z \quad , \qquad \text{(A2)}$$

where $\Phi_{E_{\mathrm{G}}}$ is the electric flux, *S* the surface area of the Gaussian pillbox, *V* the volume of the Gaussian pillbox, ε_0 the vacuum permittivity, ε_{r} the relative static permittivity of YSZ in the G–C layer, *E* the electric field in the G–C layer, and q_{enclosed} the electric charges enclosed by the Gaussian pillbox, *i.e.* the net electric charges at LSV side (with vanishingly small distance away from the LSV/YSZ interface) balanced with oxygen vacancies at oHp. Differentiating the last right hand of Eq. A2 against *z* leads to Poisson's equation,

$$\frac{\mathrm{d}^2\Psi}{\mathrm{d}z^2}=-\frac{\rho_{(z)}}{\varepsilon_{\mathrm{r}}\varepsilon_0} \quad . \qquad \text{(A3)}$$

In Eq. A3 and also in below, the subscript (*z*) is omitted merely for notational simplicity (*e.g.* $\Psi_{(z)}$ as Ψ). The relationship between ρ and Ψ lies in the defect chemistry of YSZ. The charged species in YSZ are created by doping Y_2O_3 into ZrO_2 according to the overall reaction (using Kröger–Vink notations),

$$Y_2O_3\xrightarrow{2\,ZrO_2}2Y_{Zr}^{'}+V_O^{\bullet\bullet}+3O_O^X \quad . \qquad \text{(A4)}$$

$Y_{Zr}^{'}$ and $V_O^{\bullet\bullet}$ dominants according to the Assumption *v*. Under SOFC operating conditions ρ is then given by

$$\rho_{(z)}=e_0\sum_{\mathrm{i}}n_{\mathrm{i}}z_{\mathrm{i}}=e_0\left(n_{Y_{Zr}^{'}}z_{Y_{Zr}^{'}}+n_{V_O^{\bullet\bullet}}z_{V_O^{\bullet\bullet}}\right)=e_0\left(-n_{Y_{Zr}^{'}}+2n_{V_O^{\bullet\bullet}}\right) \quad , \qquad \text{(A5)}$$

where $n_{Y_{Zr}^{'}}$ and $n_{V_O^{\bullet\bullet}}$ are the concentration of $Y_{Zr}^{'}$ and $V_O^{\bullet\bullet}$, respectively. Eq. A4 implies $n_{Y_{Zr}^{'}}$ and $n_{V_O^{\bullet\bullet}}$ fulfils

$$n_{Y_{Zr}^{'}}^0=2n_{V_O^{\bullet\bullet}}^0 \quad , \qquad \text{(A6)}$$

where $n^0_{Y'_{Zr}}$ and $n^0_{V_O^{\cdot\cdot}}$ are the bulk concentration of Y'_{Zr} and $V_O^{\cdot\cdot}$, respectively. As the mobility of Y'_{Zr} is in orders of magnitude lower than that of $V_O^{\cdot\cdot}$ at elevated temperatures, $n_{Y'_{Zr}}$ is assumed to remain constant (as $n^0_{Y'_{Zr}}$) while $n_{V_O^{\cdot\cdot}}$ is potential-dependent and follows the Boltzmann distribution law. This behaviour of charged species in YSZ is distinct to that in aqueous solutions where both cations and anions are freely mobile. Charge concentrations of YSZ are then expressed as

$$n_{Y'_{Zr}} = n^0_{Y'_{Zr}} \quad , \qquad \text{(A7–1)}$$

$$n_{V_O^{\cdot\cdot}} = n^0_{V_O^{\cdot\cdot}} \exp\left(-\frac{U}{kT}\right) \quad , \qquad \text{(A7–2)}$$

where U is the potential energy, k the Boltzmann constant, and T the absolute temperature. Here U is negative because $V_O^{\cdot\cdot}$ has to be accumulated to balance the electrons in the LSV. U simply becomes the coulombic potential energy of $V_O^{\cdot\cdot}$ with the exclusion of short-range interactions (*e.g.* dispersion forces),

$$U = z_{V_O^{\cdot\cdot}} e_0 \Psi = 2e_0 \Psi \quad (\Psi < 0) . \qquad \text{(A8)}$$

Incorporating Eqs. A3, A5, A6, A7, and A8 one gets

$$\frac{\mathrm{d}^2\Psi}{\mathrm{d}z^2} = \frac{2e_0 n^0_{V_O^{\cdot\cdot}}}{\varepsilon_r \varepsilon_0}\left[1 - \exp\left(-\frac{2e_0}{kT}\Psi\right)\right] \quad , \qquad \text{(A9–1)}$$

or in another form

$$\frac{\mathrm{d}^2\Psi}{\mathrm{d}z^2} = -\frac{4e_0 n^0_{V_O^{\cdot\cdot}}}{\varepsilon_r \varepsilon_0} \sinh\left(\frac{e_0}{kT}\Psi\right)\exp\left(-\frac{e_0}{kT}\Psi\right) \quad , \qquad \text{(A9–2)}$$

with the initial condition

$$\Psi_{z=z_{oHp}} = \Psi^{oHp} - \Psi^{YSZ} = \Psi^{oHp} \quad , \qquad \text{(A10–1)}$$

and the boundary conditions

$$\lim_{z \to z_{oHp}^{+}} \frac{\mathrm{d}\Psi_G}{\mathrm{d}z} = \lim_{z \to z_{oHp}^{-}} \frac{\mathrm{d}\Psi_H}{\mathrm{d}z} \qquad \text{(A10–2)}$$

and

$$\lim_{z\to\infty}\Psi = 0,\ \lim_{z\to\infty}\frac{\mathrm{d}\Psi}{\mathrm{d}z} = 0 \quad . \qquad \text{(A10–3)}$$

Eq. A9 has been the quintessential form that describes the spatial Volta potential variations of the G–C layer. It can be linearized if $2e_0\Psi$ is much smaller than kT (say, ten times), which is equivalent to a Ψ value not higher than 5 mV. Here the difficulty is that $\Psi_{(z)}$ is hard to be determined experimentally. To a rather qualitative guesstimate, Ψ is highly implausible of only several mV, taking typical OCV values (*ca* 1.2 V) under H_2 atmosphere into account. To conclude, Eq. A9 cannot be linearized under SOFC operating conditions. The boundary condition, Eq. A10–3, is provided only for an explanatory purpose. It is useless in solving Eq. A9, albeit useful to derive the differential capacitance (see below).

The following session is dedicated to derive the Gouy−Chapman capacitance (C_G) in function of the Volta potential. Recall the well-known relationship between E and Ψ

$$E = -\frac{\mathrm{d}\Psi}{\mathrm{d}z} \quad . \qquad \text{(A11)}$$

The $\Psi - E$ relationship is obtained by substituting Eq. A11 into Eq. A9–1,

$$E\frac{\mathrm{d}E}{\mathrm{d}\Psi} = \frac{2e_0 n^0_{V_O^{\cdot\cdot}}}{\varepsilon_r\varepsilon_0}\left[1-\exp\left(-\frac{2e_0}{kT}\Psi\right)\right] \quad . \qquad \text{(A12)}$$

One of the analytical solutions of Eq. A12 that is physically meaningful is

$$E = -\frac{\mathrm{d}\Psi}{\mathrm{d}z} = -\sqrt{\frac{2kTn^0_{V_O^{\cdot\cdot}}}{\varepsilon_r\varepsilon_0}\exp\left(-\frac{2e_0}{kT}\Psi\right)+\frac{4e_0 n^0_{V_O^{\cdot\cdot}}}{\varepsilon_r\varepsilon_0}\Psi + C} \quad , \qquad \text{(A13)}$$

where C is the constant to be determined. Applying Eq. A10–3 to Eq. A13 one gets

$$C = -\frac{2kTn^0_{V_O^{\cdot\cdot}}}{\varepsilon_r\varepsilon_0} \quad . \qquad \text{(A14)}$$

Substituting Eq. A14 back into Eq. A13 one yields

$$\left(\frac{\mathrm{d}\Psi}{\mathrm{d}z}\right)=\sqrt{\frac{2n^{0}_{V_O^{\cdot\cdot}}}{\varepsilon_r\varepsilon_0}}\sqrt{kT\left[\exp\left(-\frac{2e_0}{kT}\Psi\right)-1\right]+2e_0\Psi} \quad . \qquad \text{(A15)}$$

Eq. A15 cannot be solved analytically anymore. Fortunately Eq. A15 is quite enough to obtain C_G. According to the Gauss's law of electrostatics it reads

$$\sigma_G=\varepsilon_r\varepsilon_0\left(\frac{\mathrm{d}\Psi}{\mathrm{d}z}\right)_{z=z_{oHp}} \quad , \qquad \text{(A16)}$$

where σ_G is the area specific charge density on the faces of Gaussian pillbox (Fig. 3a). Substituting Eq. A15 into Eq. A16 one obtains

$$\sigma_G=\sqrt{2\varepsilon_r\varepsilon_0 n^{0}_{V_O^{\cdot\cdot}}}\sqrt{kT\left[\exp\left(-\frac{2e_0}{kT}\Psi_G\right)-1\right]+2e_0\Psi_G} \quad . \qquad \text{(A17)}$$

C_G is obtained by differentiating σ_G against Ψ,

$$C_G=\frac{\mathrm{d}\sigma_G}{\mathrm{d}\Psi_G} \quad . \qquad \text{(A18)}$$

Finally, one gets the relationship between C_G and Ψ_G by substituting Eq. A17 into Eq. A18,

$$C_G=e_0\left[\exp\left(-\frac{2e_0}{kT}\Psi_G\right)-1\right]\sqrt{\frac{2\varepsilon_r\varepsilon_0 n^{0}_{V_O^{\cdot\cdot}}}{kT\left[\exp\left(-\frac{2e_0}{kT}\Psi_G\right)-1\right]+2e_0\Psi_G}} \quad . \qquad \text{(A19)}$$

REFERENCES

ABBASPOUR, A., LUO, J. L. & NANDAKUMAR, K. 2010. Three-dimensional random resistor-network model for solid oxide fuel cell composite electrodes. *Electrochimica Acta,* 55**,** 3944-3950.

ABBOTT, A. P. & HARPER, J. C. 1999. Double layer capacitance and conductivity studies of long chain quaternary ammonium electrolytes in supercritical carbon dioxide. *Physical Chemistry Chemical Physics,* 1**,** 839-841.

ABUDULA, A., IHARA, M., KOMIYAMA, H. & YAMADA, K. 1996. Oxidation mechanism and effective anode thickness of SOFC for dry methane fuel. *Solid State Ionics,* 86-8**,** 1203-1209.

ADLER, S. B., LANE, J. A. & STEELE, B. C. H. 1996. Electrode kinetics of porous mixed-conducting oxygen electrodes. *Journal of the Electrochemical Society,* 143**,** 3554-3564.

AGUEY-ZINSOU, K.-F. & ARES-FERNANDEZ, J.-R. 2010. Hydrogen in magnesium: new perspectives toward functional stores. *Energy & Environmental Science,* 3**,** 526-543.

AGUILAR, L., ZHA, S. W., CHENG, Z., WINNICK, J. & LIU, M. L. 2004a. A solid oxide fuel cell operating on hydrogen sulfide (H2S) and sulfur-containing fuels. *Journal of Power Sources,* 135**,** 17-24.

AGUILAR, L., ZHA, S. W., LI, S. W., WINNICK, J. & LIU, M. 2004b. Sulfur-tolerant materials for the hydrogen sulfide SOFC. *Electrochemical and Solid State Letters,* 7**,** A324-A326.

AN, S., LU, C., WORRELL, W. L., GORTE, R. J. & VOHS, J. M. 2004. Characterization of Cu-CeO2 direct hydrocarbon anodes in a solid oxide fuel cell with lanthanum gallate electrolyte. *Solid State Ionics,* 175**,** 135-138.

ARMOR, J. N. 1999. The multiple roles for catalysis in the production of H2. *Applied Catalysis A: General,* 176**,** 159-176.

ARMSTRON.RD & MASON, R. 1973. Double-layer capacity measurments involving solid electrolytes. *Journal of Electroanalytical Chemistry,* 41**,** 231-241.

ASAMOTO, M., MIYAKE, S., SUGIHARA, K. & YAHIRO, H. 2009. Improvement of Ni/SDC anode by alkaline earth metal oxide addition for direct methane-solid oxide fuel cells. *Electrochemistry Communications,* 11**,** 1508-1511.

ASHBY, M. F. 1974. A first report on sintering diagrams. *Acta Metallurgica,* 22**,** 275-289.

ASHLEY, K., WEINERT, F. & FELDHEIM, D. L. 1991. Infrared spectroscopy to probe the electrochemical double layer. *Electrochimica Acta,* 36**,** 1863-1868.

BABAEI, A. & JIANG, S. P. 2010. Analysis of fuel oxidation reaction steps in Ni/GDC anode electrode of solid oxide fuel cells by using palladium Nanoparticles. *In:* MOHAMMED, W. S. & CHUNG, T. Y. (eds.) *Southeast Asian International Advances in Micro/Nanotechnology.*

BABAEI, A., JIANG, S. P. & LI, J. 2009. Electrocatalytic Promotion of Palladium Nanoparticles on Hydrogen Oxidation on Ni/GDC Anodes of SOFCs via Spillover. *Journal of the Electrochemical Society,* 156**,** B1022-B1029.

BAKER, J. 2008. New technology and possible advances in energy storage. *Energy Policy,* 36**,** 4368-4373.

BEK, D. 2009. Final Year Project Report (undergraduate dissertation), School of Mechanical and Aerospace Engineering, Nanyang Technological Univeristy.

BERENOV, A. V., ATKINSON, A., KILNER, J. A., BUCHER, E. & SITTE, W. 2010. Oxygen tracer diffusion and surface exchange kinetics in La0.6Sr0.4CoO3-delta, *Solid State Ionics*, 181, 819-926.

BESSLER, W. G., VOGLER, M., STORMER, H., GERTHSEN, D., UTZ, A., WEBER, A. & IVERS-TIFFEE, E. 2010. Model anodes and anode models for understanding the mechanism of hydrogen oxidation in solid oxide fuel cells. *Physical Chemistry Chemical Physics,* 12**,** 13888-13903.

BI, Z. H. & ZHU, J. H. 2009. A Cu-CeO2-LDC Composite Anode for LSGM Electrolyte-Supported Solid Oxide Fuel Cells. *Electrochemical and Solid State Letters,* 12**,** B107-B111.

BIEBERLE, A. 2000. PhD Thesis , ETH Zurich.

BIEBERLE, A. & GAUCKLER, L. J. 2000. Reaction mechanism of Ni pattern anodes for solid oxide fuel cells. *Solid State Ionics,* 135**,** 337-345.

BIEBERLE, A. & GAUCKLER, L. J. 2001. *Proceedings of Electrochemical Society,* 16**,** 728.

BIEBERLE, A., MEIER, L. P. & GAUCKLER, L. J. 2001. The electrochemistry of Ni pattern anodes used as solid oxide fuel cell model electrodes. *Journal of the Electrochemical Society,* 148**,** A646-A656.

BLENNOW, P., HANSEN, K. K., WALLENBERG, L. R. & MOGENSEN, M. 2009.

Electrochemical characterization and redox behavior of Nb-doped SrTiO3. *Solid State Ionics,* 180**,** 63-70.

BOER, B. D. 2000. PhD Thesis, University of Twente.

BOND, G. C., SÁRKÁNY, A. J. & PARFITT, G. D. 1979. The vanadium pentoxide-titanium dioxide system : Structural investigation and activity for the oxidation of butadiene. *Journal of Catalysis,* 57**,** 476-493.

BORDET, P., CHAILLOUT, C., MAREZIO, M., HUANG, Q., SANTORO, A., CHEONG, S. W., TAKAGI, H., OGLESBY, C. S. & BATLOGG, B. 1993. Structural aspects of the crystallographic magnetic transition in LaVO3 around 140-K. *Journal of Solid State Chemistry,* 106**,** 253-270.

BOULC'H. F. & DJURADO, E. 2002. Structural changes of rare-earth-doped, nanostructured zirconia solid solution, *solid state ionics,* 157, 335-340.

BOUVARD, D. & LANGE, F. F. 1991. Relation between percolation and particle coordination in binary powder mixtures. *Acta Metallurgica et Materialia,* 39**,** 3083-3090.

BRETT, C. M. A. & BRETT, A. M. O. 1994. *Electrochemistry: Principles, Methods, and Applications* New York Oxford University Press.

BRITISH PETROLEUM. 2010. BP statistical review of world energy 2010.

BROWN, M., PRIMDAHL, S. & MOGENSEN, M. 2000. Structure/performance relations for Ni/yttria-stabilized zirconia anodes for solid oxide fuel cells. *Journal of the Electrochemical Society,* 147**,** 475-485.

BULUSHEV, D. A., KIWI-MINSKER, L., ZAIKOVSKII, V. I. & RENKEN, A. 2000. Formation of active sites for selective toluene oxidation during catalyst synthesis via solid-state reaction of V2O5 with TiO2. *Journal of Catalysis,* 193**,** 145-153.

CANALES-VAZQUEZ, J., TAO, S. W. & IRVINE, J. T. S. 2003. Electrical properties in La2Sr4Ti6O19-delta: a potential anode for high temperature fuel cells. *Solid State Ionics,* 159**,** 159-165.

CANALES-VAZQUEZ, J., RUIZ-MORALES, J. C., IRVINE, J. T. S. & ZHOU, W. Z. 2005. Sc-substituted oxygen excess titanates as fuel electrodes for SOFCs. *Journal of the Electrochemical Society,* 152**,** A1458-A1465.

CAO, W., TAN, O. K., ZHU, W. & JIANG, B. 2000. Mechanical Alloying and Thermal Decomposition of (ZrO2)0.8-([alpha]-Fe2O3)0.2 Powder for Gas Sensing Applications. *Journal of Solid State Chemistry,* 155**,** 320-325.

CHAN, S. H. & XIA, Z. T. 2001. Anode micro model of solid oxide fuel cell. *Journal of*

the Electrochemical Society, 148**,** A388-A394.

CHAN, S. H., CHEN, X. J. & KHOR, K. A. 2004. Cathode micromodel of solid oxide fuel cell. *Journal of the Electrochemical Society,* 151**,** A164-A172.

CHAPMAN, D. L. 1913. *Philosophical Magazine,* 6**,** 475-481.

CHEN, D. F., LU, L., LI, J. Y., YU, Z. D., KONG, W. & ZHU, H. Y. 2011. Percolation micro-model to predict the effective properties of the composite electrode with poly-dispersed particle sizes. *Journal of Power Sources,* 196**,** 3178-3185.

CHENG, Z., ABERNATHY, H. & LIU, M. L. 2007. Raman spectroscopy of nickel sulfide Ni3S2. *Journal of Physical Chemistry C,* 111**,** 17997-18000.

CHENG, Z., ZHA, S. W., AGUILAR, L. & LIU, M. L. 2005. Chemical, electrical, and thermal properties of strontium doped lanthanum vanadate. *Solid State Ionics,* 176**,** 1921-1928.

CHENG, Z., ZHA, S. W., AGUILAR, L., WANG, D., WINNICK, J. & LIU, M. L. 2006. A solid oxide fuel cell running on H2S/CH4 fuel mixtures. *Electrochemical and Solid State Letters,* 9**,** A31-A33.

CHOI, S. H., WANG, J. H., CHENG, Z. & LIU, M. 2008. Surface modification of Ni-YSZ using niobium oxide for sulfur-tolerant anodes in solid oxide fuel cells. *Journal of the Electrochemical Society,* 155**,** B449-B454.

CIACCHI, F. T., CRANE, K. M. & BADWAL, S. P. S. 1994. Evaluation of commecial zirconia powders for solid oxide fuel-cells. *Solid State Ionics,* 73**,** 49-61.

CIMENTI, M. & HILL, J. M. 2010. Direct utilization of methanol and ethanol in solid oxide fuel cells using Cu-Co(Ru)/Zr0.35Ce0.65O2-delta anodes. *Journal of Power Sources,* 195**,** 3996-4001.

COMBEMALE, L., CABOCHE, G. & STUERGA, D. 2009. Flash microwave synthesis and sintering of nanosized La0.75Sr0.25Cr0.93Ru0.07o3-[delta] for fuel cell application. *Journal of Solid State Chemistry,* 182**,** 2829-2834.

Consultrsr, www.consultrsr.com/resources/diff-o.htm .

COOPER, M., CHANNA, K., DE SILVA, R. & BAYLESS, D. J. 2010. Comparison of LSV/YSZ and LSV/GDC SOFC Anode Performance in Coal Syngas Containing H2S. *Journal of the Electrochemical Society,* 157**,** B1713-B1718.

COSTA-NUNES, O., VOHS, J. M. & GORTE, R. J. 2003. A study of direct-conversion SOFC with n-butane at higher fuel utilization. *Journal of the Electrochemical Society,* 150**,** A858-A863.

COSTA, R., PEREIRA, C. M. & SILVA, F. 2010. Double layer in room temperature

ionic liquids: influence of temperature and ionic size on the differential capacitance and electrocapillary curves. *Physical Chemistry Chemical Physics,* 12**,** 11125-11132.

COSTAMAGNA, P., COSTA, P. & ANTONUCCI, V. 1998. Micro-modelling of solid oxide fuel cell electrodes. *Electrochimica Acta,* 43**,** 375-394.

CUMMING, D.J., KILNER & J. A., SKINNER, S. 2011. Structural properties of Ce-doped strontium titanate for fuel cell applications, *Journal of Materials Chemistry*, 21, 5021.

DANIELL, W., PONCHEL, A., KUBA, S., ANDERLE, F., WEINGAND, T., GREGORY, D. H. & KNOZINGER, H. 2002. Characterization and catalytic behavior of VOx-CeO2 catalysts for the oxidative dehydrogenation of propane. *Topics in Catalysis,* 20**,** 65-74.

DANILOVIC, N., LUO, J. L., CHUANG, K. T. & SANGER, A. R. 2009. Ce0.9Sr0.1VOx (x=3, 4) as anode materials for H2S-containing CH4 fueled solid oxide fuel cells. *Journal of Power Sources,* 192**,** 247-257.

DE, K. S. & BALASUBRAMANIAN, M. R. 1983. CUBIC HYPOVANADATE PEROVSKITE AS AN OXIDATION CATALYST. *Journal of Catalysis,* 81**,** 482-484.

DECALUWE, S. C., GRASS, M. E., ZHANG, C. J., EL GABALY, F., BLUHM, H., LIU, Z., JACKSON, G. S., MCDANIEL, A. H., MCCARTY, K. F., FARROW, R. L., LINNE, M. A., HUSSAIN, Z. & EICHHORN, B. W. 2010. In Situ Characterization of Ceria Oxidation States in High-Temperature Electrochemical Cells with Ambient Pressure XPS. *Journal of Physical Chemistry C,* 114**,** 19853-19861.

EBERHARDT, D., SANTOS, E. & SCHMICKLER, W. 1996. Impedance studies of reconstructed and non-reconstructed gold single crystal surfaces. *Journal of Electroanalytical Chemistry,* 419**,** 23-31.

EGDELL, R. G., HARRISON, M. R., HILL, M. D., PORTE, L. & WALL, G. 1984. A study of the metal non-metal transition in lanthanum strontium vanadate by high-resolution electron-spectroscopy. *Journal of Physics C-Solid State Physics,* 17**,** 2889-2900.

EG&G SERVICES, 2004. *Fuel cell handbook [electronic resource] / EG&G Technical Services, Inc,* Morgantown, WV :, U.S. Dept. of Energy, Office of Fossil Energy, National Energy Technology Laboratory.

FAGG, D. P., FEIGHERY, A. J. & IRVINE, J. T. S. 2003a. The systems Zr(Nb,Ti)(R)O2-delta, R = Yb, Ca - optimization of mixed conductivity and comparison with results of other systems (R = Y and Gd). *Journal of Solid State Chemistry,* 172**,** 277-287.

FAGG, D. P., ABRANTES, J. C. C., PEREZ-COLL, D., NUNEZ, P., KHARTON, V. V. & FRADE, J. R. 2003b. The effect of cobalt oxide sintering aid on electronic transport in Ce0.80Gd0.20O2-delta electrolyte. *Electrochimica Acta,* 48**,** 1023-1029.

FAWCETT, W. R. 2009. Monte Carlo studies of ion size effects in the diffuse double layer. *Electrochimica Acta,* 54**,** 4997-5005.

FEDOROV, M. V., GEORGI, N. & KORNYSHEV, A. A. 2010. Double layer in ionic liquids: The nature of the camel shape of capacitance. *Electrochemistry Communications,* 12**,** 296-299.

FEIGHERY, A. J., IRVINE, J. T. S., FAGG, D. P. & KAISER, A. 1999. Phase relations at 1500 degrees C in the ternary system ZrO2-Y2O3-TiO2. *Journal of Solid State Chemistry,* 143**,** 273-276.

FENG, G., HUANG, J. S., SUMPTER, B. G., MEUNIER, V. & QIAO, R. 2010. Structure and dynamics of electrical double layers in organic electrolytes. *Physical Chemistry Chemical Physics,* 12**,** 5468-5479.

FLEIG, J. 2002. On the width of the electrochemically active region in mixed conducting solid oxide fuel cell cathodes. *Journal of Power Sources,* 105**,** 228-238.

FRANTZIS, A. D., BEBELIS, S. & VAYENAS, C. G. 2000. Electrochemical promotion (NEMCA) of CH4 and C2H4 oxidation on Pd/YSZ and investigation of the origin of NEMCA via AC impedance spectroscopy. *Solid State Ionics,* 136**,** 863-872.

FU, Q. X., TIETZ, F. & STOVER, D. 2006. La0.4Sr0.6Ti1-xMnxO3-delta perovskites as anode materials for solid oxide fuel cells. *Journal of the Electrochemical Society,* 153**,** D74-D83.

FUERTE, A., VALENZUELA, R. X., ESCUDERO, M. J. & DAZA, L. 2011. Effect of cobalt incorporation in copper-ceria based anodes for hydrocarbon utilisation in Intermediate Temperature Solid Oxide Fuel Cells. *Journal of Power Sources,* 196**,** 4324-4331.

FUKUNAGA, H., ISHINO, M. & YAMADA, K. 2007. Effective thickness of

Ni-Sm-doped ceria cermet anode for solid oxide fuel cell. *Electrochemical and Solid State Letters,* 10**,** B16-B18.

GE, X. M. & CHAN, S. H. 2009a. Impedance Identification of Lanthanum Strontium Vanadate Anode in H[sub 2]-H[sub 2]O-He Atmosphere. *ECS Transactions,* 25**,** 2249-2258.

GE, X. M. & CHAN, S. H. 2009b. Lanthanum Strontium Vanadate as Potential Anodes for Solid Oxide Fuel Cells. *Journal of the Electrochemical Society,* 156**,** B386-B391.

GE, X. M., FU, C. J. & CHAN, S. H. 2011. Double Layer Capacitance of Anode/Solid-electrolyte Interfaces. *Physical Chemistry Chemical Physics.* DOI: 10.1039/c1cp20508k.

GAUDON, M., DJURADO, E. & MENZLER, N. H. 2004. Morphology and sintering behaviour of yttria stabilised zirconia (8-YSZ) powders synthesised by spray pyrolysis. *Ceramics International,* 30, 2295.

GEORGES, S., PARROUR, G., HENAULT, M. & FOULETIER, 2006. J. Gradual internal reforming of methane: A demnstration. *Solid State Ionics,* 177, 2109-2112.

GEORGIADOU, I., PAPADOPOULOU, C., MATRALIS, H. K., VOYIATZIS, G. A., LYCOURGHIOTIS, A. & KORDULIS, C. 1998. Preparation, characterization, and catalytic properties for the SCR of NO by NH3 of V2O5/TiO2 catalysts prepared by equilibrium deposition filtration. *Journal of Physical Chemistry B,* 102**,** 8459-8468.

GEWIES, S., BESSLER, W. G., SONN, V. & IVERS-TIFFIEE, E. 2007. Experimental and Modeling Study of the Impedance of Ni/YSZ Cermet Anodes. *In:* EGUCHI, K., SINGHAI, S. C., YOKOKAWA, H. & MIZUSAKI, H. (eds.) *Solid Oxide Fuel Cells 10.*

GOLBERT, J., ADJIMAN, C. S. & BRANDON, N. P. 2008. Microstructural Modeling of Solid Oxide Fuel Cell Anodes. *Industrial & Engineering Chemistry Research,* 47**,** 7693-7699.

GOODENOUGH, J. B. 2004. Electronic and ionic transport properties and other physical aspects of perovskites. *Reports on Progress in Physics,* 67**,** 1915-1993.

GOODENOUGH, J. B. & HUANG, Y. H. 2007. Alternative anode materials for solid oxide fuel cells. *Journal of Power Sources,* 173**,** 1-10.

GOUY, M. G. 1910. *J. Phys. Theor. Appl. ,* 9**,** 457-467.

GRAHAME, D. C. 1947. The electrical double layer and the therory of electrocapillarity. *Chemical Reviews,* 41**,** 441-501.

GROSS, M. D., VOHS, J. M. & GORTE, R. J. 2007a. A study of thermal stability and methane tolerance of Cu-based SOFC anodes with electrodeposited Co. *Electrochimica Acta,* 52**,** 1951-1957.

GROSS, M. D., VOHS, J. M. & GORTE, R. J. 2007b. Recent progress in SOFC anodes for direct utilization of hydrocarbons. *Journal of Materials Chemistry,* 17**,** 3071-3077.

GROSS, M. D., CARVER, K. M., DEIGHAN, M. A., SCHENKEL, A., SMITH, B. M. & YEE, A. Z. 2009. Redox Stability of SrNbxTi1-xO3-YSZ for Use in SOFC Anodes. *Journal of the Electrochemical Society,* 156**,** B540-B545.

HAAVIK, C., OTTESEN, E. M., NOMURA, K., KILNER, J. A. & NORBY, T. Temperature dependence of oxygen ion transport in Sr plus Mg-subtituted LaGaO3 (LSGM) with varying grain sizes. *Solid State Ionics,* 174, 233-243.

HANSEN, K. V., NORRMAN, K. & MOGENSEN, M. 2004. H-2-H2O-Ni-YSZ electrode performance - Effect of segregation to the interface. *Journal of the Electrochemical Society,* 151**,** A1436-A1444.

HELMHOLTZ, H. 1853. *Annalen Der Physik,* 89**,** 211-233.

HENDRIKS, M., TEN ELSHOF, J. E., BOUWMEESTER, H. J. M. & VERWEIJ, H. 2002a. The electrochemical double-layer capacitance of yttria-stabilised zirconia. *Solid State Ionics,* 146**,** 211-217.

HENDRIKS, M., TEN ELSHOF, J. E., BOUWMEESTER, H. J. M. & VERWEIJ, H. 2002b. The defect structure of the double layer in yttria-stabilised zirconia. *Solid State Ionics,* 154**,** 467-472.

HIBINO, T., HASHIMOTO, A., ASANO, K., YANO, M., SUZUKI, M. & SANO, M. 2002. An intermediate-temperature solid oxide fuel cell providing higher performance with hydrocarbons than with hydrogen. *Electrochemical and Solid State Letters,* 5**,** A242-A244.

HICKLING, A. 1942. Studies in electrode polarisation. Part IV. The automatic control of the potential of a working electrode. *Transactions of the Faraday Society,* 38**,** 0027-0033.

HITZ, C. & LASIA, A. 2001. Experimental study and modeling of impedance of the her on porous Ni electrodes. *Journal of Electroanalytical Chemistry,* 500**,** 213-222.

HOLTAPPELS, P., DE HAART, L. G. J. & STIMMING, U. 1999. Reaction of hydrogen

water mixtures on nickel-zirconia cermet electrodes I. DC polarization characteristics. *Journal of the Electrochemical Society,* 146**,** 1620-1625.

HOLTAPPELS, P., POULSEN, F. W. & MOGENSEN, M. 2000. Electrical conductivities and chemical stabilities of mixed conducting pyrochlores for SOFC applications. *Solid State Ionics,* 135**,** 675-679.

HORIKIRI, F., HAN, L. Q., IIZAWA, N., SATO, K., YASHIRO, K., KAWADA, T. & MIZUSAKI, J. 2008. Electrical properties of Nb-doped SrTiO3 ceramics with excess TiO2 for SOFC anodes and interconnects. *Journal of the Electrochemical Society,* 155**,** B16-B20.

HORITA, T., YAMAJI, K., ISHIKAWA, M., SAKAI, N., YOKOKAWA, H., KAWADA, T. & KATO, T. 1998. Active sites imaging for oxygen reduction at the La0.9Sr0.1MnO3-x/yttria-stabilized zirconia interface by secondary-ion mass spectrometry. *Journal of the Electrochemical Society,* 145**,** 3196-3202.

HSU, C. H. & MANSFELD, F. 2001. Technical note: Concerning the conversion of the constant phase element parameter Y-0 into a capacitance. *Corrosion,* 57**,** 747-748.

HUANG, B., YE, X. F., WANG, S. R., NIE, H. W., SHI, J., HU, Q., QIAN, J. Q., SUN, X. F. & WEN, T. L. 2006a. Performance of Ni/ScSZ cermet anode modified by coating with Gd0.2Ce0.8O2 for an SOFC running on methane fuel. *Journal of Power Sources,* 162**,** 1172-1181.

HUANG, X. J. & WEPPNER, W. 1996. Characteristics of transition metal oxide doping of YSZ: Structure and electrical properties. *Journal of the Chemical Society-Faraday Transactions,* 92**,** 2173-2178.

HUANG, X. L., ZHAO, H. L., QIU, W. H., WU, W. J. & LI, X. 2007. Performances of planar solid oxide fuel cells with doped strontium titanate as anode materials. *Energy Conversion and Management,* 48**,** 1678-1682.

HUANG, Y. H., DASS, R. I., XING, Z. L. & GOODENOUGH, J. B. 2006b. Double perovskites as anode materials for solid-oxide fuel cells. *Science,* 312**,** 254-257.

HUANG, Y. H., DASS, R. I., DENYSZYN, J. C. & GOODENOUGH, J. B. 2006c. Synthesis and characterization of Sr2MgMoO6-delta - An anode material for the solid oxide fuel cell. *Journal of the Electrochemical Society,* 153**,** A1266-A1272.

HUANG, Y. H., LIANG, G., CROFT, M., LEHTIMAKI, M., KARPPINEN, M. & GOODENOUGHT, J. B. 2009. Double-Perovskite Anode Materials Sr2MMoO6 (M = Co, Ni) for Solid Oxide Fuel Cells. *Chemistry of Materials,* 21**,**

2319-2326.

HUI, S. Q. & PETRIC, A. 2001. Conductivity and stability of SrVO3 and mixed perovskites at low oxygen partial pressures. *Solid State Ionics,* 143**,** 275-283.

HUI, S. Q. & PETRIC, A. 2002a. Electrical properties of yttrium-doped strontium titanate under reducing conditions. *Journal of the Electrochemical Society,* 149**,** J1-J10.

HUI, S. Q. & PETRIC, A. 2002b. Evaluation of yttrium-doped SrTiO3 as an anode for solid oxide fuel cells. *Journal of the European Ceramic Society,* 22**,** 1673-1681.

HUR, N. H., KIM, S. H., YU, K. S., PARK, Y. K., PARK, J. C. & KIM, S. J. 1994. Sturctural and magnetic-properties of the anoin-deficient LaVO3-delta. *Solid State Communications,* 92**,** 541-546.

INABA, F., ARIMA, T., ISHIKAWA, T., KATSUFUJI, T. & TOKURA, Y. 1995. Change of electronic-properties on the doping-induced insulator-metal transition in La1-xSrxVO3. *Physical Review B,* 52**,** R2221-R2224.

INTERNATIONAL ENERGY AGENCY, 2009 World Energy Outlook- 2009 Edition

INTERNATIONAL ENERGY AGENCY, 2010. Energy Technology Perspectives 2010-Scenarios & Strategies to 2050.

INTERNATIONAL ENERGY AGENCY, April 2007. IEA Energy Technology Essentials--- Hydrogen Production & Distribution.

JACOBSON, A. J. 2010. Materials for Solid Oxide Fuel Cells. *Chemistry of Materials,* 22**,** 660-674.

JAEGER, H. M. & NAGEL, S. R. 1992. Physics of the granular state. *Science,* 255**,** 1523-1531.

JANARDHANAN, V. M., HEUVELINE, V. & DEUTSCHMANN, O. 2008. Three-phase boundary length in solid-oxide fuel cells: A mathematical model. *Journal of Power Sources,* 178**,** 368-372.

JARZABEK, G. & BORKOWSKA, Z. 1997. On the real surface area of smooth solid electrodes. *Electrochimica Acta,* 42**,** 2915-2918.

JEON, D. H., NAM, J. H. & KIM, C. J. 2006. Microstructural optimization of anode-supported solid oxide fuel cells by a comprehensive microscale model. *Journal of the Electrochemical Society,* 153**,** A406-A417.

JHO, Y. S., KANDUC, M., NAJI, A., PODGORNIK, R., KIM, M. W. & PINCUS, P. A. 2008. Strong-Coupling Electrostatics in the Presence of Dielectric Inhomogeneities. *Physical Review Letters,* 101.

JI, Y., HUANG, Y. H., YING, J. R. & GOODENOUGH, J. B. 2007. Electrochemical performance of La-doped Sr2MgMoO6-delta in natural gas. *Electrochemistry Communications,* 9**,** 1881-1885.

JIANG, S. P. 2006. A review of wet impregnation - An alternative method for the fabrication of high performance and nano-structured electrodes of solid oxide fuel cells. *Materials Science and Engineering a-Structural Materials Properties Microstructure and Processing,* 418**,** 199-210.

JIANG, S. P. & BADWAL, S. P. S. 1999. An electrode kinetics study of H-2 oxidation on Ni/Y2O3-ZrO2 cermet electrode of the solid oxide fuel cell. *Solid State Ionics,* 123**,** 209-224.

JIANG, S. P. & CHAN, S. H. 2004. A review of anode materials development in solid oxide fuel cells. *Journal of Materials Science,* 39**,** 4405-4439.

JIANG, S. P., CHEN, X. J., CHAN, S. H. & KWOK, J. T. 2006a. GDC-impregnated, (La0.75Sr0.25)(Cr0.5Mn0.5)O-3 anodes for direct utilization of methane in solid oxide fuel cells. *Journal of the Electrochemical Society,* 153**,** A850-A856.

JIANG, S. P., CHEN, X. J., CHAN, S. H., KWOK, J. T. & KHOR, K. A. 2006b. (La0.75Sr0.25)(Cr0.5Mn0.5)O-3/YSZ composite anodes for methane oxidation reaction in solid oxide fuel cells. *Solid State Ionics,* 177**,** 149-157.

JIANG, S. P., LIU, L., KHUONG, P. O. B., PING, W. B., LI, H. & PU, H. 2008. Electrical conductivity and performance of doped LaCrO3 perovskite oxides for solid oxide fuel cells. *Journal of Power Sources,* 176**,** 82-89.

JIANG, Y. & VIRKAR, A. V. 2003. Fuel composition and diluent effect on gas transport and performance of anode-supported SOFCs. *Journal of the Electrochemical Society,* 150**,** A942-A951.

JIANG, Z. Y., XIA, C. R. & CHEN, F. L. 2010. Efficient Thickness of Solid Oxide Fuel Cell Composite Electrode. *Chinese Journal of Chemical Physics,* 23**,** 217-225.

JIN, C., YANG, C. H., ZHAO, F., CUI, D. & CHEN, F. L. 2011. La0.75Sr0.25Cr0.5Mn0.5O3 as hydrogen electrode for solid oxide electrolysis cells. *International Journal of Hydrogen Energy,* 36**,** 3340-3346.

JORCIN, J. B., ORAZEM, M. E., PEBERE, N. & TRIBOLLET, B. 2006. CPE analysis by local electrochemical impedance spectroscopy. *Electrochimica Acta,* 51**,** 1473-1479.

KAHIL, H., SCHOULER, E. J. L., FORESTIER, M. & GUITTON, J. 1986. Characterization of the solid composite electrode MnO2-[gamma], acetylene

black, HUP/HUP by impedance spectroscopy. *Solid State Ionics,* 18-19**,** 892-896.

KAISER, A., BRADLEY, J. L., SLATER, P. R. & IRVINE, J. T. S. 2000. Tetragonal tungsten bronze type phases (Sr1-xBax)(0.6)Ti0.2Nb0.8O3-delta: Material characterisation and performance as SOFC anodes. *Solid State Ionics,* 135**,** 519-524.

KAN, H. & LEE, H. 2010. Sn-doped Ni/YSZ anode catalysts with enhanced carbon deposition resistance for an intermediate temperature SOFC. *Applied Catalysis B-Environmental,* 97**,** 108-114.

KANNO, D., SHIKAZONO, N., TAKAGI, N., MATSUZAKI, K. & KASAGI, N. 2011. Evaluation of SOFC anode polarization simulation using three-dimensional microstructures reconstructed by FIB tomography. *Electrochimica Acta,* 56**,** 4015-4021.

KARCZEWSKI, J., RIEGEL, B., GAZDA, M., JASINSKI, P. & KUSZ, B. 2010. Electrical and structural properties of Nb-doped SrTiO3 ceramics. *Journal of Electroceramics,* 24**,** 326-330.

KEK, D., MOGENSEN, M. & PEJOVNIK, S. 2001. A study of metal (Ni, Pt, Au)/yttria-stabilized zirconia interface in hydrogen atmosphere at elevated temperature. *Journal of the Electrochemical Society,* 148**,** A878-A886.

KELAIDOPOULOU, A., SIDDLE, A., DICKS, A. L., KAISER, A. & IRVINE, J. T. S. 2001a. Methane Electro-Oxidation on a Y0.20Ti0.18Zr0.62O1.90 Anode in a High Temperature Solid Oxide Fuel Cell. *Fuel Cells,* 1**,** 219-225.

KELAIDOPOULOU, A., SIDDLE, A., DICKS, A. L., KAISER, A. & IRVINE, J. T. S. 2001b. Anodic Behaviour of Y0.20Ti0.18 Zr0.62O1.90 Towards Hydrogen Electro-Oxidation in a High Temperature Solid Oxide Fuel Cell. *Fuel Cells,* 1**,** 226-232.

KENNEY, B., VALDMANIS, M., BAKER, C., PHAROAH, J. G. & KARAN, K. 2009. Computation of TPB length, surface area and pore size from numerical reconstruction of composite solid oxide fuel cell electrodes. *Journal of Power Sources,* 189**,** 1051-1059.

KERNER, Z. & PAJKOSSY, T. 1998. Impedance of rough capacitive electrodes: the role of surface disorder. *Journal of Electroanalytical Chemistry,* 448**,** 139-142.

KHAN, R. T. A., BASHIR, J., IQBAL, N. & KHAN, M. N. 2004. Crystal structure of LaVO3 by Rietveld refinement method. *Materials Letters,* 58**,** 1737-1740.

KIJIMA, N., IKEDA, S., SHIMONO, I., MATSUMOTO, T., TSUJI, S., KUMAGAI, K.-I. & NAGATA, S. 1996. A New Strontium Vanadium Sulfide, SrV2S5. *Journal of Solid State Chemistry,* 126**,** 189-194.

KIM, H., PARK, S., VOHS, J. M. & GORTE, R. J. 2001. Direct oxidation of liquid fuels in a solid oxide fuel cell. *Journal of the Electrochemical Society,* 148**,** A693-A695.

KIM, H., LU, C., WORRELL, W. L., VOHS, J. M. & GORTE, R. J. 2002. Cu-Ni cermet anodes for direct oxidation of methane in solid-oxide fuel cells. *Journal of the Electrochemical Society,* 149**,** A247-A250.

KIM, J. H. & CHOI, G. M. 2000. Mixed ionic and electronic conductivity of (ZrO2)(0.92)(Y2O3)(0.08) (1-y) center dot (MnO1.5)(y). *Solid State Ionics,* 130**,** 157-168.

KIM, P., BRETT, D. J. L. & BRANDON, N. P. 2009. The effect of water content on the electrochemical impedance response and microstructure of Ni-CGO anodes for solid oxide fuel cells. *Journal of Power Sources,* 189**,** 1060-1065.

KIM, S. K., KIM, J. S., HAN, J. Y., SEO, J. M., LEE, C. K. & HONG, S. C. 2000. Surface alloying of a Co film on the Cu(001) surface. *Surface Science,* 453**,** 47-58.

KISZA, A. 2006. The capacitance of the diffuse layer of electric double layer of electrodes in molten salts. *Electrochimica Acta,* 51**,** 2315-2321.

KLEIN, J. M., GEORGES S. & BULTEL, Y. 2008a. Modeling of a SOFC Fueled by Methane: Anode Barrier to Allow Gradual Internal Reforming Without Coking. *Journal of the Electrochemical Society,* 155 (4)**,** B333-B339.

KLEIN, J. M., HENAULT M., GELIN, P., BULTEL, Y. & GEORGES S. 2008b. A Solid Oxide Fuel Cell Operating in Gradual Internal Reforming Conditions under Pure Dry Methane. *Electrochemical and Solid-State Letters,* 11 (8)**,** B144-B147.

KOLODIAZHNYI, T. & PETRIC, A. 2005. The applicability of Sr-deficient n-type SrTiO3 for SOFC anodes. *Journal of Electroceramics,* 15**,** 5-11.

KRAMER, S., SPEARS, M. & TULLER, H. L. 1994. Conduction in titanate pyrochlores- role of dopants. *Solid State Ionics,* 72**,** 59-66.

KUCZYNSKI, G. C. 1949. SELF-DIFFUSION IN SINTERING OF METALLIC PARTICLES. *Transactions of the American Institute of Mining and Metallurgical Engineers,* 185**,** 169-178.

KUO, C.-H. & GUPTA, P. K. 1995. Rigidity and conductivity percolation thresholds in particulate composites. *Acta Metallurgica et Materialia,* 43**,** 397-403.

KUROKAWA, H., YANG, L. M., JACOBSON, C. P., DE JONGHE, L. C. & VISCO, S. J. 2007a. Y-doped SrTiO3 based sulfur tolerant anode for solid oxide fuel cells. *Journal of Power Sources,* 164**,** 510-518.

KUROKAWA, H., SHOLKLAPPER, T. Z., JACOBSON, C. P., DE JONGHE, L. C. & VISCO, S. J. 2007b. Ceria nanocoating for sulfur tolerant Ni-based anodes of solid oxide fuel cells. *Electrochemical and Solid State Letters,* 10**,** B135-B138.

KURTZ, R. L. & HENRICH, V. E. 1983. Surface electronic-structure and chemisorption on corundum transition-metal oxides- V2O3. *Physical Review B,* 28**,** 6699-6706.

LAGUNA-BERCERO, M.A., KILNER, J. A. & SKINNER, S. J. 2010. Performance and Characterization of (La,Sr)MnO3/YSZ and La0.6Sr0.4Co0.2Fe0.8O3 Electrodes for Solid Oxide Electrolysis Cells. *Chemistry of Materials,* 22, 1134.

LAKSHMINARAYANAN, N. & OZKAN, U. S. 2011. Effect of H2O on sulfur poisoning and catalytic activity of Ni-YSZ catalysts. *Applied Catalysis a-General,* 393**,** 138-145.

LANGMUIR, D. B. 1936. Contact potential measurements on tungsten filaments. *Physical Review,* 49**,** 0428-0435.

LASHTABEG, A., CANALES-VAZQUEZ, J., IRVINE, J. T. S. & BRADLEY, J. L. 2009. Structure, Conductivity, and Thermal Expansion Studies of Redox Stable Rutile Niobium Chromium Titanates in Oxidizing and Reducing Conditions. *Chemistry of Materials,* 21**,** 3549-3561.

LEE, S. I., VOHS, J. M. & GORTE, R. J. 2004. A study of SOFC anodes based on Cu-Ni and Cu-Co bimetallics in CeO2-YSZ. *Journal of the Electrochemical Society,* 151**,** A1319-A1323.

LEE, S. I., AHN, K., VOHS, J. M. & GORTE, R. J. 2005. Cu-Co bimetallic anodes for direct utilization of methane in SOFCs. *Electrochemical and Solid State Letters,* 8**,** A48-A51.

LENG, Y. J., CHAN, S. H., KHOR, K. A. & JIANG, S. P. 2004. Development of LSM/YSZ composite cathode for anode-supported solid oxide fuel cells. *Journal of Applied Electrochemistry,* 34, 409-415.

LENG, Y. J., CHAN, S. H., KHOR, K. A. & JIANG, S. P. 2006. (La0.8Sr0.2)(0.9)MnO3-Gd0.2Ce0.8O1.9 composite cathodes prepared from

(Gd, Ce)(NO2)(x)-modified (La0.8Sr0.2)(0.9)MNO3 for intermediate-temperature solid oxide fuel cells. *Journal of Solid State Electrochemistry,* 34, 409-415.

LI, J. 2010. Decarbonising power generation in China-Is the answer blowing in the wind? *Renewable & Sustainable Energy Reviews,* 14**,** 1154-1171.

LI, K. T., HUANG, M. Y. & CHENG, W. D. 1996. Vanadium-based mixed-oxide catalysts for selective oxidation of hydrogen sulfide to sulfur. *Industrial & Engineering Chemistry Research,* 35**,** 621-626.

LI, S. L., WANG, S. R., NIE, H. W. & WEN, T. L. 2007a. A direct-methane solid oxide fuel cell with a double-layer anode. *Journal of Solid State Electrochemistry,* 11**,** 59-64.

LI, X., ZHAO, H. L., SHEN, W., GAO, F., HUANG, X. L., LI, Y. & ZHU, Z. M. 2007b. Synthesis and properties of Y-doped SrTiO3 as an anode material for SOFCs. *Journal of Power Sources,* 166**,** 47-52.

LIN, Y. B., ZHAN, Z. L. & BARNETT, S. A. 2006. Improving the stability of direct-methane solid oxide fuel cells using anode barrier layers. *Journal of Power Sources,* 158**,** 1313-1316.

LIN, Y. B., ZHAN, Z. L., LIU, J. & BARNETT, S. A. 2005. Direct operation of solid oxide fuel cells with methane fuel. *Solid State Ionics,* 176**,** 1827-1835.

LIU, J., MADSEN, B. D., JI, Z. Q. & BARNETT, S. A. 2002. A fuel-flexible ceramic-based anode for solid oxide fuel cells. *Electrochemical and Solid State Letters,* 5**,** A122-A124.

LIU, J. A. & BARNETT, S. A. 2003. Operation of anode-supported solid oxide fuel cells on methane and natural gas. *Solid State Ionics,* 158**,** 11-16.

LIU, M., WEI, G. L., LUO, J. L., SANGER, A. R. & CHUANG, K. T. 2003. Use of metal sulfides as anode catalysts in H2S-Air SOFCs. *Journal of the Electrochemical Society,* 150**,** A1025-A1029.

LIU, M. L. 1998. Equivalent circuit approximation to porous mixed-conducting oxygen electrodes in solid-state cells. *Journal of the Electrochemical Society,* 145**,** 142-154.

LIU, Q. A., YANG, C. H., DONG, X. H. & CHEN, F. L. 2010a. Perovskite Sr2Fe1.5Mo0.5O6-delta as electrode materials for symmetrical solid oxide electrolysis cells. *International Journal of Hydrogen Energy,* 35**,** 10039-10044.

LIU, Q. A., DONG, X. H., XIAO, G. L., ZHAO, F. & CHEN, F. L. 2010b. A Novel

Electrode Material for Symmetrical SOFCs. *Advanced Materials,* 22**,** 5478-5482.

LOCKETT, V., HORNE, M., SEDEV, R., RODOPOULOS, T. & RALSTON, J. 2010. Differential capacitance of the double layer at the electrode/ionic liquids interface. *Physical Chemistry Chemical Physics,* 12**,** 12499-12512.

LOHSOONTORN, R., BRETT, D. J. L. & BRANDON, N. P. 2008. The effect of fuel composition and temperature on the interaction of H2S with nickel-ceria anodes for Solid Oxide Fuel Cells. *Journal of Power Sources,* 183**,** 232-239.

LU, C., AN, S., WORRELL, W. L., VOHS, J. M. & GORTE, R. J. 2004. Development of intermediate-temperature solid oxide fuel cells for direct utilization of hydrocarbon fuels. *Solid State Ionics,* 175**,** 47-50.

LU, X. C. & ZHU, J. H. 2007. Cu(Pd)-impregnated La0.75Sr0.25Cr0.5Mn0.5O3-delta anodes for direct utilization of methane in SOFC. *Solid State Ionics,* 178**,** 1467-1475.

LU, X. C. & ZHU, J. H. 2008. Amorphous ceramic material as sulfur-tolerant anode for SOFC. *Journal of the Electrochemical Society,* 155**,** B1053-B1057.

LU, X. Y., FAGUY, P. W. & LIU, M. L. 2002. In situ potential-dependent FTIR emission spectroscopy - A novel probe for high temperature fuel cell interfaces. *Journal of the Electrochemical Society,* 149**,** A1293-A1298.

LUO, G. M., MALKOVA, S., YOON, J., SCHULTZ, D. G., LIN, B. H., MERON, M., BENJAMIN, I., VANYSEK, P. & SCHLOSSMAN, M. L. 2006. Ion distributions near a liquid-liquid interface. *Science,* 311**,** 216-218.

MA, Q. L., TIETZ, F., LEONIDE, A. & IVERS-TIFFEE, E. 2010. Anode-supported planar SOFC with high performance and redox stability. *Electrochemistry Communications,* 12**,** 1326-1328.

MACDONALD, J. R. (ed.) 1987. *Impedance spectroscopy: emphasizing solid materials and analysis* New York: Wiley

MACDONALD, J. R., SCHOONMAN, J. & LEHNEN, A. P. 1982. The applicability and power of complex non-linear least-squares for the analysis of impedance and addmittance data. *Journal of Electroanalytical Chemistry,* 131**,** 77-95.

MACOMBER, S. H., FURTAK, T. E. & DEVINE, T. M. 1982. Enhanced Raman characterization of adsorbed water at the electrochemical double-layer on silver. *Surface Science,* 122**,** 556-568.

MAHAJAN, A. V., JOHNSTON, D. C., TORGESON, D. R. & BORSA, F. 1992.

Structural, electronic, and magnetic-properties of LaxSr1-xVO3 (0.1<=x<=1.0). *Physical Review B,* 46**,** 10973-10985.

MANTZOURIS, X., ZOUVELOU, N., HAANAPPEL, V. A. C., TIETZ, F. & NIKOLOPOULOS, P. 2007. Mixed conducting oxides YxZr1-x-yTiyO2-x/2 (YZT) and corresponding Ni/YZT cermets as anode materials in an SOFC. *Journal of Materials Science,* 42**,** 10152-10159.

MARINA, O. A. & MOGENSEN, M. 1999. High-temperature conversion of methane on a composite gadolinia-doped ceria-gold electrode. *Applied Catalysis a-General,* 189**,** 117-126.

MARINA, O. A., CANFIELD, N. L. & STEVENSON, J. W. 2002. Thermal, electrical, and electrocatalytical properties of lanthanum-doped strontium titanate. *Solid State Ionics,* 149**,** 21-28.

MARINA, O. A., BAGGER, C., PRIMDAHL, S. & MOGENSEN, M. 1999. A solid oxide fuel cell with a gadolinia-doped ceria anode: preparation and performance. *Solid State Ionics,* 123**,** 199-208.

MARINA, O. A., COYLE, C. A., ENGELHARD, M. H. & PEDERSON, L. R. 2011. Mitigation of Sulfur Poisoning of Ni/Zirconia SOFC Anodes by Antimony and Tin. *Journal of the Electrochemical Society,* 158**,** B424-B429.

MARRERO-LOPEZ, D., PENA-MARTINEZ, J., RUIZ-MORALES, J. C., MARTIN-SEDENO, M. C. & NUNEZ, P. 2009. High temperature phase transition in SOFC anodes based on Sr2MgMoO6-delta. *Journal of Solid State Chemistry,* 182**,** 1027-1034.

MARRERO-LOPEZ, D., PENA-MARTINEZ, J., RUIZ-MORALES, J. C., GABAS, M., NUNEZ, P., ARANDA, M. A. G. & RAMOS-BARRADO, J. R. 2010. Redox behaviour, chemical compatibility and electrochemical performance of Sr2MgMoO6-delta as SOFC anode. *Solid State Ionics,* 180**,** 1672-1682.

MARRERO-LÓPEZ, D., PEÑA-MARTÍNEZ, J., RUIZ-MORALES, J. C., PÉREZ-COLL, D., MARTÍN-SEDEÑO, M. C. & NÚÑEZ, P. 2007. Applicability of La2Mo2-yWyO9 materials as solid electrolyte for SOFCs. *Solid State Ionics,* 178**,** 1366-1378.

MARTINEZ-ARIAS, A., HUNGRIA, A. B., FERNANDEZ-GARCIA, M., IGLESIAS-JUEZ, A., CONESA, J. C., MATHER, G. C. & MUNUERA, G. 2005. Cerium-terbium mixed oxides as potential materials for anodes in solid oxide fuel cells. *Journal of Power Sources,* 151**,** 43-51.

MARTINEZ, A. S. & BROUWER, J. 2008. Percolation modeling investigation of TPB formation in a solid oxide fuel cell electrode-electrolyte interface. *Electrochimica Acta,* 53**,** 3597-3609.

MATSUI, N. & TAKIGAWA, M. 1990. Impedance spectroscopy on YSZ with iron oxide as additive. *Solid State Ionics,* 40-41**,** 926-928.

MATSUI, T., FUJII, H., OZAKI, A., TAKEUCHI, T., KIKUCHI, R. & EGUCHI, K. 2007. Degradation Behavior of Ni-ScSZ Cermet anode under various humidified conditions for solid oxide fuel cells. *Journal of the Electrochemical Society,* 154**,** B1237-B1241.

MATSUZAKI, Y. & YASUDA, I. 2000. The poisoning effect of sulfur-containing impurity gas on a SOFC anode: Part I. Dependence on temperature, time, and impurity concentration. *Solid State Ionics,* 132**,** 261-269.

MCCOURT, F. R. W., WEIR, D., CLARK, G. B. & THACHUK, M. 2005. Transport and relaxation properties of isotopomeric hydrogen-helium binary mixtures. I. H-2-He mixtures. *Molecular Physics,* 103**,** 17-36.

MCINTOSH, S. & GORTE, R. J. 2004. Direct hydrocarbon solid oxide fuel cells. *Chemical Reviews,* 104**,** 4845-4865.

MCINTOSH, S., VOHS, J. M. & GORTE, R. J. 2002. An examination of lanthanide additives on the performance of Cu-YSZ cermet anodes. *Electrochimica Acta,* 47**,** 3815-3821.

MCINTOSH, S., VOHS, J. M. & GORTE, R. J. 2003. Role of hydrocarbon deposits in the enhanced performance of direct-oxidation SOFCs. *Journal of the Electrochemical Society,* 150**,** A470-A476.

MENZLER, N. H. & HAANAPPEL, V. A. C. 2010. Influence of anode thickness on the power output of solid oxide fuel cells with (La,Sr)(Co,Fe)-type cathode. *Journal of Power Sources,* 195**,** 5340-5343.

MENZLER, N. H., LAVERGNAT, D., TIETZ, F., SOMINSKI, E., DJURADO, E., FISCHER, W., PANG, G. S., GEDANKEN, A. & BUCHKREMER, H. P. 2003. Materials synthesis and characterization of 8YSZ nanomaterials for the fabrication of electrolyte membranes in solid oxide fuel cells. *Ceramics International,* 29, 619-628.

METCALFE, I. S. & BAKER, R. T. 1996. Temperature programmed investigation of La(Ca)CrO3 anode for the oxidation of methane in solid oxide fuel cells. *Catalysis Today,* 27**,** 285-288.

MICHIBATA, H., ITOH, K., HAGIWARA, A., KAWADA, T. & MIZUSAKI, J. 2011. Conductivity Evaluation of Rutile-Type Th1-xNbxO2 as Interconnect Material for Low Temperature Solid Oxide Fuel Cells. *Electrochemistry,* 79**,** 246-248.

MINH, N. Q. 1993. CERAMIC FUEL-CELLS. *Journal of the American Ceramic Society,* 76**,** 563-588.

MIZUSAKI, J., TAGAWA, H., SAITO, T., KAMITANI, K., YAMAMURA, T., HIRANO, K., EHARA, S., TAKAGI, T., HIKITA, T., IPPOMMATSU, M., NAKAGAWA, S. & HASHIMOTO, K. 1994. Preparation of nick pattern electrodes on YSZ and their electrochemical properties in H2-H2O atmospheres. *Journal of the Electrochemical Society,* 141**,** 2129-2134.

MOGENSEN, M. & KAMMER, K. 2003. Conversion of hydrocarbons in solid oxide fuel cells. *Annual Review of Materials Research,* 33**,** 321-331.

MOGENSEN, M., HOGH, J., HANSEN, K. V. & JACOBSEN, T. 2007. A Critical Review of Models of the H-2/H2O/Ni/SZ Electrode Kinetics. *In:* EGUCHI, K., SINGHAI, S. C., YOKOKAWA, H. & MIZUSAKI, H. (eds.) *Solid Oxide Fuel Cells 10.*

MORI, H., NONAKA, N., MIZUNO, M., ABE, H. & NAITO, M. 2008. Development of a Geometrical Model for Optimizing Porous Anode Microstructure of Solid Oxide Fuel Cells. *Journal of Chemical Engineering of Japan,* 41**,** 246-253.

MPR ASSOCIATES, I. February 2005. Hydrogen Production Methods.

MUKUNDAN, R., BROSHA, E. L. & GARZON, F. H. 2004. Sulfur tolerant anodes for SOFCs. *Electrochemical and Solid State Letters,* 7**,** A5-A7.

MURADOV, N. Z. & VEZIROGLU, T. N. 2008. "Green" path from fossil-based to hydrogen economy: An overview of carbon-neutral technologies. *International Journal of Hydrogen Energy,* 33**,** 6804-6839.

MURRAY, E. P., TSAI, T. & BARNETT, S. A. 1999. A direct-methane fuel cell with a ceria-based anode. *Nature,* 400**,** 649-651.

MURRAY, E. P., HARRIS, S. J., LIU, J. & BARNETT, S. A. 2006. Direct solid oxide fuel cell operation using isooctane. *Electrochemical and Solid State Letters,* 9**,** A292-A294.

NABAE, Y. & YAMANAKA, I. 2009. Alloying effects of Pd and Ni on the catalysis of the oxidation of dry CH4 in solid oxide fuel cells. *Applied Catalysis a-General,* 369**,** 119-124.

NABAE, Y., YAMANAKA, I., HATANO, M. & OTSUKA, K. 2006. Catalytic behavior

of Pd-Ni/composite anode for direct oxidation of methane in SOFCs. *Journal of the Electrochemical Society,* 153**,** A140-A145.

NAGY, Z. & YOU, H. 2009. vol. 45 *In:* WHITE, R. E. (ed.) *Modern aspects of electrochemistry.* New York Springer

NAIK, I. K. & TIEN, T. Y. 1979. Electrical Conduction in Nb[sub 2]O[sub 5]-Doped Cerium Dioxide. *Journal of the Electrochemical Society,* 126**,** 562-566.

NAKAGAWA, N., SAKURAI, H., KONDO, K., MORIMOTO, T., HATANAKA, K. & KATO, K. 1995. Evaluation of the effective reaction zone at Ni(NiO)/zirconia anode by using an electrode with a novel structure. *Journal of the Electrochemical Society,* 142**,** 3474-3479.

NAKAMURA, T., PETZOW, G. & GAUCKLER, L. J. 1979. Stability of the perovskite phase LaBO3 (B = V, Cr, Mn, Fe, Co, Ni) in reducing atmosphere: 1. experimental results. *Materials Research Bulletin,* 14**,** 649-659.

NAKAMURA, T., YASHIRO, K., KAIMAI, A., OTAKE, T., SATO, K., KAWADA, T. & MIZUSAKI, J. 2008. Determination of the Reaction Zone in Gadolinia-Doped Ceria Anode for Solid Oxide Fuel Cell. *Journal of the Electrochemical Society,* 155**,** B1244-B1250.

NEAGU, D. & IRVINE, J. T. S. 2010. Structure and Properties of La0.4Sr0.4TiO3 Ceramics for Use as Anode Materials in Solid Oxide Fuel Cells. *Chemistry of Materials,* 22**,** 5042-5053.

NEAGU, R., PEREDNIS, D. PRINCIVALLE, A. & DJURADO, E. 2006. Zirconia coatings deposited by electrostatic spray deposition: Influence of the process parameters, *Surface and Coating Technology*, 200, 6815-6820.

NESARAJ, A. S. 2010. Recent developments in solid oxide fuel cell technology - a review. *Journal of Scientific & Industrial Research,* 69**,** 169-176.

NISHIDA, Y. & ITOH, S. 2011. A modeling study of porous composite microstructures for solid oxide fuel cell anodes. *Electrochimica Acta,* 56**,** 2792-2800.

NOWOTNY, J. 1997. *In:* GELLINGS, P. J. & BOUWMEESTER, H. J. M. (eds.) *CRC handbook of solid state electrochemistry* Boca Raton

NOWOTNY, J. & SLOMA, M. 1991. Surface electrical properties of BaTiO3 at elevated temperatures. *Solid State Ionics,* 49**,** 129-133.

NOWOTNY, J., SLOMA, M. & WEPPNER, W. 1989. High-temperature Kelvin probe in application to ceramic materials- Investigation of nickel oxide. *Journal of the American Ceramic Society,* 72**,** 564-570.

ONDA, K., IWANARI, T., MIYAUCHI, N., ITO, K., OHBA, T., SAKAKI, Y. & NAGATA, S. 2003. Cycle analysis of combined power generation by planar SOFC and gas turbine considering cell temperature and current density distributions. *Journal of the Electrochemical Society,* 150**,** A1569-A1576.

OVALLE, A., RUIZ-MORALES, J. C., CANALES-VAZQUEZ, J., MARRERO-LOPEZ, D. & IRVINE, J. T. S. 2006. Mn-substituted titanates as efficient anodes for direct methane SOFCs. *Solid State Ionics,* 177**,** 1997-2003.

PARFITT, D., CHRONEOS, A., TARANCON, A. & KILNER, J. A. 2011. Oxygen ion diffusion in cation ordered/disordered GdBaCo2O5+δ, *Journal of Materials Chemistry*, 21, 2183.

PAGLIARO, M., KONSTANDOPOULOS, A. G., CIRIMINNA, R. & PALMISANO, G. 2010. Solar hydrogen: fuel of the near future. *Energy & Environmental Science,* 3**,** 279-287.

PAJKOSSY, T. 2005. Impedance spectroscopy at interfaces of metals and aqueous solutions - Surface roughness, CPE and related issues. *Solid State Ionics,* 176**,** 1997-2003.

PAJKOSSY, T. & KOLB, D. M. 2007. Double layer capacitance of the platinum group metals in the double layer region. *Electrochemistry Communications,* 9**,** 1171-1174.

PARK, S., GORTE, R. J. & VOHS, J. M. 2001. Tape cast solid oxide fuel cells for the direct oxidation of hydrocarbons. *Journal of the Electrochemical Society,* 148**,** A443-A447.

PARK, S. D., VOHS, J. M. & GORTE, R. J. 2000. Direct oxidation of hydrocarbons in a solid-oxide fuel cell. *Nature,* 404**,** 265-267.

PARK, Y. M. & CHOI, G. M. 1999. Mixed ionic and electronic conduction in YSZ-NiO composite. *Journal of the Electrochemical Society,* 146**,** 883-889.

PILLAI, M. R., KIM, I., BIERSCHENK, D. M. & BARNETT, S. A. 2008. Fuel-flexible operation of a solid oxide fuel cell with Sr0.8La0.2TiO3 support. *Journal of Power Sources,* 185**,** 1086-1093.

POMFRET, M. B., OWRUTSKY, J. C. & WALKER, R. A. 2010. In Situ Optical Studies of Solid-Oxide Fuel Cells. *Annual Review of Analytical Chemistry, Vol 3.*

POMFRET, M. B., MARDA, J., JACKSON, G. S., EICHHORN, B. W., DEAN, A. M. & WALKER, R. A. 2008. Hydrocarbon fuels in solid oxide fuel cells: In situ Raman studies of graphite formation and oxidation. *Journal of Physical*

Chemistry C, 112**,** 5232-5240.

PORAT, O., HEREMANS, C. & TULLER, H. L. 1997a. Phase Stability and Electrical Conductivity in Gd2Ti2O7-Gd2Mo2O7 Solid Solutions. *Journal of the American Ceramic Society,* 80**,** 2278-2284.

PORAT, O., HEREMANS, C. & TULLER, H. L. 1997b. Stability and mixed ionic electronic conduction in Gd-2(Ti1-xMox)(2)O-7 under anodic conditions. *Solid State Ionics,* 94**,** 75-83.

PORAT, O., HEREMANS, C. & TULLER, H. L. 1997c. Phase stability acid electrical conductivity in Gd2Ti2O7Gd2Mo2O7 solid solutions. *Journal of the American Ceramic Society,* 80**,** 2278-2284.

POTTER, J. G. 1940. Temperature dependence of the work function of tungsten from measurement of contact potentials by the Kelvin method. *Physical Review,* 58**,** 623-632.

PRIMDAHL, S. & MOGENSEN, M. 1997. Oxidation of hydrogen on Ni/yttria-stabilized zirconia cermet anodes. *Journal of the Electrochemical Society,* 144**,** 3409-3419.

PRIMDAHL, S. & MOGENSEN, M. 1998. Gas conversion impedance: A test geometry effect in characterization of solid oxide fuel cell anodes. *Journal of the Electrochemical Society,* 145**,** 2431-2438.

PRIMDAHL, S. & MOGENSEN, M. 1999. Gas diffusion impedance in characterization of solid oxide fuel cell anodes. *Journal of the Electrochemical Society,* 146**,** 2827-2833.

PRIMDAHL, S., HANSEN, J. R., GRAHL-MADSEN, L. & LARSEN, P. H. 2001. Sr-Doped LaCrO[sub 3] Anode for Solid Oxide Fuel Cells. *Journal of the Electrochemical Society,* 148**,** A74-A81.

PUDMICH, G., BOUKAMP, B. A., GONZALEZ-CUENCA, M., JUNGEN, W., ZIPPRICH, W. & TIETZ, F. 2000. Chromite/titanate based perovskites for application as anodes in solid oxide fuel cells. *Solid State Ionics,* 135**,** 433-438.

PUJARE, N. U., SEMKOW, K. W. & SAMMELLS, A. F. 1987. A DIRECT H2S/AIR SOLID OXIDE FUEL-CELL. *Journal of the Electrochemical Society,* 134**,** 2639-2640.

QIAO, J., ZHANG, N., WANG, Z., MAO, Y., SUN, K. & YUAN, Y. 2009. Performance of mix-impregnated CeO2-Ni/YSZ Anodes for Direct Oxidation of Methane in Solid Oxide Fuel Cells. *Fuel Cells,* 9**,** 729-739.

RAJ, E. S., KILNER, J. A. & IRVINE, J. T. S. 2006. Oxygen diffusin and surface exchange studies on (La0.75Sr0.25)0.95Cr0.5Mn0.5O3–δ. *Solid State Ionics,* 177**,** 1747-1752.

RAZ, S., SASAKI, K., MAIER, J. & RIESS, I. 2001. Characterization of adsorbed water layers on Y2O3-doped ZrO2. *Solid State Ionics,* 143**,** 181-204.

REICH, C. M., KAISER, A. & IRVINE, J. T. S. 2001. Niobia Based Rutile Materials as SOFC Anodes. *Fuel Cells,* 1**,** 249-255.

REISS, H. 1985. Ther Fermi level and the redox potential. *Journal of Physical Chemistry,* 89**,** 3783-3791.

REISS, H. 1988. *Journal of the Electrochemical Society,* 135**,** 247C-258C.

RIESS, I. 1997. What does a voltmeter measure? *Solid State Ionics,* 95**,** 327-328.

RIESS, I. & VAYENAS, C. G. 2003. Fermi level and potential distribution in solid electrolyte cells with and without ion spillover. *Solid State Ionics,* 159**,** 313-329.

ROBERTSON, N. L. & MICHAELS, J. N. 1991. Double-layer capacitance of porous platinum electrodes in zirconia electrochemical cells. *Journal of the Electrochemical Society,* 138**,** 1494-1499.

ROSSIGNOL, C., ROMAN, B., BENETTI, G. D. & DJURADO, E. 2011. Elaboration of thin and dense CGO films adherent to YSZ by electrostatic spray deposition for IT-SOFC applications. *New Journal of Chemistry*, 35, 716-723.

ROY, S. K., ORAZEM, M. E. & TRIBOLLET, B. 2007. Interpretation of Low-Frequency Inductive Loops in PEM Fuel Cells. *Journal of the Electrochemical Society,* 154**,** B1378-B1388.

RUFFORD, T. E., HULICOVA-JURCAKOVA, D., FISET, E., ZHU, Z. H. & LU, G. Q. 2009. Double-layer capacitance of waste coffee ground activated carbons in an organic electrolyte. *Electrochemistry Communications,* 11**,** 974-977.

RUIZ-MORALES, J. C., CANALES-VAZQUEZ, J., SAVANIU, C., MARRERO-LOPEZ, D., ZHOU, W. Z. & IRVINE, J. T. S. 2006. Disruption of extended defects in solid oxide fuel cell anodes for methane oxidation. *Nature,* 439**,** 568-571.

RUIZ-MORALES, J. C., CANALES-VAZQUEZ, J., SAVANIU, C., MARRERO-LOPEZ, D., NUNEZ, P., ZHOU, W. Z. & IRVINE, J. T. S. 2007. A new anode for solid oxide fuel cells with enhanced OCV under methane operation. *Physical Chemistry Chemical Physics,* 9**,** 1821-1830.

SAEKI, M. J., UCHIDA, H. & WATANABE, M. 1994. Noble-metal catalysts highly

dispersed on Sm-doped ceria for the application to internal reforming solid oxide fuel cells operated at medium-temperature. *Catalysis Letters,* 26**,** 149-157.

SAKAI, N., YAMAJI, K., HORITA, T., KISHIMOTO, H., XIONG, Y. P. & YOKOKAWA, H. 2003. Effect of water vapour on oxygen exchange kinetics of ceria and zirconia solid electrolytes. *Physical Chemistry Chemical Physics,* 5**,** 2253-2256.

SAKAMOTO, S., TAIRA, H. & TAKAGI, H. 1996. Effective electrode reaction area of cofired type planar SOFC. *Denki Kagaku,* 64**,** 609-613.

SANYAL, J., GOLDIN, G. M., ZHU, H. Y. & KEE, R. J. 2010. A particle-based model for predicting the effective conductivities of composite electrodes. *Journal of Power Sources,* 195**,** 6671-6679.

SASAKI, K., SEIFERT, H. P. & GAUCKLER, L. J. 1994. Electronic Conductivity of In[sub 2]O[sub 3] Solid Solutions with ZrO[sub 2]. *Journal of the Electrochemical Society,* 141**,** 2759-2768.

SAYER, M., CHEN, R., FLETCHER, R. & MANSINGH, A. 1975. Metal-insulator transition in lanthanum strontium vanadate. *Journal of Physics C-Solid State Physics,* 8**,** 2059-2071.

SCHINDLER, K., SCHMEISSER, D., VOHRER, U., WIEMHOFER, H. D. & GOPEL, W. 1989. Spectroscopic and electrical studies of yttria-stabilized zirconia for oxygen sensors. *Sensors and Actuators,* 17**,** 555-568.

SCHNEIDER, I. A., BAYER, M. H., WOKAUN, A. & SCHERER, G. G. 2008. Impedance Response of the Proton Exchange Membrane in Polymer Electrolyte Fuel Cells. *Journal of the Electrochemical Society,* 155**,** B783-B792.

SCHNEIDER, L. C. R., MARTIN, C. L., BULTEL, Y., BOUVARD, D. & SIEBERT, E. 2006. Discrete modelling of the electrochemical performance of SOFC electrodes. *Electrochimica Acta,* 52**,** 314-324.

SCHOULER, E. J. L. & KLEITZ, M. 1987. Electrocatalysis and inductive effects at the gas, Pt-stabilized zirconia interface. *Journal of the Electrochemical Society,* 134**,** 1045-1050.

SEELY, S. 1941. Work function and temperature. *Physical Review,* 59**,** 75-78.

SHANNON, R. D. 1976. Reversed effective ionic radii and systematic studies of interaomic distances in halides and chalcogenides. *Acta Crystallographica Section A,* 32**,** 751-767.

SHEARING, P. R., GELB, J., YI, J., LEE, W. K., DRAKOPOLOUS, M. & BRANDON,

N. P. 2010. Analysis of triple phase contact in Ni-YSZ microstructures using non-destructive X-ray tomography with synchrotron radiation. *Electrochemistry Communications,* 12**,** 1021-1024.

SHINIKE, T., SAKAI, T., ADACHI, G. & SHIOKAWA, J. 1976. STUDIES ON SOLID-SOLUTIONS OF LN1-XSRXV03-0.1X. *Materials Research Bulletin,* 11**,** 249-254.

SHONKWILER, R. W. & MENDIVIL, F. 2009. *Explorations in Monte Carlo Methods,* New York, Springer

SIMNER, S. P., HARDY, J. S., STEVENSON, J. W. & ARMSTRONG, T. R. 2000. Sintering of lanthanum chromite using strontium vanadate. *Solid State Ionics,* 128**,** 53-63.

SLATER, P. R. & IRVINE, J. T. S. 1999a. Niobium based tetragonal tungsten bronzes as potential anodes for solid oxide fuel cells: synthesis and electrical characterisation. *Solid State Ionics,* 120**,** 125-134.

SLATER, P. R. & IRVINE, J. T. S. 1999b. Synthesis and electrical characterisation of the tetragonal tungsten bronze type phases, (Ba/Sr/Ca/La)(0) 6MxNb1-xO3-delta (M = Mg, Ni, Mn, Cr, Fe, In, Sn): evaluation as potential anode materials for solid oxide fuel cells. *Solid State Ionics,* 124**,** 61-72.

SMITH, A. H. 1949. Temperature dependence of the work function of semiconductors. *Physical Review,* 75**,** 953-958.

SMITH, K. E. & HENRICH, V. E. 1990. Photoemission investigation of the interaction of SO2 with V2O3 surfaces. *Surface Science,* 225**,** 47-57.

SPRAGUE, J. J. & TULLER, H. L. 1999. Mixed ionic and electronic conduction in Mn/Mo doped gadolinium titanate. *Journal of the European Ceramic Society,* 19**,** 803-806.

STEELE, B. C. H., MIDDLETON, P. H. & RUDKIN, R. A. 1990. Material sicen aspects of SOFC technology with special reference to anode development. *Solid State Ionics,* 40-1**,** 388-393.

STEELE, B. C. H., KELLY, I., MIDDLETON, H. & RUDKIN, R. 1988. Oxidation of methane in solid oxide electrochemical reactors. *Solid State Ionics,* 28**,** 1547-1552.

STERN, O. 1924. The theory of the electrolytic double shift. *Zeitschrift Fur Elektrochemie Und Angewandte Physikalische Chemie,* 30**,** 508-516.

SUDA, E., PACAUD, B. & MORI, M. 2006. Sintering characteristics, electrical

conductivity and thermal properties of La-doped ceria powders. *Journal of Alloys and Compounds,* 408**,** 1161-1164.

SUMI, H., LEE, Y. H., MUROYAMA, H., MATSUI, T. & EGUCHI, K. 2010. Comparison Between Internal Steam and CO2 Reforming of Methane for Ni-YSZ and Ni-ScSZ SOFC Anodes. *Journal of the Electrochemical Society,* 157**,** B1118-B1125.

SUMI, H., UKAI, K., MIZUTANI, Y., MORI, H., WEN, C. J., TAKAHASHI, H. & YAMAMOTO, O. 2004. Performance of nickel-scandia-stabilized zirconia cermet anodes for SOFCs in 3% H2O-CH4. *Solid State Ionics,* 174**,** 151-156.

SUZUKI, M. 2007. *Powder Technology: Fundamentals of Particles, Powder Beds, and Particle Generation,* Boca Raton, CRC Press.

SUZUKI, M. & OSHIMA, T. 1983. Estimation of the Co-ordination number in a Multi-Component Mixture of Spheres. *Powder Technology,* 35**,** 159-166.

SWIDER, K. E. & WORRELL, W. L. 1996. Metal-organic deposition of thin-film yttria-stabilized zirconia-titania. *Journal of Materials Research,* 11**,** 381-386.

TAO, S., IRVINE, J. T. S. & KILNER, J. A. 2005. An efficient solid oxide fuel cell based upon single-phase perovskites. *Advanced Materials,* 17**,** 1734-+.

TAO, S. W. & IRVINE, J. T. S. 2002a. Study on the structural and electrical properties of the double perovskite oxide SrMn0.5Nb0.5O3-delta. *Journal of Materials Chemistry,* 12**,** 2356-2360.

TAO, S. W. & IRVINE, J. T. S. 2002b. Structure and properties of nonstoichiometric mixed perovskites A(3)B ' B1+x " O-2-x(9-delta). *Solid State Ionics,* 154**,** 659-667.

TAO, S. W. & IRVINE, J. T. S. 2003. A redox-stable efficient anode for solid-oxide fuel cells. *Nature Materials,* 2**,** 320-323.

TAO, S. W. & IRVINE, J. T. S. 2004a. Synthesis and characterization of (La0.75Sr0.25)Cr0.5Mn0.5O3-delta, a redox-stable, efficient perovskite anode for SOFCs. *Journal of the Electrochemical Society,* 151**,** A252-A259.

TAO, S. W. & IRVINE, J. T. S. 2004b. Discovery and characterization of novel oxide anodes for solid oxide fuel cells. *Chemical Record,* 4**,** 83-95.

TAO, S. W. & IRVINE, J. T. S. 2004c. Catalytic properties of the perovskite oxide La0.75Sr0.25Cr0.5Fe0.5O3-delta in relation to its potential as a solid oxide fuel cell anode material. *Chemistry of Materials,* 16**,** 4116-4121.

TIETZ, F., RAJ, I. A. & STOVER, D. 2004. Statistical design of experiments for

evaluation of Y-Zr-Ti oxides as anode materials in solid oxide fuel cells. *British Ceramic Transactions,* 103**,** 202-210.

TIKHONOV, A. M. 2006. X-ray study of the electric double layer at the n-hexane/nanocolloidal silica interface. *Journal of Chemical Physics,* 124.

TOEBES, M. L., BITTER, J. H., VAN DILLEN, A. J. & DE JONG, K. P. 2002. Impact of the structure and reactivity of nickel particles on the catalytic growth of carbon nanofibers. *Catalysis Today,* 76**,** 33-42.

TORRIE, G. M. & VALLEAU, J. P. 1979. Monte-Carlo study of an electrical double layer. *Chemical Physics Letters,* 65**,** 343-346.

TORRIE, G. M. & VALLEAU, J. P. 1980. Electrical double layers: 1. Monte-Carlo study of a uniformly charged surface. *Journal of Chemical Physics,* 73**,** 5807-5816.

TRASATTI, S. 1974. Concept of absolute electrode potential: an attempt at a calculation. *Journal of Electroanalytical Chemistry,* 52**,** 313-329.

TRASATTI, S. 1982. The concept and physical meaning of absolute electrode potential- a reassessment. *Journal of Electroanalytical Chemistry,* 139**,** 1-13.

TRASATTI, S. 1990. The absolute electrode potential- the end of the story. *Electrochimica Acta,* 35**,** 269-271.

TRIKALITIS, P. N. & POMONIS, P. J. 1995. Catalytic activity and selectivity of perovskite La1-xSrxV1-x3+Vx4+O3 for the transformation of isopropanol. *Applied Catalysis a-General,* 131**,** 309-322.

TRIKALITIS, P. N., BAKAS, T. V., MOUKARIKA, A. C., SDOUKOS, A. T., ANGELIDIS, T. & POMONIS, P. J. 1998. A Rietveld analysis of the transformation of (La-Sr-V-O)(reduced) to (La-Sr-V-O)(oxidized) solids and the effect on their surface catalytic properties. *Applied Catalysis a-General,* 167**,** 295-308.

TROVARELLI, A. 1996. Catalytic Properties of Ceria and CeO₂-Containing Materials. *Catalysis Reviews: Science and Engineering,* 38**,** 439 - 520.

TSIPLAKIDES, D. & VAYENAS, C. G. 2001. Electrode work function and absolute potential scale in solid-state electrochemistry. *Journal of the Electrochemical Society,* 148**,** E189-E202.

TSIPLAKIDES, D. & VAYENAS, C. G. 2002. The absolute potential scale in solid state electrochemistry. *Solid State Ionics,* 152**,** 625-639.

TSIPLAKIDES, D., ARCHONTA, D. & VAYENAS, C. G. 2007. Absolute potential measurements in solid and aqueous electrochemistry using two Kelvin probes and their implications for the electrochemical promotion of catalysis. *Topics in Catalysis,* 44**,** 469-479.

US DEPARTMENT OF ENERGY, 2004. Fuel Cell Handbook (Seventh Edition) Morgantown.

US DEPARTMENT OF ENERGY, August, 2006. Effects of a Transition to a Hydrogen Economy on Employment in the United States: Report to Congress.

US DEPARTMENT OF ENERGY, February 2002. A National Vision of America's Transition to a hydrogen Economy--- to 2030 and beyond.

US DEPARTMENT OF ENERGY, January, 2009. Hydrogen and Fuel Cell Activities, Progress, and Plans: Report to Congress.

VANHASSEL, B. A., BOUKAMP, B. A. & BURGGRAAF, A. J. 1991. Electrode polarization at the Au, O2 (g)/yttria stabilized zirconia interface: 1. theoretical considerations of reaction model. *Solid State Ionics,* 48**,** 139-154.

VARMA, S., WANI, B. N. & GUPTA, N. M. 2001. Synthesis, characterisation, TPR/TPO and activity studies on LaMnxV1-xO4-delta catalysts. *Applied Catalysis a-General,* 205**,** 295-304.

VARMA, S., WANI, B. N. & GUPTA, N. M. 2003. Redox behavior and catalytic activity of La-Fe-V-O mixed oxides. *Applied Catalysis a-General,* 241**,** 341-348.

VAYENAS, C. G. 2000. On the work function of the gas exposed electrode surfaces in solid state electrochemistry. *Journal of Electroanalytical Chemistry,* 486**,** 85-90.

VAYENAS, C. G., BEBELIS, S., PLIANGOS, C., BROSDA, S. & TSIPLAKIDES, D. 2001. *Electrochemical Activiation of Catalysis: Promotion, Electrochemical Promotion and Metal-support Interactions* New York Kluwer

VERNOUX, P., DJURADO, E. & GUILLODO, M. 2001. Catalytic and electrochemical properties of doped lanthanum chromites as new anode materials for solid oxide fuel cells. *Journal of the American Ceramic Society,* 84**,** 2289-2295.

VERNOUX, P., GUILLODO, M., FOULETIER, J. & HAMMOU, A. 2000. Alternative anode material for gradual methane reforming in solid oxide fuel cells. *Solid State Ionics,* 135**,** 425-431.

VOZDECKY, P., ROOSEN, A., MA, Q. L., TIETZ, F. & BUCHKREMER, H. P. 2011. Properties of tape-cast Y-substituted strontium titanate for planar anode

substrates in SOFC applications. *Journal of Materials Science,* 46**,** 3493-3499.

WANG, D. L., XIN, H. L., YU, Y. C., WANG, H. S., RUS, E., MULLER, D. A. & ABRUNA, H. D. 2010. Pt-Decorated PdCo@Pd/C Core-Shell Nanoparticles with Enhanced Stability and Electrocatalytic Activity for the Oxygen Reduction Reaction. *Journal of the American Chemical Society,* 132**,** 17664-17666.

WANG, J. & BARD, A. J. 2001. On the absence of a diffuse double layer at electronically conductive polymer film electrodes. Direct evidence by atomic force microscopy of complete charge compensation. *Journal of the American Chemical Society,* 123**,** 498-499.

WANG, S., KOBAYASHI, T., DOKIYA, M. & HASHIMOTO, T. 2000. Electrical and Ionic Conductivity of Gd-Doped Ceria. *Journal of the Electrochemical Society,* 147**,** 3606-3609.

WANG, W., ZHANG, L. & JIANG, S. P. 2008. Potential oscillation of methane oxidation reaction on (La0.75Sr0.25)(Cr0.5Mn0.5)O3 electrodes of solid oxide fuel cells. *Journal of Power Sources,* 178**,** 92-96.

WANG, Z. Y. & MA, Y. Q. 2010a. Insights from Monte Carlo simulations on charge inversion of planar electric double layers in mixtures of asymmetric electrolytes. *Journal of Chemical Physics,* 133.

WANG, Z. Y. & MA, Y. Q. 2010b. Impact of Head Group Charges, Ionic Sizes, and Dielectric Images on Charge Inversion: A Monte Carlo Simulation Study. *Journal of Physical Chemistry B,* 114**,** 13386-13392.

WEBB, J. B. & SAYER, M. 1976. High temperature transport in lanthanum strontium vanadate. *Journal of Physics C-Solid State Physics,* 9**,** 4151-4164.

WILLIAMS, G. D., SOPER, A. K., SKIPPER, N. T. & SMALLEY, M. V. 1998. High-resolution structural study of an electrical double layer by neutron diffraction. *Journal of Physical Chemistry B,* 102**,** 8945-8949.

WILLIFORD, R. E., CHICK, L. A., MAUPIN, G. D., SIMNER, S. P. & STEVENSON, J. W. 2003. Diffusion limitations in the porous anodes of SOFCs. *Journal of the Electrochemical Society,* 150**,** A1067-A1072.

WILSON, J. R., KOBSIRIPHAT, W., MENDOZA, R., CHEN, H. Y., HILLER, J. M., MILLER, D. J., THORNTON, K., VOORHEES, P. W., ADLER, S. B. & BARNETT, S. A. 2006. Three-dimensional reconstruction of a solid-oxide fuel-cell anode. *Nature Materials,* 5**,** 541-544.

WILSON, T. L. & SHEWMON, P. G. 1966. Role of the interfacial diffusion in sintering

of copper. *Transactions of the Metallurgical Society of Aime,* 236**,** 48-&.

WUENSCH, B. J., EBERMAN, K. W., HEREMANS, C., KU, E. M., ONNERUD, P., YEO, E. M. E., HAILE, S. M., STALICK, J. K. & JORGENSEN, J. D. 2000. Connection between oxygen-ion conductivity of pyrochlore fuel-cell materials and structural change with composition and temperature. *Solid State Ionics,* 129**,** 111-133.

XIAO, G. L., LIU, Q., DONG, X. H., HUANG, K. & CHEN, F. L. 2010. Sr2Fe4/3Mo2/3O6 as anodes for solid oxide fuel cells. *Journal of Power Sources,* 195**,** 8071-8074.

XU, Z. R., LUO, J. L., CHUANG, K. T. & SANGER, A. R. 2007. LaCrO3-VOx-YSZ anode catalyst for solid oxide fuel cell using impure hydrogen. *Journal of Physical Chemistry C,* 111**,** 16679-16685.

XU, Z. R., FU, X. Z., LUO, J. L. & CHUANG, K. T. 2010. Carbon Deposition on Vanadium-Based Anode Catalyst for SOFC Using Syngas as Fuel. *Journal of the Electrochemical Society,* 157**,** B1556-B1560.

YAHIRO, H., EGUCHI, K. & ARAI, H. 1989. Electrical properties and reducibilities of ceria rare earth oxide systems and their application to solid oxide fuel cell. *Solid State Ionics,* 36**,** 71-75.

YANG, L., CHENG, Z., LIU, M. L. & WILSON, L. 2010. New insights into sulfur poisoning behavior of Ni-YSZ anode from long-term operation of anode-supported SOFCs. *Energy & Environmental Science,* 3**,** 1804-1809.

YANG, X. & IRVINE, J. T. S. 2008. (La0.75Sr0.25)(0.95)Mn0.5Cr0.5O3 as the cathode of solid oxide electrolysis cells for high temperature hydrogen production from steam. *Journal of Materials Chemistry,* 18**,** 2349-2354.

YASHIRO, K., KOBAYASHI, T., HAN, L. Q., KAIMAI, A., NIGARA, Y., KAWADA, T., MIZUSAKI, J. & KAWAMURA, K. 2001. Electrochemical properties of oxide anode materials for SOFC. *In:* YOKOKAWA, H. & SINGHAL, S. C. (eds.) *Solid Oxide Fuel Cells Vii.*

YATES, C. & WINNICK, J. 1999. Anode materials for a hydrogen sulfide solid oxide fuel cell. *Journal of the Electrochemical Society,* 146**,** 2841-2844.

YE, X. F., WANG, S. R., HU, Q., CHEN, J. Y., WEN, T. L. & WEN, Z. Y. 2009. Improvement of Cu-CeO2 anodes for SOFCs running on ethanol fuels. *Solid State Ionics,* 180**,** 276-281.

YE, Y. M., HE, T. M., LI, Y., TANG, E. H., REITZ, T. L. & JIANG, S. P. 2008.

Pd-promoted La0.75Sr0.25Cr0.5Mn0.5O3/YSZ composite anodes for direct utilization of methane in SOFCs. *Journal of the Electrochemical Society,* 155**,** B811-B818.

YUN, J. W., YOON, S. P., HAN, J., PARK, S., KIM, H. S. & NAM, S. W. 2010. Ceria Coatings Effect on H2S Poisoning of Ni/YSZ Anodes for Solid Oxide Fuel Cells. *Journal of the Electrochemical Society,* 157**,** B1825-B1830.

ZHA, S. W., CHENG, Z. & LIU, M. L. 2005a. A sulfur-tolerant anode material for SOFCsGd2Ti1.4Mo0.6O7. *Electrochemical and Solid State Letters,* 8**,** A406-A408.

ZHA, S. W., CHENG, Z. & LIU, M. L. 2007. Sulfur poisoning and regeneration of Ni-based anodes in solid oxide fuel cells. *Journal of the Electrochemical Society,* 154**,** B201-B206.

ZHA, S. W., TSANG, P., CHENG, Z. & LIU, M. L. 2005b. Electrical properties and sulfur tolerance of La0.75Sr0.25Cr1-xMnxO3 under anodic conditions. *Journal of Solid State Chemistry,* 178**,** 1844-1850.

ZHAN, Z. L. & BARNETT, S. A. 2005a. An octane-fueled olid oxide fuel cell. *Science,* 308**,** 844-847.

ZHAN, Z. L. & BARNETT, S. A. 2005b. Use of a catalyst layer for propane partial oxidation in solid oxide fuel cells. *Solid State Ionics,* 176**,** 871-879.

ZHAN, Z. L. & LEE, S. I. 2010. Thin film solid oxide fuel cells with copper cermet anodes. *Journal of Power Sources,* 195**,** 3494-3497.

ZHAN, Z. L., LIN, Y. B., PILLAI, M., KIM, I. & BARNETT, S. A. 2006. High-rate electrochemical partial oxidation of methane in solid oxide fuel cells. *Journal of Power Sources,* 161**,** 460-465.

ZHANG, C. J., GRASS, M. E., MCDANIEL, A. H., DECALUWE, S. C., EL GABALY, F., LIU, Z., MCCARTY, K. F., FARROW, R. L., LINNE, M. A., HUSSAIN, Z., JACKSON, G. S., BLUHM, H. & EICHHORN, B. W. 2010a. Measuring fundamental properties in operating solid oxide electrochemical cells by using in situ X-ray photoelectron spectroscopy. *Nature Materials,* 9**,** 944-949.

ZHANG, L. L., ZHOU, Q. J., HE, Q. A. & HE, T. M. 2010b. Double-perovskites A(2)FeMoO(6-delta) (A = Ca, Sr, Ba) as anodes for solid oxide fuel cells. *Journal of Power Sources,* 195**,** 6356-6366.

ZHANG, P., HUANG, Y. H., CHENG, J. G., MAO, Z. Q. & GOODENOUGH, J. B. 2011. Sr2CoMoO6 anode for solid oxide fuel cell running on H-2 and CH4 fuels.

Journal of Power Sources, 196**,** 1738-1743.

ZHAO, F., JIANG, Y., GY, L. & VIRKAR, A. V. 2001. *Electrochemical Society Series* 16**,** 501.

ZHOU, Z. F., KUMAR, R., THAKUR, S. T., RUDNICK, L. R., SCHOBERT, H. & LVOV, S. N. 2007. Direct oxidation of waste vegetable oil in solid-oxide fuel cells. *Journal of Power Sources,* 171**,** 856-860.

ZHU, H. Y. & KEE, R. J. 2008. Modeling distributed charge-transfer processes in SOFC membrane electrode assemblies. *Journal of the Electrochemical Society,* 155**,** B715-B729.

ZHU, W., XIA, C. R., FAN, J., PENG, R. R. & MENG, G. Y. 2006. Ceria coated Ni as anodes for direct utilization of methane in low-temperature solid oxide fuel cells. *Journal of Power Sources,* 160**,** 897-902.